

Melting and freezing beneath Larsen C Ice Shelf, Antarctica

A thesis submitted to the School of Environmental Science
of the University of East Anglia in partial fulfilment
of the requirements for the degree of Doctor of Philosophy

Lianne Claire Harrison

May 2021

© This copy of the thesis has been supplied on condition that anyone who consults it is understood to recognise that its copyright rests with the author and that use of any information derived there-from must be in accordance with current UK Copyright Law. In addition, any quotation or extract must include full attribution.

© Copyright 2021
Lianne Claire Harrison

Abstract

Observations of recent surface lowering of Larsen C Ice Shelf (LCIS), Antarctica, and the calving of a large iceberg in 2017, have prompted concern about the stability of this ice shelf. The influence on grounded ice upstream that would result from ice shelf thinning or collapse could affect global sea level rise on decadal time scales. In this thesis, the extent to which oceanic basal melting has driven ice loss beneath LCIS, resulting in the observed lowering, was investigated by simulating ocean conditions in this region using a high resolution ocean model. The model included a new bathymetry containing a southern seabed trough discovered by seismic observations.

Ocean circulation within the cavity was found to be separated into two distinct components, connected by an eastward, cross-cavity flow initially steered by the trough. In a simulation using an older seabed without the trough, this circulation was not seen. The greatest melting in the cavity corresponded to the location of rapid, inflowing water from the continental shelf which followed the trough. Using a different, older bathymetry which shallowed significantly in the northern half of the cavity, intense melting shifted from the south to the northeast.

In experiments subjected to a uniform ocean warming, an increase in local melting occurred, concentrated in the trough. This does not correspond to the observed northward-intensified lowering of LCIS, suggesting oceanic forcing is not responsible for these changes. The extent of marine ice, deposited when ocean water freezes to the base of the ice shelf and advects downstream, is significantly reduced in critical regions of the ice shelf base when ocean temperatures are raised. As marine ice is thought to stabilise LCIS, potential future ocean warming may therefore lead to collapse. This demonstrates a high sensitivity of LCIS stability to even small changes in ocean forcing.

Access Condition and Agreement

Each deposit in UEA Digital Repository is protected by copyright and other intellectual property rights, and duplication or sale of all or part of any of the Data Collections is not permitted, except that material may be duplicated by you for your research use or for educational purposes in electronic or print form. You must obtain permission from the copyright holder, usually the author, for any other use. Exceptions only apply where a deposit may be explicitly provided under a stated licence, such as a Creative Commons licence or Open Government licence.

Electronic or print copies may not be offered, whether for sale or otherwise to anyone, unless explicitly stated under a Creative Commons or Open Government license. Unauthorised reproduction, editing or reformatting for resale purposes is explicitly prohibited (except where approved by the copyright holder themselves) and UEA reserves the right to take immediate 'take down' action on behalf of the copyright and/or rights holder if this Access condition of the UEA Digital Repository is breached. Any material in this database has been supplied on the understanding that it is copyright material and that no quotation from the material may be published without proper acknowledgement.

Reference map of Larsen C Ice Shelf

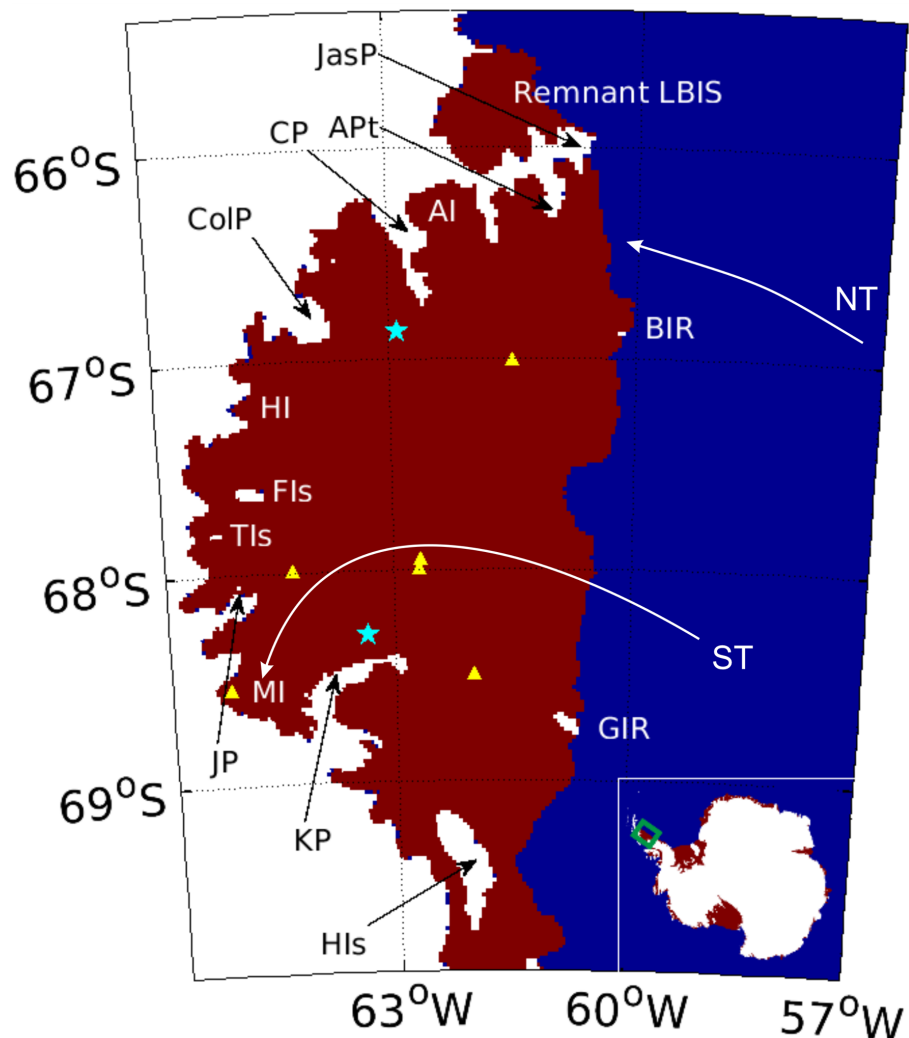


Figure 0.1: Map showing the location of Larsen C Ice Shelf on the Antarctic Peninsula (see inset) and features described throughout this thesis. This map is intended to accompany the reading of the thesis for reference when these features are discussed in the text. The extent of the floating ice is shown in red, the grounded ice sheet is shown in white and the ocean in blue, with grounding line and calving front positions taken from Bedmap2 (Fretwell et al., 2013). Note that the ice front position shows the configuration before iceberg A68 calved in July 2017. KP is Kenyon Peninsula; JP is Joerg Peninsula; JasP is Jason Peninsula; ColP is Cole Peninsula; CP is Churchill Peninsula; BIR is Bawden Ice Rise; GIR is Gipps Ice Rise; ST is the southern trough; NT is the northern trough; MI is Mobiloil Inlet; HI is Hess Inlet; AI is Adie Inlet; FIS is Francis Island; TIS is Tonkin Island; HIs is Hearst Island; APT is Argo Point; Remnant LBIS is the part of the Larsen B Ice Shelf remaining after its collapse in 2002; cyan stars are mooring sites reported by Nicholls et al. (2012); yellow triangles are locations of GPS receivers used for tidal analysis reported in King et al. (2011b).

Author's note

The research and results presented in this thesis have been summarised in a paper submitted to *Geophysical Research Letters*:

Harrison, L. C., Holland, P. R., Heywood, K. J., Nicholls, K. W., Brisbourne, A. M. (Submitted) Sensitivity of melting, freezing and marine ice beneath Larsen C Ice Shelf to changes in ocean forcing.

Creation of the seabed bathymetry grid, detailed in Chapter 2, was published as part of the following paper:

Brisbourne, A., Kulesa, B., Hudson, T., Harrison, L., Holland, P., Luckman, A., Bevan, S., Ashmore, D., Hubbard, B., Pearce, E., White, J., Booth, A., Nichols, K., Smith, A. (2020) An updated seabed bathymetry beneath Larsen C Ice Shelf, Antarctic Peninsula. *Earth System Science Data*. 12 (2), 887—896. URL: <https://doi.org/10.5194/essd-12-887-2020>.

Acknowledgements

I would not have completed this thesis without the immeasurable support and care of several people. Firstly, I would like to thank my supervisors, Paul, Karen and Keith for the fantastic help and encouragement you have given me over the past four years. Paul deserves a special mention for only letting out an audible sigh whenever I showed up his office door unannounced, with often trivial questions about ocean dynamics or the basics of numerical modelling, rather than actually ever turning me away. I could not have asked for a better supervisory team and am so thankful to have learned from the best.

I am grateful to the entire Polar Oceans team at BAS who have been quick to offer their advice and expertise to help me on my journey to becoming a proper scientist. I am especially indebted to Kaitlin who has set the bar for me to aim for as a researcher/programmer, Keith M for his patience every time I came to talk tides with only minimal cake-based bribes, Pete for even more tides discussions and continually convincing me I would in fact make it to the end, Ruth for helping me to overcome some of my more infuriating model issues, David for paying more attention than me and therefore frequently reminding me how the model works, Jake for teaching me more than any textbook could about oceanography and lastly to Rachael for more things than I can list. You've been the best housemate, officemate, oceanography reference guide, MATLAB tech support, sounding board and friend I could have hoped for. Thank you for everything. I also want to say a big thank you to Elena for always enthusiastically listening to my many rants and for being MAGIC in more ways than one.

My sanity throughout this whole endeavour, particularly while having the misfortune of writing the thesis while living through the uncertainty of a global pandemic, is owed to an incredible bunch of friends in Leeds, Cambridge and elsewhere, and my wonderful family. I appreciate all of you more than I can adequately express in words as opposed to hugs. I particularly want to thank my mum, for supporting me, physically, mentally and financially, well into my thirties because I love to learn. I promise, this is the last degree. I will get a real job now.

Contents

Abstract	v
Reference map of Larsen C Ice Shelf	vii
Author’s note	ix
Acknowledgements	xi
List of figures	xvii
List of tables	xxvii
1 Introduction	1
1.1 Ice shelf collapse	2
1.1.1 Sea level rise	4
1.2 Surface lowering	6
1.2.1 Atmospheric versus oceanic effects on lowering	8
1.3 Basal melting	9
1.3.1 Changing conditions of the Weddell Sea	13
1.4 Current knowledge of LCIS cavity oceanography	14
1.4.1 Ocean temperatures	14
1.4.2 Ocean circulation	17
1.4.3 Tides	19
1.5 Importance of cavity geometry	20
1.5.1 Recent advances in knowledge of LCIS geometry	21
1.6 Ice shelf stability	22
1.7 Marine ice	24
1.7.1 Effect of potential weakening of marine ice on LCIS	27
1.8 This study	28
1.8.1 Aims and objectives	28
1.8.2 Thesis outline	28
2 Methods	31
2.1 The MITgcm	31
2.2 Model domain	34
2.2.1 Grid resolution	34
2.2.2 Partial cells	36
2.2.3 Creation of bathymetry	37
2.2.4 Alterations near the grounding line	40
2.3 Ice shelf package	41
2.3.1 Three-equation model	41

2.3.2	Freezing	44
2.4	Boundary conditions	45
2.4.1	Tides	45
2.4.2	Sponge layer	46
2.5	Parameterisations and other settings	47
2.5.1	Model timestep	47
2.5.2	Limitations of the model	48
2.6	Experiments	49
3	Model validation	51
3.1	Confirming model had reached steady state	51
3.1.1	Domain-averaged melt rate	51
3.1.2	Domain-averaged potential temperature and salinity	53
3.1.3	Equilibrium in a single cell	53
3.2	Circulation across the model domain	54
3.2.1	Inflow	56
3.2.2	Outflow	59
3.3	Melt rate and pattern	63
3.3.1	Enhanced melting in the south	63
3.3.2	Grounding line and ice front melting	68
3.3.3	Bawden Ice Rise	70
3.4	Freezing and marine ice	70
3.5	Parameterisation of melt/freeze rate	74
3.6	Tides	75
3.6.1	Comparison to available observations	76
3.6.2	Effect of tides on circulation	78
3.6.3	Effect of tides on melting and freezing	80
3.7	Concluding remarks	83
4	Effects of seabed bathymetry on modelled conditions beneath LCIS	85
4.1	Alternate model geometries	86
4.2	Circulation differences between model cavities	88
4.2.1	Brisbourne versus Bedmap2	88
4.2.2	Brisbourne versus Mueller	91
4.3	Effects on melting and freezing at ice base	96
4.3.1	Brisbourne versus Bedmap2	96
4.3.2	Brisbourne versus Mueller	96
4.4	Sensitivity of melt rate at Bawden Ice Rise to its geometry	103
4.5	Grounding line alterations	107
4.6	Concluding remarks	110
5	Sensitivity of LCIS cavity to changes in ocean temperature forcing	113
5.1	Circulation changes in a warmer cavity	114
5.2	Melt rate increases	119
5.2.1	Relationship between temperature and melt rate	120
5.2.2	Changes to the melt pattern	122
5.2.3	Bawden Ice Rise	124

5.3	Freezing changes	126
5.4	Marine ice changes and implications for the stability of LCIS	127
5.4.1	Thickness and extent reductions	129
5.4.2	Current versus historical marine ice weakening	132
5.5	Is ocean warming responsible for the observed changes?	133
5.6	Concluding remarks	135
6	Conclusions	137
6.1	Importance of bathymetry for circulation and melt rate	138
6.2	Atmospheric or oceanic drivers of surface lowering	139
6.3	Threat to the stability of LCIS imposed by the retreat of marine ice .	141
6.4	Future work	143
6.5	Summary	144
A	Model input parameters	147
	References	150

List of figures

0.1	Map showing the location of Larsen C Ice Shelf on the Antarctic Peninsula (see inset) and features described throughout this thesis. This map is intended to accompany the reading of the thesis for reference when these features are discussed in the text. The extent of the floating ice is shown in red, the grounded ice sheet is shown in white and the ocean in blue, with grounding line and calving front positions taken from Bedmap2 (Fretwell et al., 2013). Note that the ice front position shows the configuration before iceberg A68 calved in July 2017. KP is Kenyon Peninsula; JP is Joerg Peninsula; JasP is Jason Peninsula; ColP is Cole Peninsula; CP is Churchill Peninsula; BIR is Bawden Ice Rise; GIR is Gipps Ice Rise; ST is the southern trough; NT is the northern trough; MI is Mobiloil Inlet; HI is Hess Inlet; AI is Adie Inlet; FIs is Francis Island; TIs is Tonkin Island; HIs is Hearst Island; APt is Argo Point; Remnant LBIS is the part of the Larsen B Ice Shelf remaining after its collapse in 2002; cyan stars are mooring sites reported by Nicholls et al. (2012); yellow triangles are locations of GPS receivers used for tidal analysis reported in King et al. (2011b).	vii
1.1	Map showing the Antarctic Ice Sheet (in white) and ice shelves (grey) surrounded by the Southern Ocean (blue). The East Antarctic Ice Sheet (EAIS) and West Antarctic Ice Sheet (WAIS) are divided by the Transantarctic Mountains. The Antarctic Circumpolar Current is bounded in the north by the Subantarctic Front (SAF) and to the south by the Southern Boundary (SB). This clockwise circulation brings Circumpolar Deep Water onto the continental shelf in front of the Antarctic Peninsula (AP) via the Weddell Gyre. The area investigated in this thesis is outlined in red.	2
1.2	Schematic showing the configuration of an ice shelf and some of the ocean dynamics that can contribute to the melting at an ice shelf base. The three modes of basal melting, as described in Jacobs et al. (1992), are elaborated on in Section 1.3.	3
1.3	Map showing the location of ice shelves on the Antarctic Peninsula. White area shows the extent of each ice shelf as of 2009, by which time a number of ice shelves had retreated significantly in the previous 50 years (Prince Gustav, Larsen A, Larsen B, Jones, and Wordie). Image adapted from Cook and Vaughan (2010).	5

1.4	(a) Surface elevation data from satellite radar altimeters showed a lowering of the surface of LCIS between 1994-2011. Image adapted from Holland et al. (2015). (b) Altimetry-derived lowering during the period 1992-2001 is shown using both a colour scale and white contours at intervals of 0.1 m yr^{-1} , adapted from Shepherd et al. (2003). The red contour shows the 1990 extent of the ice shelf; black dots show locations of data points used to create the map; the blue dot is the Larsen meteorological station and the black line starting at point 'B' indicates a transect used for analysis by Shepherd et al. (2003). (c) Surface lowering seen by radar altimeters between 1994-2016, adapted from Adusumilli et al. (2018). Black dots indicate regions where results have a confidence interval above 67%.	7
1.5	Map showing the potential temperature of the ocean at the sea floor around Antarctica. Black contour indicates 1000 m depth of the seabed below the ocean's surface. Image adapted from Petty et al. (2013).	10
1.6	Freezing temperature profile of sea water showing the depression with decreasing depth below the surface. This profile is based on a salinity of 34.5 throughout the water column.	12
1.7	Water masses in and around the LCIS cavity. ISW is Ice Shelf Water; MWDW is Modified Warm Deep Water; HSSW is High Salinity Shelf Water. Contours show ice thickness on the ice shelf (shaded in light grey) and bathymetry over the continental shelf (white), values given are in units of metres. Black triangles show locations of Expendable Bathythermographs measured by Bathmann et al. (1994). Black hollow squares, black circles, and green crosses show locations of Conductivity, Temperature, Depth casts taken by Bathmann et al. (1994), Nicholls et al. (2004), and Hellmer et al. (2008), respectively. Red filled squares show locations of borehole drill/mooring sites. Image adapted from Nicholls et al. (2012). . . .	16
1.8	Temperature of the ocean from Conductivity, Temperature, Depth measurements at several locations roughly traversing a longitude of 60°W , along the ice front. Numbers along the top axis indicate where an individual cast was taken (see black hollow squares in Figure 1.7 for exact locations). Casts started just south of Gipps Ice Rise, covered the southern trough and finished south of Bawden Ice Rise (see Figure 0.1 for place names). Image adapted from Bathmann et al. (1994).	17
1.9	Plume thickness and velocities adapted from Holland et al. (2009).	18
1.10	The section of ice removed from the Larsen C ice front in July 2017, when iceberg A68 calved, is shown by greyscale thermal imaging. Image obtained from O'Leary et al. (12 July 2017).	24

1.11	Proposed marine ice flow bands (yellow shading) under LCIS are inferred from missing basal returns in airborne radar sounding measurements. Blue lines show flight path of survey with red portions indicating positions where the base was not detected. Image adapted from Holland et al. (2009).	26
2.1	The model domain extends from the remnant Larsen B Ice Shelf in the north to Hearst Island in the south, and from the most westward point of the LCIS grounding line to the edge of the continental shelf in the east. Colours show the depth of the seabed adapted from Brisbourne et al. (2020) and the newly discovered extent of the southern trough is marked (ST). The black contour denotes the extent of the floating ice, and grounded ice is indicated in white. Note that this configuration represents the shape of the ice shelf before the iceberg calving in July 2017.	35
2.2	Black circles represent seismic sounding points used to construct an interpolated bathymetry for this study. Sites were selected to either verify data gathered from alternate methods, such as gravity inversions, or to confirm the extent of previously located seabed features.	38
2.3	(a) Bedmap2 surface elevation map shows relatively flat seabed under LCIS from close to the grounding line to the calving front. Gipps Ice Rise can also be seen but Bawden Ice Rise, which should be grounded at $\sim 66.9^{\circ}\text{S}$, is missing from this dataset. (b) Bathymetry under LCIS mapped by natural neighbour interpolation of seismic sounding points and Bedmap2 surface elevation data beyond the calving front of the ice shelf, marked by the black contour. (c) Bathymetry used in the model which includes all alterations close to the grounding line, as detailed in the text.	39
2.4	(a) Schematic showing the two areas of the model domain which used different datasets to create the new LCIS bathymetry used in this study. The red area depicts where direct seismic measurements were interpolated and the white areas indicate locations where bathymetry data was taken from Bedmap2. Interpolation between these two datasets across the grounding line led to the need for bathymetric alterations in this area to ensure communication between model grid cells. (b) Colour bar shows how much the bathymetry needed to be lowered to accommodate at least a 40 m clearance between the ice base and sea floor, and to open neighbouring columns to ensure lateral communication between ocean cells. As a consequence of this second constraint, the alterations at some of these locations close to the grounding line greatly exceed 40 m.	41
2.5	Ice topography used in this study shows the depth the ice base reaches in the cavity. Mean sea level is at zero.	42

2.6	Unbalanced fluxes of heat and/or salt through the ice (Q_i) and ocean (Q_o) result in a phase change at the boundary layer accompanied by an exchange of latent heat and salt ($Q_{latent/brine}$). Gradients of temperature and salinity between the far field properties of the ocean and those at the boundary ($T_o/S_o - T_b/S_b$), and between the ice interior and the interface ($T_i/S_i - T_b/S_b$), control the rate of flux through the ice-ocean boundary. Note that salt in the ice (S_i) is negligible and taken to be zero. Image adapted from Holland and Jenkins (1999).	44
3.1	Timeseries of domain-averaged melt rate (a), potential temperature (c) and salinity (e) across the standard run and the fractional change with respect to initial, annual melt rate change (b), potential temperature change (d) and salinity change (f). The fractional change is defined as the change in a variable over the preceding 12-month period for every month of model output, divided by the change in that variable across the first year of the run.	52
3.2	Timeseries of a single model grid cell melt rate (a), potential temperature (c) and salinity (e), corresponding to the southern observation site, and fractional change with respect to initial, annual melt rate change (b), potential temperature change (d) and salinity change (f).	55
3.3	(a) Water column thickness with barotropic streamfunction contours overlaid. Yellow contours are positive values (clockwise flow), green contours are negative (anticlockwise flow) and the pink contour shows zero flow. Values indicating volumetric flow rate have units of Sverdrups. (b) The barotropic streamlines, now all shown in yellow, primarily follow contours of water column thickness underneath the ice, shown in filled shades of purple.	56
3.4	Potential temperature at the sea floor with sea floor velocities overlaid. Vectors with magnitudes greater than 5 cm s^{-1} have been removed for clarity.	57
3.5	Water column thickness with sea floor velocities overlaid at the location of inflow to the cavity.	58
3.6	Potential temperature at the sea surface over the continental shelf and at the ice-ocean interface within the cavity, with surface velocities at corresponding locations overlaid. Vectors with magnitudes greater than 5 cm s^{-1} have been removed for clarity. . .	60
3.7	Water column thickness with surface velocities overlaid at locations of outflow from the cavity.	61

3.8	(a) Thickness of the meltwater plume, defined as water with a density change of more than 0.025 kg m^{-3} from initial conditions, with plume velocity vectors overlaid. Vectors with magnitudes greater than 5 cm s^{-1} have been removed for clarity. (b) Plume thickness and velocities adapted from Holland et al. (2009) shown for comparison.	62
3.9	(a) Steady state melt and freeze pattern across the ice shelf from the standard run; red shows melting, blue shows locations of refreezing. (b) Melt/freeze pattern adapted from Mueller et al. (2012) is shown for comparison. Cyan contours show extent of refreezing but no freeze rates are reported; black contours in the northeast indicate mean barotropic flow speeds of 0.2, 0.3, and 0.4 m s^{-1}	64
3.10	Flow speeds at the ice-ocean interface calculated from horizontal velocity vectors in the boundary layer directly beneath the ice base. .	65
3.11	Thermal driving is generally lower throughout the domain in the standard run which includes tidal forcing (a) versus when the model set up does not include tides (b). Velocity vectors from the ice-ocean boundary layer are overlaid for each case, with magnitudes greater than 5 cm s^{-1} removed for clarity.	68
3.12	Observations of potential temperature and salinity profiles from borehole sites (see Figure 0.1 for locations) adapted from Nicholls et al. (2012) (a). The red and blue lines each represent means of several different profiles taken in separate data gathering sessions. These profiles are shown for comparison with modelled potential temperature (b) and salinity (c) profiles at the northern observation site (grey) and southern observation site (black). The straight red lines in (a) and (b) show the potential freezing temperature profile. .	69
3.13	(a) Steady state melt and freeze pattern across the ice shelf from the standard run; red shows melting, blue shows locations of refreezing. (b) Coloured contours show melt and freeze rates adapted from Holland et al. (2009) for comparison. Positive values indicate melting and have units of m yr^{-1} . Grey contours define the ice draft.	71
3.14	(a) Marine ice thickness which would accumulate at the ice base of LCIS and advect downstream if ice velocities and modelled steady state melt and freeze rates were to persist for 500 years. (b) Yellow shading shows marine ice bands inferred from missing radar signal returns, adapted from Holland et al. (2009), match locations of modelled marine bands.	73

3.15	Melt rate difference with alternative melting parameters. Although the pattern is very similar in both cases, the melt rate using melting parameters measured and calculated by Davis and Nicholls (2019a) (a) shows much higher values than the melt rate produced using the standard run melting parameters described in the text (b).	75
3.16	Timeseries of sea surface height anomaly at six sites on the ice shelf calculated from observed ice elevation changes (red). Modelled sea surface height timeseries at corresponding locations (blue) show tides within the model cavity are behaving as expected. Site names correspond to those in King et al. (2011b) and are shown in Figure 0.1.	77
3.17	Tidal ellipses of the seven strongest constituents in the region of LCIS, computed from model boundary layer velocities at the location of the southern observation site (a) are compared with those created from measured currents 13.5 m below the ice base (b), adapted from Davis and Nicholls (2019a).	80
3.18	Water column thickness with barotropic streamfunction contours overlaid from a tides-only simulation with no contributions to buoyancy forcing from thermohaline exchange with the ice shelf. Yellow contours are positive values (clockwise flow), green contours are negative (anticlockwise flow) and the pink contour shows zero flow. Values indicating volumetric flow rate have units of Sverdrups.	81
3.19	Melting (red) and freezing (blue) produced by the standard run (a) compared with results from a simulation run without tides (b).	82
4.1	Bathymetry used in the standard run, otherwise referred to as the Brisbane bathymetry (a), the Bedmap2 run (b) and the Mueller run (c) which was used in the study by Mueller et al. (2012).	86
4.2	Difference between the Brisbane and Bedmap2 bathymetries (a); red shows where the Brisbane seabed is higher compared with Bedmap2, blue shows where it is lower. (b) Difference between the Brisbane and Mueller bathymetries with red (blue) denoting the Brisbane seabed being higher (lower) than the Mueller seabed.	87
4.3	Barotropic streamfunction contours, in yellow, overlaid onto filled purple contours of water column thickness (top row, a-c), ice topography (middle, d-f), and bathymetry (bottom row, g-i) for each of the three geometry cases. Left column shows Brisbane case, middle column shows Bedmap2, and right column shows Mueller geometry.	89
4.4	Potential temperature on the sea floor of a run using the Brisbane bathymetry (a), Bedmap2 bathymetry (b) and Mueller bathymetry (c), with sea floor velocity vectors for each case overlaid. Vectors with magnitudes greater than 5 cm s^{-1} have been removed for clarity.	90

4.5	Zoomed in view of water column thickness at the location of inflow to the cavity, with sea floor vectors overlaid, for the Brisbane bathymetry (a), Bedmap2 run (b) and the Mueller geometry (c). Yellow contour indicates the position of the calving front.	93
4.6	Zoomed in view of water column thickness at the locations of outflow from the cavity, with vectors at the ice-ocean interface or sea surface overlaid, for the Brisbane bathymetry (a), Bedmap2 run (b) and the Mueller geometry (c). Yellow contour indicates the position of the calving front.	95
4.7	Potential temperature at the sea surface over the continental shelf and in the ice-ocean boundary layer under the ice base for simulations using the Brisbane geometry (a), Bedmap2 geometry (b) and Mueller geometry (c), with surface velocity vectors for each case overlaid. Vectors with magnitudes greater than 5 cm s^{-1} have been removed for clarity.	97
4.8	Melt rate produced by simulations which used the Brisbane geometry (a), Bedmap2 geometry (b) and Mueller geometry (c). Red shows melting, blue shows locations of refreezing.	98
4.9	Speed of the ocean in the boundary layer directly beneath the ice base produced by simulations using the Brisbane geometry (a), Bedmap2 geometry (b) and Mueller geometry (c).	99
4.10	Thermal driving in the standard run (a), the Mueller run (b) and the hybrid simulation (c) which uses the Mueller bathymetry and Bedmap2 ice draft. Blue shows areas of negative thermal driving which will result in direct refreezing in the model.	100
4.11	Melt rate produced by a simulation using the Mueller geometry and initial ocean temperature of -1.9°C in the ROMS model published in Mueller et al. (2012) (a) is compared with the melt rate produced from a run using the same cavity geometry and initial ocean temperature in the MITgcm (b). (c) and (d) show the melt rate produced by each model when the initial ocean temperature is increased to -1.7°C but all other conditions remain the same. The zero contour is shown in cyan (a & c) and blue (b & d) to mark the extent of freezing across the ice shelf.	101
4.12	Difference in water column thickness between the Mueller and hybrid cavities; red shows where the hybrid cavity is shallower than the Mueller domain, blue shows where it is thicker.	103
4.13	Melt rate produced by the simulation with Mueller geometry (a) versus that produced from a simulation which uses the Mueller bathymetry and Bedmap2 ice topography (b).	104

4.14	Side view along latitude $66^{\circ}54'$ S, where dark blue represents ocean cells in the model and white signifies the seabed and ice shelf, shows Bawden Ice Rise is not grounded in the standard run with Brisbane bathymetry (a) or in the Mueller geometry (b). Artificial changes were made to the bathymetry to ground Bawden Ice Rise by a tall and thin ridge in the narrow Bawden case (c) and by a more gradually sloping ice rise in the broad Bawden geometry (d).	105
4.15	Zoomed in view of the bathymetry surrounding Bawden Ice Rise in the standard run (a), narrow Bawden (b) and broad Bawden (c) runs. White indicates grounded cells and the yellow contour shows the calving front position.	106
4.16	Melt rate surrounding Bawden Ice Rise produced by the standard run (a), narrow Bawden run (b) and broad Bawden run (c); red shows melting, blue shows locations of refreezing and black contour shows the calving front position.	106
4.17	Water column thickness surrounding Bawden Ice Rise in the standard run (a), narrow Bawden run (b) and broad Bawden run (c), with barotropic streamfunction contours overlaid (in black). The calving front is indicated in yellow and values of labels on streamfunction contours have units of Sverdrups.	107
4.18	Melt rate produced by the run with broad Bawden bathymetry; red shows melting, blue shows locations of refreezing.	108
4.19	(a) Blue shading indicates where the seabed of the no digging cavity is higher than that in standard run. Green contour shows the altered grounding line of the no digging simulation. (b) Red shading indicates how much deeper the bathymetry around the grounding line is in the double digging case than the standard run.	109
4.20	Melt rate produced by the standard (a), no digging (b) and double digging (c) runs. Red shows melting, blue shows locations of refreezing.	110
4.21	Flow speeds directly beneath the ice in the standard (a), no digging (b) and double digging (c) runs.	111
4.22	Difference between thermal driving in the standard run and double digging simulation. Red shows where the double digging run has greater thermal driving than the standard run; blue shows areas where thermal driving is lower in the double digging run.	112

5.1	Barotropic streamfunction contours, in yellow, overlaid onto filled purple contours of water column thickness (top row, a-c), ice base depth (middle, d-f), and bathymetry (bottom row, g-i) for three temperature cases. Left column shows the standard run (-1.9°C), middle column shows a mid-temperature case (-1.5°C), and right column shows the warmest case modelled here (-1.0°C). Red stars indicate locations of density profiles shown in Figure 5.2 and discussed in the text.	115
5.2	Density distribution of the water column is shown for three temperature cases near the inflow region in the south of the cavity (a) and in the path of the meltwater outflow region in the north (b). Locations of these profiles are shown by red stars in Figure 5.1a. . .	116
5.3	A closer view of the inflow region in the standard run. Colours show water column thickness with bottom vectors overlaid (a). Vectors at the sea surface or directly under the ice shelf in the same region (b) show that the flow is barotropic. Yellow contour indicates position of ice front.	117
5.4	Similar to Figure 5.3, (a) shows sea floor velocities and (b) shows surface velocities for the inflow region of the -1.0°C case. The flow is far less barotropic in this warmer case.	118
5.5	Melt rates resulting from ten different temperature sensitivity simulations. Only melting is shown here; freezing rates are shown in Figure 5.8 for more detail.	120
5.6	Surface lowering recorded from radar altimeters over the period 1994-2011, adapted from Holland et al. (2015) (a). The red line shows the profile of repeated radar surveys discussed in the text. (b) Altimetry-derived lowering between 1992-2001 is shown using both a colour scale and white contours at intervals of 0.1 m yr ⁻¹ , adapted from Shepherd et al. (2003). The red contour shows the 1990 extent of the ice shelf; black dots show locations of data points used to create the map; the blue dot is the Larsen meteorological station and the black line starting at point 'B' indicates a transect used for analysis in Shepherd et al. (2003) which is not discussed here. (c) Surface lowering seen by radar altimeters between 1994-2016, adapted from Adusumilli et al. (2018). Black dots indicate regions where results have a confidence interval above 67%.	121
5.7	Relationship between melt rate and ocean forcing temperature. Black circles show the domain-averaged net melt rate; red circles are melting only, leading to ice loss; cyan circles are freezing only, leading to ice mass gain under LCIS, all shown in units of Gt yr ⁻¹ . Green line indicates a melt/freeze rate of zero.	122
5.8	Locations and rates of refreezing to the base of LCIS resulting from ten different temperature sensitivity simulations.	127

5.9	Depth of the ice draft below the sea surface, comprised of both meteoric and marine ice.	128
5.10	Thermal driving, defined as the difference between potential temperature in the ice-ocean boundary layer and that of the potential freezing point at the ice base pressure, in the standard run (-1.9°C) (a) and the warmest run (-1.0°C) (b).	129
5.11	Marine ice thickness after 500 years of advecting steady state melt/freeze rates in each temperature case. Red triangles indicate locations of thickness calculations detailed in Table 5.2.	130

List of tables

3.1	Modelled and measured sea surface height amplitude means, averaged over a six month-long timeseries, for each GPS site. Site names correspond to those in King et al. (2011b) and are shown in Figure 0.1.	76
3.2	Ellipse parameters taken from the model boundary layer and measured 13.5 m beneath the ice base at the southern observation site, as reported in Davis and Nicholls (2019a). Abbreviations: Mod is model; Con is constituent; Semimaj is semi-major axis; Semimin is semi-minor axis; Inc is inclination angle.	79
5.1	Net ice loss from LCIS resulting from basal melting in each ocean temperature case, including differences between mass changes in the north and south of the model domain.	125
5.2	Thickness of three important marine ice bands close to the region of initial refreezing (GL) and further downstream (MS), calculated from advection of steady state melt/freeze rates from each of the ten temperature simulations. Red triangles in Figure 5.11a show locations of calculated thicknesses. Abbreviations: GL is grounding line; MS is mid-shelf.	132
A.1	Description of model parameters and values used in the ‘standard run’.	147

Chapter 1

Introduction

Antarctica is covered in a sheet of ice which is split into three parts: the East Antarctic Ice Sheet, West Antarctic Ice Sheet and the Antarctic Peninsula Ice Sheet. The East and West Antarctic ice sheets are separated by the Transantarctic Mountains and the Antarctic Peninsula branches off in the northwest (Figure 1.1). The East Antarctic Ice Sheet is currently considered to be stable but the West Antarctic Ice Sheet, which is a marine ice sheet grounded below sea level, is losing ice as a result of increased oceanic melting (Shepherd et al., 2018). At the edges of the ice sheets, the ice flowing off the continent forms ice shelves, defined as those parts of the ice which are no longer grounded on the Antarctic continent and therefore float on the ocean. The transition point where the ice sheet becomes an ice shelf is referred to as the grounding line (Figure 1.2).

The Southern Ocean surrounding Antarctica, into which the ice is discharged, is unique in that no other land masses block the flow of the ocean around Antarctica. Hence, the Antarctic Circumpolar Current, which travels west to east around the continent, is the largest current found in any of the world's oceans (Rintoul, 2018) (Figure 1.1). As a result of this uninterrupted circulation, water masses from the Southern Ocean have access to the Atlantic, Pacific, and Indian oceans, influencing global thermohaline circulation. The Southern Ocean is divided into several shelf seas. This thesis focuses on the Weddell Sea region of Antarctica, which is bounded to the west by the eastern border of the Antarctic Peninsula (Figure 1.1), on which Larsen C Ice Shelf (LCIS) lies. The effect that regional changes may have had on ocean dynamics within and surrounding the LCIS cavity, and the state of the ice shelf itself, are investigated here.

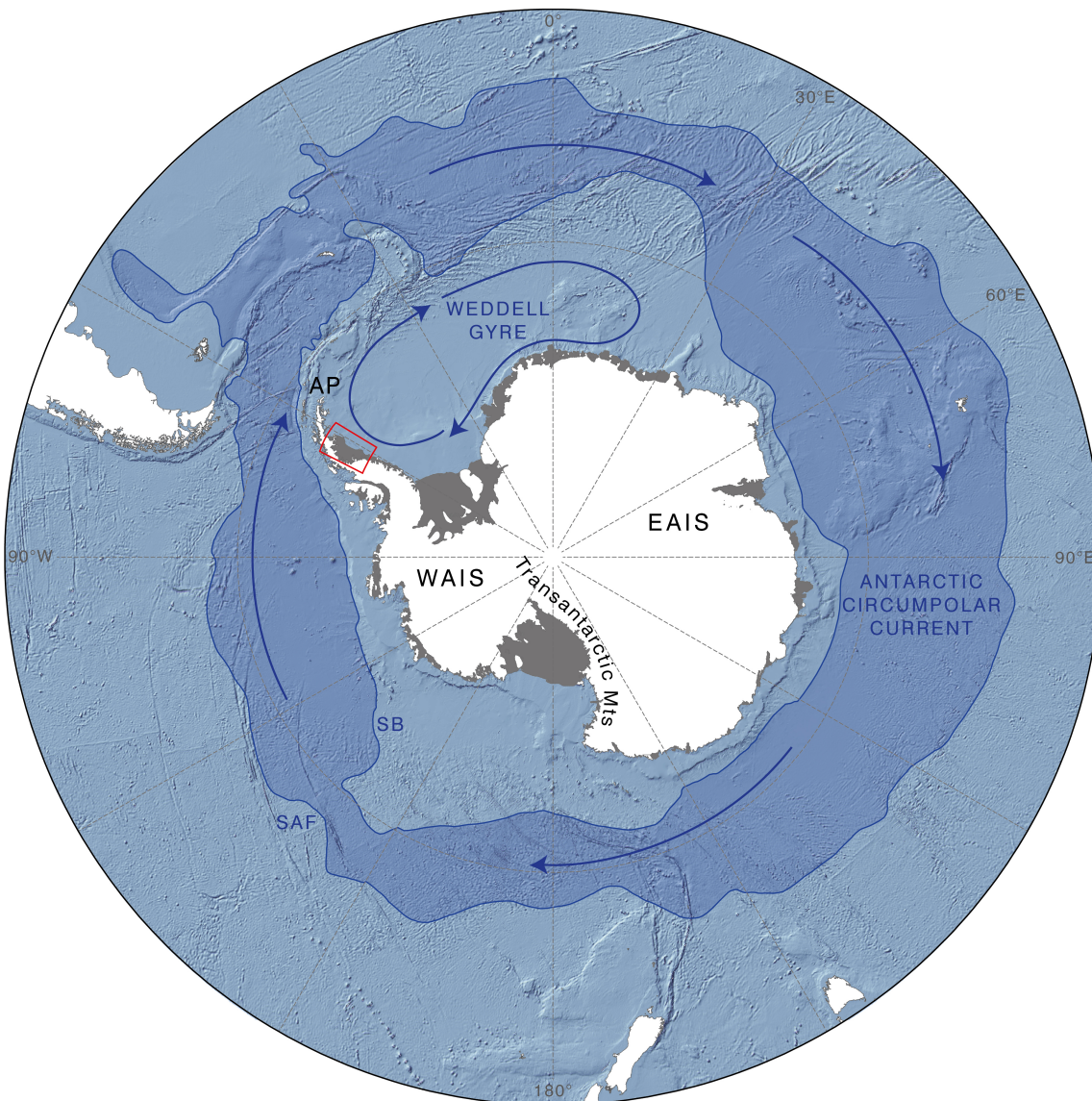


Figure 1.1: Map showing the Antarctic Ice Sheet (in white) and ice shelves (grey) surrounded by the Southern Ocean (blue). The East Antarctic Ice Sheet (EAIS) and West Antarctic Ice Sheet (WAIS) are divided by the Transantarctic Mountains. The Antarctic Circumpolar Current is bounded in the north by the Subantarctic Front (SAF) and to the south by the Southern Boundary (SB). This clockwise circulation brings Circumpolar Deep Water onto the continental shelf in front of the Antarctic Peninsula (AP) via the Weddell Gyre. The area investigated in this thesis is outlined in red.

1.1 Ice shelf collapse

In one of their latest reports, the Intergovernmental Panel on Climate Change described a global temperature increase of 0.87°C since the pre-industrial era (1850-1900) up to the present day (IPCC, 2018). The Antarctic Peninsula in particular has experienced a rate of warming several times the global average

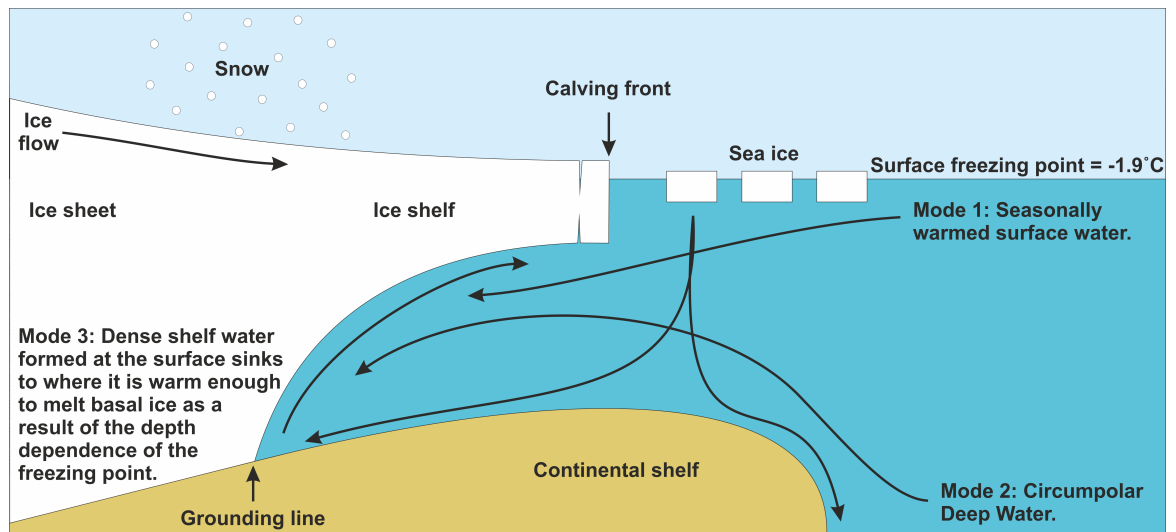


Figure 1.2: Schematic showing the configuration of an ice shelf and some of the ocean dynamics that can contribute to the melting at an ice shelf base. The three modes of basal melting, as described in Jacobs et al. (1992), are elaborated on in Section 1.3.

up to the end of the 20th century (Vaughan et al., 2003; Khazendar et al., 2011; Turner et al., 2016). These conditions have led some to consider whether certain ice shelves in this region have been pushed past the limit of thermal viability (Vaughan and Doake, 1996) as a number of ice shelves on the northern peninsula have collapsed during the last several decades (Vaughan and Doake, 1996; Skvarca et al., 1999). The apparent correlation between the southward-progressing trend of ice shelf retreat and warming atmospheric conditions on the peninsula suggests there may be a link between high latitude warming and ice shelf collapse (Skvarca et al., 1998). The origin of these changes is unclear; there is great uncertainty about the contributions from anthropogenic forcing and natural variability. The observed warming hiatus (Turner et al., 2016) suggests natural variability is responsible. However, it is possible that the warming and its effect on the stability of Antarctic Peninsula ice shelves is the result of a combination of anthropogenically-forced climate change and natural cycles of deglaciation.

Ice shelf collapse has several important implications for water mass formation and ocean dynamics. Ice shelf meltwater produces cold, low salinity plumes which stratify surface waters because buoyancy is controlled primarily by salinity in the high latitudes. This drives ocean currents as a result of density gradients. Changes in fresh meltwater production are one control over the rate of formation of Antarctic Bottom Water, which requires dense water to sink off the continental shelf (Fogwill et al., 2015). The loss of ice shelves therefore effects a significant change in the stratification of the water column and consequently, the formation

of Antarctic Bottom Water.

Antarctic Bottom Water formation in the Southern Ocean is critical to large-scale ocean dynamics by supplying cold, saline water to drive the global thermohaline circulation (Jacobs, 2004). This water mass has been reported to have freshened in recent years, in part resulting from the collapses of Larsen A and Larsen B ice shelves (Jullion et al., 2013). Although evidence shows that Antarctic Bottom Water is freshening, the collapse of an ice shelf could also drive an opposite effect: when an ice shelf collapses, the area of open water left by the ice shelf's disappearance could potentially lead to heightened sea ice production as a result of greater atmosphere-ocean exchange, eventually increasing the formation rate of Antarctic Bottom Water. Sea ice is a key factor in the formation of this water mass, as brine rejection during the formation of sea ice produces dense, high salinity water which promotes the formation of Antarctic Bottom Water (Jullion et al., 2013). These interactions demonstrate a complex relationship between ice shelves and the ocean.

1.1.1 Sea level rise

Aside from affecting the volume of particular water masses within the ocean, ice shelf retreat also affects the volume of the ocean as a whole through sea level rise. The Antarctic Ice Sheet holds 27 million km³ of fresh water, corresponding to a potential sea level rise of approximately 58 m (Fretwell et al., 2013). Mass loss from ice sheets in the polar regions, triggered by ice shelf thinning and collapse, is expected to be the principal contributor to sea level rise by the end of the century (Rignot et al., 2011b). Following the collapse of Larsen A Ice Shelf in 1995 (Rott et al., 1996) and Larsen B Ice Shelf in 2002 (Rack and Rott, 2004), many have speculated that this southward-progressing trend may soon result in the loss of the largest remaining ice shelf on the peninsula, LCIS (Figure 1.3).

The collapse of LCIS would not immediately cause any significant sea level rise as the ice is already floating, with the exception of a little volume expansion resulting from the density difference between ice and fresh meltwater (Jenkins and Holland, 2007). However, ice shelves act as a plug for inland glaciers. Once this plug disappears there is nothing to buttress the glaciers feeding the ice shelf, which drain approximately 27,000 km² of ice into LCIS (Riedl et al., 2004). Buttressing is the resistance to ice sheet flow imposed by drag at the boundaries between ice and bedrock, which prevents further ice discharge into the ocean. This can result from lateral stress at ice shelf embayment walls or where the floating

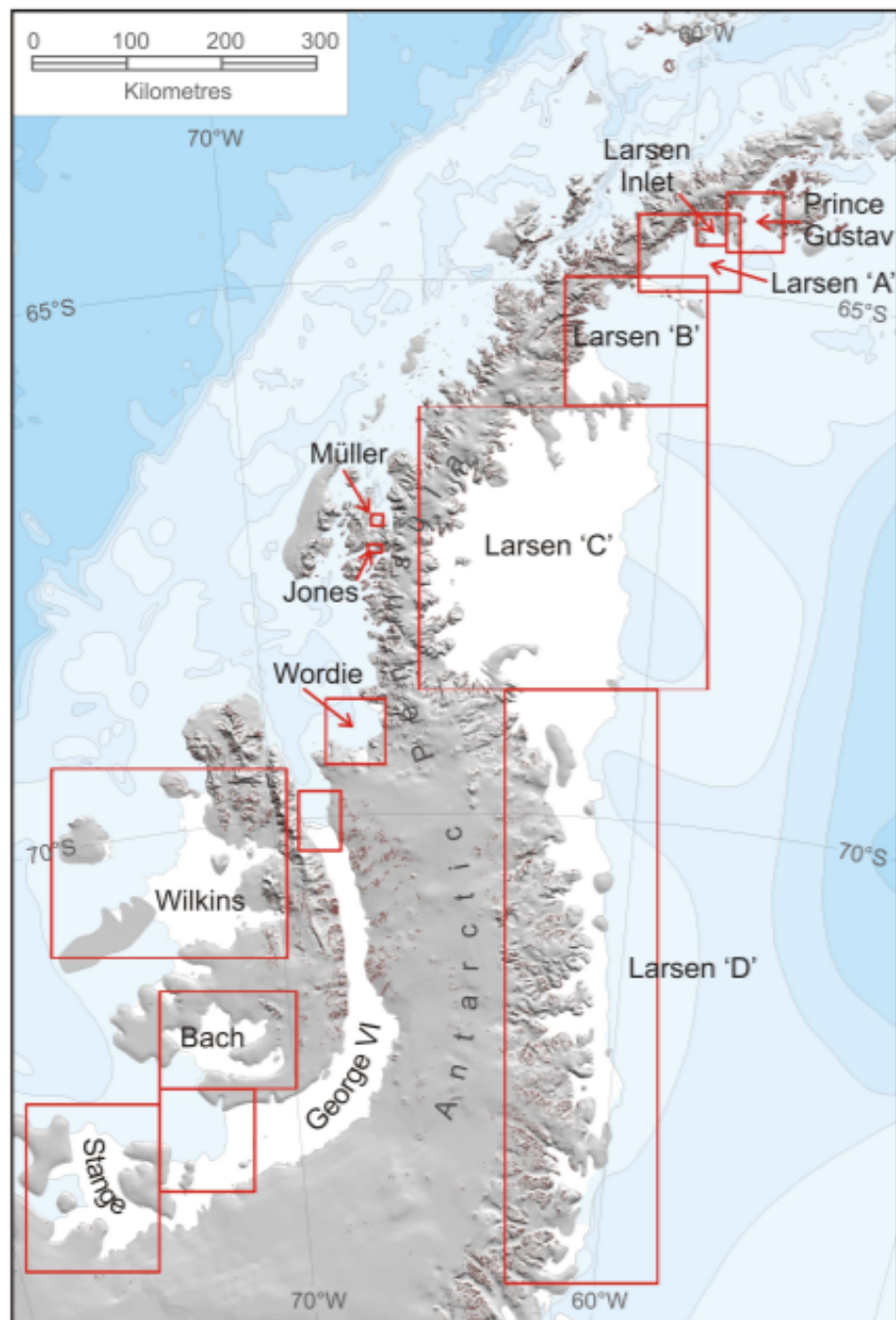


Figure 1.3: Map showing the location of ice shelves on the Antarctic Peninsula. White area shows the extent of each ice shelf as of 2009, by which time a number of ice shelves had retreated significantly in the previous 50 years (Prince Gustav, Larsen A, Larsen B, Jones, and Wordie). Image adapted from Cook and Vaughan (2010).

ice shelf meets a bathymetric high in the seabed, which would transmit resistance back to the grounding line.

The loss of Larsen A and Larsen B ice shelves led to an instantaneous acceleration of tributary glaciers, which was maintained for several years beyond

their initial collapse periods (Scambos et al., 2004; Wuite et al., 2015; Royston and Gudmundsson, 2016). The collapse of Larsen B Ice Shelf was estimated to have led to a mass loss of 27 km^3 from feeding glaciers over the course of the following year and the deterioration of LCIS is expected to lead to even greater mass loss from the ice sheet on land (Rignot et al., 2004). The projected sea level contributions up to the year 2300, following a total collapse of LCIS, are estimated from ice sheet modelling to be up to 4.2 mm (Schannwell et al., 2018). Even without the total collapse of an ice shelf, the buttressing effect that the ice shelf imposes onto the grounded ice sheet to slow its seaward progression, and therefore its influence on sea level rise, reduces as the ice shelf thins. Rignot et al. (2004) reported up to an eight-fold acceleration of some glaciers feeding into Larsen B Ice Shelf in the two years prior to its collapse, which can be attributed to a reduction in buttressing as the ice shelf was also observed to be fractured and thinning.

1.2 Surface lowering

Satellite radar altimetry measurements from various studies have reported a surface elevation lowering of LCIS (Shepherd et al., 2003; Fricker and Padman, 2012; Pritchard et al., 2012; Holland et al., 2015; Paolo et al., 2015; Adusumilli et al., 2018), with estimates ranging from 0.06 to 0.4 m yr^{-1} taken over different time periods between 1978 and 2016. The substantial variation between measured values results from changes in the lowering rate at different points in time, as opposed to differences between methods of measurement in separate studies. Higher rates of lowering were largely reported in the late 20th century, particularly 1992-1996 (Fricker and Padman, 2012). Different lowering rates have also been reported across distinct sub-sections of LCIS, as seen in Figure 1.4, with higher rates recorded in the north of the ice shelf (Shepherd et al., 2003; Pritchard et al., 2012; Holland et al., 2015; Paolo et al., 2015, 2016). Across the literature measurements are therefore, spatially and temporally, highly variable.

Several authors assumed that the lowering results from thinning of the ice. Satellite observations have also shown the northern part of LCIS sped up by 15% between 2000 and 2006 (Khazendar et al., 2011). Further to these observations of thinning and acceleration, there have also been reports of meltwater ponding on the surface of the ice, all of which are potential precursors to collapse (Luckman et al., 2014). The cause of this lowering is unclear and debate is ongoing as to whether its origin results primarily from atmospheric or oceanic processes.

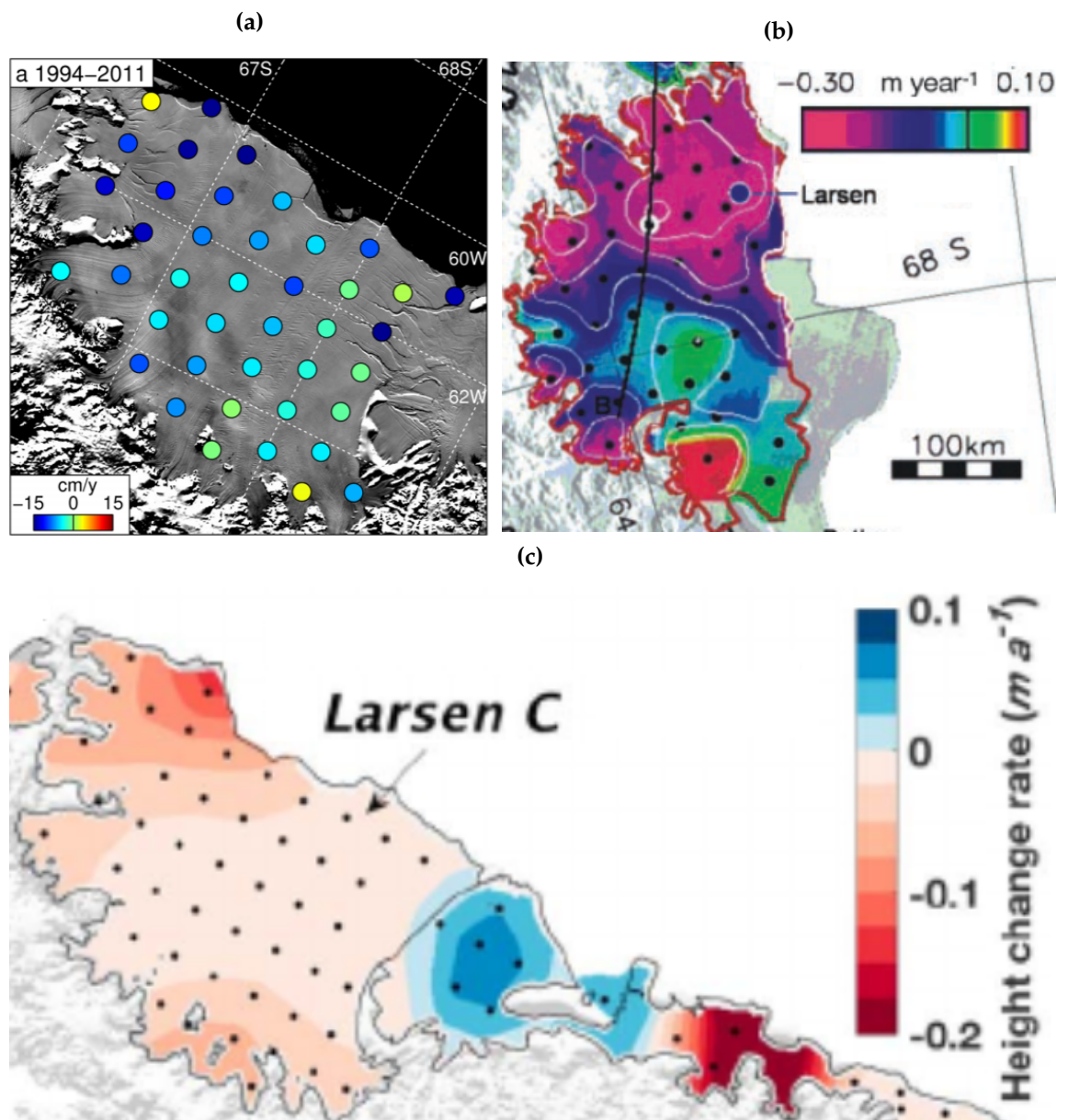


Figure 1.4: (a) Surface elevation data from satellite radar altimeters showed a lowering of the surface of LCIS between 1994–2011. Image adapted from Holland et al. (2015). (b) Altimetry-derived lowering during the period 1992–2001 is shown using both a colour scale and white contours at intervals of 0.1 m yr⁻¹, adapted from Shepherd et al. (2003). The red contour shows the 1990 extent of the ice shelf; black dots show locations of data points used to create the map; the blue dot is the Larsen meteorological station and the black line starting at point 'B' indicates a transect used for analysis by Shepherd et al. (2003). (c) Surface lowering seen by radar altimeters between 1994–2016, adapted from Adusumilli et al. (2018). Black dots indicate regions where results have a confidence interval above 67%.

1.2.1 Atmospheric versus oceanic effects on lowering

One competing theory about the dominant cause of the lowering is ice loss resulting from either an increase in basal melting or reduction in refreezing onto the ice base. Shepherd et al. (2003) concluded that an increase in oceanic melting at the base of LCIS was the most likely cause of the observed lowering, after evaluating and ruling out all other processes that could have contributed to the surface height reduction. They determined that no decrease in snowfall or glacial input to ice shelf had taken place and stated that although firn densification could account for the lowering, and therefore could not be ruled out as the sole cause, this mechanism would require a greater amount of meltwater production in the north than is estimated to have taken place.

An alternative mechanism potentially responsible for some or all of the lowering is increased ice divergence, which would thin the ice at a given point on the ice shelf, resulting in ice loss. Reports from investigations of this ice shelf thinning mechanism have been mixed; Sutterley et al. (2019) found that increased ice divergence accounted for the majority of observed changes, whereas Vieli et al. (2007) concluded that it only accounted for 20% of the changes.

Other research has found compaction of the ice firn in the upper layers of the ice column, resulting from a loss of air from the snow pack, was primarily responsible for the surface elevation changes (Pritchard et al., 2012; Holland et al., 2015; Adusumilli et al., 2018). The firn layer of an ice sheet/shelf is comprised of snow deposited on the surface in previous years which compacts under the pressure of the material above it. Firn therefore has a density between that of snow and glacial ice, which gradually increases throughout the depth of the firn layer. Firn compaction is caused by higher air temperatures over LCIS leading to surface melting, which allows water to percolate through the firn layer and replace the air in the firn. Melt ponds are able to form on the surface of LCIS when the surface layers are dense, evidencing the loss of this firn air (Scambos et al., 2000; Luckman et al., 2014).

Reports of decreased summertime surface melting (Adusumilli et al., 2018) and a reduction in melt season length in the 21st century by 1-2 days yr^{-1} (Bevan et al., 2018) have coincided with the reported decline in Antarctic Peninsula warming since the late 20th century (Turner et al., 2016). However, prior to this, mean annual air temperatures rose by almost $0.4^{\circ}\text{C decade}^{-1}$ in the mid-late 20th century (Vaughan et al., 2003), which may have fuelled surface melting and resulted in a loss of firn air. A reduction in snow accumulation could also be

responsible for air loss on the surface of LCIS, however, no decrease in snow accumulation overall has been seen (Kuipers Munneke et al., 2017).

Holland et al. (2015) inferred that ice loss (resulting from ice divergence and/or increased basal melting) and a loss of air from the ice shelf firn layer had each contributed to the surface lowering, meaning at least two types of forcing are responsible. The distinction between surface and basal losses is important because altimetry-derived lowering of a given amount signifies much greater changes to the ice shelf if they are caused by mass loss at the base of the ice shelf than if they result from surface changes. As the ice shelf is floating, the density difference between the ice and ocean means that only about 10% of the ice shelf is visible above the sea surface. This in turn means that if ice loss at the ice shelf base were to take place, only 10% of the total loss would be observed on the surface. A loss of air from the firn layer does not affect the mass of the ice shelf and therefore does not affect floatation. This means any elevation change at the surface has a 1:1 ratio with surface air loss, but a 1:10 ratio with basal loss. For example, if an ice shelf is found to have lowered by 1 m yr^{-1} , this could result from either a loss of surface air of around 1 m yr^{-1} or a mass loss at the ice base of approximately 10 m yr^{-1} . Both processes would result in the same surface elevation change. Although Holland et al. (2015) determined that air loss and ice loss have led to equal magnitudes of lowering, they therefore concluded that ice loss, resulting from ice divergence, basal melting or a combination of these two processes, was the dominant mechanism.

1.3 Basal melting

The different reports of the root causes of the observed lowering mean there is still uncertainty about how much of the lowering has been driven by ocean-induced basal melting. It is now well documented that several ice shelves fringing the West Antarctic Ice Sheet, such as Pine Island Ice Shelf, are undergoing rapid basal melting by the warm waters of the Amundsen and Bellingshausen seas (e.g. Shepherd et al. (2004)). These warm temperatures are not ubiquitous in the Southern Ocean and much colder waters are found elsewhere on the continental shelf, at the periphery of Antarctica (Figure 1.5), including in the Weddell Sea surrounding LCIS. These two regimes are controlled by differing atmospheric forcing; contrasting fluxes at the ocean's surface and subsequent disparities in sea ice production affect the temperature of the entire water column through mixing

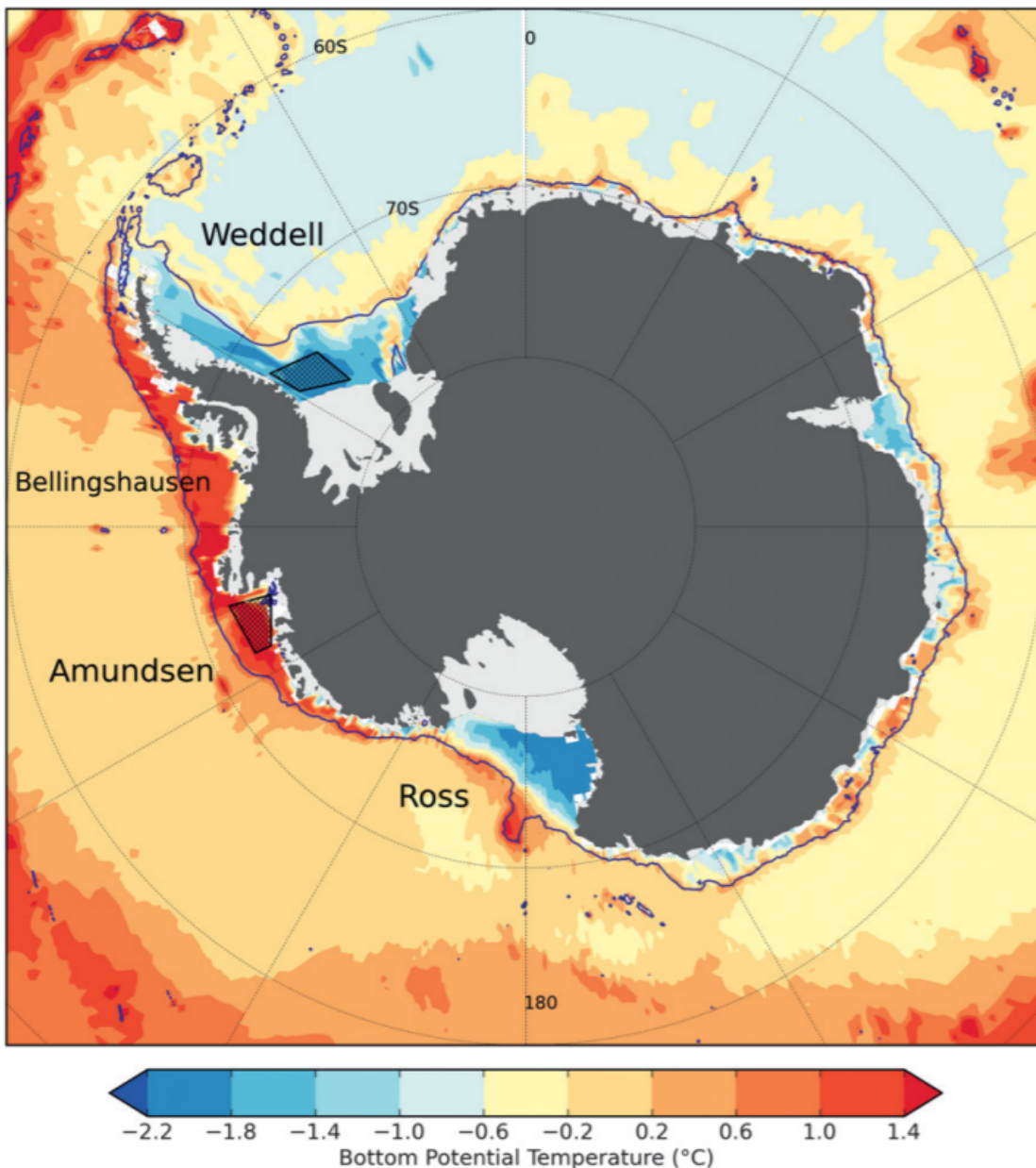


Figure 1.5: Map showing the potential temperature of the ocean at the sea floor around Antarctica. Black contour indicates 1000 m depth of the seabed below the ocean's surface. Image adapted from Petty et al. (2013).

(Petty et al., 2013). In addition, winds control whether or not the transport of relatively warm ($\sim 1^\circ\text{C}$) Circumpolar Deep Water is directed onto the continental shelves (Thoma et al., 2008). Troughs in the seabed then funnel this warm water into ice shelf cavities (Walker et al., 2007).

While Circumpolar Deep Water enters the cold-water region of the Weddell Sea from the Antarctic Circumpolar Current, via the Weddell Gyre (Nicholls et al., 2009), the ice shelves in this region are thought to be protected from this

water mass because of the cold, well-mixed water column which results from sea ice formation over the continental shelf (Petty et al., 2013). The production of sea ice leads to brine rejection causing cold, saline water to sink, therefore mixing the water column and deepening the mixed layer. In the Amundsen and Bellingshausen seas, the mixed layer resulting from sea ice formation is shallower, meaning the Circumpolar Deep Water at depth is able to encroach onto the continental shelf and therefore into ice shelf cavities to affect basal melting (Petty et al., 2013).

There are three modes of ice shelf basal melting identified by Jacobs et al. (1992) (Figure 1.2). Firstly, surface waters that have warmed as a result of higher atmospheric temperatures during the summer can enter the cavity beneath an ice shelf and drive melting. The second mode involves the inflow of Circumpolar Deep Water, which is typically a few degrees warmer than the surface freezing point and can therefore lead to rapid melting. Finally, dense shelf water, which has high salt concentrations resulting from the expulsion of brine during sea ice formation, sinks to the seabed where it is warm enough to melt basal ice because the freezing point of seawater decreases with depth (Figure 1.6). This means that cold waters with temperatures insufficient to melt ice near the surface have adequate heat to melt ice further down the draft. For example, sea ice production forms water at the surface freezing temperature of -1.9°C , but at the deepest parts of the LCIS grounding line, the freezing point is much colder, at around -2.5°C , and therefore this water can melt the deep ice. This latter mechanism is thought to be dominant in the cold waters of the Weddell Sea (Jacobs et al., 1992) and is therefore the most relevant mode to LCIS basal melting.

Melting of ice shelves by cold ocean waters is thought to affect the mass balance of an ice shelf even if the melt rate is very small. Holland et al. (2015) argued that without basal melting, the components of LCIS' mass budget, accumulation versus divergence, are approximately balanced. Therefore only small changes in melting taking place at the base of the ice shelf are required to lead to mass loss. Estimates of basal melt rates of LCIS from modelling and remote and *in situ* observations range from $0.1\text{-}1.3\text{ m yr}^{-1}$, averaged across the ice shelf (Huhn et al., 2008; Holland et al., 2009; Mueller et al., 2012; Nicholls et al., 2012; Borstad et al., 2013; Rignot et al., 2013; McGrath et al., 2014; Holland et al., 2015; Bernales et al., 2017; Davis and Nicholls, 2019a; Sutterley et al., 2019). The lowest of these estimates come from two in depth modelling studies of LCIS (Holland et al., 2009; Mueller et al., 2012) which will be discussed in greater detail in Section 1.4.2. The highest melt rate quoted here also comes from a modelling study (Borstad et al.,

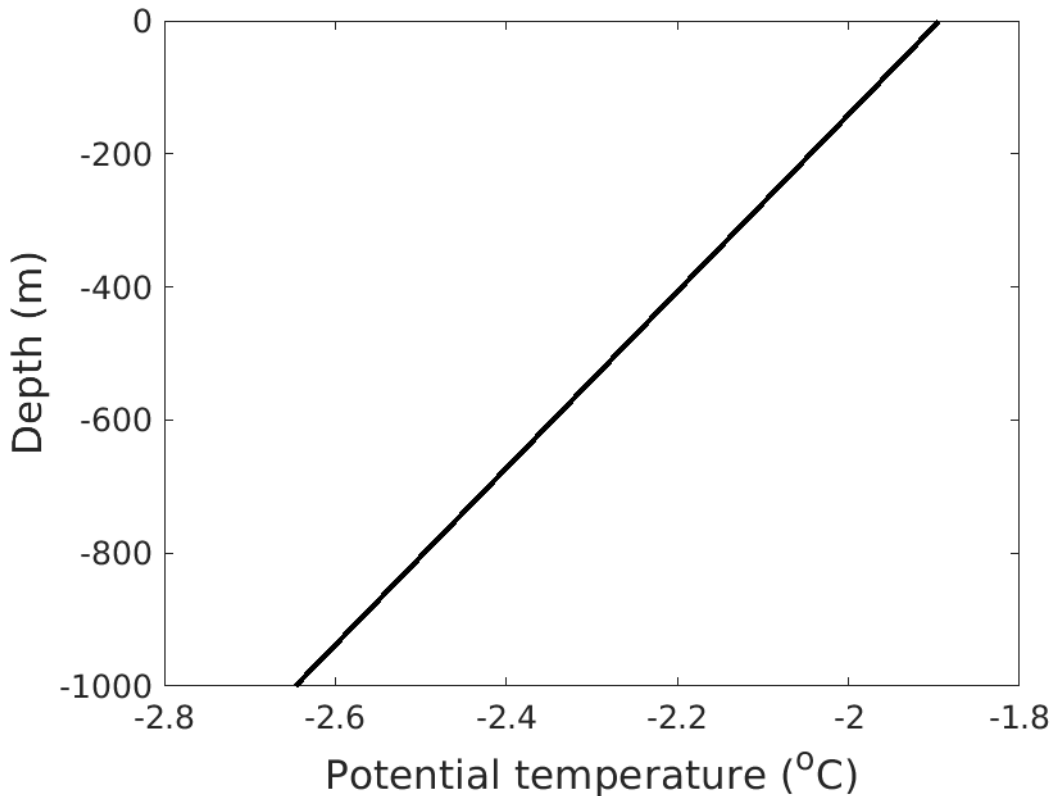


Figure 1.6: Freezing temperature profile of sea water showing the depression with decreasing depth below the surface. This profile is based on a salinity of 34.5 throughout the water column.

2013) and this melt rate is significantly higher than the mean annual observational melt rates included in this range. Observational estimates are on the lower end of this spectrum ($\sim 0.3\text{-}0.4 \text{ m yr}^{-1}$) and were taken in the early 2000s (Huhn et al., 2008; Rignot et al., 2013; Holland et al., 2015), when melting was expected to have slowed based on lowering estimates.

The spatial pattern of basal melting is highly variable in the literature, with some studies showing melting concentrated along the grounding line (Holland et al., 2009; Borstad et al., 2013), where the deepest parts of the ice draft are found, in line with the theory of Jacobs et al. (1992) that higher thermal driving drives the greatest melting in this region. Holland et al. (2009) postulated that their high modelled melt rates were caused by high turbulent heat fluxes originating from rapid currents and large thermal driving. Other research showed strong melting around Bawden Ice Rise (see Figure 0.1 for location) in the northeast (Mueller et al., 2012; McGrath et al., 2014), which is thought to be an important region for the stability of LCIS; greater basal melting here could have significant consequences for potential collapse. Additionally, a further observational study

discovered high melting moving over time from the northeast to the southwest (Sutterley et al., 2019). If a pattern can be discerned across various other reports, it is that melt rates were higher in the north of LCIS over earlier time periods in the observational range.

1.3.1 Changing conditions of the Weddell Sea

In order to induce lowering of the surface height of the ice shelf, basal melt rates would need to increase. The melt rate of an ice shelf floating on the ocean is controlled by the temperature of the water and the velocity of the current directly beneath the ice base (Holland et al., 2008). Therefore if the basal melt rate of LCIS has risen, leading to the observed lowering, then either the temperature or the ocean velocity must have increased, and this change would have to be more pronounced in the north to agree with the lowering pattern.

1.3.1.1 Warming and freshening

Global oceans have warmed by $0.11^{\circ}\text{C decade}^{-1}$ at the surface between 1971 and 2010 because 90% of the increase in energy accumulated in the climate system is stored in the oceans (IPCC, 2014). The Southern Ocean has taken on a disproportionate amount of the increasing heat content of the global oceans since 1970 (IPCC, 2019) and has reportedly warmed as a result of this, as well as freshening, over the latter half of the twentieth century. This freshening is thought to be a consequence of increased ice shelf basal melting (see review by Jacobs (2006)). Any change in the currents experienced under LCIS would most likely result from a change in the salinity field over the continental shelf driving changes in the thermohaline circulation (Nicholls et al., 2012), but there is little evidence to suggest large changes in the salinity of the Weddell Sea. There have been reports of a southward decline in sea ice extent and measurements of a freshening of 0.09 between 1989-2006 in the northern Weddell Sea have therefore been attributed, in part, to a potential decline in sea ice formation (Hellmer et al., 2011). However, sea ice cover in the Weddell Sea as a whole has not shown a great overall change in the 40 years since satellite observations began, with only a slight increase in sea ice extent since 1979, but has shown large variability over time and a recent significant low in 2016 (Turner et al., 2020). There is evidence of ocean warming in the deep Weddell Sea which could affect basal melting if these warmer waters were to make their way onto the continental shelf in front of LCIS. The Weddell

Sea was found to have warmed by approximately $0.012^{\circ}\text{C yr}^{-1}$ between the 1970s and 1990s (Robertson et al., 2002).

1.4 Current knowledge of LCIS cavity oceanography

The link between melt rate and ocean circulation beneath LCIS remains somewhat elusive as a result of the complexities and expense of collecting data from such an extreme, remote environment. The difficulties of making observations in the western Weddell Sea also mean little is known about the ocean processes in this region. The ocean over the continental shelf, offshore of the LCIS ice front, is frequently covered by sea ice year-round, meaning there are few ship-based observations of ocean conditions (Bathmann et al., 1994; Nicholls et al., 2004; Huhn et al., 2008). Winter measurements of LCIS are harder to obtain than in summer as the sea ice surrounding the ice shelf becomes impenetrable to research vessels. Consequently, the majority of observations that are available of the area adjacent to the LCIS cavity are good weather-biased.

Further onshore, collecting direct observations from within the ice shelf cavity carries greater difficulty; they can be obtained through boreholes (Nicholls et al., 2012; Davis and Nicholls, 2019a) but these are sparse. Nicholls et al. (2012) left two moorings under the ice base via hot water drilling to provide year-round observations of currents and melt rate beneath the base of the ice (blue stars in Figure 0.1). As well as affording a first look at conditions directly beneath the ice, these observations have provided a long-term record, which is especially beneficial to our understanding of the temporal variability of oceanography in the LCIS cavity. From these data and modelling studies of LCIS (Holland et al., 2009; Mueller et al., 2012), some details of the current state of oceanography within the cavity are known.

1.4.1 Ocean temperatures

Ocean waters adjacent to the ice shelf appear to be constrained to surface freezing temperatures by nearby sea ice formation (Nicholls et al., 2004). Consistent sea ice conditions have been recorded in the Weddell Sea (Turner et al., 2020), leading to the conclusion that temperatures in this part of the ocean are not subject to much variability. However, much warmer water than this has been observed over the continental shelf. Expendable Bathythermographs and Conductivity,

Temperature, Depth measurements along the ice front have been conducted by Bathmann et al. (1994) and Nicholls et al. (2004), respectively (see Figure 1.7 for exact locations). Waters sampled in 1993 by Bathmann et al. (1994) found ocean temperatures of up to 2°C at the sea surface close to the ice front and approximately -1.5°C below ~200 m depth (Figure 1.8). Water at -1.5°C is relatively warm in terms of basal melting and would have a large effect on melt rates if it were to gain access to the ice shelf, because melting rapidly intensifies with increases in ocean temperature. A temperature change in the ocean beneath an ice shelf from the surface freezing point (-1.9°C) to -1.5°C could mean the difference between a stable and unviable ice shelf.

There are several different water masses within the vicinity of LCIS (Figure 1.7). Warm Deep Water is a local version of Circumpolar Deep Water. Nicholls et al. (2004) deduced from their casts that LCIS is flushed with a cooler, more saline version of Warm Deep Water, which travels via troughs across the continental shelf from the deep Weddell Sea, as opposed to High Salinity Shelf Water, which forms as a result of brine rejection during sea ice formation, coming from south of the ice shelf (Figure 1.7). They suggest that consistent sea ice growth offshore of LCIS would remove heat from the modified Warm Deep Water, whereupon it would be lost to the atmosphere, as this water mass crosses the continental shelf to get to the cavity. This would insulate LCIS from any Weddell Sea warming. The measurements taken by Bathmann et al. (1994) and Nicholls et al. (2004) are only from single points in time and covered different geographical areas of the ocean near the ice front (see Figure 1.7). Several cruises that have since attempted to sample the area in front of LCIS have failed as a result of unfavourable sea ice conditions, suggesting that these measurements may have been anomalous.

LCIS is known to be a cold-water cavity and water samples at the two borehole sites were found to be below the surface freezing point throughout the water column, with little variability in temperature and salinity with depth (Nicholls et al., 2012). However, the mixed layers directly beneath the ice base were found to have temperatures above the *in situ* freezing point, because the freezing point decreases with depth, providing heat with which to melt the ice. Greater thermal driving was recorded at the southern site compared with the northern site (Nicholls et al., 2012).

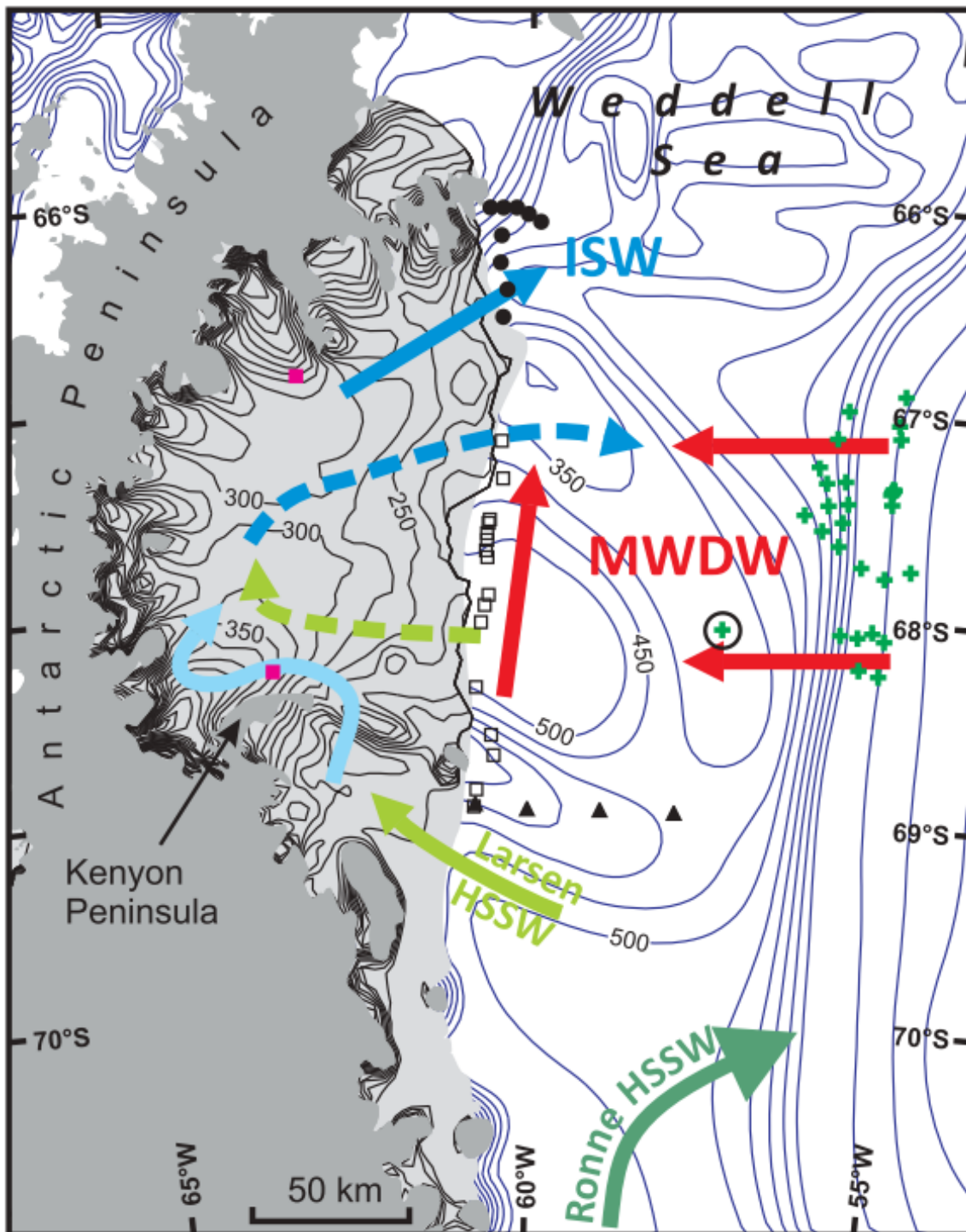


Figure 1.7: Water masses in and around the LCIS cavity. ISW is Ice Shelf Water; MWDW is Modified Warm Deep Water; HSSW is High Salinity Shelf Water. Contours show ice thickness on the ice shelf (shaded in light grey) and bathymetry over the continental shelf (white), values given are in units of metres. Black triangles show locations of Expendable Bathythermographs measured by Bathmann et al. (1994). Black hollow squares, black circles, and green crosses show locations of Conductivity, Temperature, Depth casts taken by Bathmann et al. (1994), Nicholls et al. (2004), and Hellmer et al. (2008), respectively. Red filled squares show locations of borehole drill/mooring sites. Image adapted from Nicholls et al. (2012).

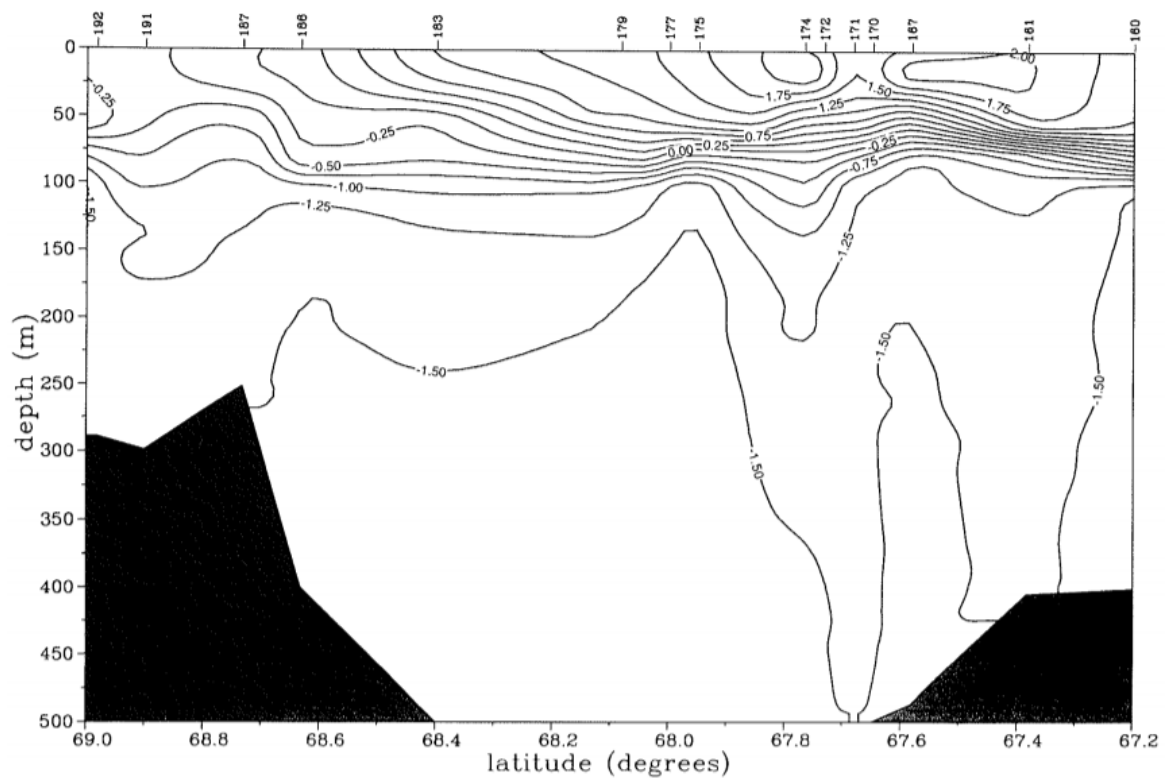


Figure 1.8: Temperature of the ocean from Conductivity, Temperature, Depth measurements at several locations roughly traversing a longitude of 60°W , along the ice front. Numbers along the top axis indicate where an individual cast was taken (see black hollow squares in Figure 1.7 for exact locations). Casts started just south of Gipps Ice Rise, covered the southern trough and finished south of Bawden Ice Rise (see Figure 0.1 for place names). Image adapted from Bathmann et al. (1994).

1.4.2 Ocean circulation

The plume model of Holland et al. (2009) simulated the path and thickness of the buoyant ice shelf meltwater plume below the ice shelf. They showed that meltwater from the entire grounding line was deflected to the left by the Coriolis force and gathered into a central plume which exited the cavity at Jason Peninsula (Figure 1.9; see Figure 0.1 for location of Jason Peninsula). Their model did not use tides to drive currents in the cavity and the plume had no influence of bathymetry beneath it to control the flow; circulation was driven by buoyancy and the shape of the ice topography. A frazil ice model was included in their set up to simulate refreezing of ocean water to the base of the ice shelf. Frazil ice is the dominant mechanism by which ice grows beneath an ice shelf base (see Section 1.7 for further details).

The most thorough modelling study of LCIS to date was carried out by Mueller et al. (2012), who used a three-dimensional model of the cavity which included

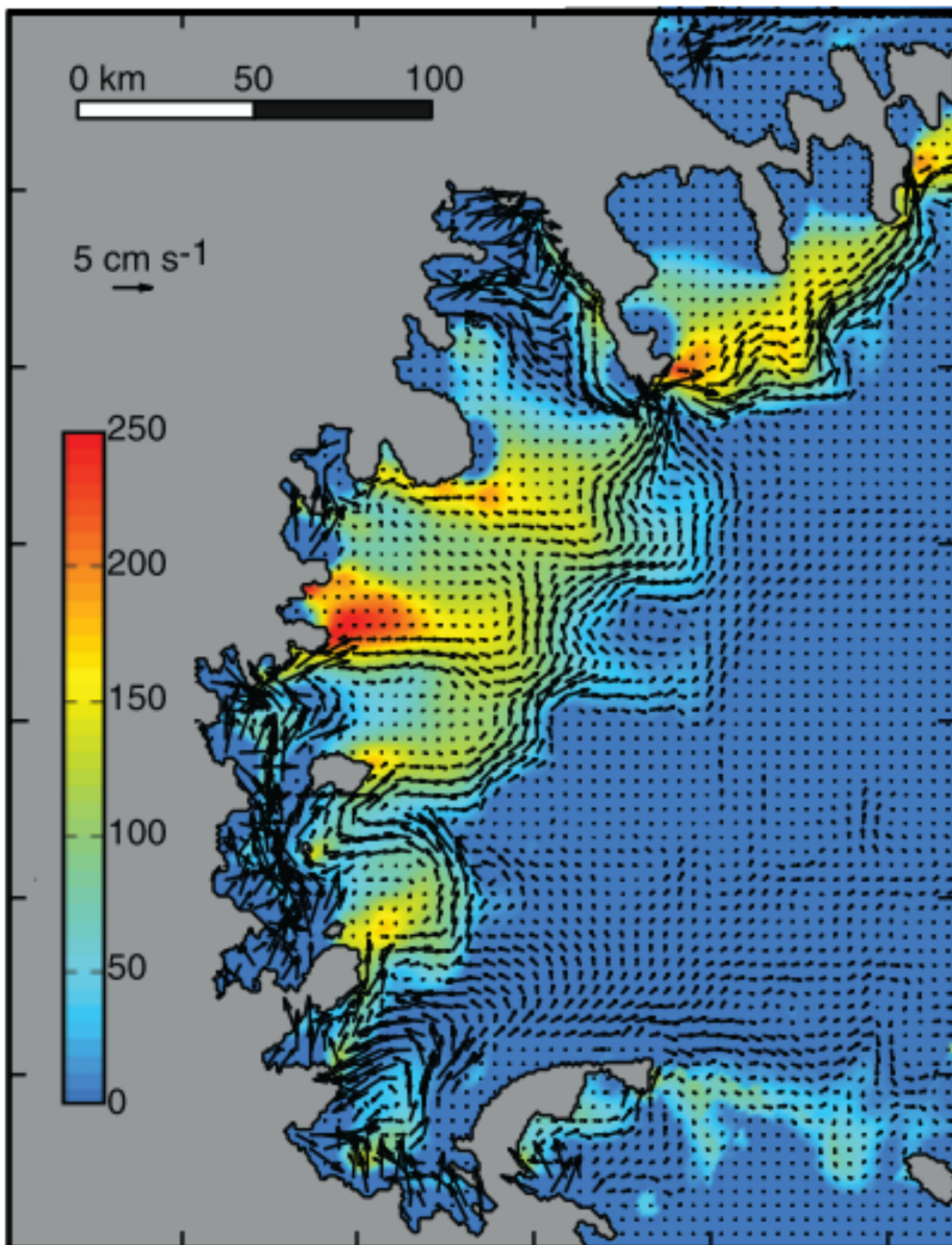


Figure 1.9: Plume thickness and velocities adapted from Holland et al. (2009).

tidal forcing and two different seabed configurations but did not include a frazil ice model. They simulated an inflow at Gipps Ice Rise (see Figure 0.1 for location) and outflow south of Jason Peninsula, which was the same outflow location found by Holland et al. (2009). High tidal speeds were simulated in the northeast of the cavity, near Bawden Ice Rise, which led to high melt rates in this region.

Much of what is presently known about the ocean processes beneath LCIS comes from these handful of observational and modelling studies and can be summarised as follows. Inflow to the cavity takes place in the south, with deep water travelling west towards the tip of Kenyon Peninsula (Mueller et al., 2012) (see Figure 0.1 for location), after interaction with the ice base here (Nicholls et al., 2004), inflowing water is then funnelled towards the grounding line. Outflow from the cavity in the form of Ice Shelf Water, defined as water with a temperature below the surface freezing point, has been inferred from observations in the north of LCIS, just south of Jason Peninsula (Nicholls et al., 2004) (Figure 1.7). The layer of Ice Shelf Water exiting the cavity at this location was observed by Nicholls et al. (2004) to be approximately 200 m thick with a temperature of $\sim -2^{\circ}\text{C}$. Model simulations have captured this outflow and suggested its origin was a central plume which had gathered meltwater from all along the grounding line (Holland et al., 2009).

1.4.3 Tides

Tides are especially important within ice shelf cavities as wind forcing cannot penetrate the ice to influence circulation beneath the shelf, therefore mixing under the ice shelf is predominantly driven by tidal forcing. Tides influence basal melting by mixing water masses and therefore entraining warmer waters beneath cooler boundary layers, providing heat with which to melt the ice base. The important role tides play in ocean circulation beneath ice shelves and the spatial distribution of melting has been confirmed for the Filchner-Ronne Ice Shelf (Makinson et al., 2011), which neighbours LCIS to the south and is flushed by waters of the Weddell Sea.

Until recently, there were no measurements of currents under LCIS to inform us of tidal effects; instead there was a reliance on barotropic tide models (Mueller et al., 2012). The limited observations from current meters under LCIS show that flow speeds in the cavity are dominated by tides (Nicholls et al., 2012; Davis and Nicholls, 2019a), dwarfing any buoyancy-driven contribution. The greatest speed recorded 13.5 m below the ice base at the southern mooring site was 0.28 m s^{-1} (Davis and Nicholls, 2019a), with an annual-mean speed of 0.09 m s^{-1} (Davis and Nicholls, 2019b), whereas the mean long-term flow speed after the tidal signal was filtered out was found to account for only around 0.02 m s^{-1} (Nicholls et al., 2012).

The ocean model of Mueller et al. (2012) further highlighted the importance

of tidal influence on controlling ocean circulation and the melt pattern beneath LCIS. They investigated the modelled relationship between tides, cavity geometry, initial ocean temperature and melt rate. Whereas models without tides, such as that of Holland et al. (2009), predict melting deep along the grounding line across the entire shelf, Mueller et al. (2012) found the largest melt rates of $\sim 2 \text{ m yr}^{-1}$ occurred in the northeast of LCIS, a region where strong diurnal currents of greater than 0.4 m s^{-1} were also predicted by the model. However, the bathymetry in this model is inconsistent with observations of the seabed, for example it does not include Bawden Ice Rise, which may have significantly altered the water column thickness in this region and therefore skewed melt rate results. Tidal currents along the grounding line were reported to be small in this model domain which may have been an effect of imposing a minimum water column thickness of 100 m. As currents get stronger with smaller water column thicknesses, errors in bathymetry may also affect modelled tidal currents. When Mueller et al. (2012) increased the water column thickness in their model substantially, to a minimum of 350 m, the altered tidal forcing was found to decrease the melt rate in the northeast substantially.

1.5 Importance of cavity geometry

Data gathered from the moorings beneath LCIS mean that, for the first time, we now know a little about the oceanography within the cavity. However, extrapolation of these data from two locations to an ice shelf approximately one third the size of England is impossible. In order to understand how the ocean circulates within the ice shelf cavity, modelling is required. It is clear from prior modelling studies of LCIS (Holland et al., 2009; Mueller et al., 2012; Borstad et al., 2013), which have produced varying melt patterns, that using the correct geometry of the cavity is essential to produce an accurate melt pattern.

Mueller et al. (2012) showed how sensitive modelled melt rates are to the bathymetry and ice topography of the LCIS cavity by creating two different geometries with different water column thicknesses. One was constructed by interpolation between the bedrock depths at the grounding line and ice front positions, which resulted in a shallow water column thickness under the northern half of ice shelf of $\sim 100 \text{ m}$. This was the minimum water column thickness they imposed everywhere in the model cavity. Their second geometry prescribed a minimum water column thickness of 350 m across the domain which resulted

in a relatively flat seabed. Neither configuration featured Bawden Ice Rise. The authors reported that the thicker cavity resulted in a much lower melt rate in the northeast, as a result of decreased velocities in this region where their thicker cavity was far less narrow, but a similar melt pattern and rates elsewhere in the cavity.

Uncertainties in cavity geometry have been noted to have a large effect on melt rates (Mueller et al., 2012) and a lack of direct measurements of the seabed geometry under ice shelves may lead to very large errors in water column thickness. The most up to date topography maps of Antarctica are the Bedmap2 gridded products (Fretwell et al., 2013). Bedmap2 used available data such as multibeam swath bathymetry, Moderate Resolution Imaging Spectroradiometer (MODIS) imagery and Ice, Cloud and land Elevation Satellite (ICESat) altimetry, in part gathered and processed by others (e.g. Timmermann et al. (2010) for LCIS data), to construct bathymetry, ice thickness and surface height maps for the entire Antarctic continent below 60°S. Constructing these maps from multiple other datasets meant resolving conflicts, such as the appearance of multiple grounding lines, by using best estimates. Any change in values since the measurements were taken are thought to be negligible compared with the uncertainties in the calculated values (Fretwell et al., 2013).

Each cell on the grid represents the mean value for a square kilometre; relatively dense measurements exist for the Antarctic Peninsula so these averages are expected to be more accurate in comparison to other parts of the continent (Fretwell et al., 2013). However, data detailing the bathymetry beneath ice shelves in Bedmap2 are extremely limited, and as a consequence, the Bedmap2 bathymetry beneath LCIS is relatively flat beyond the grounding line, with no notable features. An improved map of the seabed under the ice shelf is therefore required to accurately model ocean currents and the melt pattern and rates in the LCIS cavity.

1.5.1 Recent advances in knowledge of LCIS geometry

There are different indirect techniques used to map the bathymetry of ice shelf cavities such as LCIS, but few direct measurements to confirm the features that are discovered (Brisbourne et al., 2014, 2020). One such technique that has been used to map the seabed underneath LCIS is a free air gravimetric inversion, which assumes uniform density of the seabed material so that the gravity field conforms to the seabed (Cochran and Bell, 2012). Seismic surveys of LCIS, undertaken over

several decades, are a more robust and reliable method. *In situ* seismic soundings are sparse because they are time consuming and given the current, possibly unstable state of LCIS, they are also more dangerous than gravimetric surveys undertaken by flying over the ice shelf. In spite of the scarcity of individual seismic measurements, they can be extremely useful in confirming the conclusions obtained from gravimetric data and constraining the interpretation of results from such surveys.

Seismic surveys have shown that some of the features that gravimetric data suggests are present in the LCIS cavity are not actually there, likely as a result of non-uniform geology of the seabed (Brisbourne et al., 2014). Further, these measurements have revealed the presence of features in the seabed that have not been included in previous modelling studies of LCIS (Brisbourne et al., 2014, 2020). Most notably, a trough in the south of LCIS (see Figure 0.1 for location) was recently discovered to be much deeper and wider than indicated by gravimetry (Brisbourne et al., 2020). This trough, which appears to traverse the entire width of the cavity, from the continental shelf to the grounding line, might be very important for funnelling modified Warm Deep Water from the continental shelf to the grounding line. Troughs discovered leading into other ice shelf cavities around Antarctica have been found to perform similar roles. For example, a trough in the continental shelf offshore of Totten Ice Shelf in East Antarctica was reported to funnel modified Circumpolar Deep Water towards the Totten Ice Shelf cavity, likely leading to enhanced basal melting (Nitsche et al., 2017). Some of the largest basal melt rates of ice shelves have been reported when troughs in the continental shelf channel the access of deep, warm water to ice shelves (Pritchard et al., 2012).

Topographic control over water masses has been observed elsewhere at the LCIS ice front, with Nicholls et al. (2004) reporting a slope in the north of the continental shelf leading out to the shelf break (see Figure 0.1 for location of 'northern trough'), which may direct modified Warm Deep Water across the shelf and into the cavity. The troughs in the vicinity of LCIS suggest potential pathways for warming waters of the Weddell Sea to enter the cavity and possibly interact with the ice shelf at the grounding line.

1.6 Ice shelf stability

The link between the stability of an ice shelf and the conditions of the ocean surrounding it is not a simple linear relation between temperature and melt rate

(Holland et al., 2009). As ice shelves thin, they become more vulnerable to fracture via crevassing (Shepherd et al., 2003) and iceberg calving from ice shelves that are thinning has been found to be more frequent than from those which are in a steady state or thickening (Liu et al., 2015). A fast-propagating rift in LCIS, which resulted in the calving of iceberg A68 in July 2017 (Jansen et al., 2015; Hogg and Gudmundsson, 2017) (Figure 1.10), prompted speculation that the ice shelf's collapse may be imminent.

The stability of an ice shelf depends on how quickly the ice flow field adapts to the new ice front configuration after a calving event (Jansen et al., 2015), and retreat beyond a critical limit may result in collapse (Doake et al., 1998). In their study, Doake et al. (1998) determined that offshore of a critical arch, which is usually found between two glacial pinning points such as the ice rises grounding parts of LCIS, as shown in Figure 0.1, the least principal strain rates are extensive rather than compressive, and therefore removal of this ice will not affect the flow dynamics inland of the arch. However, any retreat that leads to ice loss beyond this arch may cause the ice shelf to collapse, likely resulting in retreat back to the next critical arch. Evidence has been put forward to suggest that the collapses of Larsen A and Larsen B ice shelves resulted from crevassing caused by meltwater pooling on the surface (Scambos et al., 2000), leading to calving beyond stable geometries of compressive arches in strain rates (Doake et al., 1998).

A different study by Fürst et al. (2016) found that there was a passive portion of ice at the front of LCIS, amounting to approximately 10% of the total ice mass of the shelf, which could calve off without affecting the dynamics of ice shelf buttressing. However, the authors concluded that if the ice front retreated beyond this passive section, the ice streams feeding LCIS would accelerate. The 2017 calving event removed around 10% of the ice shelf (Hogg and Gudmundsson, 2017). Fürst et al. (2016) also made a prediction, before the calving of A68, that the new ice front geometry would be concave, which is the same formation as that of Larsen A and Larsen B ice shelves just prior to their collapses.

Retreat beyond a compressive arch within the ice shelf is one of several potential mechanisms of rapid collapse for LCIS (Holland et al., 2015). Another process which has been identified as a gateway to potential collapse is an ungrounding from Bawden Ice Rise. At its highest point in the south, Bawden Ice Rise stands approximately 40 m above floatation (Holland et al., 2015). Even a small increase in basal melt rate in the region of Bawden Ice Rise could therefore compromise the stability of the ice shelf. Satellite altimetry has shown accelerated lowering in the region surrounding Bawden Ice Rise for a number of years

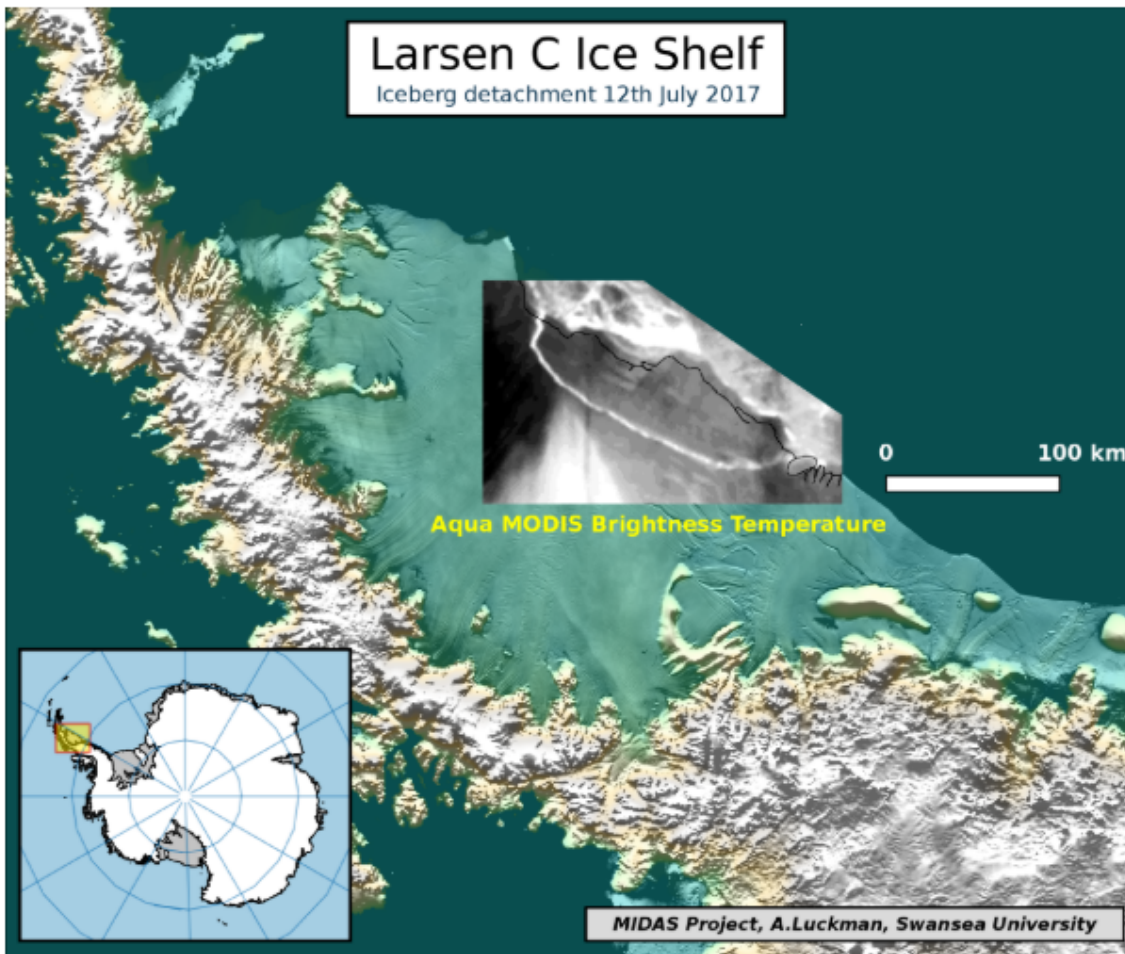


Figure 1.10: The section of ice removed from the Larsen C ice front in July 2017, when iceberg A68 calved, is shown by greyscale thermal imaging. Image obtained from O’Leary et al. (12 July 2017).

(Adusumilli et al., 2018). Borstad et al. (2013) speculated that resistive backstresses upstream of Bawden Ice Rise would reduce as ice in this area thins, compromising the stability of the ice shelf.

1.7 Marine ice

Oceanic contributions to the potential instability of LCIS go beyond simply thinning the ice shelf. Whether or not increases in basal melting are contributing to the observed surface elevation changes, LCIS is vulnerable to changes in ocean forcing via its marine ice. Marine ice forms on the base of an ice shelf as a result of oceanic freezing; buoyant meltwater rising under an ice shelf may supercool as a result of the pressure-induced increase in the freezing point (Robin, 1979;

Holland et al., 2009). This leads to the collection of a slushy layer of frazil ice crystals which gather in basal hollows under the shelf and compact under buoyancy forces beneath the ice shelf (Robin, 1979; Oerter et al., 1992; Holland et al., 2009). The Coriolis force deflects meltwater plumes, causing them to gather in basal hollows downstream of peninsulas and islands at or near the grounding line with grounded ice to the left of the flow, meaning marine ice accumulation is localised here (Holland et al., 2009). Near to the grounding line, marine ice can grow to be several hundred metres in thickness (Glasser et al., 2009). After accumulation, the marine ice is advected downstream by the ice flow.

There are two additional types of marine ice which may be present on LCIS. Firstly, the freezing of seawater near the surface of the ice shelf, which is able to infiltrate the firn layer horizontally when it dips below sea level, leads to a different type of marine ice formation. Secondly, the growth of sea ice within rifts in an ice shelf acts in a similar way to fast ice at the calving front of an ice shelf, compacting and healing these fractures (Holland et al., 2009). Marine ice has been confirmed on LCIS by missing basal returns during airborne radar sounding surveys (Figure 1.11). Marine ice has a higher salinity than meteoric ice and therefore a signal which hits a meteoric-marine ice boundary is diffusive, meaning the interface is not clear. Ground-based radar surveys have since located the boundaries between marine and meteoric ice, as well as the marine ice-ocean boundary, however, the airborne radar used by Holland et al. (2009) was not optimised for this. The marine ice was located between flow bands of different ice streams, downflow of promontories or islands, but the type of marine ice inferred from these missing radar signals cannot be distinguished by this method of detection (Holland et al., 2009).

Thick bands of marine ice have been found under other cold-water ice shelves, including the Filchner-Ronne and Amery ice shelves, as well as LCIS, and are thought to impose an important stabilising effect through binding together individual glacial ice flow units originating from different areas of the inland ice sheet (Oerter et al., 1992; Grosfeld et al., 1998; Craven et al., 2009; Holland et al., 2009; McGrath et al., 2014; Kulesa et al., 2019). Marine ice is warmer, softer and less brittle than meteoric ice and therefore has a lower critical crevassing strain rate. Consequently, it deforms rather than fracturing in response to stress and hence, marine ice inhibits the propagation of rifts by accommodating strain in a way meteoric ice cannot (Holland et al., 2009). Evidence for this has been seen by the deceleration and termination of rifts in suture zones between ice flow units (Holland et al., 2009; Glasser et al., 2009; Jansen et al., 2015). Figure 1.11 shows

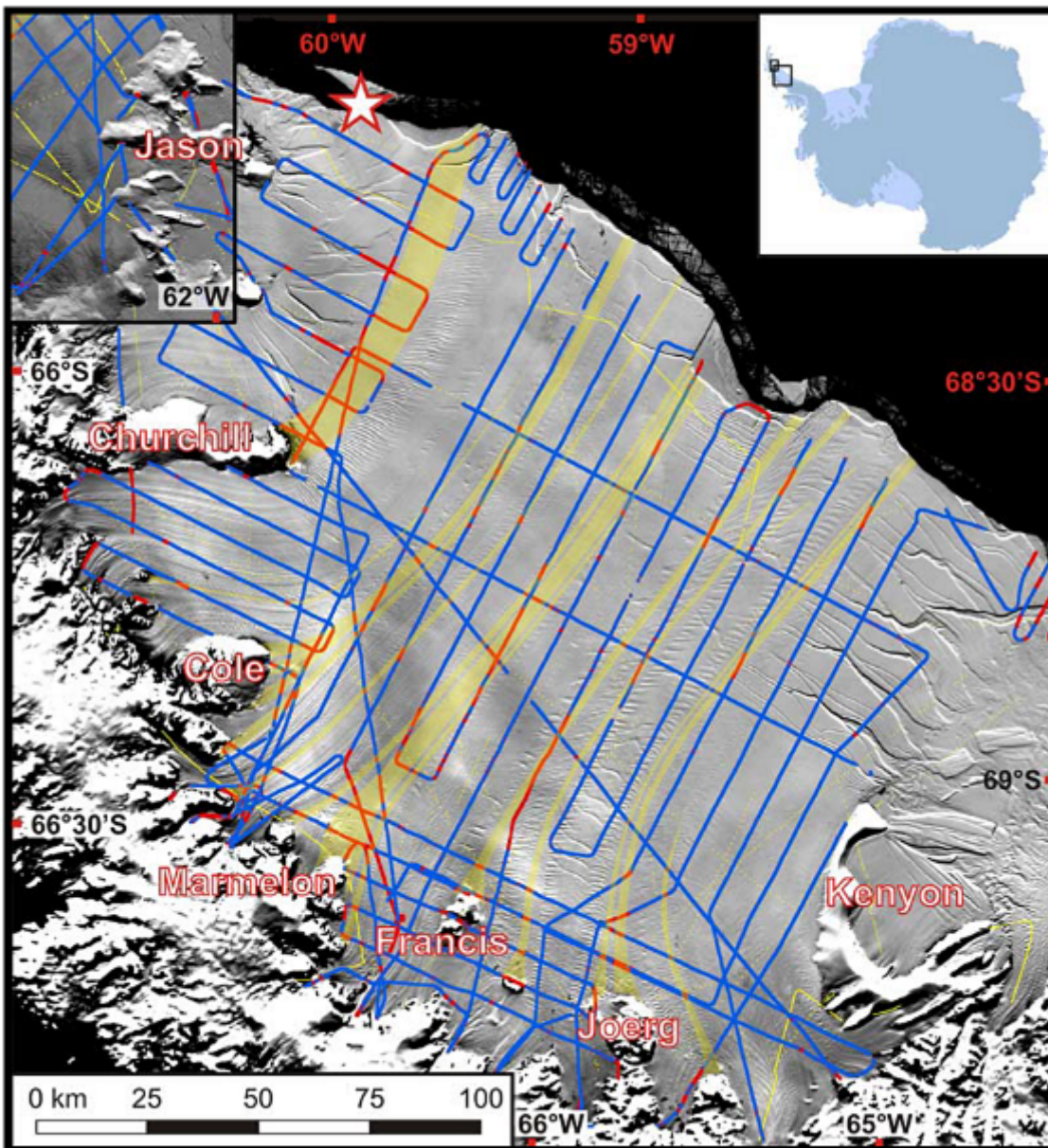


Figure 1.11: Proposed marine ice flow bands (yellow shading) under LCIS are inferred from missing basal returns in airborne radar sounding measurements. Blue lines show flight path of survey with red portions indicating positions where the base was not detected. Image adapted from Holland et al. (2009).

several visible rifts, travelling from the south of LCIS, east of Kenyon Peninsula, appear to have halted along the track of the proposed marine band emanating from Joerg Peninsula.

1.7.1 Effect of potential weakening of marine ice on LCIS

It has been suggested that LCIS would likely collapse without the presence of marine ice. Bands of marine ice downstream of Churchill, Cole and Joerg peninsulas (see Figure 0.1 for locations) have all been identified as particularly important for LCIS, in terms of coupling ice flow units and curtailing rift propagation (McGrath et al., 2014). Borstad et al. (2017) proposed that the stability of LCIS rests entirely on the Joerg Peninsula marine ice band, which has arrested dozens of rifts seen in the south of the ice shelf until recently, when a rift penetrated this band and calved iceberg A68 (Jansen et al., 2015; Hogg and Gudmundsson, 2017). One possible explanation for this could be that the marine ice here has weakened, potentially resulting from erosion due to changing ocean conditions. Weakening of marine ice in these suture zones, by either an increase in basal melting or simply a reduction in oceanic refreezing, may decouple ice flow units with different ice velocities (Jansen et al., 2010), leaving unstable stress fields (Kulesa et al., 2014). Acceleration of part of LCIS, such as that seen in the early 2000s, could be an artefact of this decoupling and demonstrates potential instability (Khazendar et al., 2011).

The timescales across which marine ice can affect the stability of LCIS are uncertain as a result of the different processes which can alter the strength of marine ice bands. Any changes in stability that are currently being seen could indicate sustained ocean forcing changes had taken place hundreds of years ago. Persistent intrusions of warmer water into the cavity around 250-300 years ago may have led to reduced marine ice accumulation at the tip of Joerg Peninsula. This time estimate is based on the distance from the tip of Joerg Peninsula to the tip of Kenyon Peninsula being approximately half the distance from the tip of Joerg Peninsula to the calving front, combined with an ice shelf flow residence time of 560 years for the floating portion of LCIS (Glasser et al., 2009). Advection of this hypothetical thinner marine ice section would mean that the marine ice near the ice front would now be weaker and less able to prevent rift propagation, such as that which led to the 2017 calving. Additionally, any recent changes in ocean forcing that may have occurred in the LCIS cavity may not affect the ability of marine ice to stabilise the ice shelf for centuries. However, reduced freezing at the grounding line is not the only consequence of ocean forcing changes. Present day changes can affect marine ice shelf-wide through increased melting of established marine ice bands.

1.8 This study

Much of the research that has been conducted on the surface height changes of LCIS is derived from satellite data. Several of the studies that concluded basal melting is the root cause of lowering came to this conclusion after discounting other possibilities, as opposed to finding direct evidence that basal melting has increased. The sparse and relatively short term observational record means there are insufficient observations from the extreme, isolated environment of LCIS with which to assess whether ocean conditions in this region have undergone recent changes. Consequently, it is not possible to determine, with a great level of confidence, if increased melting at the base of the ice shelf has led to the observed lowering or weakened marine ice bands beneath LCIS. This subject is an important one, given the implications for ice shelf collapse outlined here (see Section 1.1), and warrants further investigation.

1.8.1 Aims and objectives

This thesis aimed to investigate the plausibility of ocean-driven melting as the predominant cause of the lowering and ascertain how much of observed lowering, if any, can be attributed to an increase in basal melting. By determining the sensitivity of LCIS melt rate to changes in ocean temperature, the potential effects of past, present or future warming on both melting and marine ice distribution have been examined. This will ultimately help to establish whether Antarctic Peninsula atmospheric warming and ice shelf collapse are related. The difficulties in monitoring this cavity, especially year-round, makes ocean modelling of this region a pragmatic choice to investigate the sensitivity of the ice shelf to changes in ocean forcing. This thesis presents melt and freeze rates from LCIS simulations using a high resolution ocean model with a new seabed bathymetry created from an interpolation of seismic soundings (Brisbourne et al., 2020).

1.8.2 Thesis outline

Recent advances in the knowledge of LCIS' ocean circulation and cavity geometry, detailed above (see Sections 1.4 & 1.5), allow significant improvements to modelling melting, freezing, and circulation within the cavity. New seismic soundings taken through the surface of the ice shelf have been used to produce a more accurate map of bathymetry for the model. Data reported in Nicholls et al.

(2004) and Nicholls et al. (2012) from in front of and below the ice shelf indicate properties of the water masses entering and circulating within the cavity, such as temperature and salinity. These have been used to set up initial conditions for model simulations and indicate the boundary conditions needed to represent a true reflection of ocean conditions in this region. Creation of the bathymetry grid and other details of the model configuration are described in Chapter 2.

New current data taken from one of the moorings placed under LCIS, described in Nicholls et al. (2012) and Davis and Nicholls (2019a), have served as a useful point of validation to ensure the model has successfully captured ocean dynamics within the cavity. An assessment of the model's performance with respect to observations is discussed in Chapter 3.

Experiments using a model set up with the features described above have provided insight into what controls the basal melt rate of LCIS. Mueller et al. (2012) found that ocean temperature controlled the amount of melting but cavity geometry determined where the melting occurs. However, as the authors pointed out, errors in the topography of the ice shelf and seabed can lead to large uncertainties in melt rate magnitude and distribution. Therefore, a model domain with a greater likeness to the true bathymetry and ice topography of LCIS, as well as ocean properties which are well constrained by observations, may produce very different melt rate results. A thorough understanding of the ocean processes beneath LCIS with accurate representation of its bathymetry and ice topography is a valuable contribution to this field of study. An evaluation of the effects the cavity geometry has on the pattern of melting under LCIS is presented in Chapter 4.

A series of ocean warming scenarios are used to investigate the response of the cavity to changes in ocean forcing and their impact on melting, freezing, and marine ice accumulation. Results from these experiments are discussed in Chapter 5. Not only will sensitivity studies such as this indicate the effects of potential changes in the climate on the future of LCIS, including illuminating possible changes in marine ice distribution or magnitude that may occur, they will also determine what further observations are necessary to assess the stability of LCIS. The main conclusions drawn from this set of modelling experiments are outlined in Chapter 6, along with suggestions for future work that this research has identified as valuable next steps.

Chapter 2

Methods

2.1 The MITgcm

The Massachusetts Institute of Technology general circulation model (MITgcm) is a numerical model that can be used to simulate fluid flow in either the ocean or atmosphere. This project utilised the ocean-only model with a spherical coordinate system. In the equations that follow, all terms are shown in spherical polar coordinates where λ is the longitude, ϕ is latitude and r is the vertical coordinate. The MITgcm solves the Navier-Stokes equations of motion for a Boussinesq fluid. The Navier-Stokes equations apply the laws of thermodynamics and classical mechanics to a fluid in order to define the state of that fluid (Marshall et al., 1997a,b). These equations result from applying the theory of continuity to mass, momentum, heat and salinity. The continuity equation states that the rate of change of a property, ψ , over a specified volume, equates to the amount of that property entering or leaving that volume, plus any amount of the property being created or consumed, Q , within that volume:

$$\frac{\partial \psi}{\partial t} = \nabla \cdot (\psi \mathbf{u}) + Q \quad (2.1)$$

where $\mathbf{u} = (u, v, w)$ is the ocean velocity in the zonal, meridional and vertical directions, respectively.

Applying this equation to the mass per unit volume of a fluid, ρ , the equation for the conservation of mass is obtained:

$$\frac{\partial \rho}{\partial t} + \nabla \cdot (\rho \mathbf{u}) = 0 \quad (2.2)$$

In this case, the Q term in Equation 2.1 is dropped because mass cannot be created or destroyed.

The Boussinesq approximation assumes that variations in density are small and can therefore be neglected, except where they are important to drive buoyancy forcing. Density is therefore treated as constant in non-buoyancy terms. Applying the Boussinesq approximation to Equation 2.2, this expression is reduced:

$$\nabla \cdot \mathbf{u} = 0 \quad (2.3)$$

Applying Equation 2.1 to the momentum of a fluid, $\rho \mathbf{u}$, the Boussinesq form of the Navier-Stokes equations for the conservation of momentum are obtained:

$$\frac{\partial u}{\partial t} = -\mathbf{u} \cdot \nabla u - \frac{1}{\rho_c r \cos \phi} \frac{\partial(\delta P)}{\partial \lambda} + 2\Omega v \sin \phi + \frac{uv \tan \phi}{r} + F_u \quad (2.4)$$

$$\frac{\partial v}{\partial t} = -\mathbf{u} \cdot \nabla v - \frac{1}{\rho_c r} \frac{\partial(\delta P)}{\partial \phi} - 2\Omega u \sin \phi - \frac{u^2 \tan \phi}{r} + F_v \quad (2.5)$$

$$\frac{\partial w}{\partial t} = -\mathbf{u} \cdot \nabla w - \frac{1}{\rho_c} \frac{\partial(\delta P)}{\partial r} + F_w - g \frac{\delta \rho}{\rho_c} \quad (2.6)$$

where δP is the pressure anomaly with respect to a hydrostatic ocean at rest with density ρ_c , Ω is the angular speed of the Earth's rotation, and g is the acceleration due to gravity. Equations 2.4 & 2.5 show the horizontal conservation of momentum, which include inertial, pressure, Coriolis, metric and viscous dissipation/other forcing terms, respectively, on the right-hand side. The latter, undefined terms (F_u, F_v) include a viscosity term which is parameterised (see Section 2.5), as well as contributions from external forcings which depend on the specific set up of the simulation. When required, they are added to the equations using packages in the model. For this study, external forcing is added in the form

of tides which will be discussed in greater detail in Section 2.4.1. The metric terms relate the distance between grid cell calculation points, which changes at different latitudes given the curvilinear coordinates of the spherical polar grid used here.

The hydrostatic assumption means that the pressure felt at a certain point in the model domain results solely from the acceleration due to gravity imposed by the weight of the fluid above that point. The hydrostatic assumption of a precise vertical balance between buoyancy and pressure forcing means fewer calculations are required to determine the physical state of the ocean in the domain. Many smaller scale forcings of fluid flow can be dropped from the vertical momentum equation because the horizontal scale of investigation is much larger than the vertical scale (~ 2 km versus 20 m, see Section 2.2.1). For example, vertical inertial accelerations and viscosity are thought to be negligible compared with the accelerations due to buoyancy. The benefit of using a reduced form of the equations of motion for a fluid is computational efficiency, as simulations take less time to run while still being a sufficient tool to address the aims of the research, namely to identify how ocean processes in the cavity control the melt rate of the ice shelf. The vertical conservation of momentum shown in Equation 2.6 therefore reduces significantly with the hydrostatic approximation to a balance between vertical pressure and buoyancy:

$$\frac{1}{\rho_c} \frac{\partial(\delta P)}{\partial r} = -g \frac{\delta \rho}{\rho_c} \quad (2.7)$$

The movement of water within the model domain results in a tilting of the free surface, which causes a pressure gradient. The model uses a non-linear free surface equation to simulate the movement of the surface height:

$$\frac{\partial \eta}{\partial t} + \nabla \cdot [(H + \eta) \hat{\mathbf{u}}] = m \quad (2.8)$$

where η is the height of the free surface, H is the depth of the water column below a reference sea surface, $\hat{\mathbf{u}}$ is the depth-averaged velocity, and m is a freshwater flux source term discussed in Section 2.3.1. A gradient in η drives a pressure gradient which subsequently drives a flow in the domain.

Finally, the equations for the conservation of heat and salt also include dissipative/external forcing terms, F_θ & F_S , which will be discussed further in

Sections 2.3 & 2.5:

$$\frac{\partial \theta}{\partial t} = -\mathbf{u} \cdot \nabla \theta + F_{\theta} \quad (2.9)$$

$$\frac{\partial S}{\partial t} = -\mathbf{u} \cdot \nabla S + F_S \quad (2.10)$$

where θ is potential temperature and S is practical salinity. Solving Equations 2.4, 2.5, 2.7, 2.8, 2.9 and 2.10, along with an equation of state, for a given set of boundary conditions shows how the variables \mathbf{u} , θ , S , P , and ρ are related to each other. The non-linear equation of state used in this study is that of McDougall et al. (2003).

The MITgcm code is open source and the version used in this study was c65z.

2.2 Model domain

The model domain includes the LCIS cavity and a small area of the western Weddell Sea (Figure 2.1). It stretches ~ 500 km from the remnant Larsen B Ice Shelf in the north to Hearst Island in the south (see Figure 0.1 for locations of place names), and ~ 400 km from the most western reach of the grounding line to the continental shelf break in the east. These domain boundaries were chosen to ensure the domain was small enough to be computationally efficient when the model is run at high resolution but still covered a large enough area to successfully fulfill the project's aims. Combined with the spatial and temporal resolution detailed subsequently in this chapter, a simulation using this domain took approximately 5 hours to run a model year on 96 cores of the Archer supercomputer.

2.2.1 Grid resolution

The domain is modelled on a 3D spherical polar grid with a uniform grid resolution of $1/20^\circ$ in the longitudinal, horizontal direction and approximately $1/50^\circ$ in latitude, which corresponds to isotropic grid cells of ~ 2 km at the latitudes of LCIS, and 20 m in the vertical. The curvilinear coordinate system

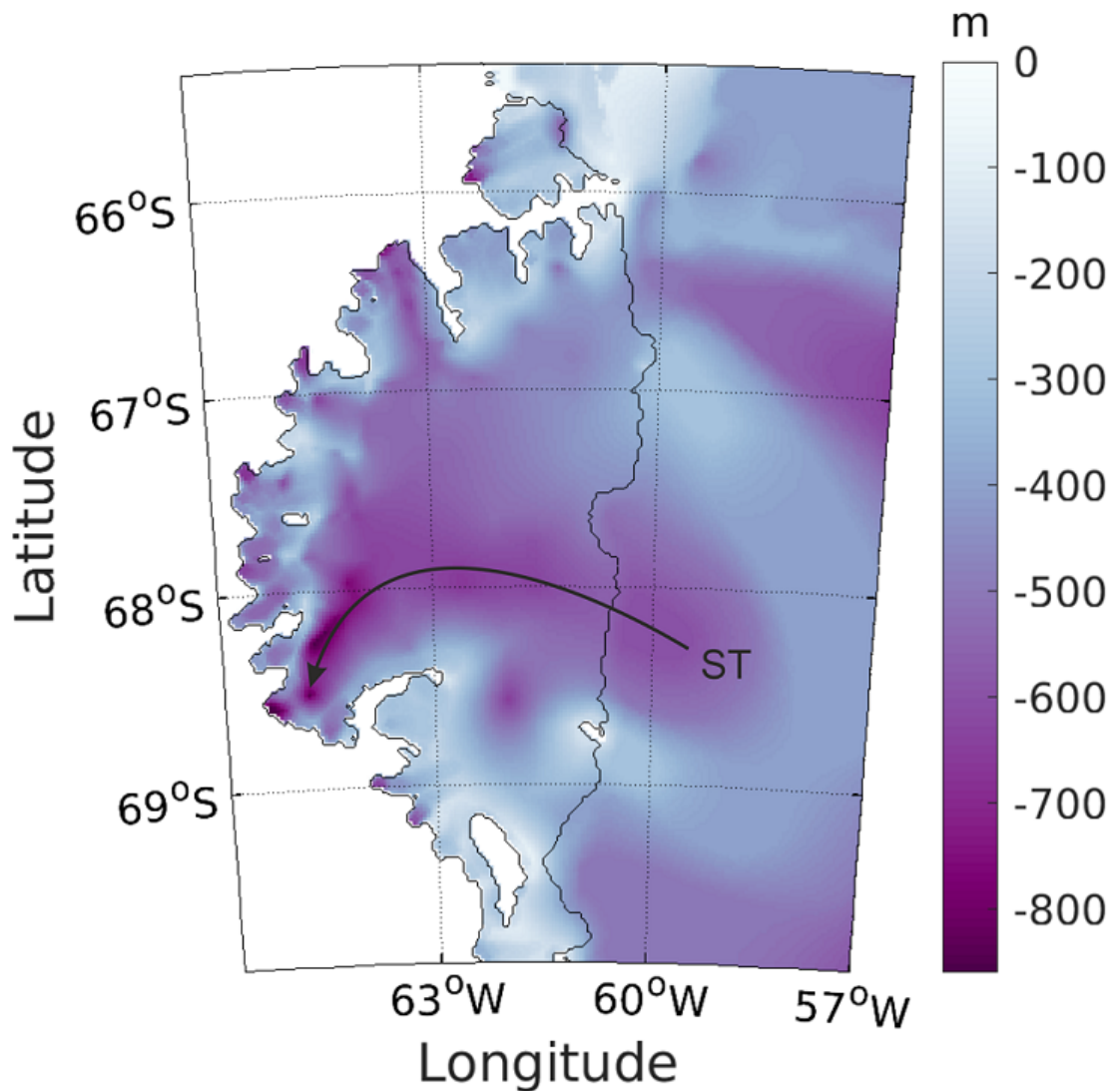


Figure 2.1: The model domain extends from the remnant Larsen B Ice Shelf in the north to Hearst Island in the south, and from the most westward point of the LCIS grounding line to the edge of the continental shelf in the east. Colours show the depth of the seabed adapted from Brisbourne et al. (2020) and the newly discovered extent of the southern trough is marked (ST). The black contour denotes the extent of the floating ice, and grounded ice is indicated in white. Note that this configuration represents the shape of the ice shelf before the iceberg calving in July 2017.

means the horizontal resolution varies from 2.3 km in the north of the domain to 1.9 km in the south. There are 184 x 240 grid cells in the horizontal domain and 44 vertical levels.

The choice of horizontal resolution was chosen to be eddy-permitting while keeping computational expense to a minimum, preventing time consuming simulations. Mesoscale eddies constitute a significant proportion of the transport of heat and salt within the ocean which is important for the mixing of these properties, especially within an ice shelf cavity. While it is not possible to

fully resolve all eddies in an ocean model of the size described here, the chosen resolution captures the largest and most influential eddies in the model domain. The Rossby radius of deformation defines the length scale over which ocean mesoscale eddies act, and is known to be on the order of a few kilometres over the Weddell Sea's continental shelf (Hallberg, 2013). In order to adequately resolve an eddy of this size, model grid resolution needs to be much smaller than the Rossby radius. The roughly 2 km horizontal resolution used here allows the model some representation of mesoscale eddies which are affected by the rotation of the Earth but is not high enough to fully resolve all mesoscale or smaller scale eddies, meaning their effects need to be parameterised (see Section 2.5). Mueller et al. (2012) also used a 2 km horizontal resolution on a Cartesian grid and had only 21 vertical levels for their simulations, but using a sigma (terrain-following) coordinate system. This led to a higher resolution at key regions in the model domain, such as near the ice base. Computational resources limited the vertical resolution used in simulations presented here to 20 m.

2.2.2 Partial cells

Vertical partial cells are included in the model to allow for a more accurate model domain by preventing spurious, long stretches of flat seabed, where an incline occurs in reality, and reducing large bathymetric stepping between cells, which can result in extra mixing redistributing heat to increase melt rates. To create the model domain, the height of the seabed and depth of the ice draft are provided exactly, but are subsequently vertically discretised into 20 m deep grid cells. Where a 20 m grid cell is part ocean, part ice/bedrock, the cell may be split to accommodate both, provided it meets a minimum criteria. In order to avoid numerical problems resulting from grid cells becoming too thin, the minimum value for the dimensionless fraction of the cell that is filled with ocean (hFacMin) was set to 0.3, or 6 m with a cell depth of 20 m. If the ocean fraction of a cell is 0.3 or greater, the cell will be modelled as partially ocean (open) and partially ice/bedrock (closed). If the fraction of ocean in the cell is less than 0.3 once the domain has been configured, the fraction is either rounded up to 0.3 or rounded down to zero, depending on which value the true fraction is closest to.

The value of hFacMin was chosen as a balance to avoid large steps appearing in the modelled bathymetry, which would have incorrectly resulted in vigorous mixing, and reducing the timestep to the point excessive computational time would be necessary to complete a simulation. If hFacMin is too small, the timestep

would need to be reduced in order to prevent the model from failing and this is computationally inefficient (see Section 2.5.1 for explanation).

A non-linear free surface was applied to the top of the water column in the model domain to allow for increasing or decreasing sea surface height, especially in the presence of tidal fluctuations (see Equation 2.8). Surface layer ocean grid cells were given minimum and maximum values that the cell could shrink or grow to as the simulation develops. The fractions of the surface cells' minimum and maximum height were 0.05 and 2, corresponding to 1 m and 40 m, respectively, given the cell depth of 20 m.

Each grid cell on the backward staggered C grid used in this model, whether partial or full, has a tracer point at the centre of the cell to compute θ, S, P and ρ . The velocity points are located on the eastern, southern and bottom faces of each grid cell where the zonal (u), meridional (v) and vertical (w) velocity are calculated, respectively. The pressure gradient being calculated by the model is therefore centred on a velocity point in this configuration.

2.2.3 Creation of bathymetry

The bathymetry was created using a composite of Bedmap2 data (Fretwell et al., 2013) and data processed from various seismic survey expeditions. The Bedmap2 dataset is the most up to date gridded product detailing the surface elevation of the Antarctic Ice Sheet. The incorporation of data from land and ship-based surveys means that the grounding line of LCIS (where the ice begins to float, represented by the red/white border in Figure 2.2) and bathymetry seaward of the ice shelf's calving front are quite well known. Unfortunately, data available to inform the shape of the seabed below the ice shelf is far more limited as a result of the difficulties of obtaining direct measurements from the surface of the ice. Consequently, the Bedmap2 representation of the bathymetry below LCIS is relatively flat, eastward of the grounding line (Figure 2.3a), as very few measurements with which to interpolate an accurate seabed dataset were available when this product was created. Smoothing techniques utilised during the generation of the final Bedmap2 surface elevation map have also removed or reduced other prominent features from the seabed, such as Bawden Ice Rise.

Various aircraft and satellite-based techniques have been employed in an attempt to ascertain details of the seabed topography under LCIS. One such technique uses a gravimetric inversion, obtained from flight paths over the ice

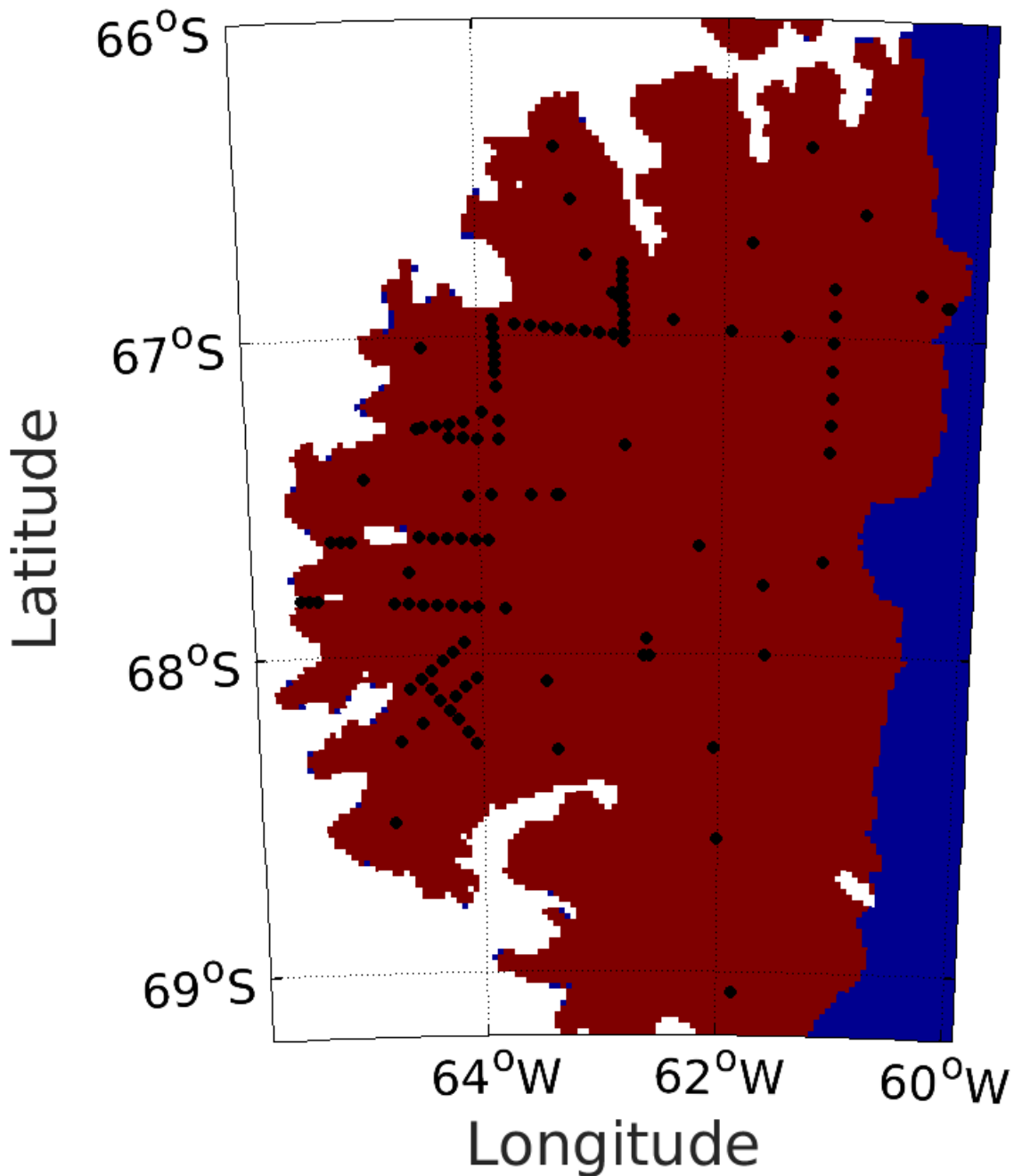


Figure 2.2: Black circles represent seismic sounding points used to construct an interpolated bathymetry for this study. Sites were selected to either verify data gathered from alternate methods, such as gravity inversions, or to confirm the extent of previously located seabed features.

shelf, to infer peaks and troughs in the seabed from changes in measured gravity. This method requires knowledge of the density of the material being measured, and as the geological composition of the seabed underneath LCIS is not known, it can be unreliable; it has produced features in the bathymetry that other, more trusted measurement techniques have shown to be erroneous (Brisbourne et al.,

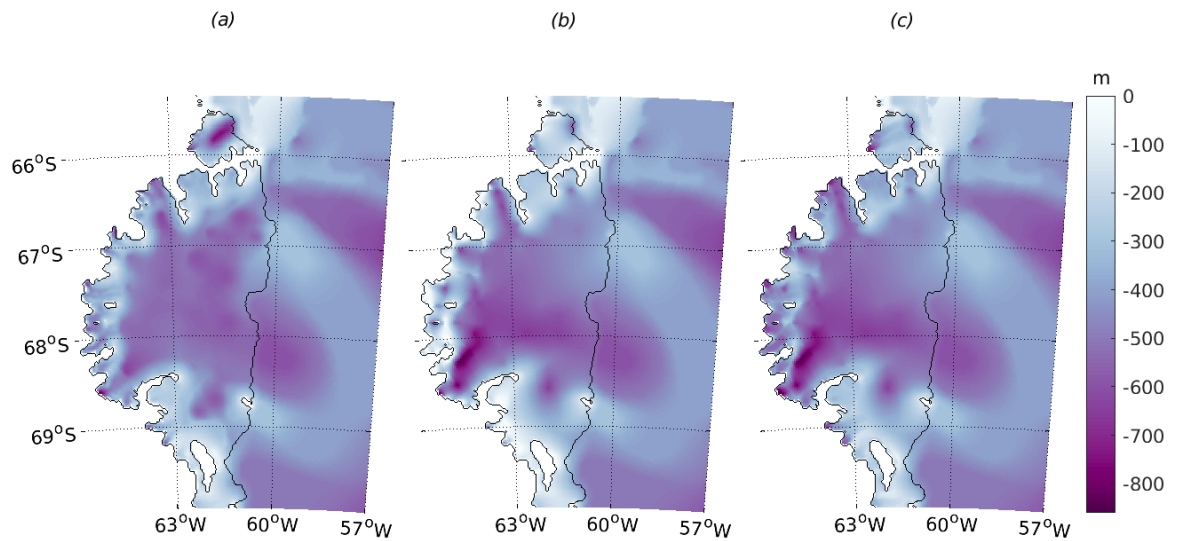


Figure 2.3: (a) Bedmap2 surface elevation map shows relatively flat seabed under LCIS from close to the grounding line to the calving front. Gipps Ice Rise can also be seen but Bawden Ice Rise, which should be grounded at $\sim 66.9^{\circ}\text{S}$, is missing from this dataset. (b) Bathymetry under LCIS mapped by natural neighbour interpolation of seismic sounding points and Bedmap2 surface elevation data beyond the calving front of the ice shelf, marked by the black contour. (c) Bathymetry used in the model which includes all alterations close to the grounding line, as detailed in the text.

2014). Direct measurements, such as seismic soundings, are much harder to obtain in the quantities needed to truly inform the shape of the seabed, but are considered far more accurate.

Seismic surveys have indicated the presence of features under the shelf, for example, a large trough leading into Mobiloil Inlet (see Figure 0.1 for location) from the calving front (Figure 2.1), which are not seen in Bedmap2. The inclusion of features such as this in the model domain is essential as they may have a pivotal role in driving ocean currents under the ice shelf. Along with radar altimetry data from Bawden Ice Rise and direct measurements of the seabed depth through boreholes drilled through the ice shelf, a total of 114 seabed points have been recorded and interpolated for use in this model (Figure 2.2). Natural neighbour interpolation was used because it is well suited to a dataset with an uneven distribution of data points and the polynomial fit to these points ensures the interpolated values are never higher or lower than data values.

Figure 2.3b shows the bathymetry resulting from the combination of these sources, which consisted of an interpolation of predominantly seismic sounding data of the seabed directly below the floating ice of LCIS (shown in red in Figure 2.4a), coupled with Bedmap2 elevation data in all areas of the domain beyond the ice shelf (shown in white in Figure 2.4a). This bathymetry was first presented in

Brisbourne et al. (2020) along with details of the data collection.¹ Both this newly created seabed grid and a grid of ice base depth below the sea surface, calculated from Bedmap2 datasets, were combined to form the model cavity geometry.

2.2.4 Alterations near the grounding line

Following interpolation of the bathymetry grid, the seabed was modified near the grounding line to ensure that all parts of the model domain to which the ocean has access have at least two open velocity points in the vertical column for the ocean to flow between. This also ensured that the ice in the model is correctly floating eastward of the known grounding line, after interpolation of the seabed. The location of the LCIS grounding line, and therefore which sections of ice are floating, is well constrained by satellite altimeter observations of tidal flexure (Fretwell et al., 2013).

'Digging,' or deepening, of the seabed close to the grounding line was undertaken to ensure lateral borders between neighbouring ocean columns are connected, allowing unhindered flow and communication between cells. The backward staggered grid means that in the case of sharp inclines in seabed and the ice base close to the grounding line, columns can easily be disconnected from neighbouring columns, preventing flow. The digging process involved locating those parts of the domain where the water column thickness was less than 40 m, and therefore the ocean did not occupy at least two full grid cells in the vertical direction. Where this was found to be the case, the seabed was altered to make the water column thickness at least 40 m. A 40 m minimum water column thickness ensured that at least two cells in each column were opened, even though two partial cells could have achieved this with a lower depth threshold. Neighbouring cells were also checked to ensure the ocean could flow laterally and, if necessary as a result of the staggered grid, the seabed was deepened to the level of the lowest neighbouring cell position (Figure 2.4b). The final bathymetric product that was used in this modelling study is shown in Figure 2.3c.

¹All data used in this interpolation was collected by others and is not my work. The creation of the bathymetry grid using these data was done by me as part of this project and as a result, I am a co-author of this paper.

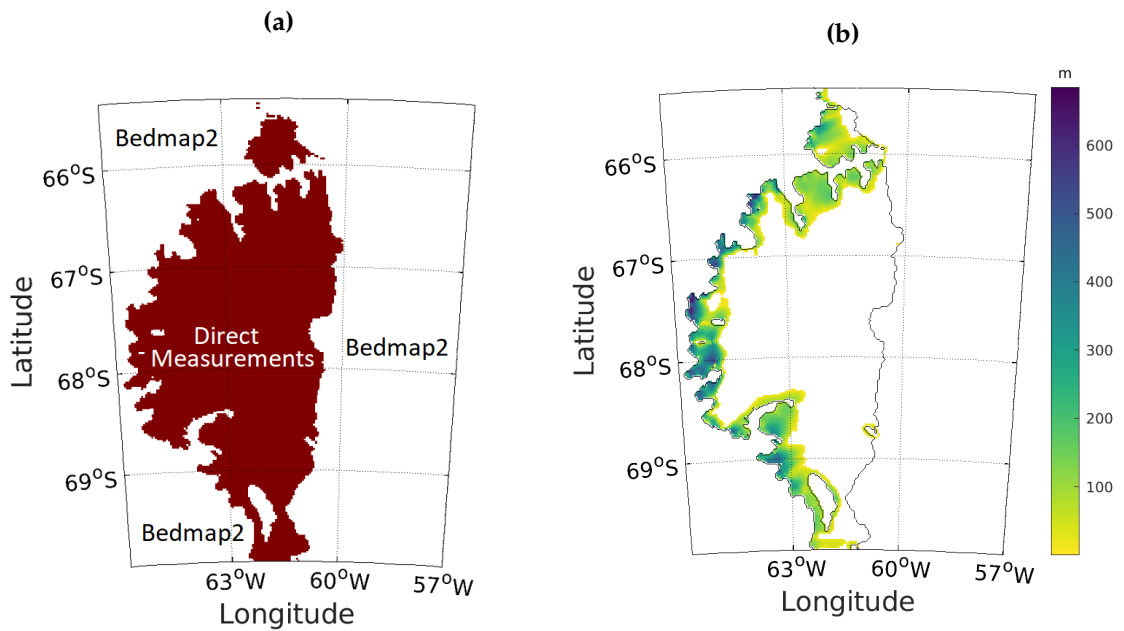


Figure 2.4: (a) Schematic showing the two areas of the model domain which used different datasets to create the new LCIS bathymetry used in this study. The red area depicts where direct seismic measurements were interpolated and the white areas indicate locations where bathymetry data was taken from Bedmap2. Interpolation between these two datasets across the grounding line led to the need for bathymetric alterations in this area to ensure communication between model grid cells. (b) Colour bar shows how much the bathymetry needed to be lowered to accommodate at least a 40 m clearance between the ice base and sea floor, and to open neighbouring columns to ensure lateral communication between ocean cells. As a consequence of this second constraint, the alterations at some of these locations close to the grounding line greatly exceed 40 m.

2.3 Ice shelf package

The MITgcm has a built in thermodynamic ice shelf package that can be turned on to simulate basal melting and freezing taking place at the ice-ocean interface as a result of heat and salt transfer (Losch, 2008). The package uses a static ice shelf, with the depth of the ice base below the surface of the ocean (Figure 2.5) calculated from Bedmap2 datasets (Fretwell et al., 2013). This ice topography was created by subtracting the Bedmap2 ice thickness dataset from the surface elevation data detailing the height of the surface of the ice.

2.3.1 Three-equation model

A three-equation model is used to parameterise ice shelf melting and freezing by balancing heat and freshwater fluxes at the ice-ocean interface. When fluxes

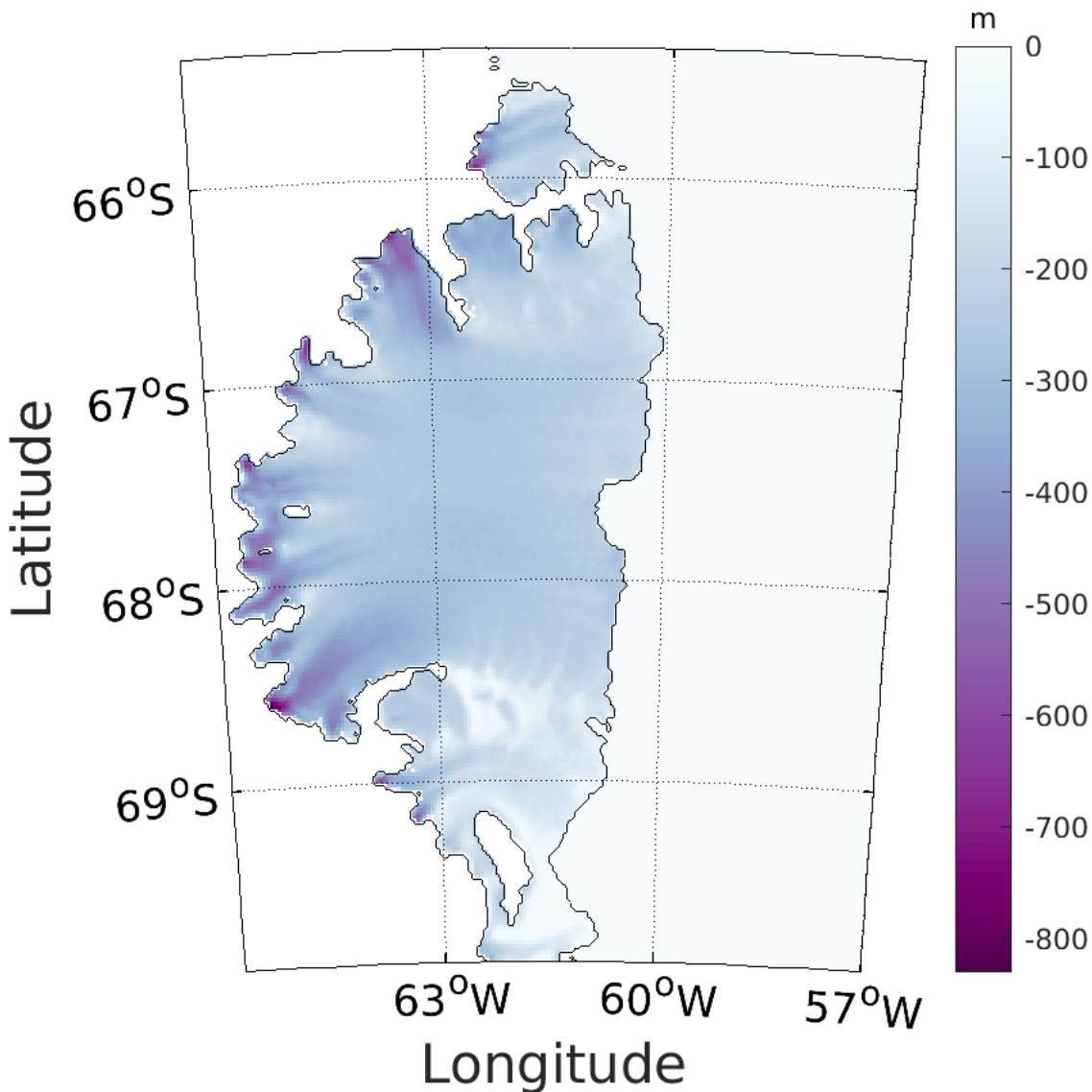


Figure 2.5: Ice topography used in this study shows the depth the ice base reaches in the cavity. Mean sea level is at zero.

through the ice-ocean boundary are not equal, a phase change occurs and latent heat and salt/freshwater are exchanged (Figure 2.6). Three assumptions are made in order for the three equations to hold: the temperature at the interface between the ice shelf and the ocean boundary layer is at the *in situ* freezing point and the heat and salt content of the ice-ocean system are conserved during phase changes (Holland and Jenkins, 1999). The three equations include an expression for the freezing point of seawater at a particular depth, which is used to constrain values for temperature and salinity at the ice-ocean boundary, as heat and salt fluxes occur during a phase change which takes place at the freezing temperature, as well as statements of the conservation of heat and salt:

$$T_b = aS_b + b + cP_b \quad (2.11)$$

$$\rho_i mL = \rho_i c_{p,i} m (T_i - T_b) - \rho_o c_{p,o} \gamma_T (T_b - T_o) \quad (2.12)$$

$$\rho_i m (S_b - S_i) = -\rho_o \gamma_S (S_b - S_o) \quad (2.13)$$

where T, S, P , and ρ are temperature, salinity, pressure, and density, with subscripts b, i , and o indicating boundary, ice, and ocean, respectively (see Figure 2.6). S_i is taken to be zero. The values of the constants a, b , and c have been found empirically. c_p is the specific heat capacity, L is the latent heat of fusion and m is the melt rate given in m s^{-1} . γ_T and γ_S are the thermal and salinity exchange coefficients and are defined as:

$$\gamma_{T/S} = (\sqrt{C_d} u_o) \Gamma_{T/S} \quad (2.14)$$

where C_d is the drag coefficient, u_o is the ocean speed, and $\Gamma_{T/S}$ is a dimensionless, turbulent heat/salt transfer coefficient. The drag coefficient ($C_d = 0.0022$) used in these simulation was derived from recent observations under LCIS (Davis and Nicholls, 2019a) and heat and salt transfer coefficients ($\Gamma_T = 0.011$, $\Gamma_S = 3.1 \times 10^{-4}$) were taken from Jenkins et al. (2010). The second term in Equation 2.12 is a parameterisation of diffusive heat flux into the ice following Holland and Jenkins (1999) and Jenkins et al. (2010).

Equations 2.11, 2.12, & 2.13 can be solved simultaneously to compute T_b, S_b and m . The model calculates the heat and salt fluxes resulting from differences in the conditions at the ice-ocean interface compared with those in the ice interior, which has set values for temperature and salinity (see Appendix A), and the far-field ocean. The gradients of heat and salt between these two extremes are used to drive fluxes, however, salt cannot diffuse through ice and therefore this term is neglected in the three equations. The far field values for the ocean temperature and salinity (T_o & S_o) are taken from the model boundary layer, which is a 20 m-thick layer of ocean below the ice base. In some cases this is a whole grid cell,

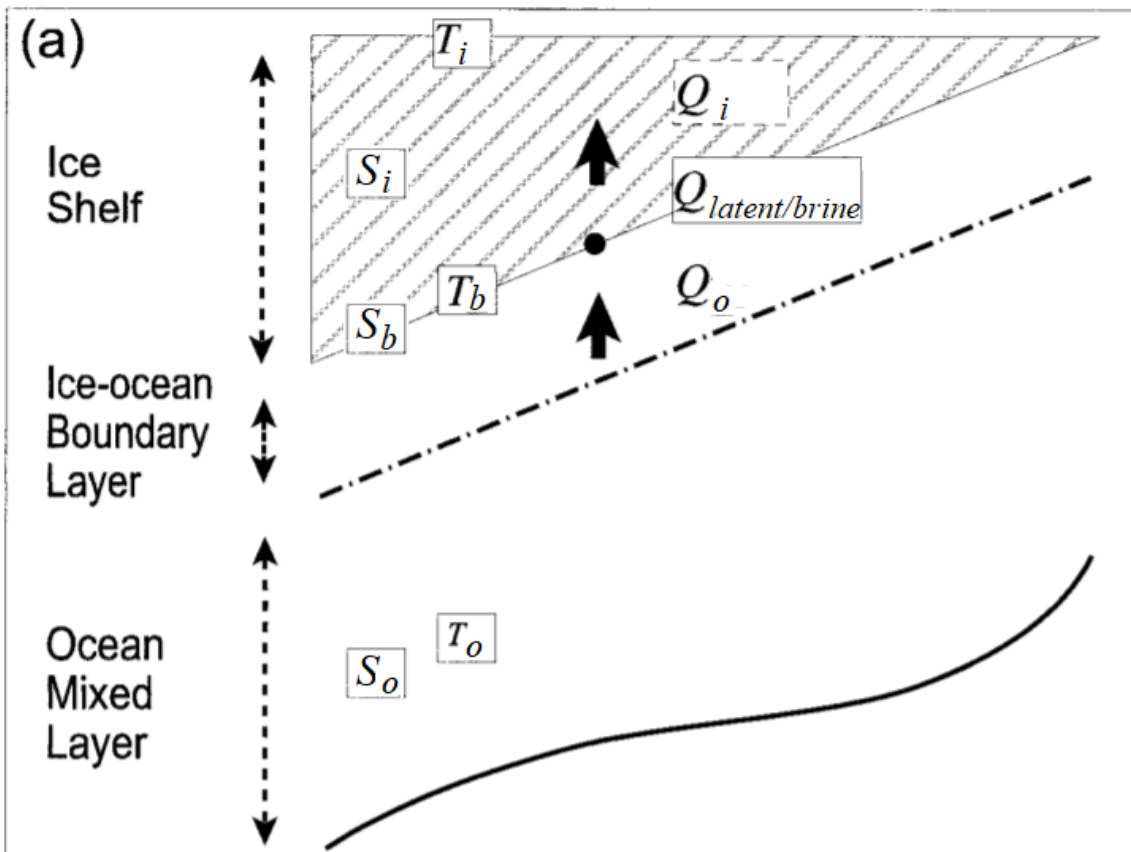


Figure 2.6: Unbalanced fluxes of heat and/or salt through the ice (Q_i) and ocean (Q_o) result in a phase change at the boundary layer accompanied by an exchange of latent heat and salt ($Q_{latent/brine}$). Gradients of temperature and salinity between the far field properties of the ocean and those at the boundary ($T_o/S_o - T_b/S_b$), and between the ice interior and the interface ($T_i/S_i - T_b/S_b$), control the rate of flux through the ice-ocean boundary. Note that salt in the ice (S_i) is negligible and taken to be zero. Image adapted from Holland and Jenkins (1999).

but not always, as a result of the presence of partial cells. For the case where the cell below the ice base is a partial cell, the value in the boundary layer is a weighted mean of the values in the partial cell and the cell below, proportional to the fraction of that cell needed to make a 20 m-thick layer when combined with the partial cell above. When the melt rate is calculated, the ocean heat and salt fluxes from the right-hand side of Equations 2.12 & 2.13 form part of the external forcing terms in Equations 2.9 & 2.10.

2.3.2 Freezing

Despite being regarded as the dominant mechanism by which marine ice grows at the base of ice shelves (Bombosch and Jenkins, 1995; Oerter et al., 1992), frazil ice

formation, which comprises small ice crystals which compress under buoyancy to the ice base, is not included in this model as a result of the high resolution required to resolve this process properly. Instead, the model calculates a negative meltwater flux and ocean water freezes directly onto the base of the ice shelf when ocean water becomes supercooled, which takes place when water at a particular depth has a lower temperature than the local freezing point. Consequently, freeze rates calculated by this package may differ from expected values.

2.4 Boundary conditions

Considering the high resolution needed to address the aims of this research (see Section 1.8.1) the model domain needed to be relatively small to keep computational expense to a reasonable level. Hence, the domain is too small to represent the complex processes occurring in the wider Weddell Sea, so all surface forcing is neglected and instead the model is forced in an idealised fashion, by prescribing constant ocean properties on the lateral boundaries. A seasonal cycle in the temperature and salinity forcing on the boundaries is not included because little variability in ocean conditions in this region has been reported, as a result of year-round sea ice cover (Gordon et al., 1993). The north, south and east boundaries of the model domain were opened to allow the simulation of non-periodic tidal flows across these boundaries while specifying the temperature and salinity of any inflowing water. The temperature and salinity of water at these boundaries was set to a constant, vertical profile matching the initial conditions. The research hypotheses are therefore tested in an idealised manner rather than aiming for the most realistic model possible.

2.4.1 Tides

Tides are implemented in the model by imposing velocities on the open boundaries, directed normal to each boundary, meaning zonal velocities are forced on the east boundary and meridional velocities on the north and south boundaries. They are calculated using the amplitude, A , phase, ϕ , and period, T , of ten tidal constituents (M2, S2, N2, K2, O1, K1, P1, Q1, MM, and MF) at timestep, t :

$$u = A \cos\left(2\pi \frac{t - \phi}{T}\right) \quad (2.15)$$

Velocities in Equations 2.4 & 2.5 are restored to these prescribed values on the domain boundaries.

The different constituents result from different interactions between the Earth and the Sun or Moon. For example, two of the strongest constituents influencing the currents under LCIS are the M2 and S2 constituents, which result from the Earth's rotation with respect to the Moon and Sun, respectively. The amplitude of each tidal constituent is defined as the largest magnitude of the current driven by that constituent, in units of m s^{-1} . The phase of the tidal constituent represents a time lag between an arbitrary reference time and the time at which the constituent is at maximum velocity; this is measured in degrees. One tidal period is the time taken for one wave cycle to be completed (i.e. from maximum velocity to maximum velocity), and in this time, the tip of a rotating velocity vector would trace out a tidal ellipse. Values for the amplitude and phase of each constituent at the coordinates of the domain boundaries were extracted from the CATS2008 tidal model (Howard et al., 2019). CATS2008 is an inverse, circum-Antarctic, barotropic tidal model, with a horizontal resolution of 4 km. The performance of tidal forcing in the model is evaluated in Chapter 3.

2.4.2 Sponge layer

A sponge layer was added to each open boundary in order to dampen internal reflections resulting from large difference between values of temperature, salinity, and velocity on the boundary and in grid cells adjacent to the boundary. The sponge achieves this by adding a relaxation term to Equations 2.4 & 2.5, which absorbs disturbances and gradually dampens them towards prescribed boundary values. The sponge was ten cells wide, with a relaxation time of 30 days at the innermost cell (furthest into the domain) and 60 seconds at the outermost cell, on the very edge of the domain. The eight cells in between had linearly spaced relaxation timescales between these two extremes. These timescales dictate the time taken to damp oscillations of ocean property values back to the boundary value. A range of values for the inner and outer relaxation timescales were tested and did not show any significant change in ocean properties in the domain, therefore, the values presented here were chosen because they optimised the model's computational load.

2.5 Parameterisations and other settings

Many physical processes important for modelling the ocean accurately are either too small to be resolved, even on a relatively high resolution grid such as the one described here, or cannot all be included as a result of time and computational power restrictions. Often, the fine spatial and temporal resolutions needed require the exclusion of certain ocean processes from models. Parameterisations are therefore employed to account for sub-grid scale processes, so that results are not skewed by leaving their effects out entirely.

Mixing of heat and salt is parameterised using constant horizontal diffusivities of $10 \text{ m}^2 \text{ s}^{-1}$ and vertical diffusivities of $1 \times 10^{-4} \text{ m}^2 \text{ s}^{-1}$, following Holland (2017). A non-linear, second order, flux limiter advection scheme is used to compute the movement of tracers such as heat and salt in the flow field (Adcroft et al., 1997). The effect that the shearing of eddies against the surrounding ocean have on the turbulent mixing of momentum is represented by lateral and vertical eddy viscosity coefficients of $50 \text{ m}^2 \text{ s}^{-1}$ and $1 \times 10^{-3} \text{ m}^2 \text{ s}^{-1}$, respectively, also following Holland (2017). Slightly higher values were chosen for viscosity coefficients than diffusivity values for the sake of numerical stability. Momentum transfer requires a shorter timestep than heat or salt transfer, meaning a lower value could be used for diffusivity parameterisation. A drag coefficient of 2.5×10^{-3} was applied to parameterise friction against the bottom and sides of the seabed.

2.5.1 Model timestep

Several simulations were run using different timesteps of between 20 seconds and 6 minutes, to test the effect that the timestep had on model ocean circulation and ascertain the longest timestep that was sufficient to address the aims of this thesis, while minimising computational expense. A 60 second timestep was the longest possible timestep which did not cause the model to fail. This timestep was therefore chosen as a compromise to keep the overall time taken for the model to run to a minimum, while still fulfilling the Courant-Friedrichs-Lewy (CFL) condition:

$$\frac{c\Delta t}{\Delta x} < 1 \quad (2.16)$$

where c is the propagation speed of information, Δt is the timestep and Δx is the diameter of a grid cell. The CFL condition states that the timestep selected for a simulation needs to be small enough that the propagation of information across a model grid cell does not exceed the distance across a cell in one timestep. The high resolution required to effectively resolve ocean dynamics in the high latitudes necessitates a short timestep if the model is to perform correctly. For example, if the tides in a model domain cause a wave to travel across a grid cell in an amount of time that is shorter than the timestep of the model, the ocean velocity information cannot be computed correctly. The explicit timestepping scheme used here was the Adams-Bashforth scheme, which calculates values for dependent variables at the current timestep using quantities calculated at previous timesteps. A polynomial is fit to multiple timesteps, as opposed to just the current and previous values, for smoother results.

The smallest timestep of 20 seconds was tested as this simulation would represent barotropic gravity waves. The phase speed of barotropic gravity waves in the domain is calculated as follows:

$$c = \sqrt{gH} \quad (2.17)$$

where g is the acceleration due to gravity and H is the depth of the water column. For the maximum value of H in the model domain (680 m), the greatest phase speed is 82 m s^{-1} , which gives a minimum timestep of approximately 23 seconds that would satisfy the CFL condition. No discernible differences were found between the 20 second and 60 second timestep runs, therefore, the timestep used in the simulations described in this thesis was 60 seconds, unless stated otherwise.

Values chosen for all fixed parameters used in the model simulations are listed in Appendix A.

2.5.2 Limitations of the model

There are many factors known to affect water mass properties and ocean circulation into and within an ice shelf cavity, including winds, thermohaline exchange between ice and ocean, sea ice production, and tides. The model leaves out some of these processes which are less fundamental to the research questions being addressed. The model does not include wind forcing or any other surface

forcing; no flux is allowed through either the sea surface or the surface of the ice shelf. As wind and solar forcing only affect the surface layers of the ocean, they should not have a large effect on circulation within the cavity, as the ice shelf provides protection from these processes; any surface forcing outside the cavity would not penetrate the water column far enough to reach below the depth of the ice front to drive flow into the cavity. Therefore, not including their effects in the model should not invalidate the modelled cavity circulation at all.

Salinity is a greater driver of ocean currents in the cold polar regions as a result of very small temperature gradients and the small thermal expansion coefficient. Sea ice over the continental shelf in front of LCIS is likely very important for currents entering the cavity. As this thesis focused primarily on the effects ocean temperature has on the melt and freeze rates of LCIS, not including a sea ice package in the model should not detract from the results presented here, as the effects of sea ice formation in the wider Weddell Sea are simulated through boundary conditions.

2.6 Experiments

The main simulation performed in this study was set up based on what is presently known about the current conditions of the ocean in and around the LCIS cavity, and is referred to as the 'standard run' throughout the remainder of this thesis. The standard run uses a potential temperature of -1.9°C and practical salinity of 34.5 for its initial and boundary conditions throughout the water column. This salinity was taken from measurements made by Conductivity, Temperature, Depth profiles near the ice front by Nicholls et al. (2004). The temperature value was chosen because evidence has been found to suggest that water masses at this temperature have access to the cavity (Nicholls et al., 2012), as sea ice formation over the continental shelf constrains water masses here to the surface freezing point ($\sim -1.9^{\circ}\text{C}$). An evaluation of the model's performance and ability to capture the main features of the cavity's ocean circulation is assessed in Chapter 3.

Several other simulations were run for comparison with the standard run, to test the sensitivity of LCIS' ocean circulation and melt/freeze rates to changes in cavity geometry and ocean temperature. Simulations using two different seabed bathymetries were run to test the impact of the southern trough on the ocean processes beneath LCIS and confirm the findings of Mueller et al. (2012), that the

melting pattern is dependent on the shape of the cavity. If the primary cause of the observed lowering of LCIS is basal melting resulting from changes in the ocean, then either the temperature of the water or the velocity of the currents in the ice shelf cavity must be increasing, or both. Further idealised simulations with warmer initial and boundary condition temperatures of up to -1.0°C were run to test the sensitivity of the ice shelf cavity to changes in ocean forcing. The upper value in this range is roughly the middle ground between the warmest waters found from two sets of oceanic observations taken in front of the ice shelf during austral summer (Bathmann et al., 1994; Nicholls et al., 2004). These experiments show the melt rates that might result were these water masses able to enter the cavity.

All cases had an initial and boundary salinity of 34.5 and did not include a thermocline or halocline; initial and boundary values of temperature and salinity were invariant throughout the water column. The results of these bathymetry and ocean temperature sensitivity tests are discussed in Chapters 4 & 5, respectively.

Chapter 3

Model validation

The standard run is believed to be a simplified setup of current conditions under LCIS and was therefore used to validate the model by comparing results with information previously gathered from observations and other modelling studies. Observations of the ice shelf cavity are few because of the difficulties of reaching LCIS, but those that are available, from ship-based explorations and moorings beneath the ice base, are used to determine if the model is capturing key features of cavity circulation.

3.1 Confirming model had reached steady state

Simulations were run for ten years, after which the model was deemed to have reached equilibrium with the boundary conditions. Several checks were performed to ensure the model had reached a steady state and was no longer spinning up.

3.1.1 Domain-averaged melt rate

As the melt rate of LCIS is a focal point of this investigation, this output variable was checked first to ensure the model had reached steady state. Figure 3.1a shows that after an initial, steep change in domain-averaged melt rate, the values quickly become steady. A calculation was performed to ensure the change in melt rate over the final year of the simulation was small compared with the change in melt rate in the first year:

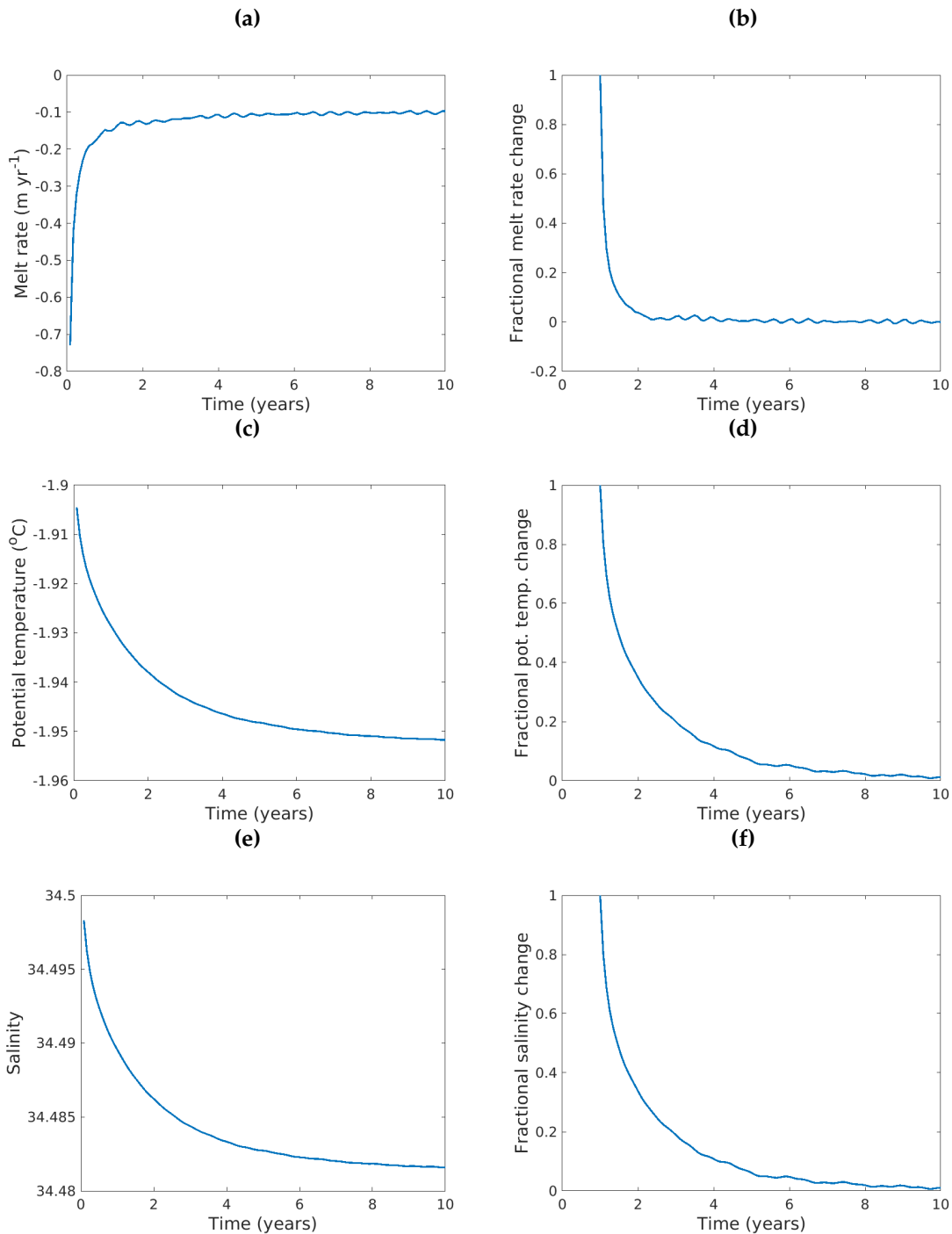


Figure 3.1: Timeseries of domain-averaged melt rate (a), potential temperature (c) and salinity (e) across the standard run and the fractional change with respect to initial, annual melt rate change (b), potential temperature change (d) and salinity change (f). The fractional change is defined as the change in a variable over the preceding 12-month period for every month of model output, divided by the change in that variable across the first year of the run.

$$\frac{\Delta meltrate_{finalyear}}{\Delta meltrate_{firstyear}} < 0.1 \quad (3.1)$$

The melt rate across the domain was therefore deemed to be steady, as the resulting value in the tenth and final year of the run was less than 0.1% (9.1×10^{-4}), which is well below the 10% threshold that was aimed for. A timeseries of this calculation (Figure 3.1b) shows that in comparison with the initial unsteady fractional melt rate change, the values become relatively steady within two years.

3.1.2 Domain-averaged potential temperature and salinity

As a further test that the domain had reached steady state, timeseries of domain-averaged potential temperature and salinity were also plotted (Figure 3.1c & e) and show the variables had levelled off in the second half of the simulation. While these properties do not appear to have steadied as much as the melt rate, the steady state calculation (Equation 3.1) produced values of 1% for both potential temperature and salinity, which is deemed to be steady. Figures 3.1d & f further demonstrate that at the end of the ten-year run, the monthly fractional change in both potential temperature and salinity, with respect to the initial simulation year, has reduced significantly.

3.1.3 Equilibrium in a single cell

In order to check that individual elements of the domain had reached a steady state, the same tests were conducted on a single cell of the domain, corresponding to the location of the southern observation site, where many aspects of the model validation were tested, as detailed in this chapter. The left column of Figure 3.2 shows the timeseries of melt rate, potential temperature, and salinity at this location also reached equilibrium for the final few years of the simulation. Equation 3.1 resulted in a value of 0.08 for the melt rate of this cell, with values of 0.15 and 0.16 for potential temperature and salinity, respectively.

The timeseries of these variables display an apparent tidal signal with a period of approximately six months. The melt rate also shows a separate signal with a period of around two and a half years. These phenomena result from the frequencies of some of the tidal constituents used to force the model not averaging

to zero over the model output averaging period (30 days) because they do not have a 30-day repeat cycle. Constituent frequencies will beat together to create their own signal when discretised using a period that does not match the length of their cycle, leaving a 'phantom' residual tidal frequency. This signal leads to larger values than 10% resulting from Equation 3.1 despite the figures clearly showing a long-term mean has been reached towards the end of the simulation.

Unless otherwise stated, all results presented from now on are averaged over the final year of the ten-year simulation, when the model had reached equilibrium with the boundary conditions.

3.2 Circulation across the model domain

The domain's circulation is largely divided by the calving front of the ice shelf (Figure 3.3a). Nicholls et al. (2012) suggested that a potential vorticity step at the ice front acts as a barrier preventing inflow. Results show only small amounts of water make their way from the continental shelf into the cavity, suggesting that along the vast majority of the ice front this is true. There is a sudden change in water column thickness of a few hundred metres between the ocean over the continental shelf and under the ice shelf. Conserving angular momentum as the water column stretches or shrinks to move between this divide would be impossible in an unstratified ocean, without other forces such as friction intervening.

Circulation beneath the ice is split into two distinct components. One component, in the south, consists of inflow following contours of water column thickness to make its way into Mobiloil Inlet and then heading north from here, driven by seabed contours (Figure 3.3b). The second component is located in the northeast and sees meltwater that has crossed the ice shelf flowing clockwise around water column thickness contours to exit the cavity at Jason Peninsula. Throughout the remainder of this thesis, these circulation components will be referred to as the 'southern circulation component' and the 'northern circulation component,' respectively. Water flowing eastward between these two circulation components, from approximately 64°W to 61°W, crosses contours of water column thickness in order to connect the two components despite both components' clockwise flow directions. A potential barrier to flow near the grounding line at Francis and Tonkin islands (see Figure 0.1 for locations) was noted by Brisbourne et al. (2014), who measured very shallow bathymetry here compared with the rest

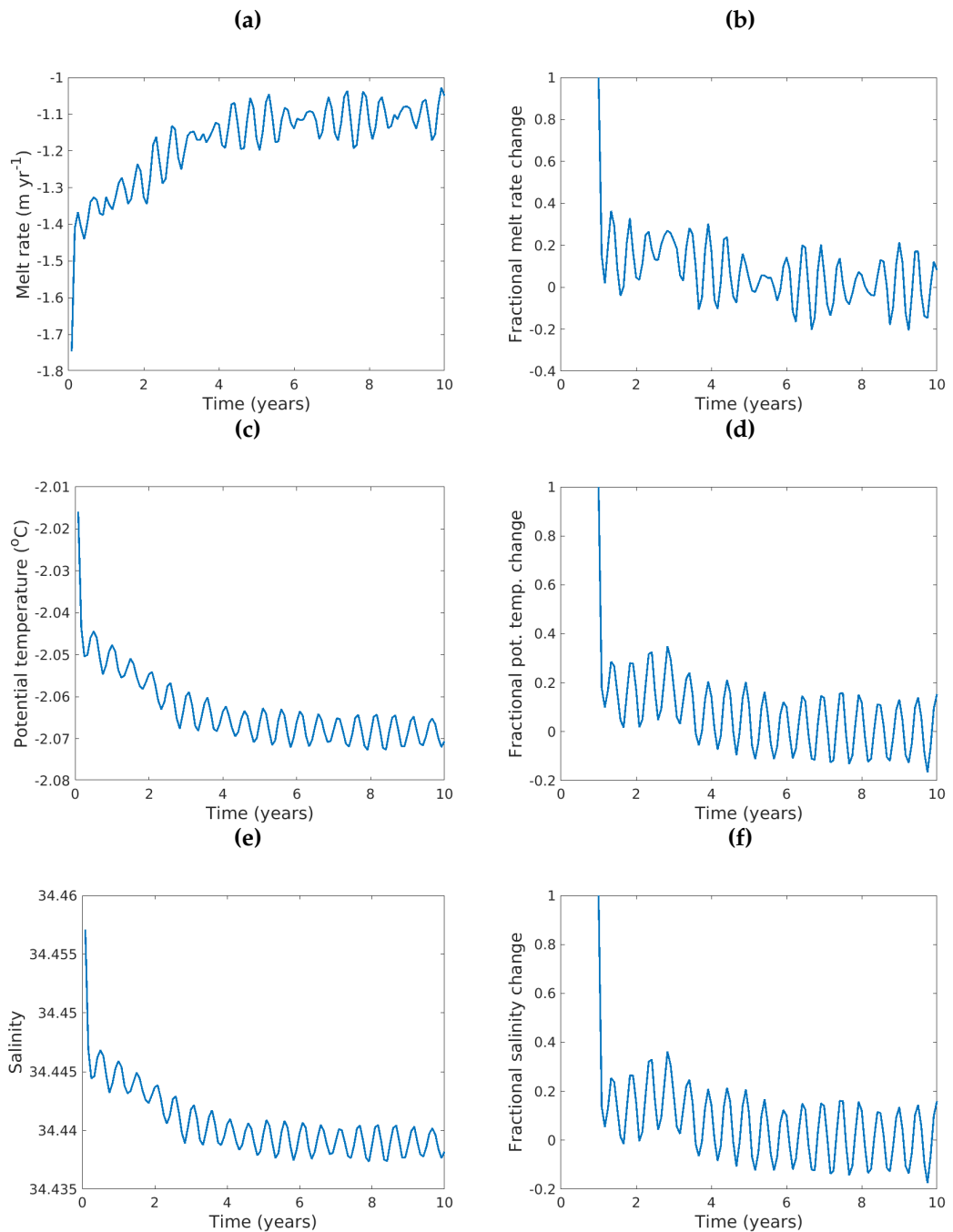


Figure 3.2: Timeseries of a single model grid cell melt rate (a), potential temperature (c) and salinity (e), corresponding to the southern observation site, and fractional change with respect to initial, annual melt rate change (b), potential temperature change (d) and salinity change (f).

of the grounding line. They suggested that this barrier may result in two separate circulations within the cavity, which has manifested in the simulation.

Flow in the cavity is not entirely barotropic and therefore the streamfunctions presented in Figure 3.3 are used only as an indication of the depth-averaged

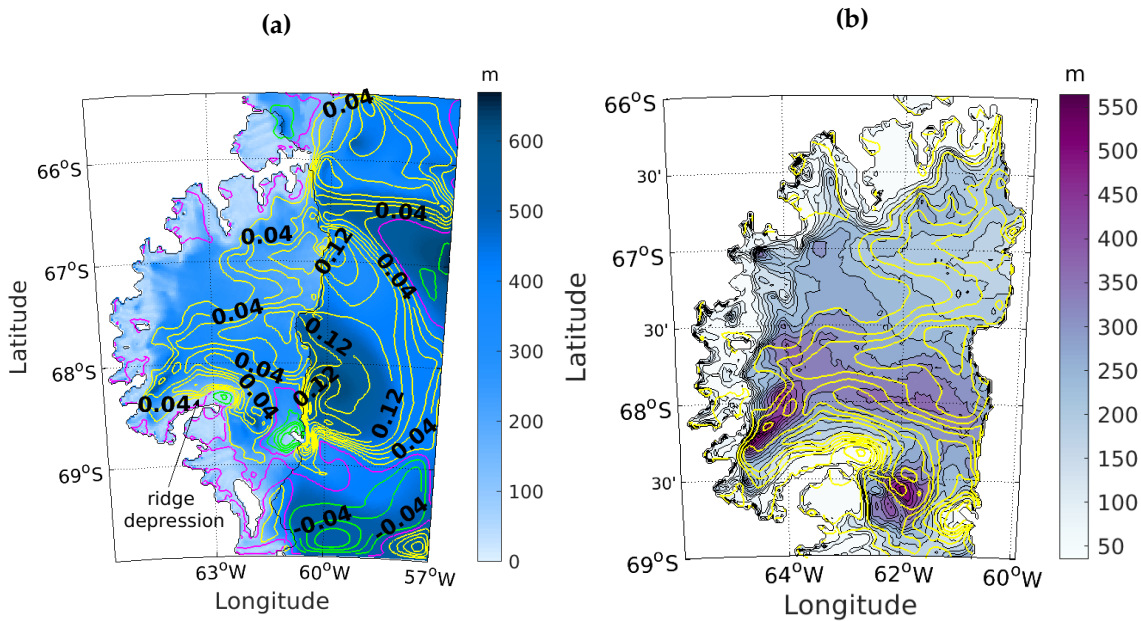


Figure 3.3: (a) Water column thickness with barotropic streamfunction contours overlaid. Yellow contours are positive values (clockwise flow), green contours are negative (anticlockwise flow) and the pink contour shows zero flow. Values indicating volumetric flow rate have units of Sverdrups. (b) The barotropic streamlines, now all shown in yellow, primarily follow contours of water column thickness underneath the ice, shown in filled shades of purple.

circulation. The north and south circulation components shown here are dominated by outflow and inflow, respectively. Therefore, looking at the flow velocities at the top and bottom of the water column (respectively) is more useful to identify the finer details of these aspects of the circulation.

3.2.1 Inflow

Figure 3.4 shows deep water close to the surface freezing point ($\sim -1.95^{\circ}\text{C}$) entering the cavity at Gipps Ice Rise, which agrees with the location of inflowing water in the simulations of LCIS described in Mueller et al. (2012). Water is able to enter the cavity at this location, despite the vorticity constraints at the ice front, as a result of friction and the shape of Gipps Ice Rise in relation of the ice front, which directs water column thickness contours into the cavity.

A closer look at this inflow region (Figure 3.5) shows that once inside the cavity, water travels north, in line with the ice front, then meets a southward-flowing recirculation of part of the meltwater plume out of Mobiloil Inlet. Upon meeting at $\sim 68.2^{\circ}\text{S}$, the flow is deflected west by the southern trough in the seabed. From here, currents parallel to Kenyon Peninsula, deflected eastward by part of the flow

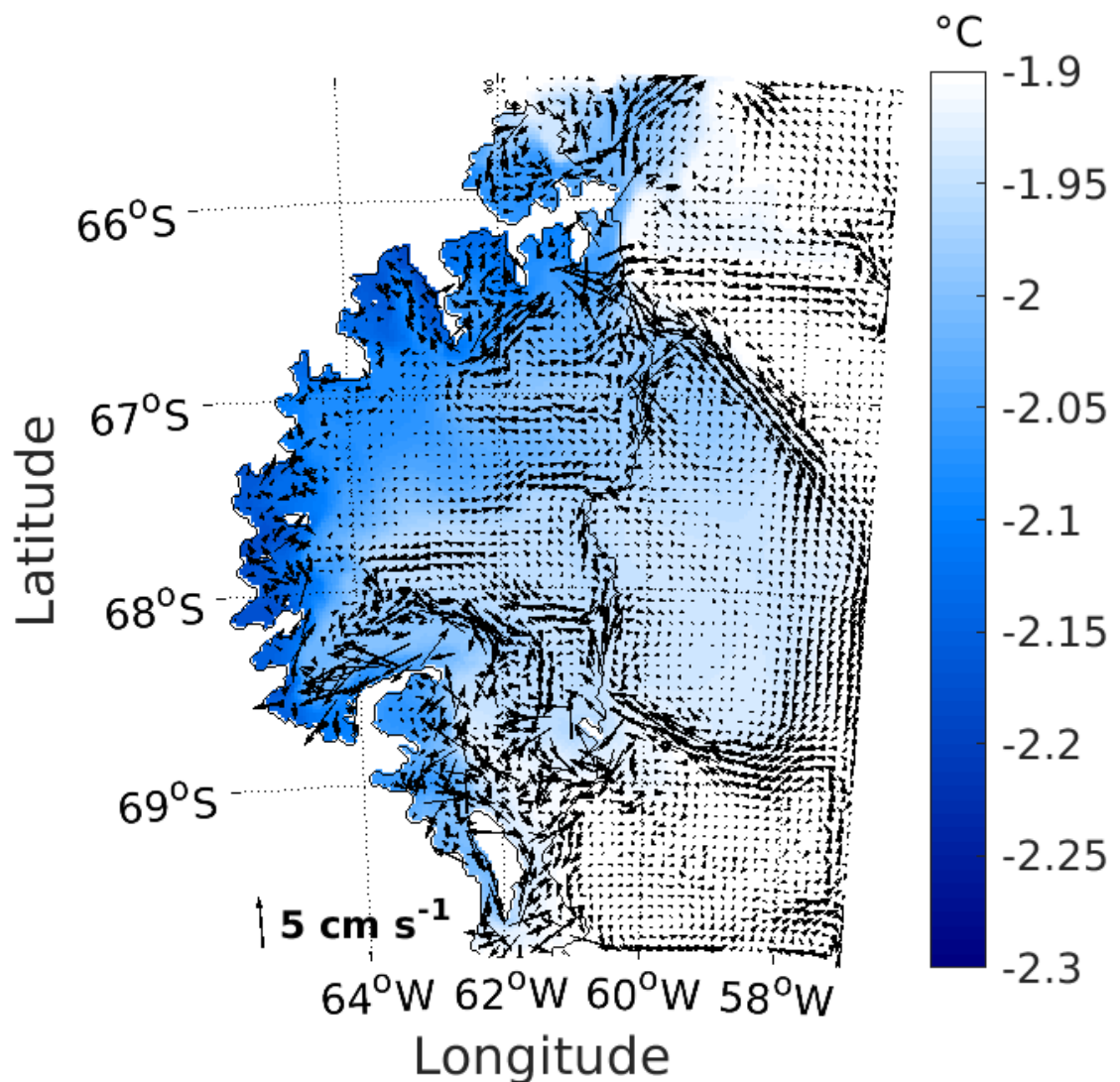


Figure 3.4: Potential temperature at the sea floor with sea floor velocities overlaid. Vectors with magnitudes greater than 5 cm s^{-1} have been removed for clarity.

of meltwater out of Mobiloil Inlet, leads the inflow southeast before a steepening of the seabed at Hearst Island funnels the flow back north. This circulation then joins a rapid westward flow directly over the north face of Kenyon Peninsula and into the grounding line in Mobiloil Inlet. As the depth-averaged circulation is dominated by this inflow, the path described here is most clearly seen in Figure 3.3b.

Nicholls et al. (2004) and Nicholls et al. (2012) suggested that an inflow of High Salinity Shelf Water, resulting from salinification and cooling of modified Warm Deep Water through sea ice formation and heat loss to the atmosphere over the continental shelf, enters the cavity north of Gipps Ice Rise and makes its way to the grounding line at Mobiloil Inlet. A long-term mean westward current

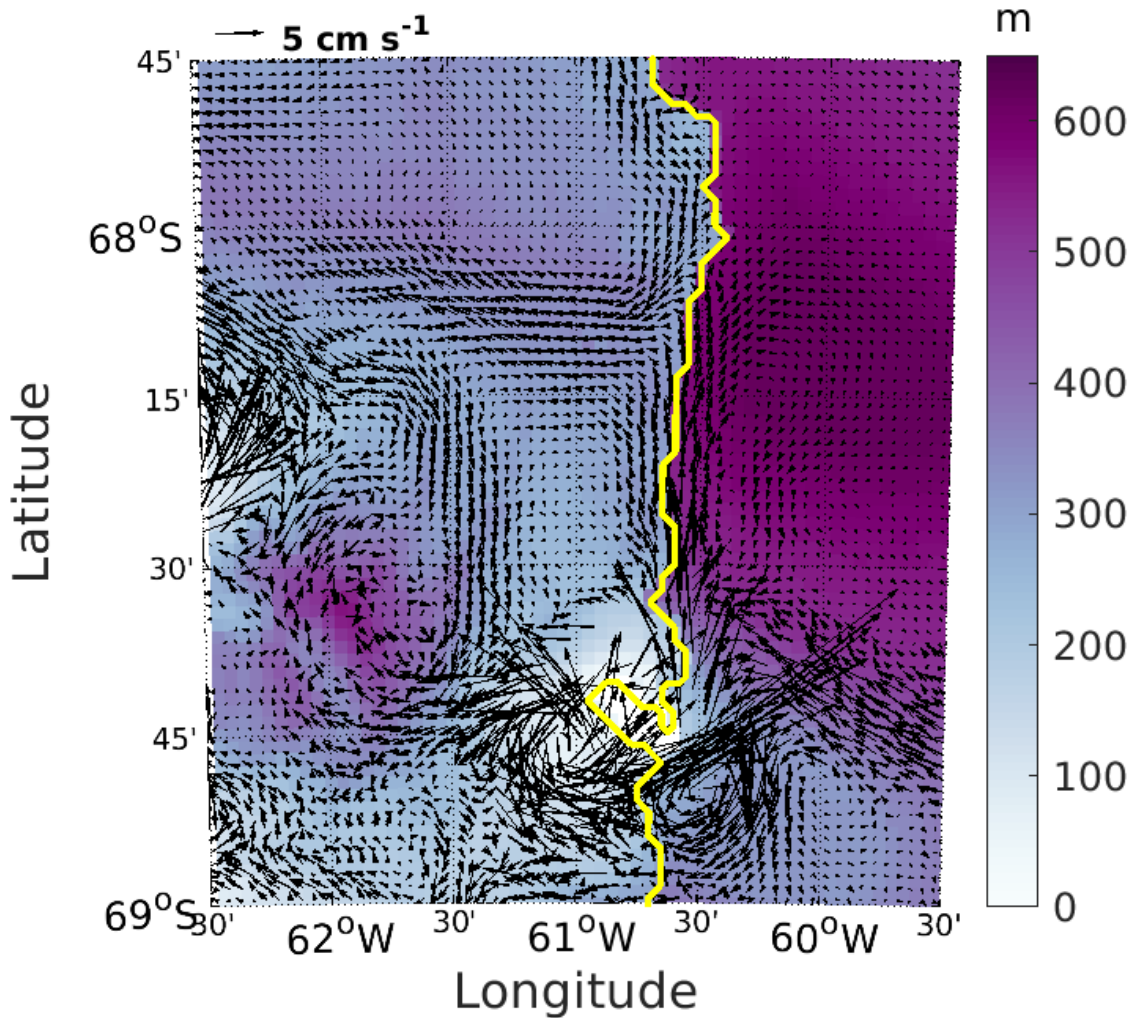


Figure 3.5: Water column thickness with sea floor velocities overlaid at the location of inflow to the cavity.

was measured at the southern observation site (Nicholls et al., 2012). The main features of this inflow are captured, with the model revealing a more detailed route into Mobiloil Inlet.

Inflow is limited to the location north of Gipps Ice Rise. The simulation shows that a westward inflow in the north of the domain along the northern trough is blocked by the strong, barotropic outflow guided by the meltwater plume. Evidence for this secondary inflow was reported by Nicholls et al. (2004) who deduced that modified Warm Deep Water accesses the continental shelf via troughs in the seabed, meaning this is the primary source of water to flush the LCIS cavity. They found that a relatively warm intrusion of water had interacted with the ice shelf near Bawden Ice Rise, but did not speculate as to whether the warm water had accessed the shelf via the northern trough or an alternate

route. Adusumilli et al. (2018) hypothesized that warm water was able to gain access to the ice at this location as a result of a reduction in the strength of a meltwater-driven current making its way out of Mobiloil Inlet. They proposed that this slowdown of the flow of meltwater as it exited the cavity meant it was no longer strong enough to block inflow at the ice front, but this theory is based on model results from a study of a different ice shelf cavity (Mueller et al., 2018). Interaction with the ice base of water inflowing along the northern trough is not seen here. Figure 3.4 shows the warmest water in the domain (-1.9°C) encroaches on the ice shelf via the northern trough but is prevented from entering the cavity by outflowing water at Jason Peninsula and Bawden Ice Rise, therefore protecting the ice at these locations.

3.2.2 Outflow

The main outflow, in the form of a cold and fresh meltwater plume, takes place at the northern-most point of the cavity, just south of Jason Peninsula. Outflow at this location has been observed (Nicholls et al., 2004) and captured by other models (Holland et al., 2009; Mueller et al., 2012). Velocities beneath the ice base (Figure 3.6) reveal that the plume originates from enhanced melting in Mobiloil Inlet and meanders northward to Francis Island, in line with water at depth which follows seabed contours. Here, a thinning of the water column results from a rise in bathymetry to the north and leads a large portion of the plume northeastward along the northern edge of the southern trough at approximately 67.5°S , towards Bawden Ice Rise. This plume direction was also seen by Mueller et al. (2012), despite stark differences between the two domain geometries.

On approach to the ice front, a gradient in water column thickness south of Bawden Ice Rise, caused by shallower seabed near the ice front, then steers the majority of the plume northwest towards Churchill Peninsula. A weaker, secondary plume, which hugs the grounding line, then merges with the main plume to drive water out of the cavity in the northeast, at the tip of Jason Peninsula, where it then travels north past the remnant Larsen B Ice Shelf (Figure 3.6).

A smaller part of the plume escapes from the cavity at Bawden Ice Rise (Figure 3.7). From here, this weaker outflow navigates south, where it becomes entrained in the barotropic flow migrating along the eastern edge of a raised semicircular ridge in the continental shelf seabed (Figure 3.3a). This feature deflects the flow towards the ice shelf cavity, where it joins the inflowing water in the south of the

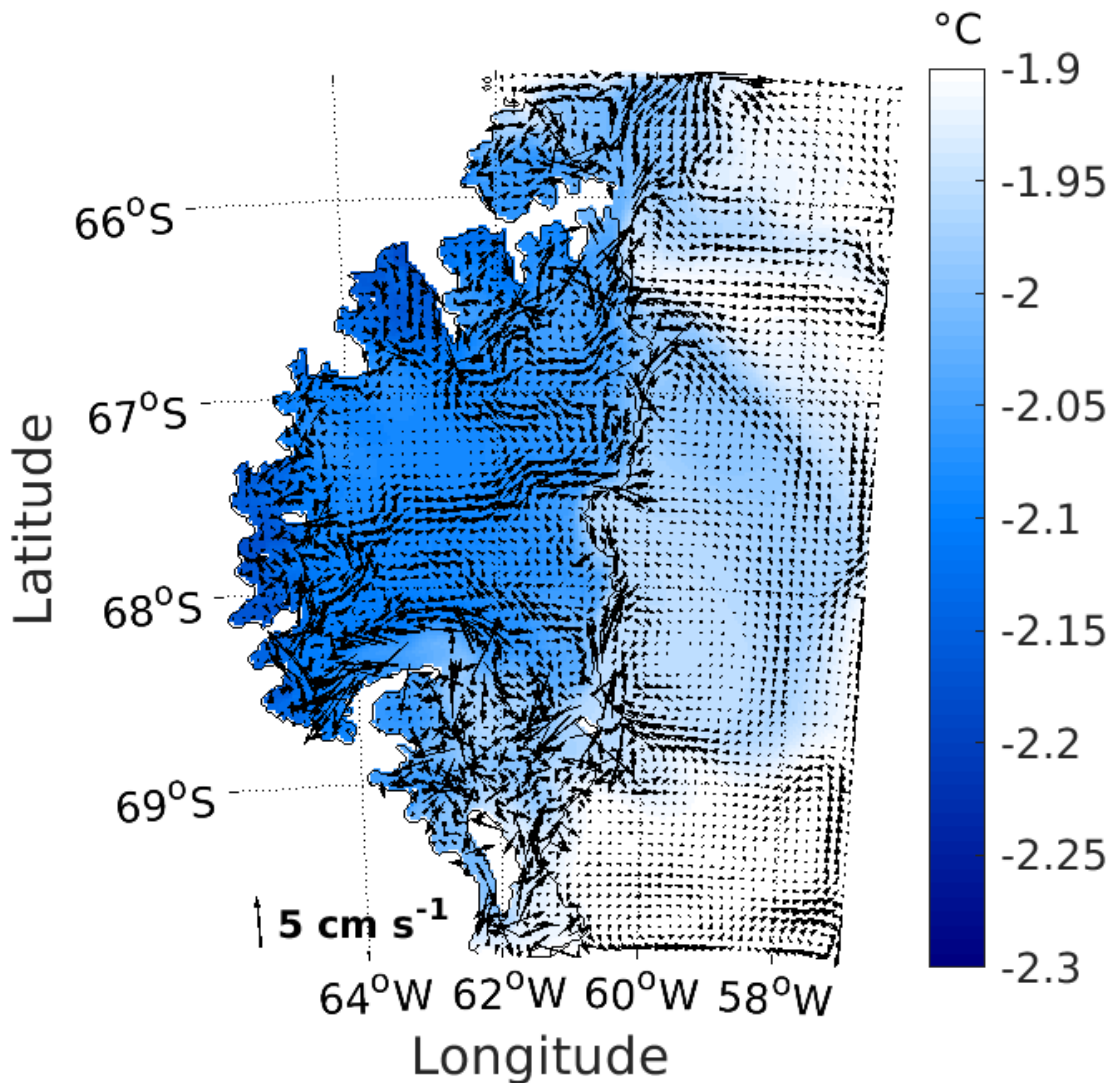


Figure 3.6: Potential temperature at the sea surface over the continental shelf and at the ice-ocean interface within the cavity, with surface velocities at corresponding locations overlaid. Vectors with magnitudes greater than 5 cm s^{-1} have been removed for clarity.

domain. Although the flow of the plume follows water at depth which makes its way into the cavity at Gipps Ice Rise, water at the surface does not penetrate the cavity, but instead travels north, parallel to the calving front. Only waters slightly below the surface freezing point, at depth, are shown to enter the cavity.

The meltwater plume, shown in Figure 3.8a, is defined here as all waters 0.025 kg m^{-3} lighter than the uniform initial density conditions. This is because the MITgcm calculates and outputs only a density anomaly from a static, pressure dependent, horizontally uniform reference density grid. Any change in density from this initial density structure drives a flow in the model. The value of 0.025 kg m^{-3} was chosen simply for clarity in Figure 3.8a, rather than for any particular

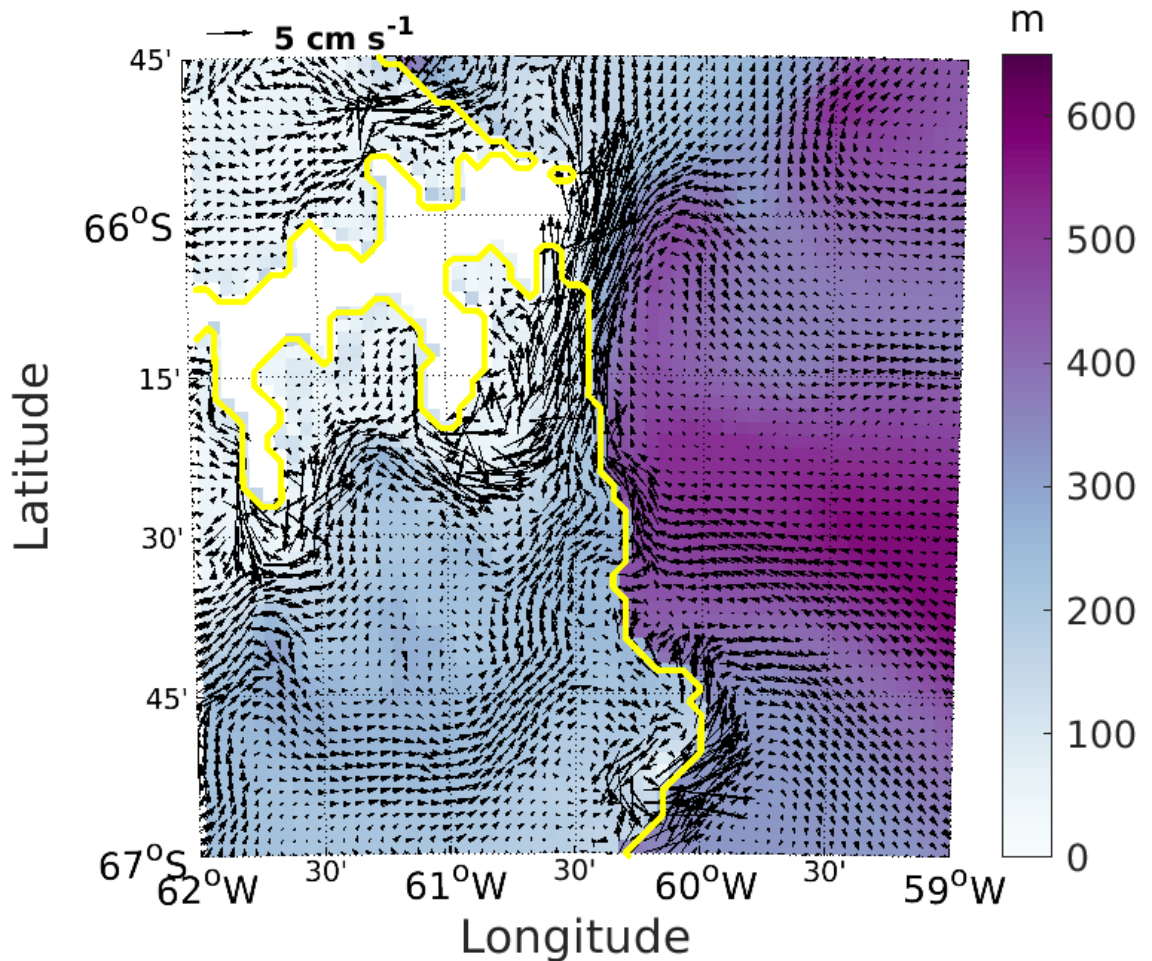


Figure 3.7: Water column thickness with surface velocities overlaid at locations of outflow from the cavity.

significance.

The plume differs to that simulated by the reduced model of Holland et al. (2009) (Figure 3.8b), which predicted that meltwater travelled close to the grounding line after leaving Mobiloil Inlet, to flow more directly north to Churchill Peninsula, gathering water from overflowing basal hollows adjacent to peninsulas along the way. Their plume had a peak thickness of 250 m at Hess Inlet (see Figure 0.1 for location). The model of Holland et al. (2009) solves equations specifically for the depth of the plume, whereas the plume depth reported here is approximated by the number of cells in the water column with a density below an arbitrary value. As a consequence, values taken from the maps in Figure 3.8 cannot be directly compared. However, the pattern of relative plume thickness across the domain is comparable, irrespective of the differences between model configurations.

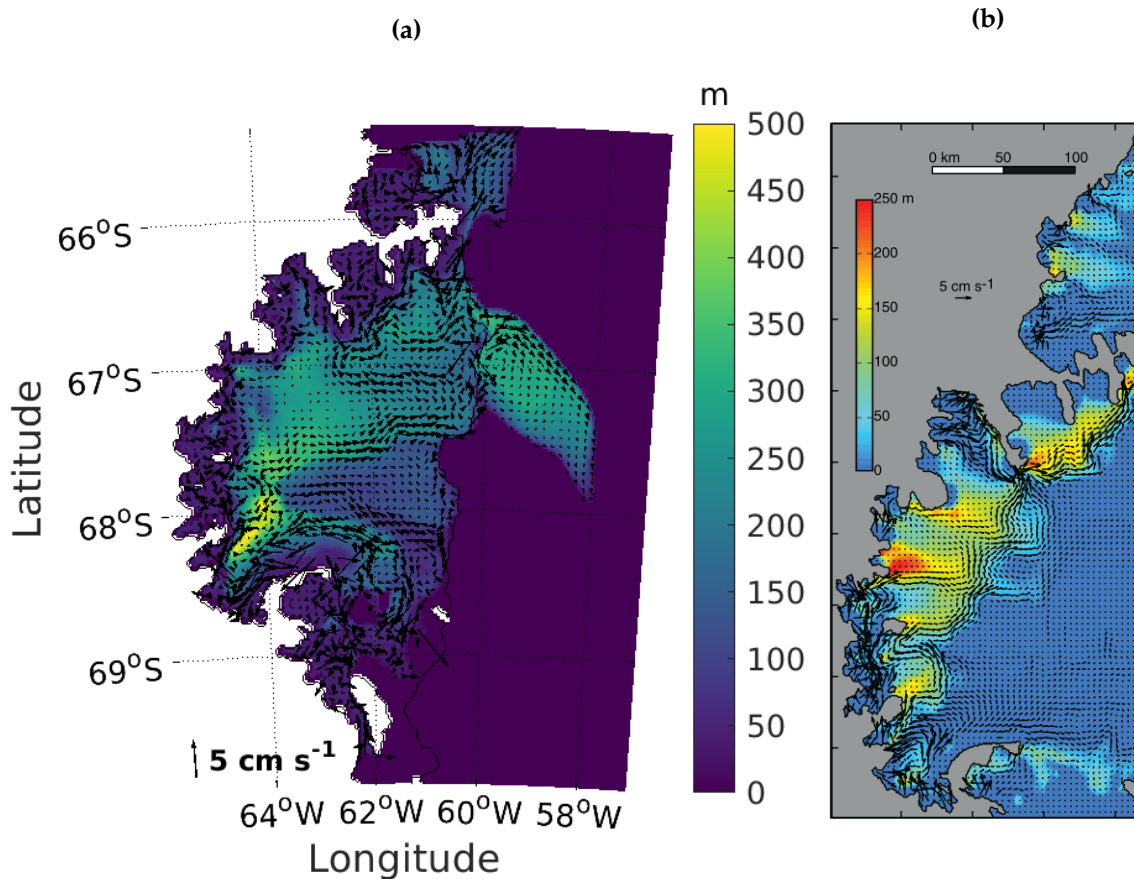


Figure 3.8: (a) Thickness of the meltwater plume, defined as water with a density change of more than 0.025 kg m^{-3} from initial conditions, with plume velocity vectors overlaid. Vectors with magnitudes greater than 5 cm s^{-1} have been removed for clarity. (b) Plume thickness and velocities adapted from Holland et al. (2009) shown for comparison.

The greatest plume thickness in this study is not seen at Hess Inlet, despite a high, wide hollow in the base of the ice in this geometry, because the plume is deflected away from this region by steep seabed south of this location. Additionally, tidal mixing within the cavity, which is not included in the model of Holland et al. (2009), leads to greater entrainment of warm, salty water as the plume progresses under the ice shelf. The plume's maximum depth is instead found at its origin in Mobiloil Inlet, where meltwater from enhanced melting over Kenyon Peninsula is transported and collected. The present study shows that the seabed bathymetry, neglected in the model presented by Holland et al. (2009), has a significant influence on steering the plume path eastwards. This has implications for our knowledge of the freezing pattern under the ice base, as well as the residence time of water in the cavity.

3.3 Melt rate and pattern

The spatially-averaged, steady state basal melt rate for the standard run is approximately 0.1 m yr^{-1} , which is at the lower end of the range of other modelling and satellite-derived observational results ($0.1\text{-}1.3 \text{ m yr}^{-1}$, Huhn et al. (2008); Holland et al. (2009); Mueller et al. (2012); Borstad et al. (2013); Rignot et al. (2013); McGrath et al. (2014); Holland et al. (2015); Bernales et al. (2017); Adusumilli et al. (2018)). Mueller et al. (2012) got the same spatially-averaged result from their modelling study but with a markedly different melt pattern. The pattern of melting is the greater focus of this study as modelled melt rates are highly dependent on values selected for model parameters, such as the drag coefficient and heat and salt transfer coefficients, and there are not a great deal of observations to inform the choices of these parameters. Previous studies have noted the influence of cavity geometry on modelled melt patterns (Mueller et al., 2012; Seroussi et al., 2017; Mueller et al., 2018) and Mueller et al. (2012) noted that their melt pattern results were limited primarily by inadequate knowledge of the LCIS seabed and a lack of hydrographic observations from within the cavity. The melting pattern produced here is therefore expected to be an improvement as both of these limitations have been addressed.

Many previous studies of LCIS' basal melting disagree about whether the greatest melting in the domain, other than at the grounding line, takes place in the northeast, around Bawden Ice Rise, or in the southwest, in the vicinity of the southern trough. For example, McGrath et al. (2014) found melting was greatest close to Bawden Ice Rise (up to 2 m yr^{-1}), whereas Borstad et al. (2013) reported very little melting in this area, but instead showed the highest melt rates in their model domain in Mobiloil Inlet, where the southern trough terminates. A recent study by Sutterley et al. (2019), who determined that LCIS was in an almost steady state for the period of their remote observations, inferred higher rates of basal melting, of up to 4 m yr^{-1} , shifting from the northeast at the beginning of the century to the southwest after 2008.

3.3.1 Enhanced melting in the south

The standard run shows that the greatest melting in the domain occurs just north of the tip of Kenyon Peninsula (Figure 3.9a), with a value peaking at $\sim 3 \text{ m yr}^{-1}$. Rapid inflow parallel to Kenyon Peninsula, one of two regions in the domain with the greatest velocities at the ice shelf base of up to 0.5 m s^{-1} (Figure 3.10), leads to

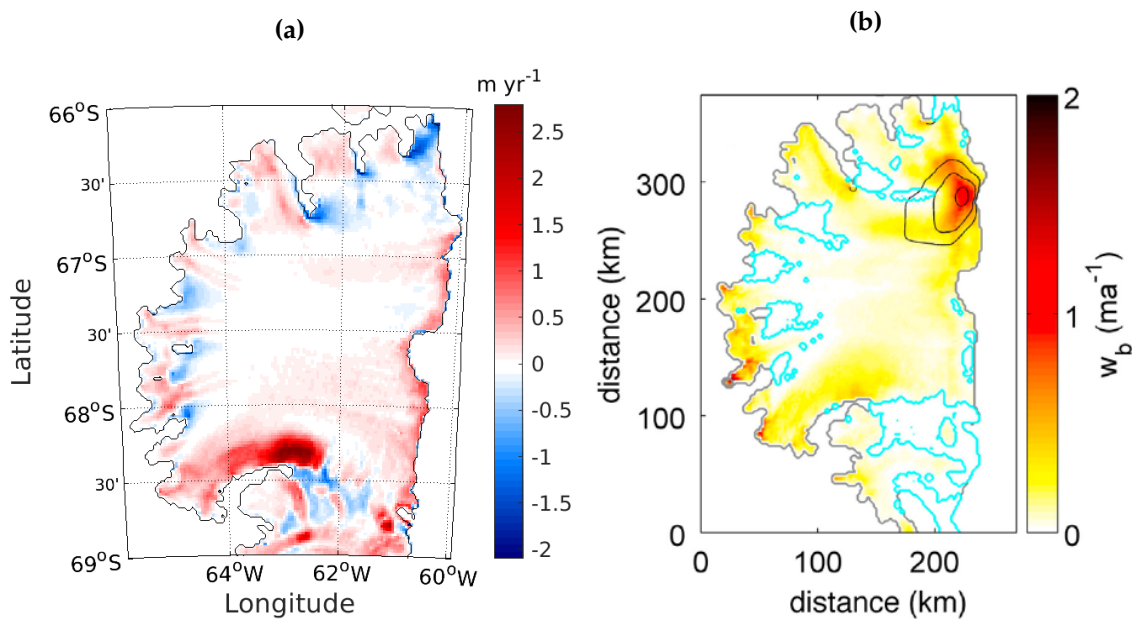


Figure 3.9: (a) Steady state melt and freeze pattern across the ice shelf from the standard run; red shows melting, blue shows locations of refreezing. (b) Melt/freeze pattern adapted from Mueller et al. (2012) is shown for comparison. Cyan contours show extent of refreezing but no freeze rates are reported; black contours in the northeast indicate mean barotropic flow speeds of 0.2, 0.3, and 0.4 m s^{-1} .

high melt rates in this southern region. Greater melting results from an increase in turbulent heat flux, which is dependent on flow speeds adjacent to the ice base, as represented in Equation 2.14. High melt rates were also seen by Mueller et al. (2012) north of Kenyon Peninsula, however, their signal is dwarfed by the intense melt pattern they found in the northeast (Figure 3.9b).

3.3.1.1 Observations at the southern mooring site

Recent observations from moored instruments left beneath the base of LCIS via hot water drilling (Nicholls et al., 2012), close to this enhanced melt region, have been used to validate the model's performance. Davis and Nicholls (2019a) report an annual-mean melt rate of 0.7 m yr^{-1} with a standard deviation of 1.0 m yr^{-1} at the observation site, measured by upward-looking sonar, with the wide range being caused by high temporal variability. The modelled mean melt rate at this location is slightly higher than the measured value, at 1.2 m yr^{-1} , with a standard deviation of 0.7 m yr^{-1} calculated using hourly output from a simulation restarted at the end of the ten-year standard run. The lower variability in the model compared with measured variability is an expected consequence of the absence of a seasonal cycle in the model.

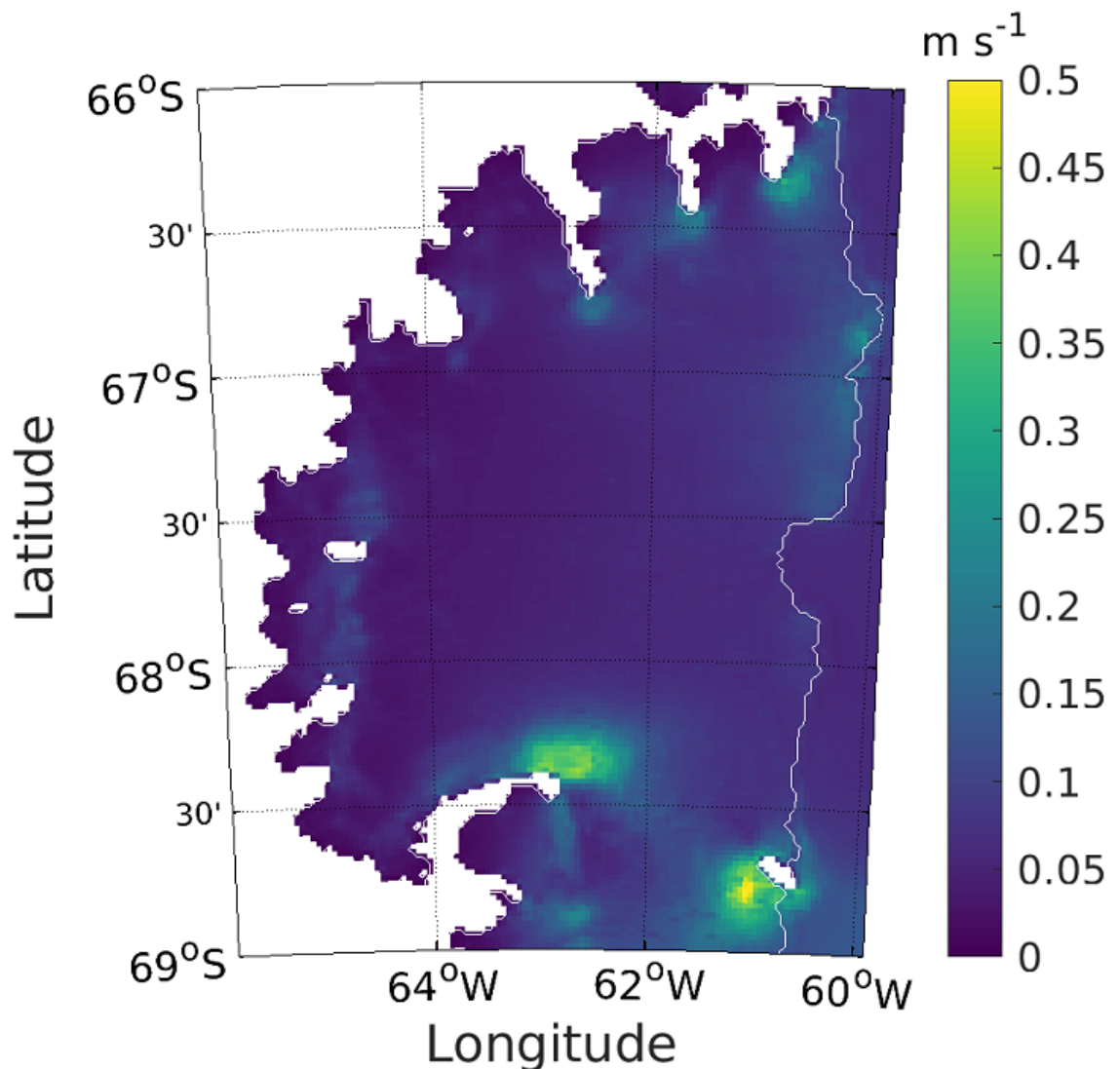


Figure 3.10: Flow speeds at the ice-ocean interface calculated from horizontal velocity vectors in the boundary layer directly beneath the ice base.

The higher modelled mean melt rate is explained by higher average speeds adjacent to the ice base at this location than those measured. Mean modelled speeds in this region of approximately 0.13 m s^{-1} were recorded, averaged over the hourly-output of the 180-day restart simulation, whereas Modular Acoustic Velocity Sensors attached to the mooring, which discretised measurements into 15 minute-averaged burst intervals taken every two hours, measured average speeds to be closer to 0.09 m s^{-1} (Davis and Nicholls, 2019b). While velocity values represented by vectors shown on the figures in this thesis (e.g. Figures 3.4-3.7) represent residual velocities after the effect of tides has been removed by monthly-averaging, the modelled and measured speeds from the southern mooring site do include the effects of tides. Similarly, the values depicted on

Figure 3.10 are not residual ice base speeds; they also include the effect of tidal velocities.

The mismatch in velocities between the model and those measured by Davis and Nicholls (2019b) is attributable to a difference between modelled and real tides as a result of inaccurate bathymetry at this location, detailed in Section 3.6.1.2. Model tides were validated against the available observations and found to have slightly larger amplitudes than observations suggest (see Section 3.6.1). High speeds near the mooring site are therefore found to be a consequence of a squeezing of the water column at a steep seabed slope towards the Kenyon Peninsula grounding line, which may not be an accurate representation of the actual bathymetry. A depression in the interpolated seabed ridge parallel to Kenyon Peninsula (Figure 3.3a), resulting from a single direct measurement of the seabed depth, indicates the water column in this region may be thicker than the interpolated seabed suggests. The high modelled melt rate in this region should therefore be treated with some caution.

High temporal variability in observed basal melting has been noted over the course of two decades (Adusumilli et al., 2018). Davis and Nicholls (2019a) also noted great variability in basal melt rate over their much shorter observation period, reporting that the maximum melt rate value in their timeseries, measured by upward looking sonar and low-pass filtered to remove noise, was 3.88 m yr^{-1} , while the annual-average value was 0.7 m yr^{-1} . The initial mean melt rate at this site, published by Nicholls et al. (2012), was $1.3 \pm 0.2 \text{ m yr}^{-1}$, which was averaged over an eight-day measurement period in the summer of 2011. Although this value has now been superseded by the annually-averaged melt rate reported by Davis and Nicholls (2019a), the higher mean melt rate value of Nicholls et al. (2012) can be explained by the part of the spring-neap cycle the tides were in during the short measurement period. The observation period used by Davis and Nicholls (2019a) began in mid-December 2011. Timeseries of burst-averaged flow speeds beneath the ice for this period showed that the tides were entering the neap phase of the cycle at this time. Nicholls et al. (2012) recorded their higher melt rate over the eight days prior to the period reported by Davis and Nicholls (2019a), between 8-16th December 2011. Faster velocities during spring tides would lead to higher melt rates than a monthly or annual average would show.

3.3.1.2 Thermal driving

Further evidence to support the enhanced melting pattern in the south of LCIS comes from the modelled thermal driving (Figure 3.11a), and observational verification to support this result was reported by Nicholls et al. (2012), who found greater thermal driving in the south of LCIS than in the north (Figure 3.12a). Thermal driving is defined as the difference between the depth dependent freezing point at the ice base pressure and the potential temperature of the 20 m-thick ocean boundary layer directly beneath the ice. Higher thermal driving increases heat flux through the ice shelf, which subsequently increases melt rates (see Equation 2.12).

Measured thermal driving immediately adjacent to the ice base at the southern observation site, calculated as the difference between the *in situ* temperature and the freezing point at the ice base pressure, was measured to be 0.08°C by Nicholls et al. (2012), which matches modelled thermal driving at this location. The modelled *in situ* temperature was converted from the potential temperature calculated by the model so as to compare directly with values reported by Nicholls et al. (2012).

Nicholls et al. (2012) reported greater *in situ* thermal driving at the southern observation site, which is located 12 km north of Kenyon Peninsula, close to the enhanced modelled melting, than the northern site near Churchill Peninsula (Figure 3.12a), which is reproduced here. Figure 3.12b shows there is almost zero thermal driving at the model ice base at the location of the northern drill site, but a substantial difference between the freezing temperature and the temperature of the water in contact with the ice base in the south. This indicates that much more heat is available with which to melt the ice base at this southern location, in agreement with the findings of Nicholls et al. (2012). The depth variation of temperature and salinity (Figures 3.12b & c) indicate that the model has slightly less variability in both potential temperature and salinity throughout the water column than that found by Nicholls et al. (2012). No temperatures above the surface freezing point were simulated at either the north or south locations, in line with observations, however, Nicholls et al. (2012) reported higher salinities at the northern site than the south, whereas the simulation shows slightly fresher water in the north by 0.01.

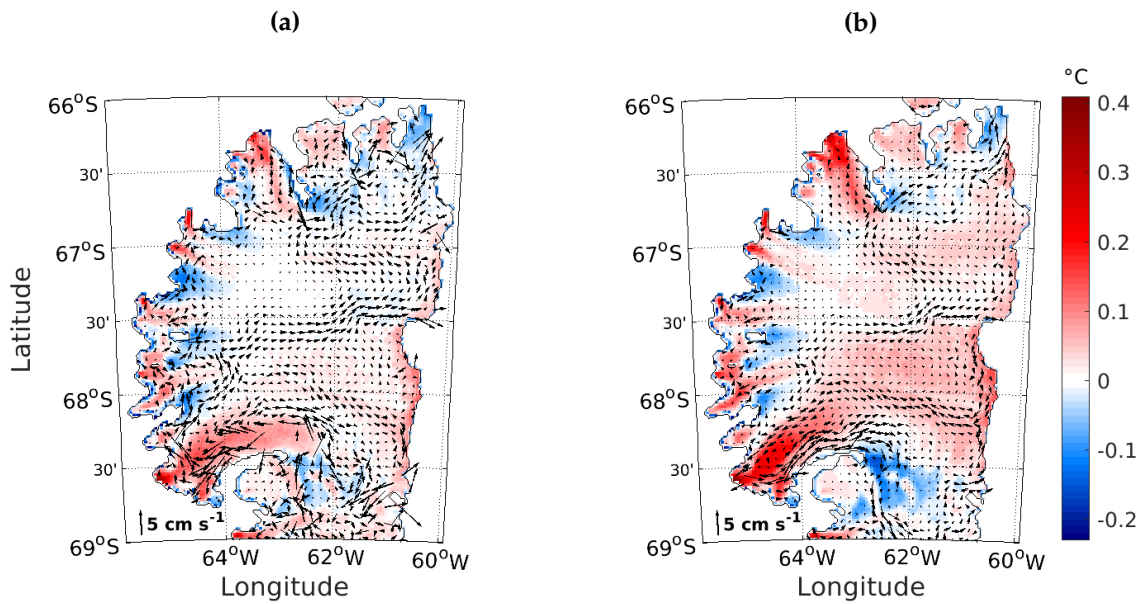


Figure 3.11: Thermal driving is generally lower throughout the domain in the standard run which includes tidal forcing (a) versus when the model set up does not include tides (b). Velocity vectors from the ice-ocean boundary layer are overlaid for each case, with magnitudes greater than 5 cm s^{-1} removed for clarity.

3.3.2 Grounding line and ice front melting

Thermal driving in other regions close to the grounding line is also high and appears to have resulted in melting in several inlets where the ice draft is deep, particularly Mobiloil Inlet, in line with other modelling studies (Holland et al., 2009; Mueller et al., 2012; Borstad et al., 2013; McGrath et al., 2014). Figure 3.12 shows that the deepest waters within the cavity are colder than measured values at these observation points. These results indicate that thermal driving at the grounding line is perhaps greater in reality than has been modelled. This would have implications for melt rates at the grounding line, which are highly sensitive to thermal driving and would therefore result in significantly higher melting of the deep, thick ice found here. The grounding line of an ice shelf is the most vulnerable region to melting, as a result of high levels of thermal driving as well as strong currents leading to turbulent heat flux (Holland et al., 2009), but it is also a critical region in terms of affecting the stability of an ice shelf, as enhanced melting reduces the buttressing holding back inland grounded ice (Fürst et al., 2016; Reese et al., 2018).

Gipps Ice Rise, in the south of LCIS, also experiences high modelled melt rates in this study as a result of high flow speeds (Figure 3.10). Inflowing water is topographically steered around the semicircular feature on the continental shelf

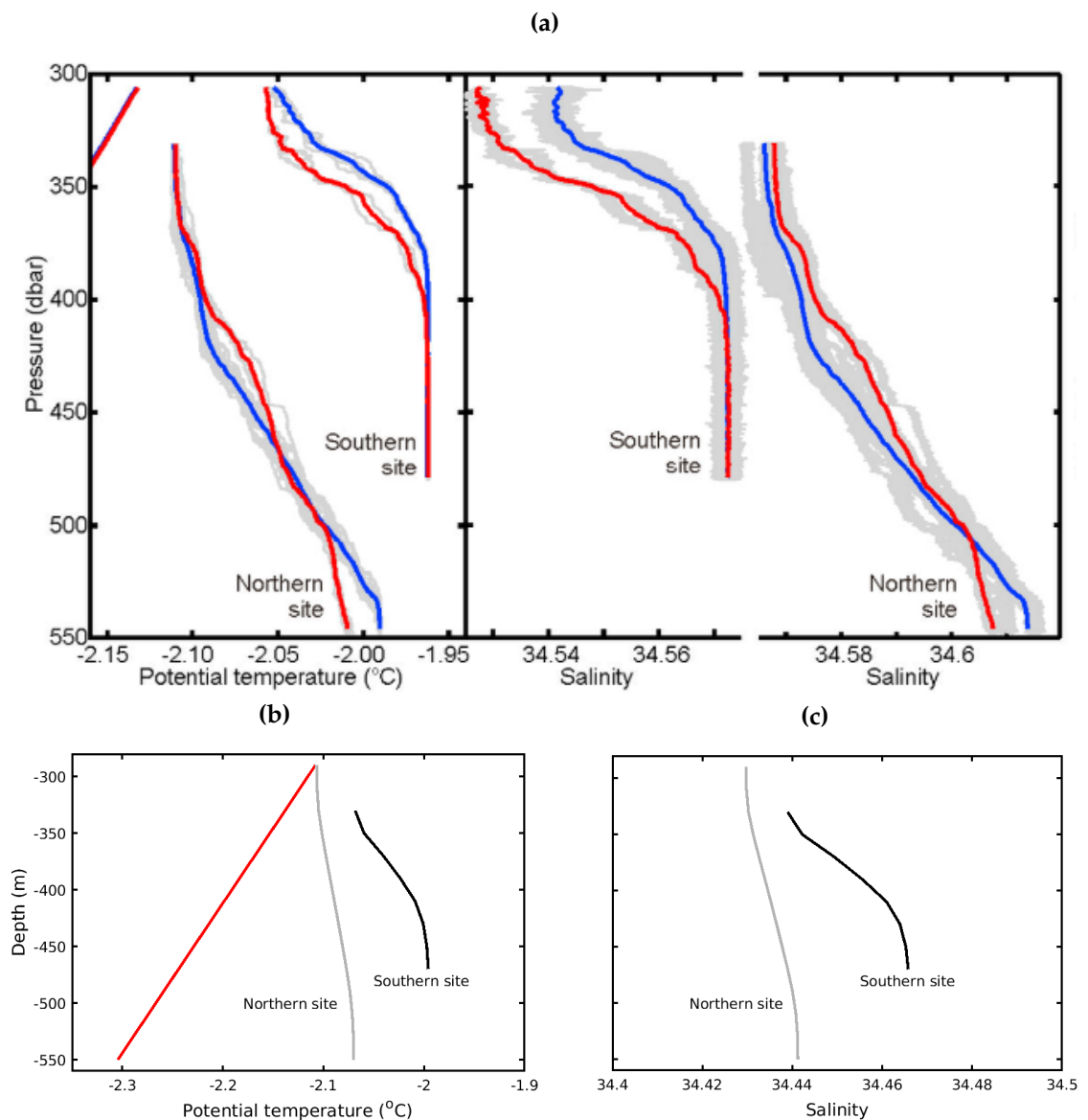


Figure 3.12: Observations of potential temperature and salinity profiles from borehole sites (see Figure 0.1 for locations) adapted from Nicholls et al. (2012) (a). The red and blue lines each represent means of several different profiles taken in separate data gathering sessions. These profiles are shown for comparison with modelled potential temperature (b) and salinity (c) profiles at the northern observation site (grey) and southern observation site (black). The straight red lines in (a) and (b) show the potential freezing temperature profile.

towards Gipps Ice Rise and forms a rapid anticlockwise circulation around it (Figure 3.3a), which leads to high melt rates in this region. The seabed is very poorly known here as the closest seismic shot to Gipps Ice Rise is almost 50 km away and no ships have surveyed the seabed so far south. Consequently, the melt rates at this location may not be accurate because correct simulation of the local circulation here is limited by knowledge of the bathymetry. Water at the

surface, flowing towards Gipps Ice Rise, is funneled northward by the ice wall at the calving front (Figure 3.6) and leads to high melt rates at the ice front all the way up to Bawden Ice Rise. Enhanced melting at the ice front was also reported by (Holland et al., 2015).

3.3.3 Bawden Ice Rise

The greatest melting in the study by Mueller et al. (2012) peaked in the northeast (Figure 3.9b), close to Bawden Ice Rise which is thought to be an extremely important pinning point for LCIS. Bawden Ice Rise is only around 40 m above floatation at its highest point in the south (Holland et al., 2015), meaning high melt rates in this region would have a large impact on the stability of LCIS. Adusumilli et al. (2018) found basal melt rates of up to 5 m yr^{-1} surrounding Bawden Ice Rise during their observation period. Enhanced melting around Bawden Ice Rise was not seen in the standard run; melt rate values of $\sim 0.2 \text{ m yr}^{-1}$ were modelled in the vicinity of Bawden Ice Rise, which is a third of that modelled by Mueller et al. (2012) for initial ocean temperature conditions of -1.9°C .

High melt rates in this region found by Mueller et al. (2012) are thought to result from inaccurate bathymetry leading to high flow speeds under the ice; this possibility will be investigated in Chapter 4. The extremely high melt rate found by Adusumilli et al. (2018) was temporally variable, with this quoted value of $5 \pm 2 \text{ m yr}^{-1}$ being found over a short four-year period, and consequently is attributed to a change in ocean conditions rather than reflecting steady state melting. The effect of such changes will be explored in Chapter 5.

3.4 Freezing and marine ice

Freezing in the standard run occurs at or close to the grounding line, offshore of all peninsulas and islands (Figure 3.13a), which compares well with freezing simulated by Holland et al. (2009) (Figure 3.13b), with peak rates of $\sim 2 \text{ m yr}^{-1}$. It has been noted that refreezing is seen at these locations because the ice is thinner there (Holland et al., 2009). Buoyant meltwater rising under an ice shelf may become *in situ* supercooled as a result of the pressure-induced increase in the freezing point, causing ice to form on the ice shelf base (Robin, 1979; Holland et al., 2009). Jansen et al. (2013) reported high accumulation of ice close to the LCIS grounding line, and a sharp decline further downstream. The greatest refreezing

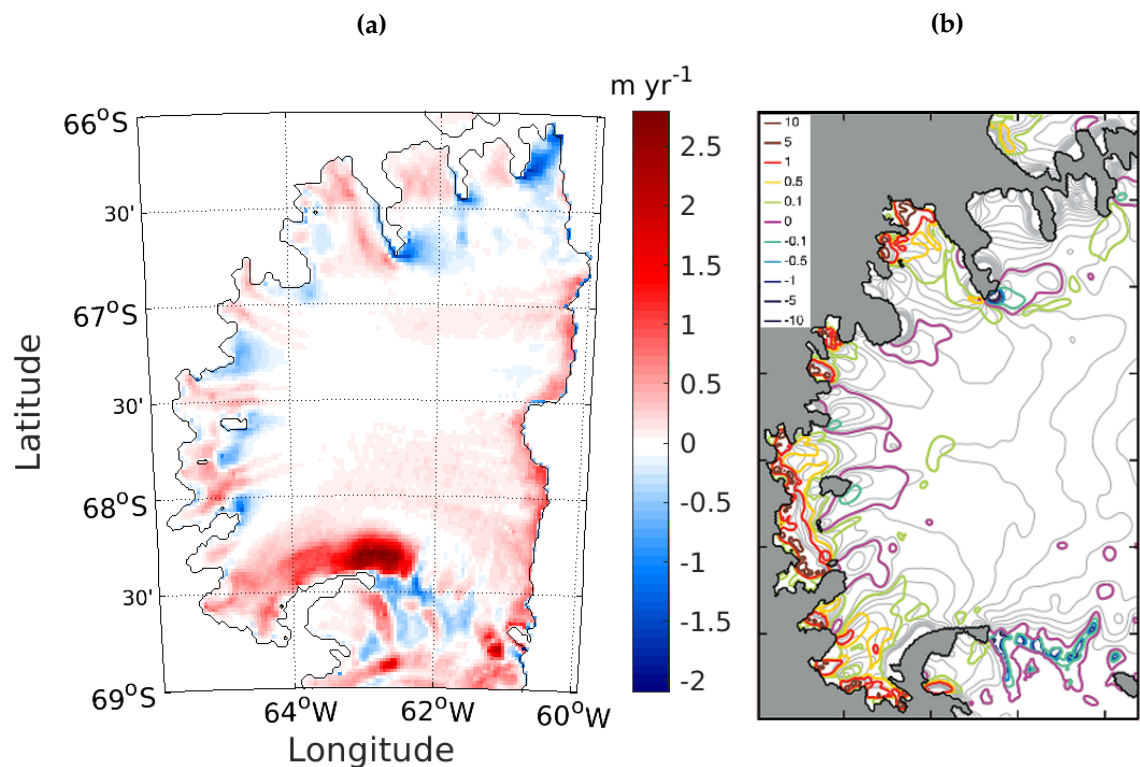


Figure 3.13: (a) Steady state melt and freeze pattern across the ice shelf from the standard run; red shows melting, blue shows locations of refreezing. (b) Coloured contours show melt and freeze rates adapted from Holland et al. (2009) for comparison. Positive values indicate melting and have units of m yr^{-1} . Grey contours define the ice draft.

in the domain takes place east of Argo Point (see Figure 0.1 for location), south of the tip of Jason Peninsula, where the plume of cold, fresh meltwater exits the cavity. Results also show high rates of freezing at the tip of Churchill Peninsula, which was reported as the location of greatest refreezing in other modelling studies (Holland et al., 2009; Khazendar et al., 2011; McGrath et al., 2014).

The simulation of Holland et al. (2009) showed high rates of refreezing off Churchill Peninsula as a result of the accumulation of frazil ice (Figure 3.13b). Where the water column is supercooled, tiny ice crystals form a slushy layer which settles upwards and compacts against the base of the ice shelf as a result of buoyancy forces (Oerter et al., 1992). In the current simulations, freezing only occurs directly at the ice base, as the model has no explicit representation of frazil ice growth or deposition. Therefore, wherever the *in situ* temperature of the ocean is lower than the freezing point of seawater at that depth, a negative meltwater flux occurs. In reality, the dominant freezing mechanism and subsequent creation of marine ice is through the accretion of frazil ice crystals (Oerter et al., 1992; Craven et al., 2009; Holland et al., 2009). Consequently, modelled freezing rates

are expected to differ from measured rates.

The marine ice which forms as a result of the refreezing located downstream of islands and peninsulas on LCIS, advects towards the calving front, forming bands of marine ice between glacier flow units (Glasser et al., 2009; Jansen et al., 2010). While freezing rates in this study are uncertain because of the lack of frazil ice in the model, they have been used to give an indication of what the marine ice below LCIS may look like and how thick it would be if these refreezing rates were to persist beneath a steady LCIS. The steady state marine ice thickness field, produced using observed LCIS ice velocities and the modelled melting and freezing field, is shown in Figure 3.14a. This calculation is performed by assuming that the ice flow and melt/freeze rates are steady in time, and then calculating the marine ice field that would result. Specifically, modelled melt/freeze rates and ice shelf velocities taken from MEaSUREs InSAR-based ice velocity map, version 2 (Mouginot et al., 2012; Rignot et al., 2011a) are interpolated onto a 100 m grid, and marine ice thickness is time-stepped on this grid for 500 years (approximately the residence time of ice on LCIS (Glasser et al., 2009)) using a simple upwind advection scheme.¹ High spatial resolution is used to minimise numerical diffusion. The marine ice field is purely illustrative, since the 500-year steady assumption is very unlikely to hold. Modelled melting and freezing are also highly uncertain, as a result of limitations in modelled ocean circulation, temperature and melting, and the lack of a frazil ice model. Nevertheless, the results show a marine ice distribution that is very similar to observations reported by Holland et al. (2009), who used missing signal returns from airborne radar surveys to determine where marine ice was present beneath the ice (Figure 3.14b).

There are extremely limited observations of marine ice beneath LCIS to know how far these marine bands extend in depth and across the ice shelf. Holland et al. (2009) found evidence that marine ice reached all the way to the ice front, at least in some locations such as the case of the thick band emanating from Churchill Peninsula. Marine ice extent calculated here shows a thick band of marine ice starting from the tip of Churchill Peninsula and progressing all the way to the ice front. High accumulation in the wake of Churchill Peninsula, which leads to the thick band, was also found by Khazendar et al. (2011). McGrath et al. (2014) found neither Cole nor Churchill marine ice bands reached the calving front using radar observations. Modelled melt/freeze rates indicate the crucial marine ice band from Joerg Peninsula does not extend all the way to the ice front. The Joerg

¹The code to calculate and produce the grid of marine ice thickness is not my work. This code was written by Paul Holland.

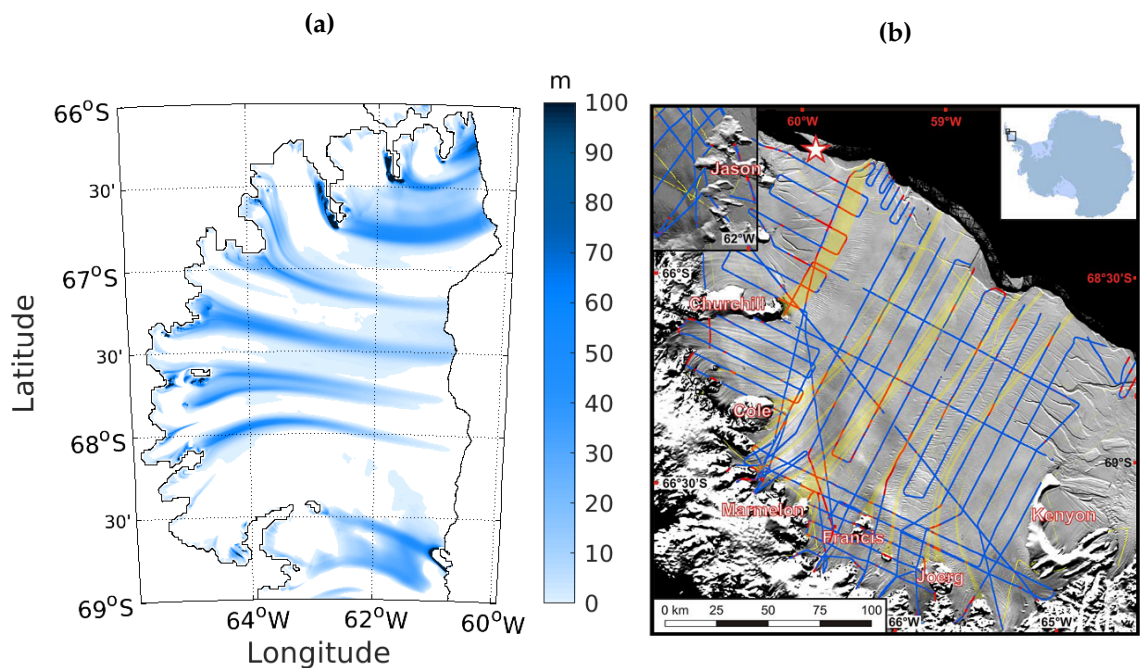


Figure 3.14: (a) Marine ice thickness which would accumulate at the ice base of LCIS and advect downstream if ice velocities and modelled steady state melt and freeze rates were to persist for 500 years. (b) Yellow shading shows marine ice bands inferred from missing radar signal returns, adapted from Holland et al. (2009), match locations of modelled marine bands.

marine ice band is thought to be responsible for stopping various southern rifts, as seen in visible imagery, and therefore likely does extend to the calving front. As the model does not include frazil ice, marine ice accumulation is expected to differ from real values, explaining the shortfall.

The thickness of marine bands calculated in this study is up to ~ 100 m, with bands becoming thinner towards the calving front, caused by melting and ice divergence, in line with observations. Seismic exploration by Brisbourne et al. (2014) revealed that marine ice becomes thinner towards the calving front, as ice base reflectors are more obvious here than at the grounding line. Jansen et al. (2013) found the mean thickness of the Joerg marine band close to the grounding line to be 100-200 m, which suggests that freezing rates simulated here are too low, possibly resulting from the lack of frazil ice in the model. However, McGrath et al. (2014) reported thicknesses of Churchill and Cole marine bands of 56 ± 25 m and 26 ± 9 m, respectively, which are found to be in good agreement with those calculated here.

3.5 Parameterisation of melt/freeze rate

Modelled melt rates are very sensitive to parameters used in the melt rate calculation. Mueller et al. (2012) concluded that one of the greatest sources of uncertainty within their modelling study was the parameterisation of heat and salt transfer, and Mueller et al. (2018) noted that melt rate is highly susceptible to the melt parameters used. For the standard run, melting parameters used in the three-equation model, which resulted in the annual-mean melt rate of 1.2 m yr^{-1} at the southern observation site, included a drag coefficient taken from Davis and Nicholls (2019a) ($c_d = 0.0022$), and heat and salt transfer coefficients taken from Jenkins et al. (2010) ($\gamma_T = 0.011$, $\gamma_S = 3.1 \times 10^{-4}$). This combination was used in an effort to reduce high modelled melt rates when parameters taken solely from Davis and Nicholls (2019a) were used.

The annual-mean melt rate at the observation site when the drag coefficient ($c_d = 0.0022$) and heat and salt transfer coefficients ($\gamma_T = 0.0235$, $\gamma_S = 6.7 \times 10^{-4}$) calculated by Davis and Nicholls (2019a) were used was 1.5 m yr^{-1} . Figure 3.15 shows the increased melting and freezing across the domain which results from using these different parameters. When the three coefficients ($c_d = 0.0097$, $\gamma_T = 0.011$, $\gamma_S = 3.1 \times 10^{-4}$) were taken from Jenkins et al. (2010), an annual-mean melt rate at the observation site of 1.4 m yr^{-1} was modelled.

The parameters reported by Jenkins et al. (2010) were determined partly from data collected using sea ice observations and tuned using observations from the Filchner-Ronne Ice Shelf. Jenkins et al. (2010) measured melt rates beneath this ice shelf and used a best fit to their data to determine a value for the Stanton number ($C_d^{1/2}\gamma_{TS}$). Using the γ_{TS} found by McPhee (1992) from sea ice observations, they calculated C_d . By finding further best fits to observations from under the Filchner-Ronne Ice Shelf for $C_d^{1/2}\gamma_T$ and $C_d^{1/2}\gamma_S$, the drag coefficient was then used to find the turbulent transfer coefficients (γ_T and γ_S). Davis and Nicholls (2019a) more directly derived a value for C_d using measured friction velocity and flow speeds beneath LCIS at the southern observation site but used the same relationship between drag coefficient and transfer coefficients used by Jenkins et al. (2010), determined from observations of melting under the Filchner-Ronne Ice Shelf, to compute different values for γ_T and γ_S .

Using coefficients calculated based on melting observations under a different ice shelf may explain why the melt rate in the model is too high. Overall, it seems best to use a model drag coefficient determined from LCIS observations, though it is noted that this drag coefficient is valid for flow speeds $>0.1 \text{ m s}^{-1}$

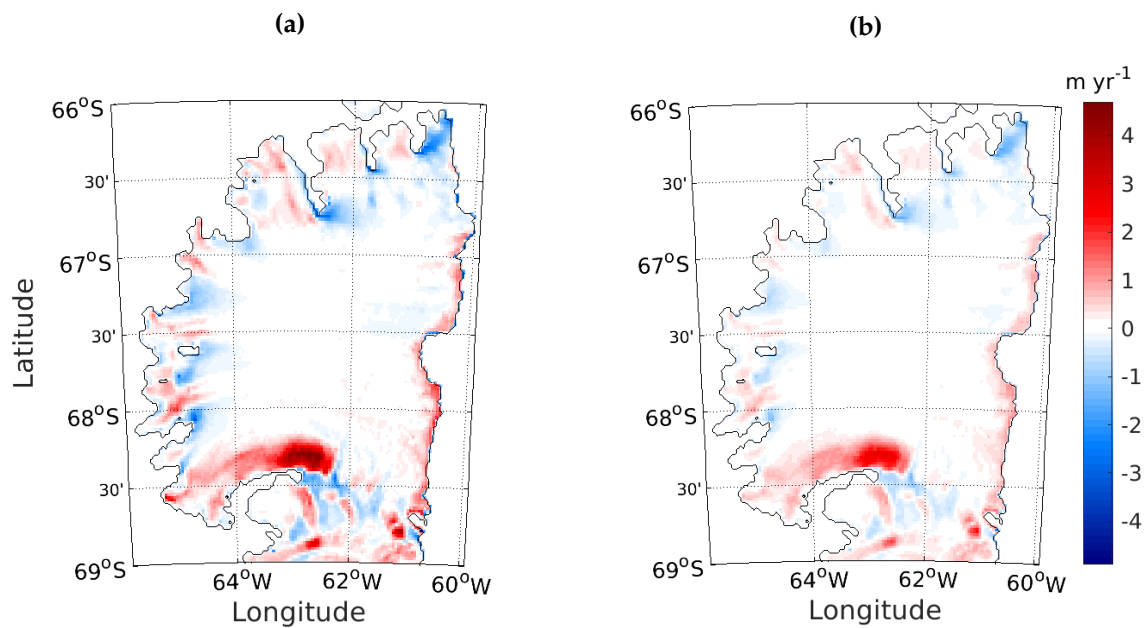


Figure 3.15: Melt rate difference with alternative melting parameters. Although the pattern is very similar in both cases, the melt rate using melting parameters measured and calculated by Davis and Nicholls (2019a) (a) shows much higher values than the melt rate produced using the standard run melting parameters described in the text (b).

and the majority of flow speeds at the ice-ocean interface, other than north of Kenyon Peninsula, around Gipps Ice Rise and along the northern ice front, are substantially lower than this threshold. Davis and Nicholls (2019a) stated that the drag coefficient is likely to be highly spatially and temporally variable. This suggests a different drag coefficient may be more appropriate elsewhere in the domain, particularly where marine ice accretion may have resulted in a rougher ice base.

3.6 Tides

Strong, mixed tides are known to be crucial to the circulation below LCIS, and influence the mean state considered in this research (King et al., 2011a; Nicholls et al., 2012; Mueller et al., 2012; Davis and Nicholls, 2019a). As wind forcing does not affect velocities within the cavity, the only sources driving flow are buoyancy forcing, which becomes stronger with an increase in meltwater in the cavity, and tides. Current meters at the southern mooring site found tides dominated the flow under LCIS (Davis and Nicholls, 2019a), dwarfing any buoyancy-driven contribution.

Padman et al. (2018) noted that the performance of an inverse tidal model such as CATS2008 depends on the accuracy of the cavity geometry, and errors in water column thickness, as well as a paucity of high latitude tidal observation data to constrain such models, can lead to large uncertainties. The LCIS cavity in CATS2008 has known inadequacies (Padman et al., 2002) and therefore the tides are not necessarily expected to be correct beneath the ice. As the CATS2008 model output is used to force the simulations in the current study, with tidal forcing only applied on the boundaries of the domain, the tidal signal propagating across a domain with a different geometry could result in inaccurate tidal amplitudes or speeds. This possibility was investigated and the outcome is detailed below.

3.6.1 Comparison to available observations

3.6.1.1 Surface elevation data

To validate the tidal signal in the model against real tides under LCIS, timeseries of modelled, hourly sea surface height anomalies from the 180-day restart simulation were compared with timeseries computed from observed ice surface elevation changes using geodetic quality GPS receivers. Observed timeseries at six locations on LCIS (see yellow triangles in Figure 0.1 for exact positions) were reconstructed from mean tidal amplitudes and phases for each of the eight major tidal constituents (King et al., 2011b) using the UTide package (Codiga, 2011) and compared with modelled timeseries (Figure 3.16). Comparison of modelled and measured amplitude means, averaged over a six month-long timeseries for each GPS site, are given in Table 3.1. The site names correspond to those given in King et al. (2011b). The close match of less than a 5 cm difference between the reconstructed and modelled mean tidal amplitudes at several locations beneath the ice shelf demonstrates that modelled tidal amplitudes are accurate.

Table 3.1: Modelled and measured sea surface height amplitude means, averaged over a six month-long timeseries, for each GPS site. Site names correspond to those in King et al. (2011b) and are shown in Figure 0.1.

Site name	Data mean (m)	Model mean (m)
LAR1 (north)	0.72	0.70
LAR2 (west, mid-shelf)	0.75	0.76
LAR3 (south)	0.70	0.69
SLGN1 (mid-shelf)	0.71	0.72
SLGS1 (mid-shelf)	0.74	0.72
MOBIL OIL INLET	0.81	0.79

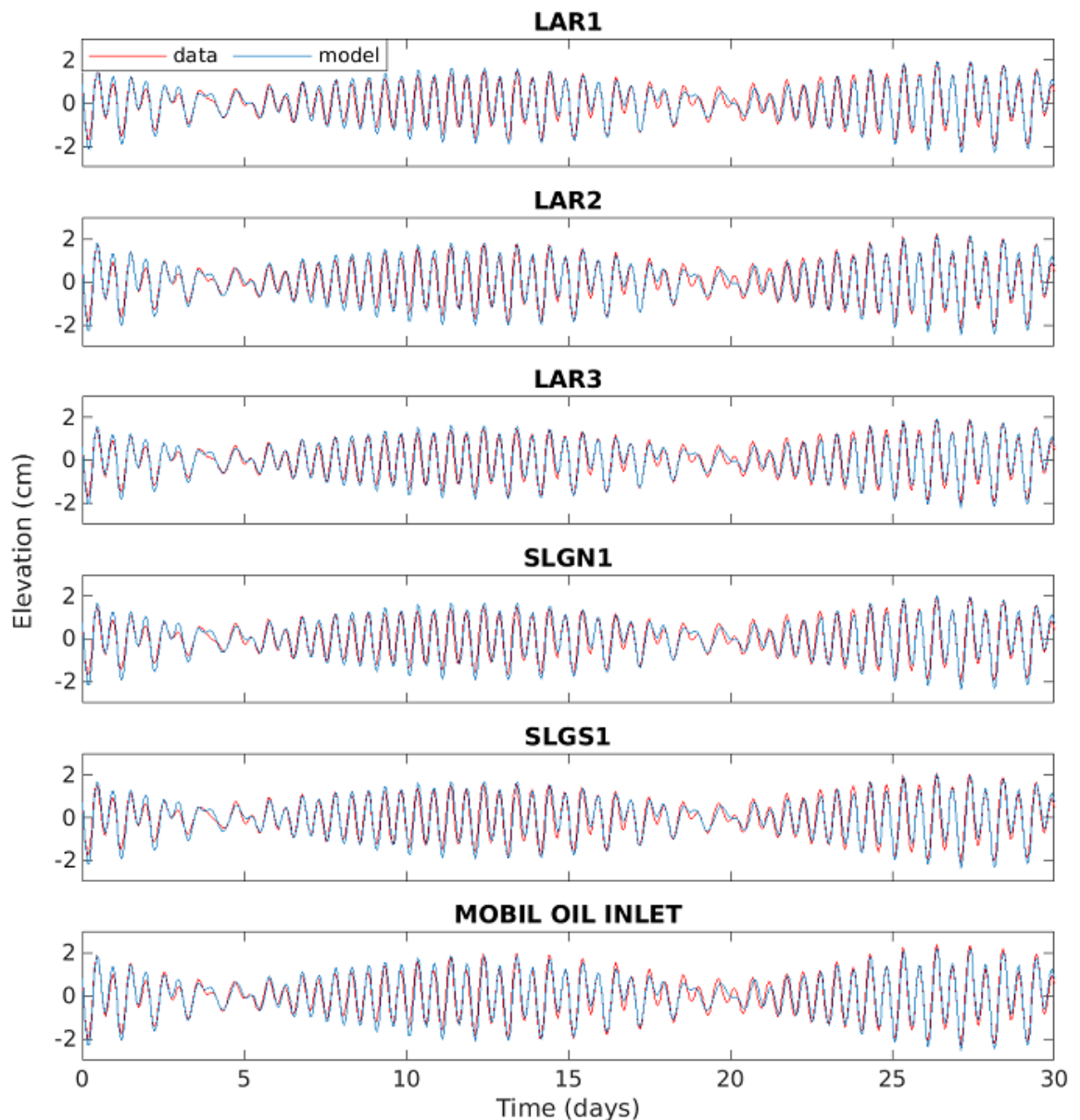


Figure 3.16: Timeseries of sea surface height anomaly at six sites on the ice shelf calculated from observed ice elevation changes (red). Modelled sea surface height timeseries at corresponding locations (blue) show tides within the model cavity are behaving as expected. Site names correspond to those in King et al. (2011b) and are shown in Figure 0.1.

3.6.1.2 Current data at the southern mooring site

Tidal currents derived from current meters at the southern drill site were compared with modelled currents in the ice-ocean boundary layer at this location. The model boundary layer is the top 20 m of the water column, immediately below the ice base. Modelled tidal ellipse parameters were computed from tidal analysis of hourly model velocities from the six month-long simulation at the

location of the southern observation site, using the UTide package (Codiga, 2011). The calculated ellipse parameters are listed in Table 3.2 and the resulting ellipses are shown in Figure 3.17, along with those reported by Davis and Nicholls (2019a) for comparison. These ellipses, are comparable to the lower Modular Acoustic Velocity Sensor measurements in Davis and Nicholls (2019a), recorded 13.5 m below the ice base.

Figure 3.17 and Table 3.2 show that all constituents display largely the correct directionality. The semi-major axes of all but the modelled P1 constituent are larger than measured values, on average $\sim 30\%$ higher but by up to 100% (K2). This has resulted in modelled speeds being too high at the southern site. The measured water column thickness at the southern site of 192 m is thicker than that of the model domain after interpolation of the seismic soundings to create the bathymetry, which is only 149 m. This would contribute to higher tidal constituent amplitudes and ocean velocities at this location. Of the four strongest constituents (M2, S2, O1, and K1) that are reported to dominate flow speeds under LCIS (King et al., 2011b; Mueller et al., 2012; Davis and Nicholls, 2019a), the relative amplitudes (semi-major axes) of M2, S2 and K1 with respect to each other show a similar pattern to measured amplitudes but O1 is not quite as well matched as it is larger than K1, unlike observations. This could be a consequence of this constituent being inaccurate in the CATS2008 forcing. More observations of currents elsewhere under the ice would allow this hypothesis to be tested in future, to see if this constituent has consistently greater amplitudes in other locations in the cavity.

3.6.2 Effect of tides on circulation

A simulation without tidal forcing demonstrates that including tides in models of LCIS is vital to ensure accurate circulation and melt rate results. Without tidal energy, this simulation took longer to reach steady state than the standard run and so values and figures presented from this simulation are taken from an average over the final year of a 30-year run. The timestep used for this simulation was also increased to six minutes as velocities in the domain were substantially slower than in the standard run.

At the location of the southern observation site, average flow speed at the ice base in the non-tidal run is 0.02 m s^{-1} , whereas the buoyancy-driven speed in the standard run, defined as the residual speed once the tidal velocities have been annually-averaged to cancel out, is a factor of three higher, at 0.06 m s^{-1} .

Table 3.2: Ellipse parameters taken from the model boundary layer and measured 13.5 m beneath the ice base at the southern observation site, as reported in Davis and Nicholls (2019a). Abbreviations: Mod is model; Con is constituent; Semimaj is semi-major axis; Semimin is semi-minor axis; Inc is inclination angle.

	Data	Mod	Data	Mod	Data	Mod	Data	Mod
Con	Semimaj (cm s ⁻¹)	Semimaj (cm s ⁻¹)	Semimin (cm s ⁻¹)	Semimin (cm s ⁻¹)	Phase (°)	Phase (°)	Inc (°)	Inc (°)
O1	6.8	10.8	1.2	3.7	295	320	147	158
P1	2.5	1.2	0.01	0.3	328	358	155	156
K1	7.4	9.2	0.8	2.8	325	328	152	154
N2	0.9	1.2	-0.2	-0.07	326	337	3	20
M2	6.2	8.5	-1.1	-0.6	345	349	3	23
S2	4.6	5.4	-0.4	-0.9	17	38	0	11
K2	1.5	3.0	-0.4	0.4	232	232	150	163

Buoyancy forcing within the cavity increases with the addition of tides because melting also increases, leading to greater amounts of meltwater and hence, greater pressure gradients within the cavity to drive flow. As a consequence, buoyancy forcing in the standard run is higher than that in the non-tidal run.

The residual flow speed resulting from buoyancy found by Nicholls et al. (2012) when tidal velocities were removed from their current signal was 0.02 m s⁻¹, which is much lower than the residual speed seen in the model. The modelled melt rate in the standard run simulation is high compared with the measured melt rate at the southern mooring site (see Section 3.3.1.1), which would provide stronger buoyancy forcing in the model, potentially explaining this discrepancy. When Mueller et al. (2012) excluded tides from their model, they found velocities in their domain, driven by buoyancy-forced pressure gradients, were only half the size of residual velocities in the tidally-forced run when tidal velocities were subtracted.

Another explanation for higher modelled velocities in this region is tidal rectification, which exerts a significant influence on the circulation across the south of the cavity, including at the southern observation site. Rectified tides occur as a result of inclines in the water column, from either slopes in the bathymetry or titled isopycnals in a density layer of the water column with respect to the seabed. This leads to tidal velocities in different directions being unbalanced and results in a residual, net flow in one direction. A simulation performed without thermodynamic calculations of melting and freezing shows the effect of these tidal residual velocities, as no meltwater would enter the water column to alter buoyancy and drive flow. Long-term mean velocities from this run show

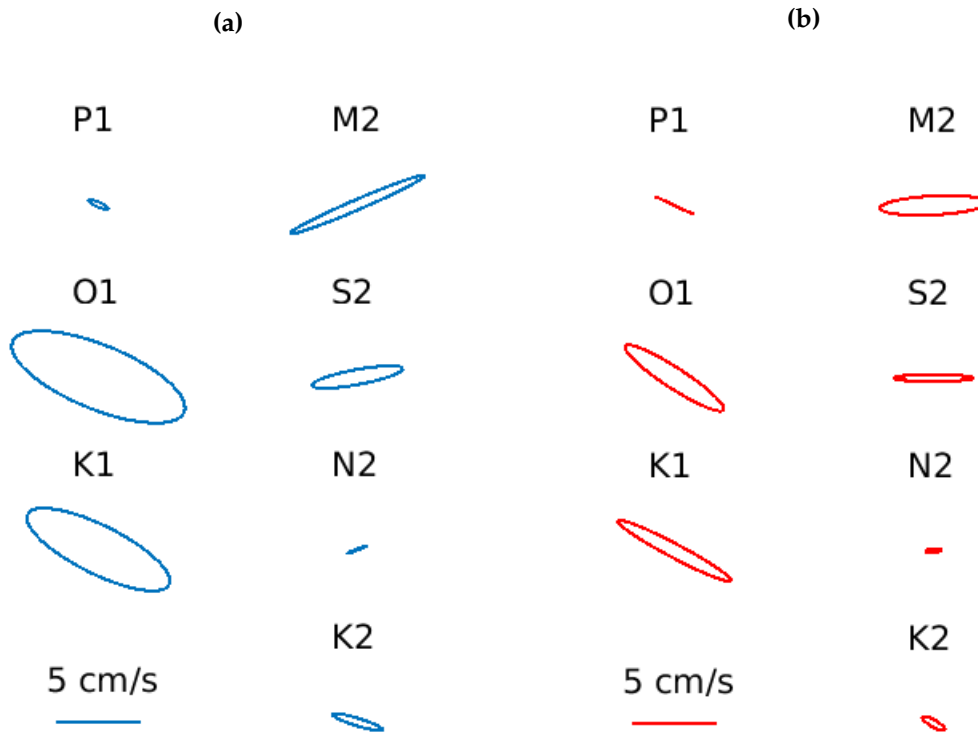


Figure 3.17: Tidal ellipses of the seven strongest constituents in the region of LCIS, computed from model boundary layer velocities at the location of the southern observation site (a) are compared with those created from measured currents 13.5 m below the ice base (b), adapted from Davis and Nicholls (2019a).

that a residual flow driven solely by tides is present in the south of the cavity. Streamfunction contours in Figure 3.18 indicate the paths of ocean currents with non-zero velocities along the length of the southern trough and at the inflow region surrounding Gipps Ice Rise. Mueller et al. (2012) also found rectified tides held substantial control over cavity circulation. However, in contrast to the pattern found here, they discovered tidal rectification in the northeast, where the strongest tidal currents in their model domain were also simulated, likely as a result of the rapid thinning of the water column at this location in their cavity geometry.

3.6.3 Effect of tides on melting and freezing

Figure 3.19 shows melting in the simulation run without tides lowers predictably in most areas of the domain, with the average melt rate reduced by a factor of two, as a result of diminished velocities and a lowering of turbulence in the ice-ocean boundary layer. Mueller et al. (2012) similarly reported melt rates in their domain halved without tidal forcing. Freezing rates also decrease in both magnitude and

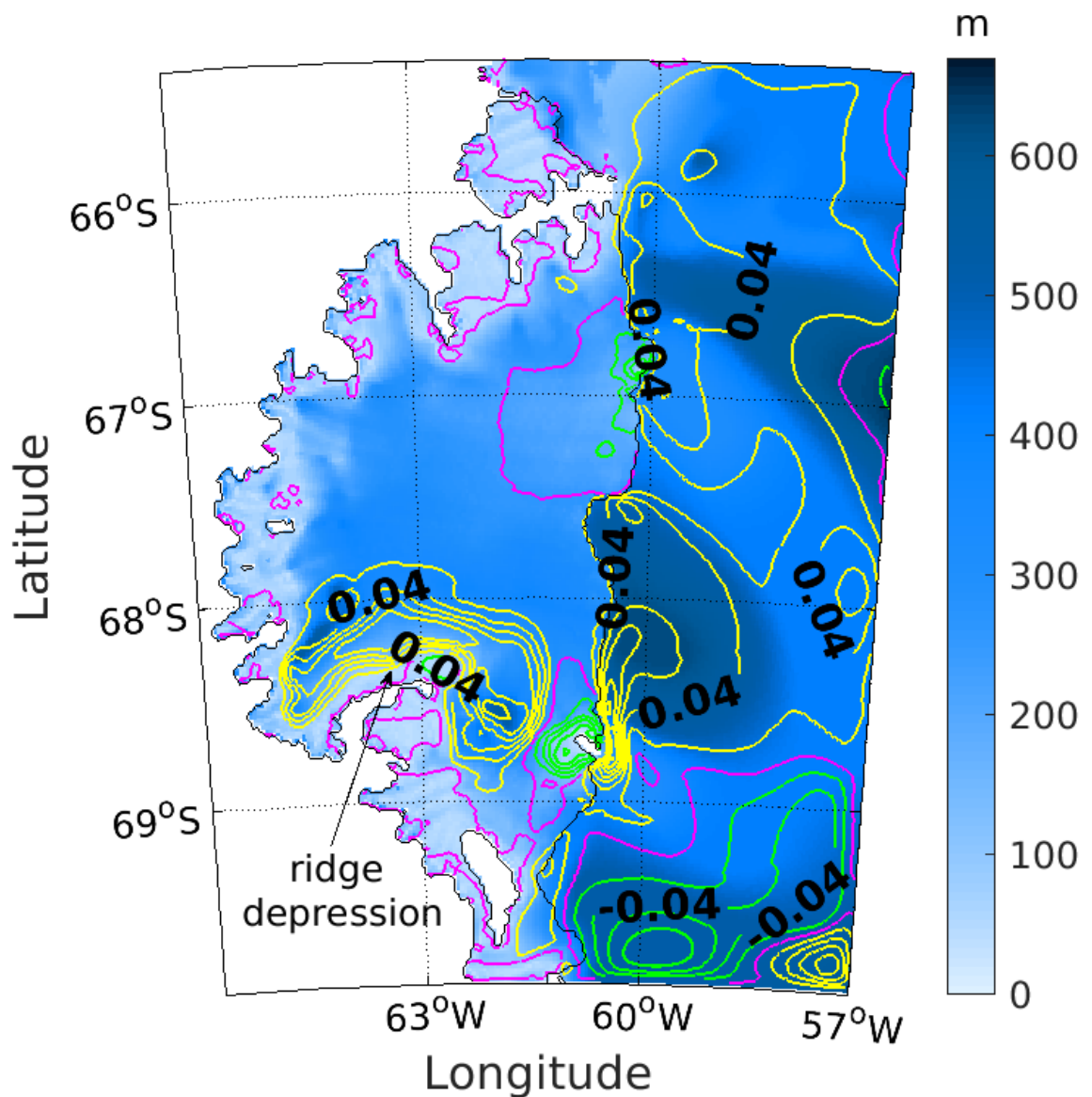


Figure 3.18: Water column thickness with barotropic streamfunction contours overlaid from a tides-only simulation with no contributions to buoyancy forcing from thermohaline exchange with the ice shelf. Yellow contours are positive values (clockwise flow), green contours are negative (anticlockwise flow) and the pink contour shows zero flow. Values indicating volumetric flow rate have units of Sverdrups.

extent without tides forcing the model, as a result of lower velocities adjacent to the ice base (Figure 3.11). These velocities are used in the calculation of melting and freezing along with the differences in temperature and salinity between the ocean and ice-ocean boundary (see Equations 2.12-2.14). Lower levels of melting will also produce less meltwater to travel up the ice base slope and refreeze higher up the draft. A change in freezing with differences in tidal forcing was also seen in a study of another cold-water cavity near LCIS. Makinson et al. (2011) reported

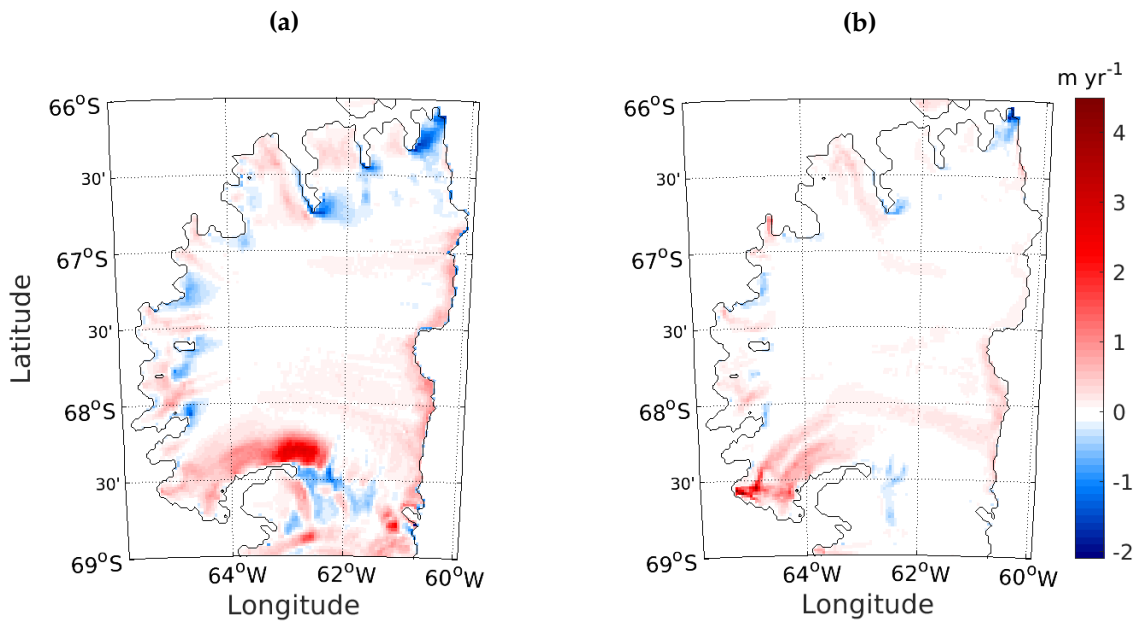


Figure 3.19: Melting (red) and freezing (blue) produced by the standard run (a) compared with results from a simulation run without tides (b).

freeze rates increase by a factor of six, on average, when tides were added to their model of the Filchner-Ronne Ice Shelf cavity, as well as tripling melt rates. However, they also showed that the melting pattern of their domain did not differ considerably when tides were added to the model.

If the magnitude of melting and freezing within the model domain were the only difference between these runs, it may be possible to alter the melting parameterisation to account for slower currents and the altered distribution of heat below the ice (Figure 3.11) in the non-tidal case, and the resulting change in melt/freeze rates could be diagnosed accordingly. This would enable future simulations of LCIS to potentially be run without tides, reducing computational expense significantly, as the model timestep could be increased. The non-tidal simulation ran with a timestep six times larger than that used in the standard run (6 minutes versus 60 seconds). Although the simulation without tides did take three times longer to reach steady state, this still resulted in a total run time of less than half the time taken to reach steady state in the standard run. However, the melt/freeze pattern which results from a run without tides differs considerably to the standard run; although the domain-averaged melt rate for the non-tidal run is half that of the standard run, the value at the southern observation site is only a quarter of the melt rate output by the standard run (0.3 m yr^{-1} compared with 1.2 m yr^{-1}).

The melt rate in Mobiloil Inlet actually increases with no tides, particularly

where the deepest ice draft is found, in contrast to most other parts of the ice shelf. This result agrees with those of Mueller et al. (2012), who reported the grounding line experienced higher melt rates than the northeast region when tides were excluded from their model, which was a distinctly different pattern of melting compared with their tidal run. Enhanced melting in Mobiloil Inlet in the non-tidal run results from greater thermal driving (Figure 3.11), which increases substantially in this region, as well as across the ice shelf, without the effect of tides to drive mixing of the cold meltwater with the ambient ocean flowing into the cavity. These results demonstrate that tides are essential to create the correct melt/freeze pattern and are therefore necessary for accurate modelling of this ice shelf cavity.

3.7 Concluding remarks

The model's performance was assessed and found to be in good agreement with observations as key features of the cavity circulation have been seen in the standard run simulation. Flow speeds under the ice at the location of the southern mooring are faster than measured speeds however, as a result of overly strong tidal forcing, which had led to the melt rate being too high in this region. As a consequence of this and other uncertainties in modelled melt parameters, a greater focus has been applied to analysis of the modelled pattern of basal melting and freezing under LCIS. The pattern is more rigidly determined by physics than the melt/freeze rates, which could have been tuned to result in higher or lower values.

Bathymetry was found to play an important role in the circulation under LCIS, with the barotropic streamfunction (Figure 3.3b) showing two distinct circulation components within the cavity, largely following water column thickness contours which are primarily influenced by changes in seabed depth. Rapid inflow in the south, heavily influenced by the deep trough in the seabed, leads to the greatest melting in the domain. This result highlights the importance of using accurate model geometry, which is crucial to the evaluation of the LCIS melt pattern. This is explored further in Chapter 4.

The new melt/freeze pattern and ocean circulation presented in this thesis are key advancements in our understanding of the basal processes beneath LCIS. They improve upon previous modelled melt pattern and circulation estimates (e.g. Mueller et al. (2012)) as a result of using a more accurate cavity geometry,

which is known to greatly affect oceanic flow and locations of ice shelf melting and freezing. Evaluating the ability of the model to replicate the circulation and melt/freeze pattern under LCIS was done in order to increase confidence in the ability to predict changes which would be expected if ocean conditions were to change. If basal melting is responsible for the observed surface elevation changes, this would result from a change in ocean conditions, not steady state melting. Potential changes LCIS might experience, which may have consequences for circulation, melting, and freezing, are investigated in Chapter 5.

Chapter 4

Effects of seabed bathymetry on modelled conditions beneath LCIS

Ice shelf and seabed geometries are principal drivers of the direction of flow around an ice shelf cavity, which in turn affects the melt pattern of the ice shelf. This geometrical influence on ocean circulation results from the conservation of angular momentum of a fluid. In the absence of a source of heat such as friction, an unstratified ocean would flow along contours of water column thickness to avoid stretching or shrinking of the water column in order to conserve angular momentum. This is why inflow to the cavity in the standard run travels via the southern trough, where the largest and therefore most comparable water column thickness to that outside the cavity is found. If the ocean were stratified, this conservation law would apply to each density layer within the water column. This means that the uppermost density layer would follow contours of ice topography and the deepest density layer would follow bathymetry contours. Therefore, altering the shape of the bathymetry or ice shelf cavity as a whole would have implications for ocean circulation, and consequently, where ice shelf melting and freezing takes place.

One of the novel aspects of this study is the new bathymetry used in the model (Figure 4.1a), which includes the wide, deep trough that has been shown to play an important role in guiding water to the grounding line. In order to see the effects features such as this have on melt rates, two further simulations with different bathymetries were run. One simulation used the Bedmap2 (Fretwell et al., 2013) bathymetry (Figure 4.1b), which is generally flat, and the second used the ice topography and bathymetry created by Mueller et al. (2012) (Figure 4.1c), which is shallow in the north. Both runs had the same set up as the standard run,

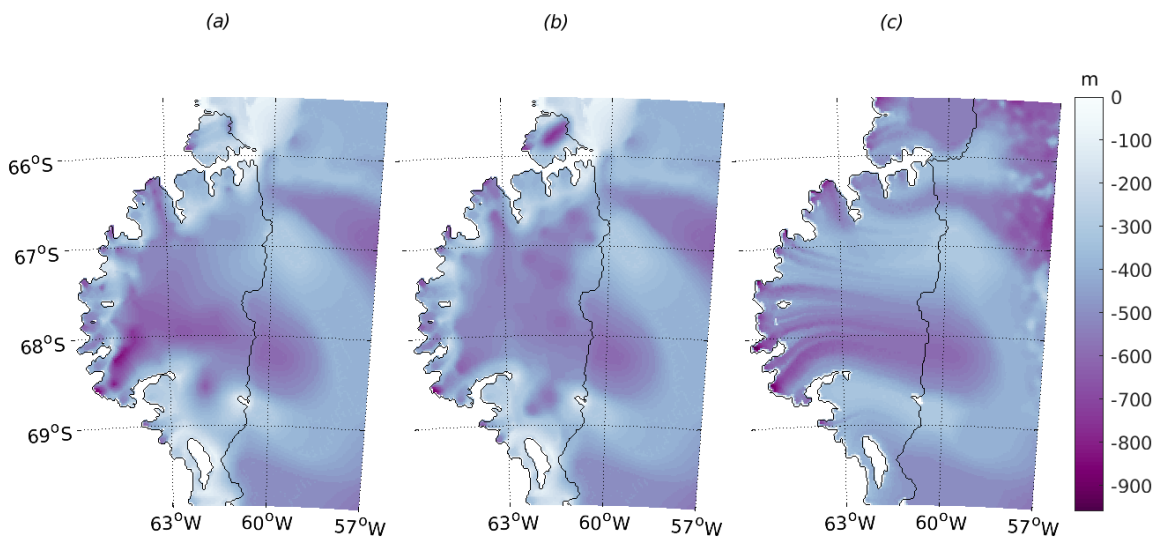


Figure 4.1: Bathymetry used in the standard run, otherwise referred to as the Brisbane bathymetry (a), the Bedmap2 run (b) and the Mueller run (c) which was used in the study by Mueller et al. (2012).

otherwise.

The crucial role accurate bathymetry plays in effectively modelling accurate melt patterns has been noted in previous studies of other ice shelves around Antarctica (Nitsche et al., 2017; Seroussi et al., 2017). While an earlier study of LCIS also noted the important influence of cavity geometry on the resulting melt pattern of the ice shelf (Mueller et al., 2012), this thesis presents the first modelling study of LCIS which has used a bathymetry created from direct measurements and has used *in situ* observations from inside the cavity to validate the model melt rate and ocean circulation results.

4.1 Alternate model geometries

The biggest difference between the newly created ‘Brisbourne’ bathymetry (Brisbourne et al., 2020), used in the standard run described in Chapter 3, and the Bedmap2 bathymetry is the depth of the trough. The Bedmap2 seabed is significantly shallower in the southwest, where the trough is absent (Figure 4.2a). It is also deeper in the northeast, south of Jason Peninsula and surrounding Bawden Ice Rise. The Mueller bathymetry is shallower than the Brisbane seabed almost everywhere except the grounding line, surrounding Gipps Ice Rise, and an area in the south of LCIS, to the north of Kenyon Peninsula (Figure 4.2b). While the trough into Mobiloil Inlet is not as deep as in the Brisbane seabed, deeper

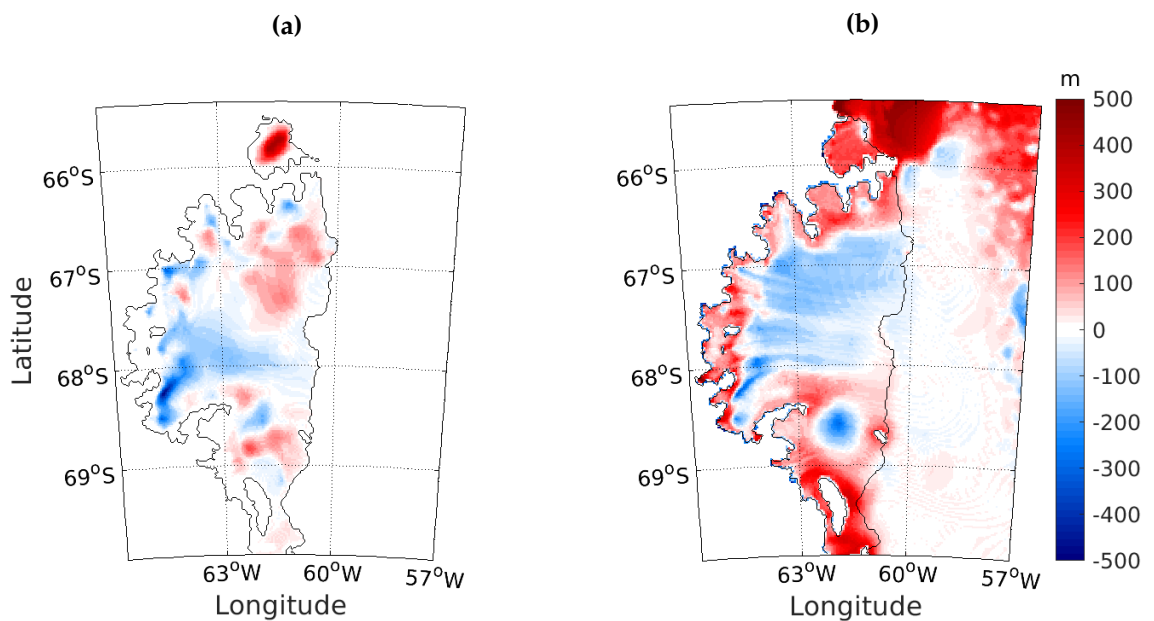


Figure 4.2: Difference between the Brisbane and Bedmap2 bathymetries (a); red shows where the Brisbane seabed is higher compared with Bedmap2, blue shows where it is lower. (b) Difference between the Brisbane and Mueller bathymetries with red (blue) denoting the Brisbane seabed being higher (lower) than the Mueller seabed.

bathymetry than the standard run is seen just south of the southern trough in the Mueller cavity, extending from $\sim 63^\circ\text{W}$ to the calving front. All three geometries have similar characteristics outside of the cavity, over the continental shelf.

Mueller et al. (2012) created their bathymetry by interpolating along ice flow lines, between the known grounding line and the seabed height at the calving front of the ice shelf, with no knowledge of features within the cavity. This method assumes that any features in their bathymetry have been left from ice flow during the Last Glacial Maximum (Mueller et al., 2012) and results in a striated seabed below the ice shelf, which would direct flow east-west. They also chose to impose a minimum water column thickness of 100 m to ensure numerical stability in their terrain-following coordinate model. As the Brisbane bathymetry has been constructed using seismic data, it has therefore captured features of the seabed that are not present in either the Bedmap2 or Mueller geometries.

4.2 Circulation differences between model cavities

4.2.1 Brisbane versus Bedmap2

While circulation around the Brisbane cavity is split into two components that connect by crossing water column thickness contours, circulation in the Bedmap2 cavity is much simpler. The barotropic streamfunction, shown in Figure 4.3, reveals depth-averaged flow travels more directly north after leaving Mobiloil Inlet, more closely following contours of water column thickness than in the Brisbane case, and flows directly out of the cavity without circling back on itself like in the standard run.

4.2.1.1 Inflow

Bottom circulation in the southern half of the cavity is markedly different for the Bedmap2 case, because of the absence of the trough (Figure 4.4a & b). The inflow of water to the Bedmap2 cavity takes place at Gipps Ice Rise, as in the Brisbane case (Figure 4.5a & b), and travels north along the ice front. While bottom flow in the Brisbane case is deflected west at $\sim 68.2^\circ\text{S}$, resulting from the trough's influence and strong southward recirculation of the plume within the cavity, the flow in the Bedmap2 case is deflected westward further north at $\sim 68^\circ\text{S}$. This is because the recirculation of meltwater is much weaker in this case and the trough is absent from the Bedmap2 seabed. In fact, the flat Bedmap2 seabed means the water column thickness of the cavity is much more influenced by the ice topography in this geometry than in the Brisbane case (see first two columns in Figure 4.3).

Inflowing water then makes its way into Mobiloil Inlet via a different route and more slowly than seen in the standard run (Figure 4.4a & b). From the point of deflection at $\sim 68^\circ\text{S}$, water travels northwest towards the centre of the cavity, following contours of water column thickness (Figure 4.3b), before splitting to either join the barotropic flow driven by the meltwater plume, travelling northeastward out of Mobiloil Inlet, or heading south to the tip of Kenyon Peninsula, where it joins a flow past Hearst Island in the south. From here the flow rounds the tip of Kenyon Peninsula, but with lower velocities in this region than those seen in the Brisbane case, and eventually makes its way into Mobiloil Inlet.

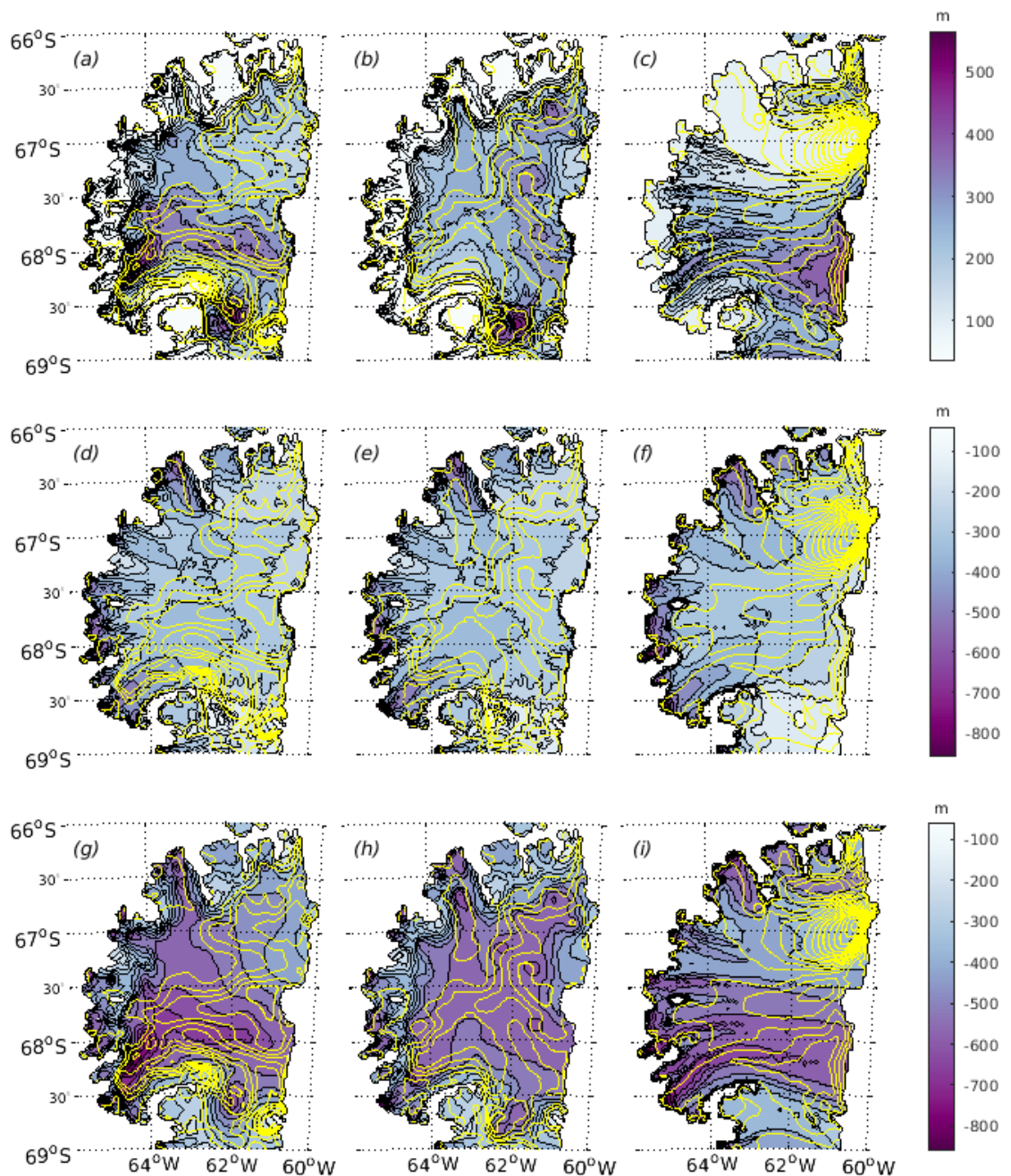


Figure 4.3: Barotropic streamfunction contours, in yellow, overlaid onto filled purple contours of water column thickness (top row, a-c), ice topography (middle, d-f), and bathymetry (bottom row, g-i) for each of the three geometry cases. Left column shows Brisbane case, middle column shows Bedmap2, and right column shows Mueller geometry.

4.2.1.2 Outflow

The meltwater plume exits the cavity at the same places in the Bedmap2 case as for the Brisbane case, at Jason Peninsula and a weaker outflow at Bawden Ice Rise (Figure 4.6a & b), but the path of the plume within the cavity is distinctly

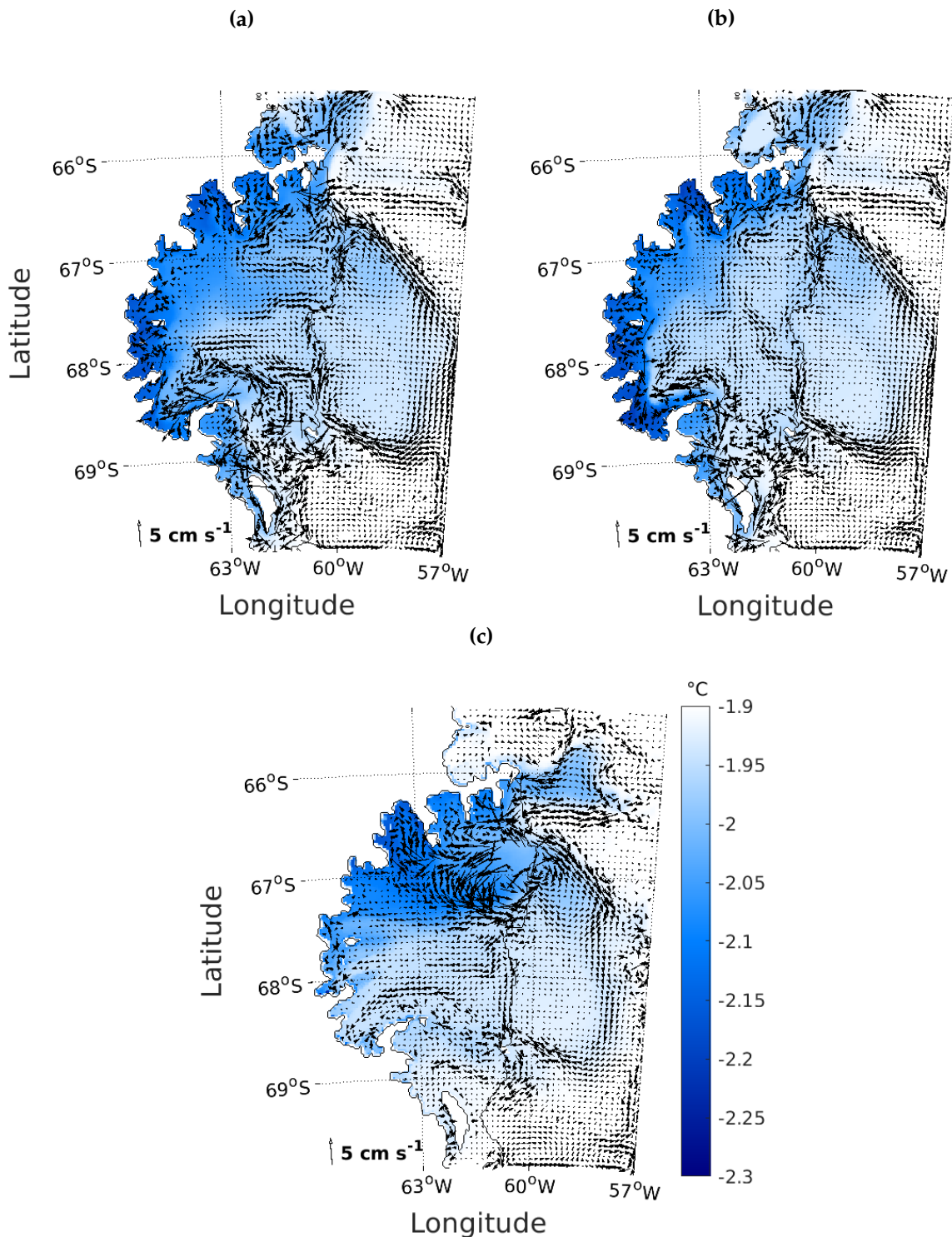


Figure 4.4: Potential temperature on the sea floor of a run using the Brisbane bathymetry (a), Bedmap2 bathymetry (b) and Mueller bathymetry (c), with sea floor velocity vectors for each case overlaid. Vectors with magnitudes greater than 5 cm s⁻¹ have been removed for clarity.

different. The northward plume originating in Mobiloil Inlet travels more directly north towards Churchill Peninsula, closer to the grounding line, in the Bedmap2 case than in the standard run (Figure 4.7a & b) because there is no trough to follow in the relatively flat Bedmap2 seabed. This meltwater outflow from Mobiloil Inlet drives the flow of the entire water column in this location near the grounding line, as the bottom waters are shown to match the direction of the plume (Figure 4.4b and Figure 4.7b).

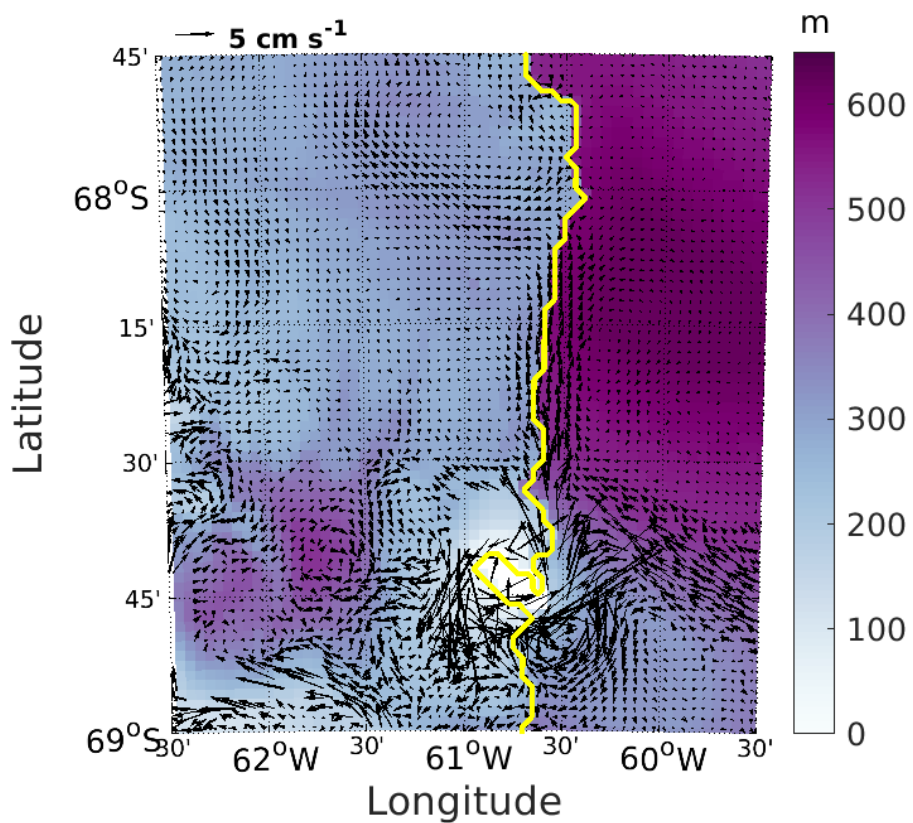
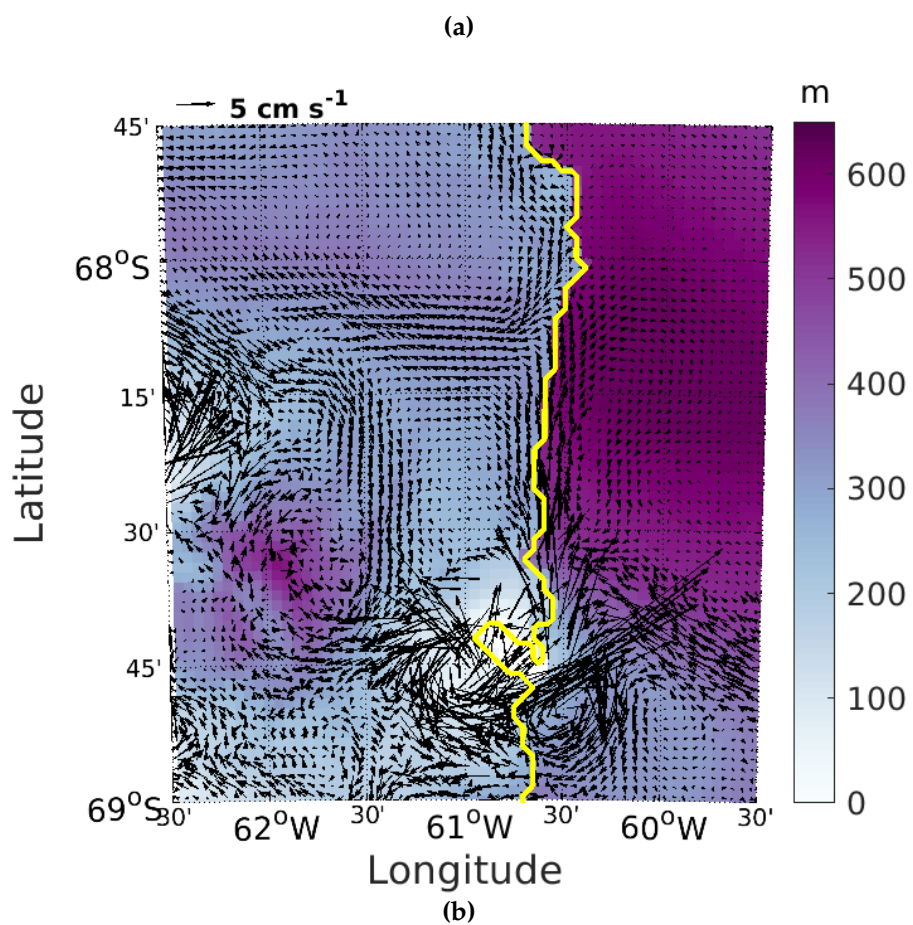
This is not seen in the standard run; with the Brisbane cavity geometry, the outflowing plume does not influence the barotropic flow until it reaches the mid-shelf region, where bottom waters are directed northeastward. This difference is because the inflow across the seabed floor via the southern trough is significantly stronger in the Brisbane case than for the Bedmap2 case, which does not have a trough to direct flow, and is therefore more greatly influenced by the ice topography (Figure 4.3e). This explains why the plume's path more closely resembles the path found by Holland et al. (2009), who used a two-dimensional plume model that had no influence of bathymetry. The water column thickness of the Brisbane cavity is primarily influenced by the bathymetry, which shows much greater spatial changes than the ice draft.

4.2.2 Brisbane versus Mueller

Circulation within the Mueller cavity is radically different to flow under the ice in the standard run because it is split into multiple components as a result of rapid anticlockwise flow in the northeast. Inflow in the south and outflow in the very north of the cavity are separated from this extremely strong, depth-averaged circulation cell near the ice front by the shallow water column in this region of the cavity (Figure 4.3).

4.2.2.1 Inflow

Water at depth enters the LCIS cavity in the Mueller domain at the same location as in the standard run (Figure 4.5a & c), at Gipps Ice Ridge. Once inside, the inflow immediately heads north along the ice front, following contours of water column thickness, until a steep change in seabed height mid-shelf deflects the flow southwest, where it then makes its way directly into Mobiloil Inlet (Figure 4.4c). Although the temperature of the incoming water is very similar to the standard run inflow, the path taken into Mobiloil Inlet is very different as a result of the



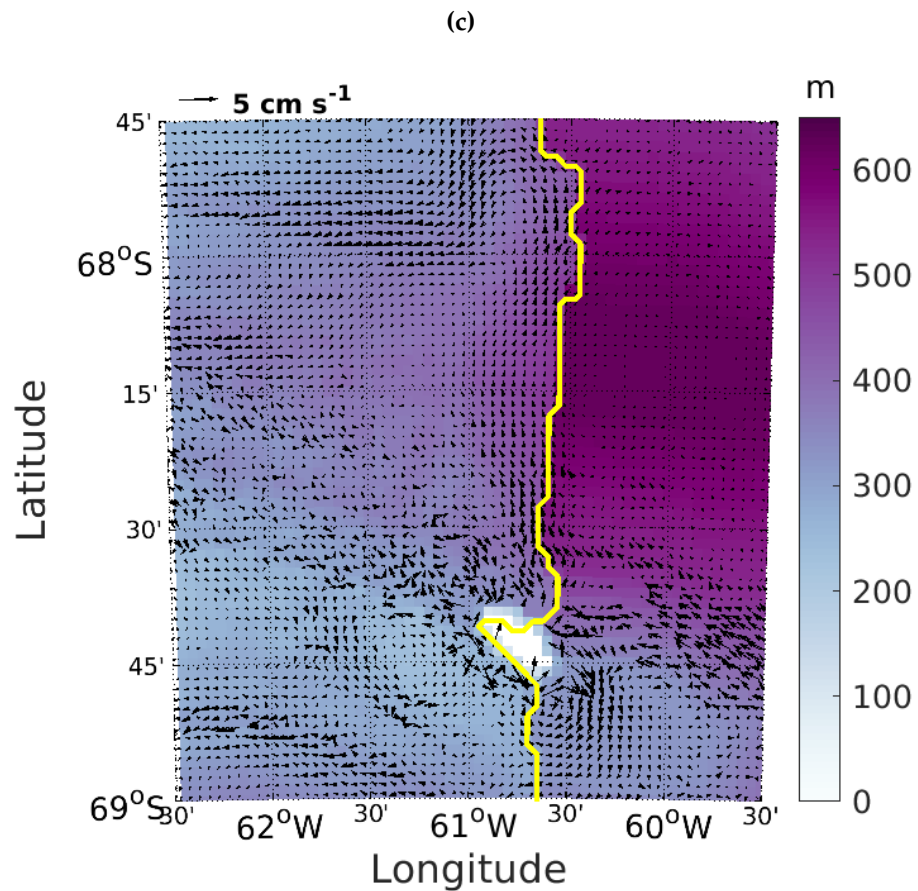


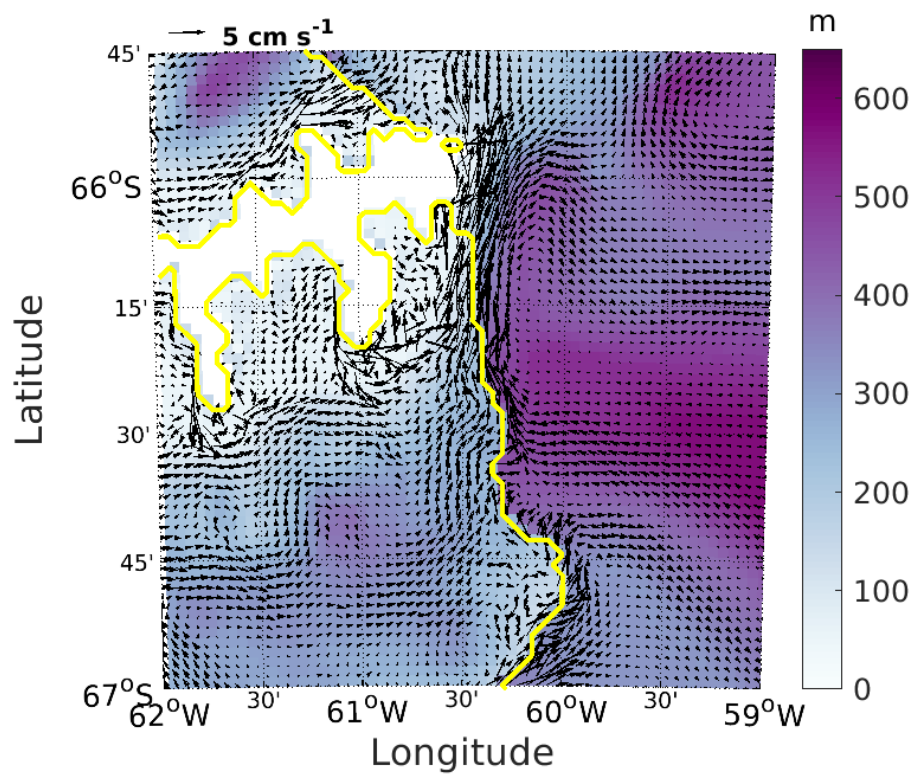
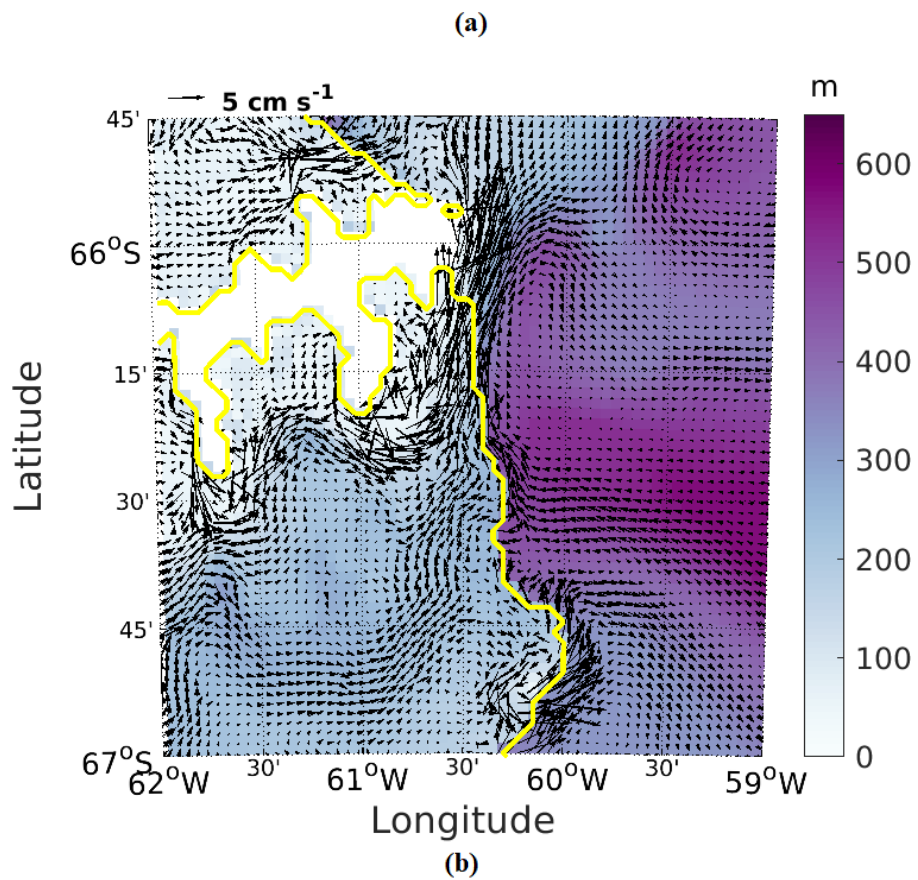
Figure 4.5: Zoomed in view of water column thickness at the location of inflow to the cavity, with sea floor vectors overlaid, for the Brisbane bathymetry (a), Bedmap2 run (b) and the Mueller geometry (c). Yellow contour indicates the position of the calving front.

different bathymetry.

4.2.2.2 Outflow

In the Mueller simulation, the plume from Mobiloil Inlet crosses the centre of the shelf via a slightly different route to both the Brisbane and Bedmap2 cases (Figure 4.7). The plume heads north up to Francis Island, hugging the grounding line, where it travels around both sides of the promontory before meeting back up and being deflected eastward at $\sim 67.5^\circ\text{S}$ by the raised seabed in the north of the domain.

The grounding line is generally deeper in the Mueller case than for the standard run (Figure 4.2b), particularly in the south of the domain and around Francis Island; these deep channels allow water to flow close to the grounding line in this simulation. The Brisbane domain only has a minimum water column



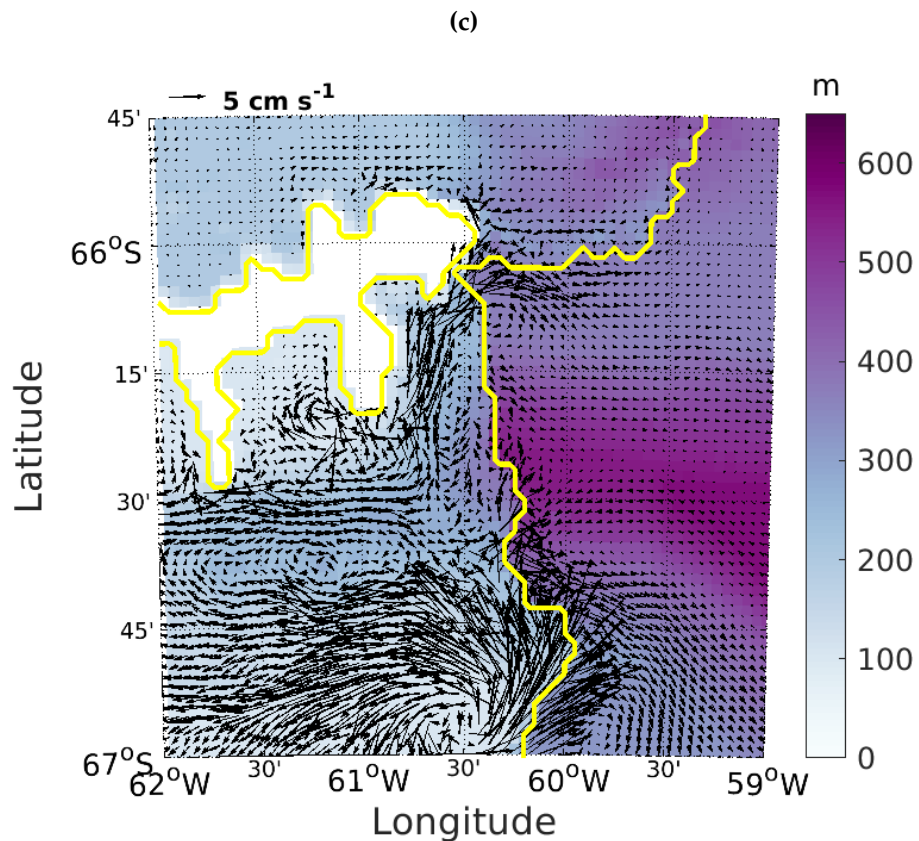


Figure 4.6: Zoomed in view of water column thickness at the locations of outflow from the cavity, with vectors at the ice-ocean interface or sea surface overlaid, for the Brisbane bathymetry (a), Bedmap2 run (b) and the Mueller geometry (c). Yellow contour indicates the position of the calving front.

thickness of 40 m (see Section 2.2.4) whereas the Mueller geometry has a 100 m minimum water column thickness, which would allow greater access to this area of the cavity in the Mueller setup. Shallow bathymetry surrounding Francis Island was found by Brisbane et al. (2014) from seismic surveys of this region and it was suggested that this may be a significant barrier to flow from the south of the cavity. Therefore, the circulation around Francis Island seen in the Mueller domain is unlikely to reflect the true flow in this vicinity, suggesting that the plume path in the run using the Brisbane bathymetry is more likely to be correct.

Upon crossing the ice shelf, the plume gets caught in a rapid anticlockwise circulation in the northeast of the domain, which arises from the shallow water column (~ 100 m) in this region. Modelled ocean velocities increase as the water column shallows to conserve volume flux, despite potential vorticity barriers and enhanced bottom and top stresses, which result from increased drag with faster flow speeds over the seabed and ice base (e.g. Mueller et al. (2012)).

After this starkly different route to the plume's path taken in the standard run, water exits the cavity at the same locations as in the standard run: just south of Jason Peninsula and at Bawden Ice Rise (Figure 4.6a & c). Circulation across the continental shelf is similar to that seen in the standard run as a result of the similarities between their seabed geometries. However, the alternate ice topography in the Mueller run includes the more prominent ice draft of the pre-collapse Larsen B Ice Shelf, which causes the northern fork of the outflowing plume to travel almost entirely east in the Mueller case, as opposed to mostly north in the Brisbane case. This eastward plume opposes the inflow along the northern trough far more strongly than in the standard run and consequently, the warm inflow here does not reach the ice front like it does in the standard run.

4.3 Effects on melting and freezing at ice base

4.3.1 Brisbane versus Bedmap2

The Bedmap2 bathymetry produced a broadly similar melt pattern to the standard run except for lower melting at the tip of Kenyon Peninsula and a more intense area of melting in Mobiloil Inlet (Figure 4.8a & b). The intense patch of melting seen in this region in the Bedmap2 case, along with a patch of freezing south of Joerg Peninsula, is not observed in the standard run. This shows the importance of the trough to melting and refreezing projections.

The Mobiloil Inlet melt pattern in the Bedmap2 case is caused by higher flow speeds at the base of the ice, resulting from a squeezing of the water column as the seabed rises just beyond the grounding line (Figure 4.9). This feature is not present in the Brisbane bathymetry because of the depth of the trough. A slight rise in the Bedmap2 bathymetry west of Churchill Peninsula produces the same result of greater speeds, and therefore amplified melting here, compared with the Brisbane case. Less melting is seen at both Bawden and Gipps ice rises in the Bedmap2 case as a result of lower ice base speeds. Flow speeds directly beneath the ice north of Kenyon Peninsula are also appreciably lower than in the Brisbane run, which explains the much lower melt rate in this location.

4.3.2 Brisbane versus Mueller

Mueller et al. (2012) used a very different cavity geometry in their modelling study

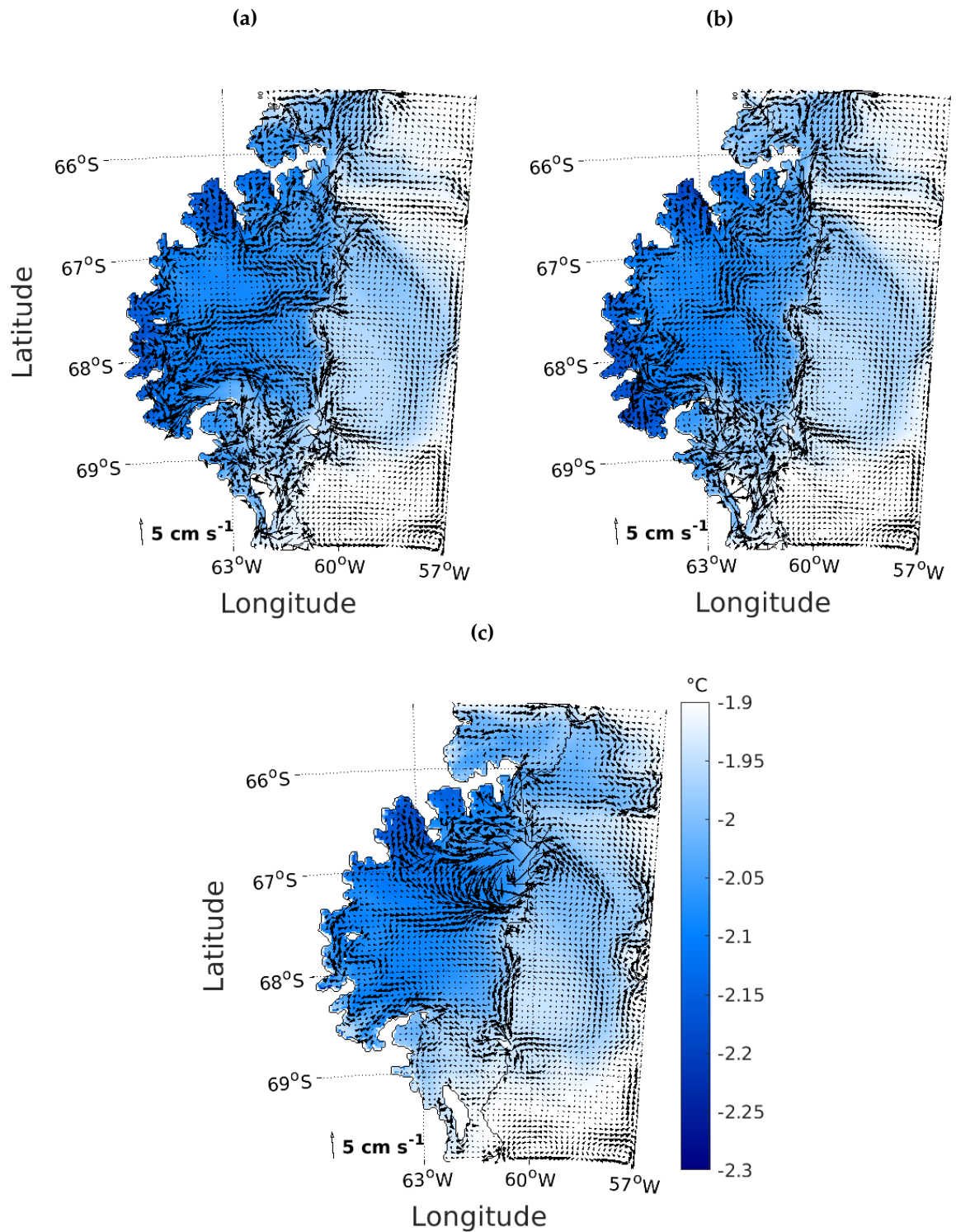


Figure 4.7: Potential temperature at the sea surface over the continental shelf and in the ice-ocean boundary layer under the ice base for simulations using the Brisbane geometry (a), Bedmap2 geometry (b) and Mueller geometry (c), with surface velocity vectors for each case overlaid. Vectors with magnitudes greater than 5 cm s⁻¹ have been removed for clarity.

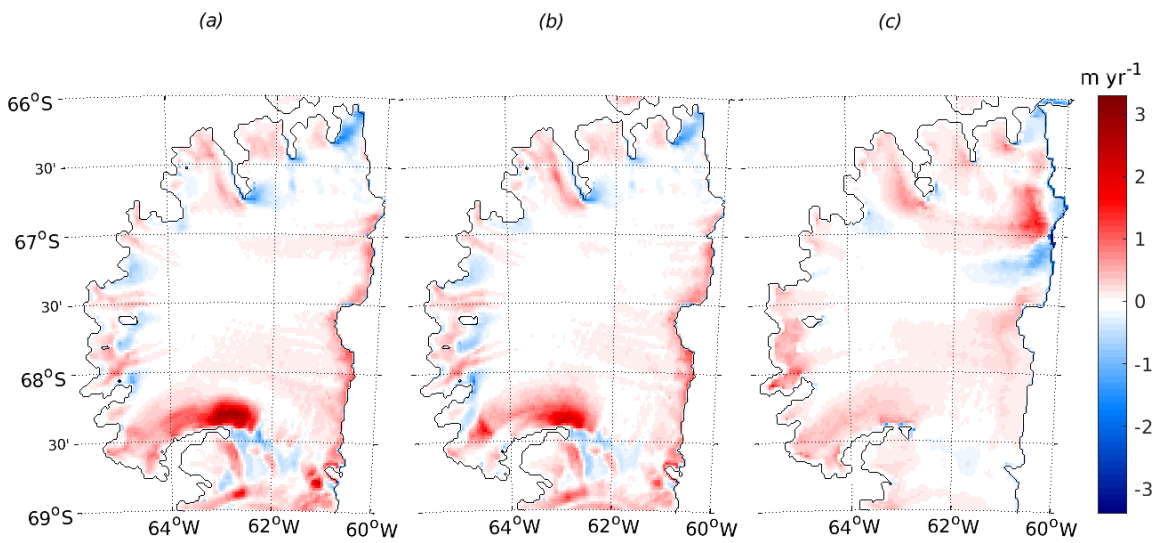


Figure 4.8: Melt rate produced by simulations which used the Brisbane geometry (a), Bedmap2 geometry (b) and Mueller geometry (c). Red shows melting, blue shows locations of refreezing.

which resulted in a significantly different melt pattern, including rapid melting around Bawden Ice Rise. This entire ice rise is less than 40 m above flotation (Holland et al., 2015), so rapid melting in this region could have a significant impact on the stability of LCIS (Borstad et al., 2013; Holland et al., 2015). As the standard run did not show evidence of enhanced melting at this critical pinning point, the simulation using the bathymetry and ice topography of Mueller et al. (2012) was used to investigate whether the different melting pattern resulted from the different model geometries or if other modelling parameters were the cause.

Figure 4.8c shows the resulting melt rate pattern with the Mueller geometry applied to the model which indeed does result in heightened melting in the northeast, near Bawden Ice Rise. As this signal was found using the same set up as the standard run, it shows that the different geometry was responsible for the differing melt pattern, confirming the conclusions of Mueller et al. (2012) that the spatial distribution of the melting pattern is sensitive to the water column thickness of the domain.

The shallow water column thickness in most of the northern half of the Mueller domain results in much faster flow speeds under the ice in the northeast, as seen in Figure 4.9. They exceed ice base speeds seen anywhere in the standard run. The anticyclonic circulation here leads to a region of intense melting, with high freeze rates surrounding the melting patch as a result of excess meltwater circulating the outer rim of this region. Flow speeds are far slower elsewhere in the domain, notably in the southern half of the cavity, explaining the melt rate difference

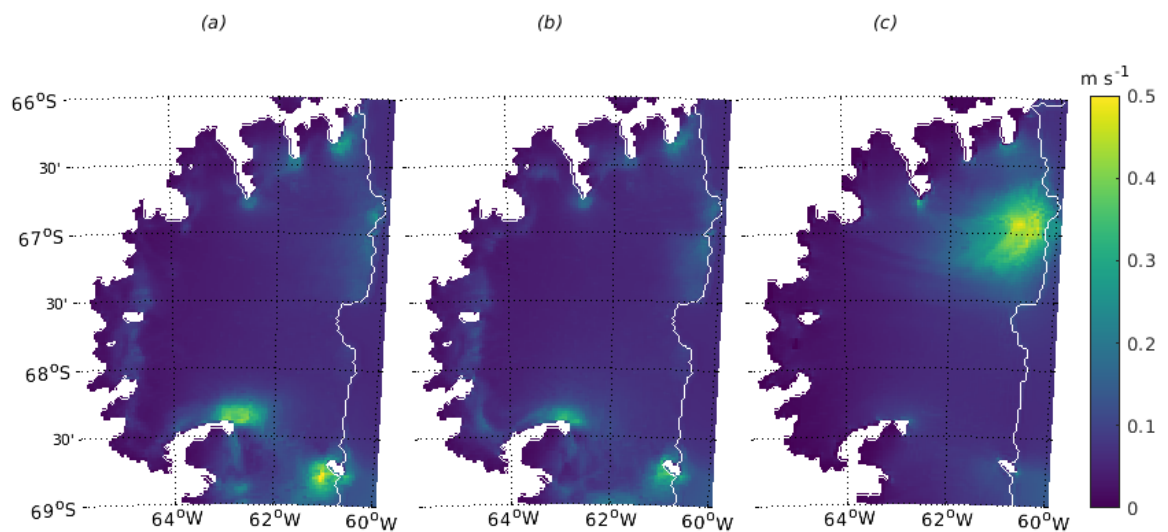


Figure 4.9: Speed of the ocean in the boundary layer directly beneath the ice base produced by simulations using the Brisbane geometry (a), Bedmap2 geometry (b) and Mueller geometry (c).

between the two cases. The melt rate in Mobiloil Inlet is much lower in the Mueller case than for the standard run because the velocities of inflowing water are far smaller than with the Brisbane bathymetry. This is because the water column thickness north of the tip of Kenyon Peninsula is greater in the Muller case compared with the standard run, which explains the decreased velocities in this region leading to a lower melt rate. The Mueller run produced no melting near Gipps Ice Rise, which differs from the standard run where high melt rates were simulated. This is a result of much lower speeds around Gipps Ice Rise in the Mueller run (Figure 4.9) because the bathymetry is not raised surrounding the ice rise as it is in the Brisbane seabed (Figure 4.1).

Freezing takes place in the wake of almost all peninsulas and islands at the grounding line in the Mueller run, as with the Brisbane bathymetry, yet freezing is greatly reduced compared with the standard run. Thermal driving at the grounding line in the Mueller case far exceeds that seen in the standard run (Figure 4.10a & b), and there is little negative thermal driving across the domain, leading to less refreezing at the grounding line.

The freezing pattern surrounding the northeast melting patch in the Mueller run is by far the greatest in the domain and is not found by Mueller et al. (2012) (Figure 4.11a & b). This may be a result of differences in transport between the coordinate systems used by these respective models; the MITgcm uses z-level coordinates, whereas Mueller et al. (2012) used the Regional Ocean Modeling System (ROMS, Shchepetkin and McWilliams (2009)) which employs

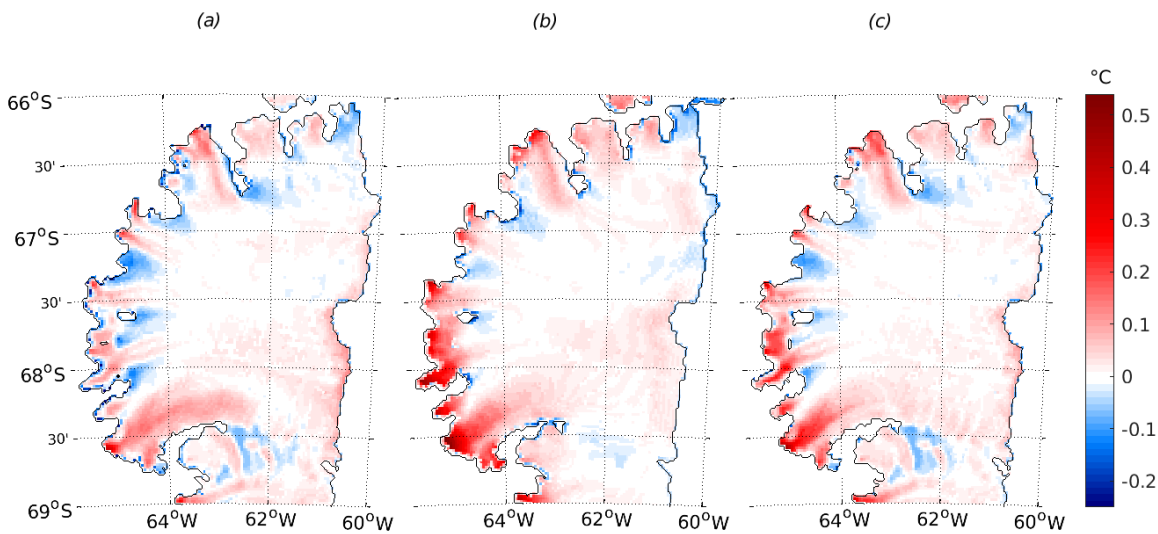


Figure 4.10: Thermal driving in the standard run (a), the Mueller run (b) and the hybrid simulation (c) which uses the Mueller bathymetry and Bedmap2 ice draft. Blue shows areas of negative thermal driving which will result in direct refreezing in the model.

a terrain-following, sigma coordinate system. Mueller et al. (2012) chose not to report their freezing rates because they deemed the rates unreliable without a frazil ice model, therefore, the only comparison that can be made with freezing results found using the MITgcm is the extent of freezing areas. The extent of freezing downstream of all promontories at the grounding line is similar in the MITgcm run compared with the ROMS results, except for freezing downstream of Cole Peninsula. The blue contours in Figure 4.11b show refreezing in the MITgcm close to the ice front, surrounding Bawden Ice Rise, extends far enough upstream to connect with freezing downstream of Cole Peninsula.

The ‘base case’ in the study by Mueller et al. (2012) used an initial ocean temperature of -1.7°C . A comparable MITgcm simulation using the Mueller bathymetry and ice topography, with an initial and boundary condition temperature of -1.7°C , produced reduced grounding line freezing and did not result in the large freezing patch surrounding Bawden Ice Rise at the ice front, as seen in the -1.9°C case (Figure 4.11c & d). Greater thermal driving across the cavity with increased ocean temperatures reduces the availability of supercooled water to refreeze to the base, resulting in much lower freezing rates in this simulation.

The Mueller et al. (2012) ‘base case’ produced an amplified melting patch in the northeast, enhanced melting at the grounding line, particularly in the south, and amplified melting north of the tip of Kenyon Peninsula. Results from the MITgcm run with a heightened initial and boundary ocean temperature of -1.7°C show a very similar melt pattern but with generally higher melt rates than those

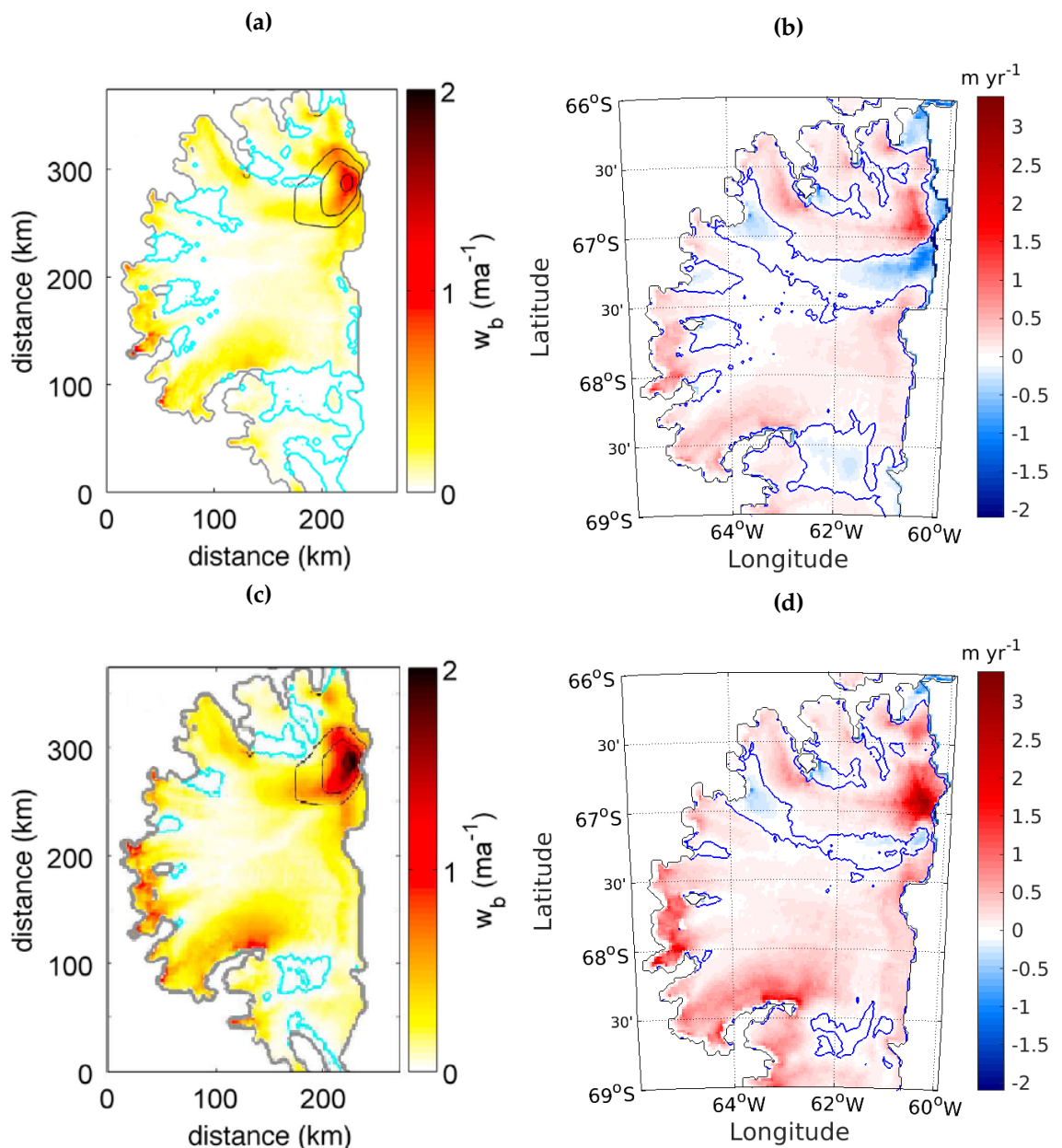


Figure 4.11: Melt rate produced by a simulation using the Mueller geometry and initial ocean temperature of -1.9°C in the ROMS model published in Mueller et al. (2012) (a) is compared with the melt rate produced from a run using the same cavity geometry and initial ocean temperature in the MITgcm (b). (c) and (d) show the melt rate produced by each model when the initial ocean temperature is increased to -1.7°C but all other conditions remain the same. The zero contour is shown in cyan (a & c) and blue (b & d) to mark the extent of freezing across the ice shelf.

reported by Mueller et al. (2012). The difference between melt rates is a result of values chosen for melting parameters. The heat transfer coefficient used in the Mueller et al. (2012) model was significantly lower than that used in the MITgcm (5×10^{-3} versus 0.011).

4.3.2.1 Influence of ice shelf geometry on melting and freezing

Mueller et al. (2012) concluded that the water column thickness of the cavity influenced the melting pattern and that has been evidenced in the current study using different seabed configurations. The novel aspect of the current study is the new bathymetry; to investigate the sole effect of altering the bathymetry rather than the bathymetry and ice topography as a whole, a simulation using the Mueller bathymetry and Bedmap2 ice topography was carried out (the 'hybrid' run) and compared with the full Mueller geometry. As the ice topographies are very similar, only relatively small changes are seen in the shape of the cavity when the Mueller ice topography is replaced with the Bedmap2 ice draft (Figure 4.12). The exceptions to this are at the grounding line, where the hybrid cavity produces thick water columns in some areas, and at the calving front, where smoothing of the ice here, to avoid numerical instability in a sigma coordinate model, has led to a significant difference between the depth of the ice drafts.

Although the melting patch near Bawden Ice Rise has the highest melt rate in the domain in the hybrid run, the melt rate is far lower and there is much less refreezing in this region than in the Mueller case (Figure 4.13). As the only difference between the two runs is the ice topography, the altered water column thickness change must be responsible for lowering the melt rate here. A shallow water column in the northern half of the cavity is present in the hybrid simulation, as it was for the Mueller run, however, the water column in the full Mueller geometry is significantly thinner than in the hybrid version, by up to 50 m. This alteration, combined with the less severe gradient in water column thickness at the ice front resulting from the lack of smoothing in the hybrid run, leads to lower velocities at the ice base near Bawden Ice Rise. Therefore, in the hybrid case, there is less turbulent mixing of heat from the ambient ocean below the layer of cold Ice Shelf Water, reducing the amount of heat reaching the ice base to contribute to high melting in this region. The freezing rate has reduced as there is less cold meltwater available to supercool and refreeze to the ice base.

Aside from this significant change, the hybrid run has greater refreezing in Hess Inlet and at Churchill and Kenyon peninsulas as a result of greater negative thermal driving at the ice base in these regions of LCIS (Figure 4.10b & c). Further, a difference in thermal driving between these two cases at the grounding line north of Joerg Peninsula also results in a slightly lower melt rate in the hybrid case at this location.

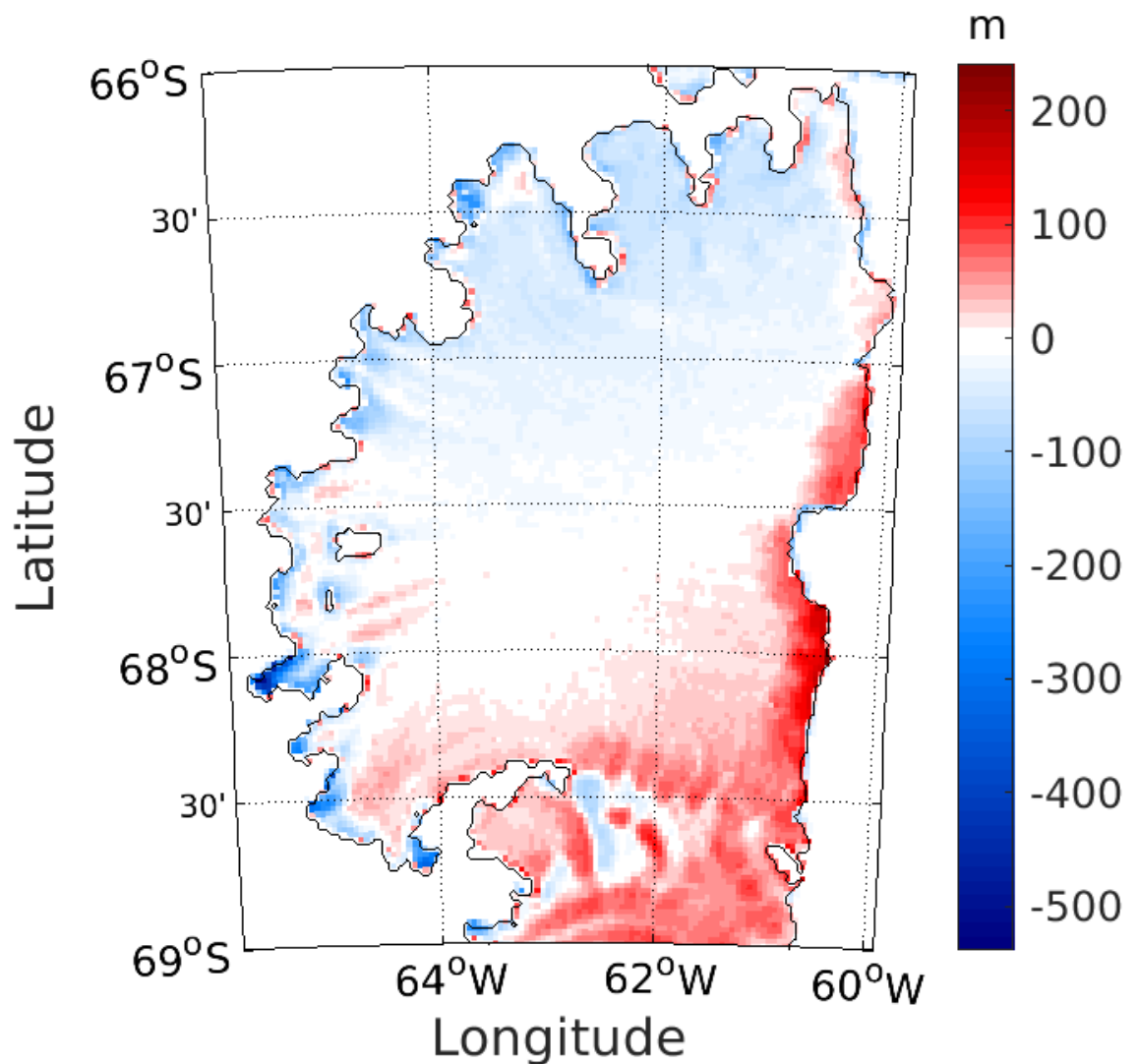


Figure 4.12: Difference in water column thickness between the Mueller and hybrid cavities; red shows where the hybrid cavity is shallower than the Mueller domain, blue shows where it is thicker.

4.4 Sensitivity of melt rate at Bawden Ice Rise to its geometry

The amplified patch of melting surrounding Bawden Ice Rise in the Mueller case raises key questions about the importance of using the correct bathymetry in order to simulate accurate melt rates for this ice shelf. Bawden Ice Rise is known to be a critical pinning point for LCIS (Borstad et al., 2013) and the loss of grounding at an ice shelf pinning point has been shown to result in changes to the stress field across the entire shelf (Reese et al., 2018). Holland et al. (2015) identified the ungrounding of LCIS from Bawden Ice Rise as being one of the most likely

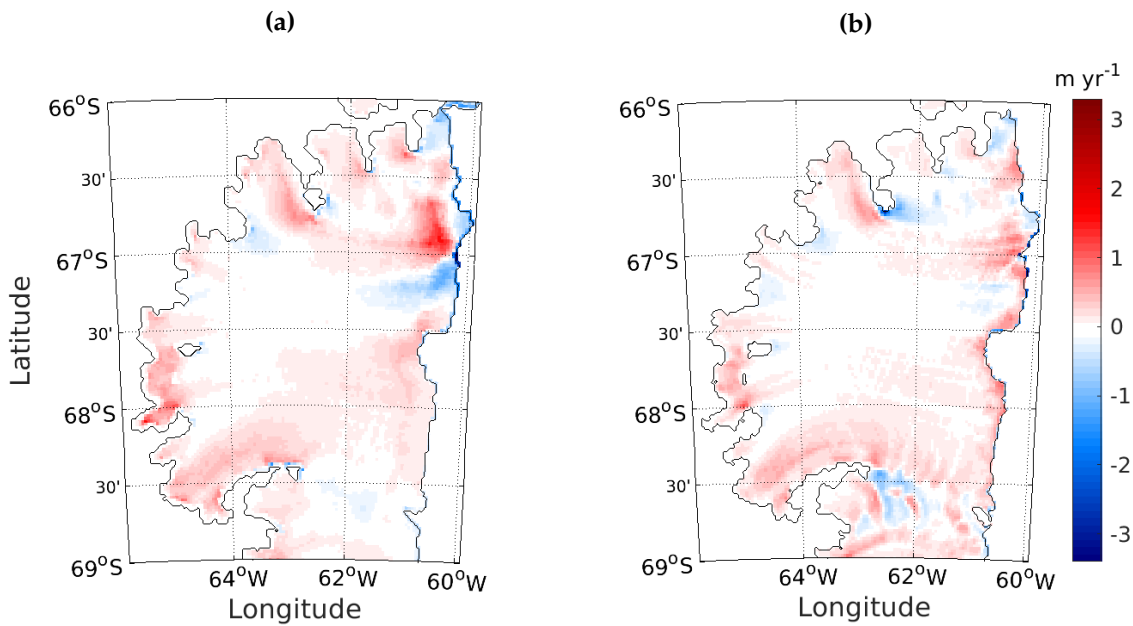


Figure 4.13: Melt rate produced by the simulation with Mueller geometry (a) versus that produced from a simulation which uses the Mueller bathymetry and Bedmap2 ice topography (b).

pathways to the collapse of LCIS and many other studies have noted high melt rates in this vicinity (Mueller et al., 2012; McGrath et al., 2014; Adusumilli et al., 2018).

Melting in this region of LCIS in the standard run is not exceptionally high or extensive, which calls into question how vulnerable the ice shelf is to melting near Bawden Ice Rise. However, the ice rise is not grounded in the standard run (Figure 4.14a) as a result of smoothing during the interpolation process when creating the bathymetry. The Mueller geometry also features an ungrounded Bawden Ice Rise (Figure 4.14b), yet a great deal of melting is seen in this region. The enhanced melting in this area of the northeast Mueller cavity results from a very shallow water column from the grounding line to the calving front, producing fast flowing water circulating anticlockwise under the ice shelf (Figure 4.7c). This rapid circulation feature was also found by Mueller et al. (2012) using the ROMS model, which they attributed to high barotropic tidal current speeds dominated by diurnal tidal constituents.

Two further runs were carried out using the Brisbane seabed with manually altered bathymetry at the coordinates of Bawden Ice Rise ($\sim 66^{\circ}54' \text{ S}$, $60^{\circ}12' \text{ W}$) after the interpolation process was complete (Figure 4.15). One simulation, which will be referred to as the 'narrow Bawden' case, featured two cell columns in the domain, corresponding to the coordinates of Bawden Ice Rise, being raised to

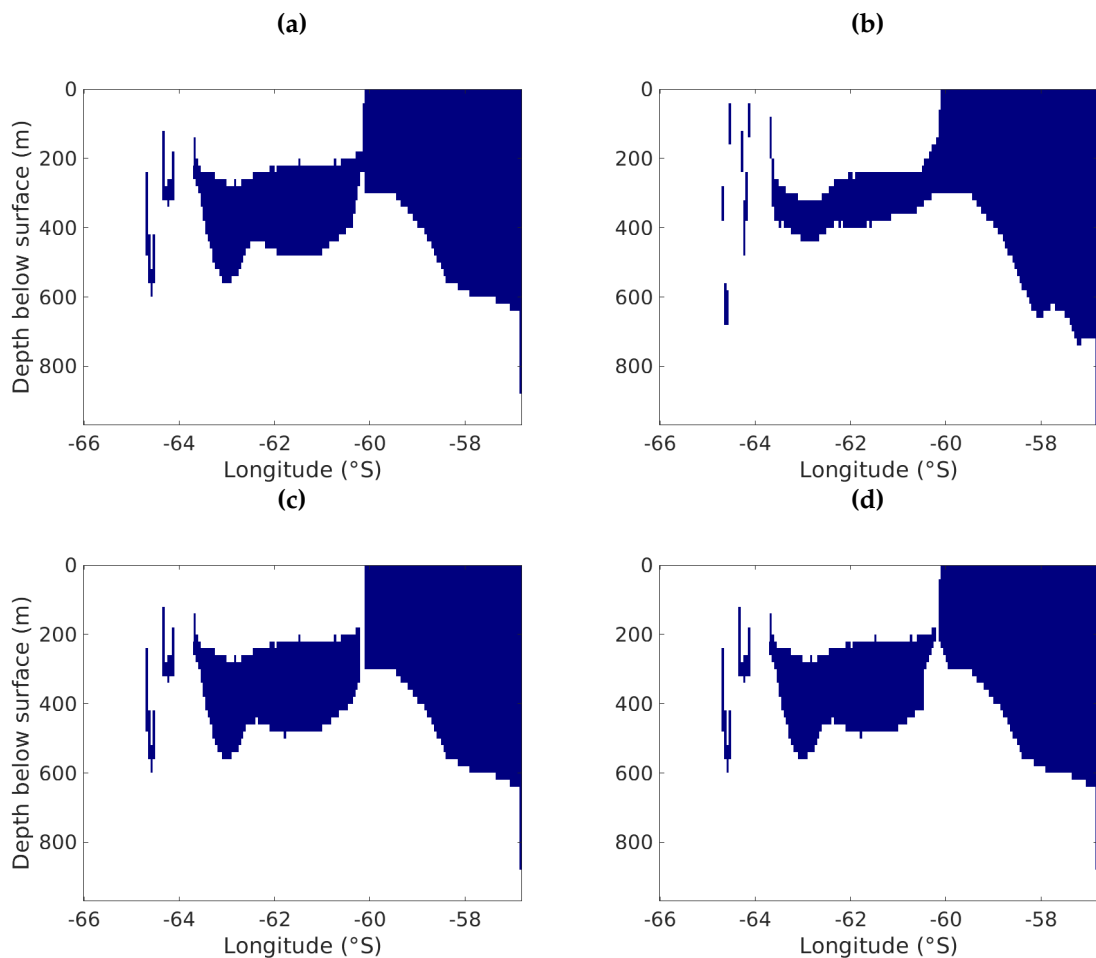


Figure 4.14: Side view along latitude $66^{\circ}54' S$, where dark blue represents ocean cells in the model and white signifies the seabed and ice shelf, shows Bawden Ice Rise is not grounded in the standard run with Brisbane bathymetry (a) or in the Mueller geometry (b). Artificial changes were made to the bathymetry to ground Bawden Ice Rise by a tall and thin ridge in the narrow Bawden case (c) and by a more gradually sloping ice rise in the broad Bawden geometry (d).

meet the ice depth, with no further alterations to the surrounding seabed (Figure 4.14c & Figure 4.15b). Another simulation, referred to as the 'broad Bawden' run, included several fully grounded columns as well as a heightening of the surrounding cells' topography in order to create a broader ice rise (Figure 4.14d & Figure 4.15c) than the very sharp and narrow ice rise of the former run.

Figure 4.16 shows the resulting melt/freeze patterns arising from the standard run, and the two altered bathymetry runs. The artificial, broader ice rise produces a higher melt rate in this region, however, this is still greatly reduced in extent compared with the Mueller case. The melt rate in this broad Bawden case, averaged over the area covered by the raised cells of the artificial ice rise, was more than double that in the same area of the standard run with the original

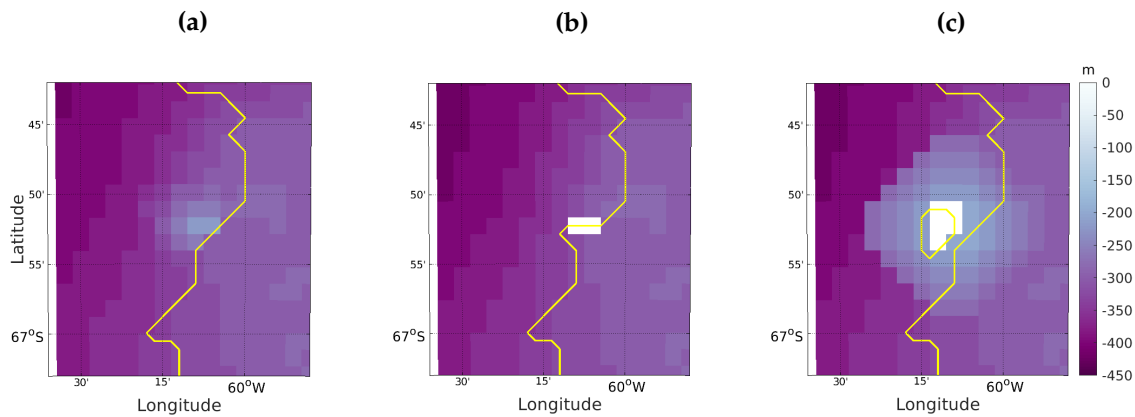


Figure 4.15: Zoomed in view of the bathymetry surrounding Bawden Ice Rise in the standard run (a), narrow Bawden (b) and broad Bawden (c) runs. White indicates grounded cells and the yellow contour shows the calving front position.

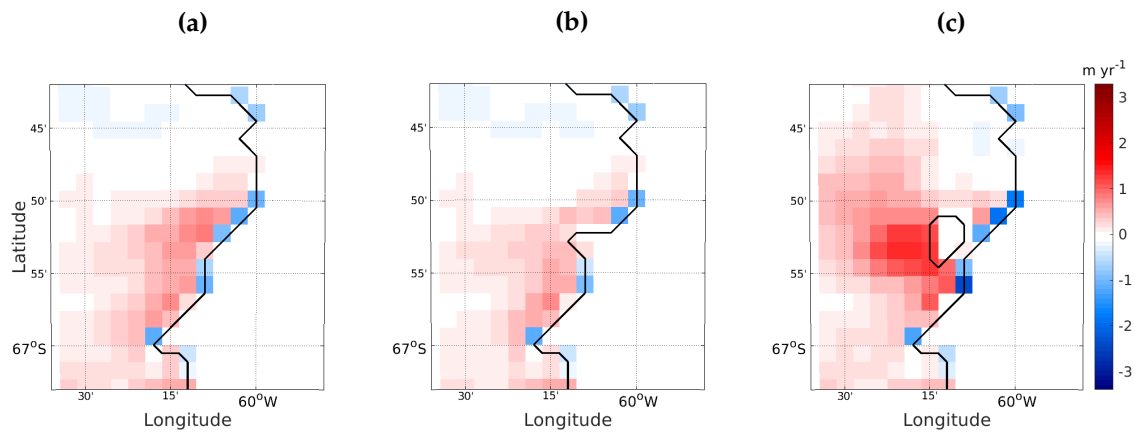


Figure 4.16: Melt rate surrounding Bawden Ice Rise produced by the standard run (a), narrow Bawden run (b) and broad Bawden run (c); red shows melting, blue shows locations of refreezing and black contour shows the calving front position.

ungrounded seabed (0.25 and 0.10 m yr^{-1} , respectively). The melt rate in the narrow Bawden case is halved in comparison with the standard run, which indicates that the shape of the ice rise is more important than the fact it is grounded, in terms of influencing ocean dynamics and consequent melt rates.

The broad Bawden simulation results in a small but rapid circulation around Bawden Ice Rise (Figure 4.17), on a much smaller scale than that seen in the Mueller run, but producing a similar result. Even with the intensified melt rate near Bawden Ice Rise in the broad Bawden simulation, the signal was still smaller by approximately a factor of two in comparison with the high melt rate north of Kenyon Peninsula (Figure 4.18).

This seabed change was relatively minor but demonstrated an important change in melt rate at this critical area of LCIS. Merely grounding the ice rise

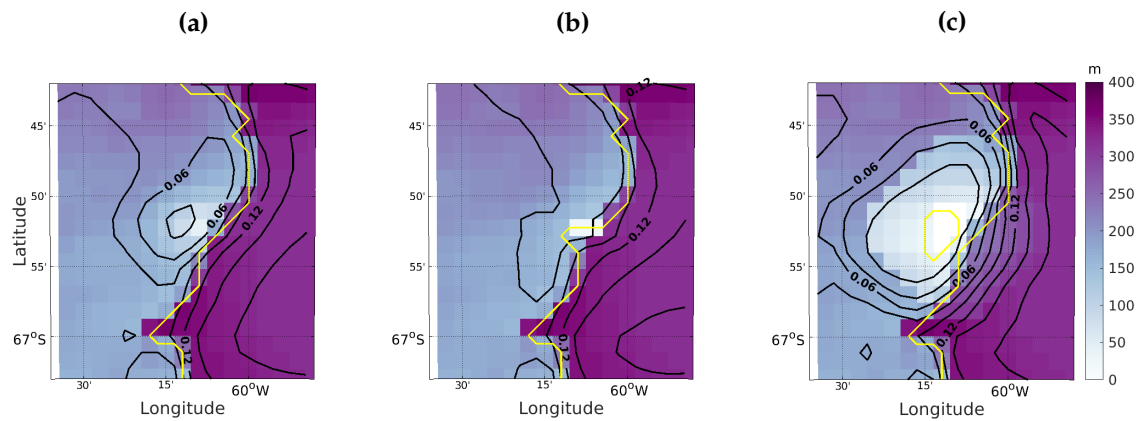


Figure 4.17: Water column thickness surrounding Bawden Ice Rise in the standard run (a), narrow Bawden run (b) and broad Bawden run (c), with barotropic streamfunction contours overlaid (in black). The calving front is indicated in yellow and values of labels on streamfunction contours have units of Sverdrups.

was not enough to alter melt rates substantially, the shape of the ice rise played a crucial role. These simulations show the significant effect uncertainty in the modelled cavity geometry can have on modelled ocean circulation and melt rate. Although we have detailed knowledge of the grounded area of Bawden Ice Rise from airborne radar surveys (Holland et al., 2015), there is not enough data from the surrounding area to confirm the shape of the seabed surrounding this ice rise; a single seismic shot in the vicinity of Bawden Ice Rise is still ~ 10 km away. Further surveys are needed to constrain the bathymetry map in this region, for future modelling studies of LCIS to produce accurate melt rates in this region. As basal melting at Bawden Ice Rise has been identified as paramount to the stability of the ice shelf, this thesis has shown how vital more detailed knowledge of the bathymetry in this area of LCIS is.

4.5 Grounding line alterations

Digging of the bathymetry near the grounding line was performed to ensure communication between cells. Grid cells in the domain are either ‘open,’ representing ocean, or ‘closed,’ indicating ice or land mass. Model calculations are only performed on open cells. Closed columns beneath known floating ice are opened during the digging process so that lateral borders between neighbouring ocean columns are connected. The minimum water column thickness of 40 m was set to ensure that at least two grid cells in a column were open so as not to inhibit flow in the shallowest parts of the cavity.

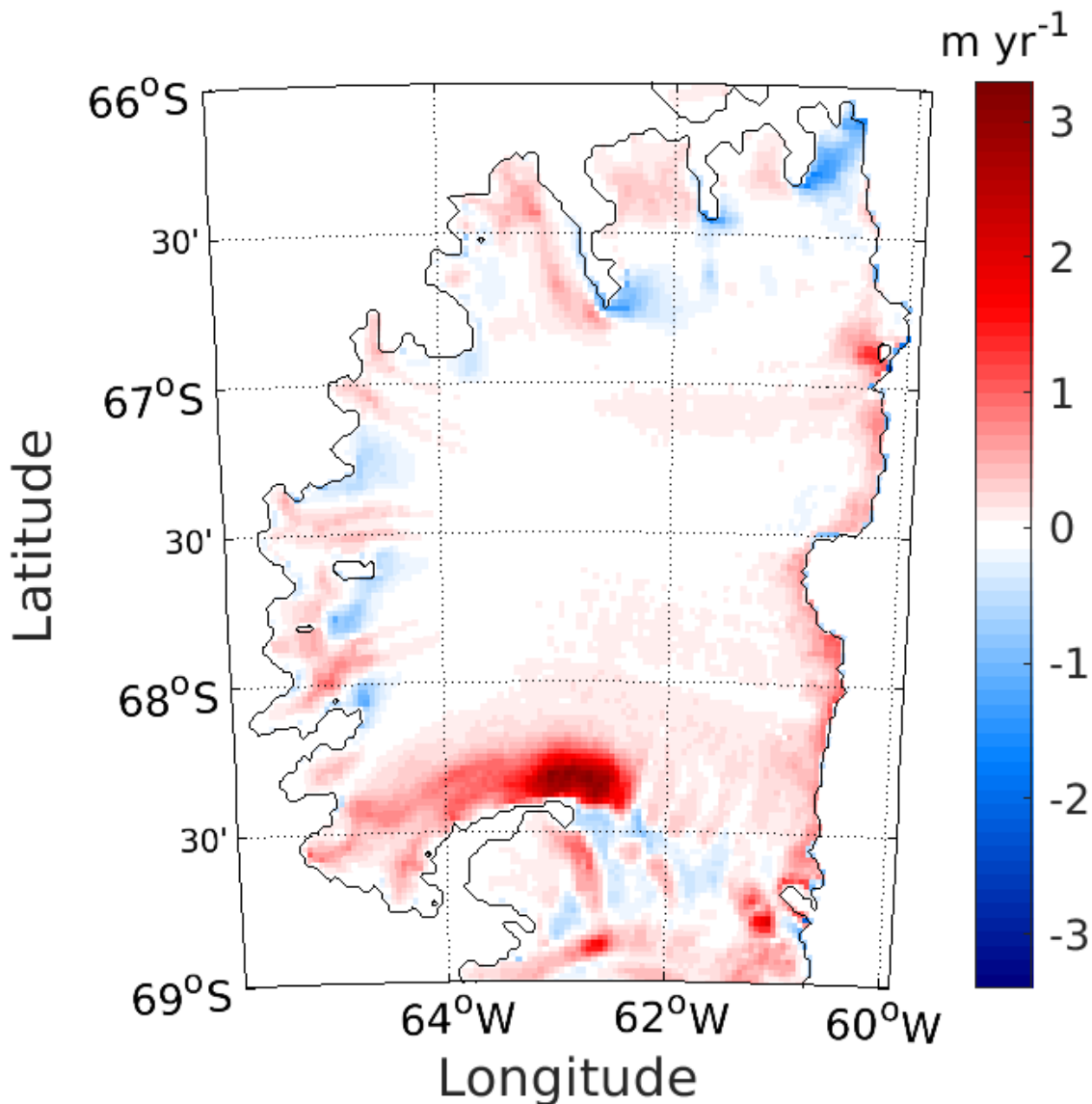


Figure 4.18: Melt rate produced by the run with broad Bawden bathymetry; red shows melting, blue shows locations of refreezing.

Two simulations were run to test the effect of this digging on the melt rate results. One run featured a bathymetry which was not altered near the grounding line from the original interpolated seabed ('no digging' run) and therefore does not have a minimum water column thickness. The Bedmap2 ice draft used in these simulations is deeper than much of the bathymetry near to the grounding line of the unaltered, interpolated seabed grid. Consequently, much more of the ice is grounded in the no digging run, significantly modifying the grounding line position (green contour in Figure 4.19a). The bathymetry offshore of this contour is largely the same as for the standard run, with just a few cells of higher seabed adjacent to the new grounding line position. The second simulation had

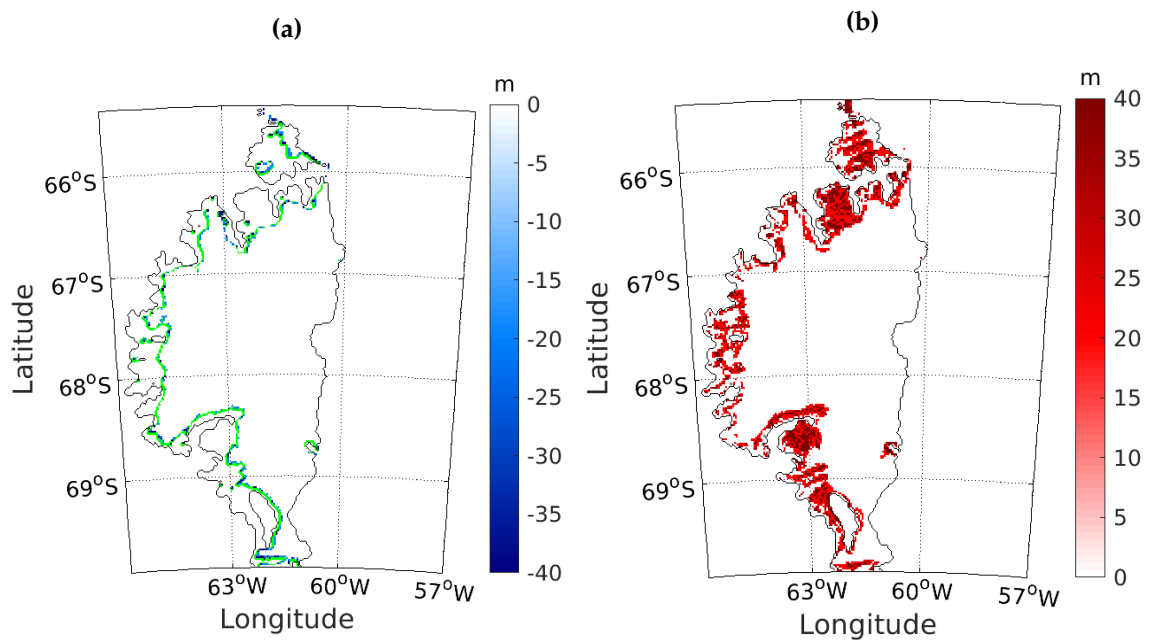


Figure 4.19: (a) Blue shading indicates where the seabed of the no digging cavity is higher than that in standard run. Green contour shows the altered grounding line of the no digging simulation. (b) Red shading indicates how much deeper the bathymetry around the grounding line is in the double digging case than the standard run.

its bathymetry deepened (Figure 4.19b) to allow for a minimum water column thickness of 80 m everywhere ('double digging' run), doubling the 40 m minimum water column thickness of the standard run.

While the no digging simulation has reduced melting and freezing in the domain because of the modified grounding line, beyond this altered grounding line, the melting extent and magnitude is very similar to the standard run, with the exception of the pattern of enhanced melting at the tip of Kenyon Peninsula moving further east in the no digging run (Figure 4.20). This is because the highest flow speeds under the ice base migrate eastward in the no digging run as a result of the different grounding line position (Figure 4.21).

The main change in the melt pattern and rate in the double digging case is also in the south of the cavity. The enhanced melting north of Kenyon Peninsula, while still the highest in the domain, is lower in magnitude than in the standard run, and melting in Mobiloil Inlet is slightly higher. Thermal driving along most of the grounding line in the double digging case is a little higher than in the standard run (Figure 4.22), particularly in Mobiloil Inlet. This is likely a result of a greater volume of warmer water making its way to the grounding line here as the water column is thicker, meaning there is more warm water to mix with the meltwater being produced in this region. Speeds below the ice base are a little

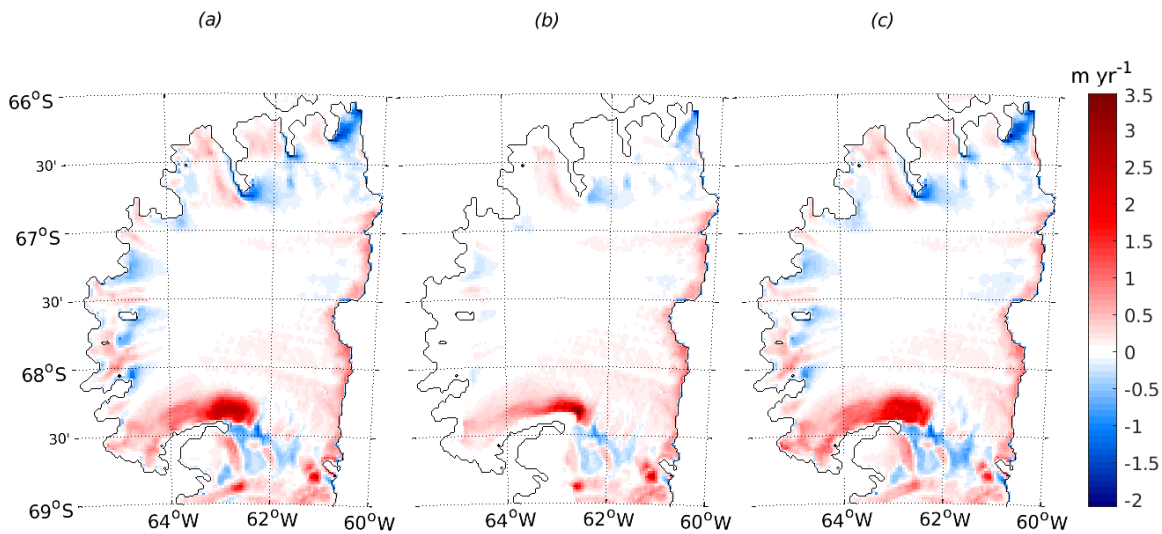


Figure 4.20: Melt rate produced by the standard (a), no digging (b) and double digging (c) runs. Red shows melting, blue shows locations of refreezing.

lower in the double digging run, because the water column is thicker close to the grounding line than in the standard run, resulting in the lowered melt rate at Kenyon Peninsula.

The no digging run shows why digging of the newly created bathymetry is a necessary and justifiable alteration to the model domain. The Bedmap2 grounding line and ice topography are well constrained by altimeter observations of tidal flexure and surface height measurements combined with the assumption of hydrostatic equilibrium, respectively (Fretwell et al., 2013). Interpolation of the seabed grid in unsampled areas leads to sections of bathymetry close to the grounding line being shallower than the ice draft. Consequently, this grounds a great deal of ice that is known to be floating and signals that the seabed is in fact deeper in this region than the interpolation has determined, necessitating the digging process. In addition to this issue, the no digging geometry also contains some unconnected pockets of ocean behind the grounding line, which the standard run avoids. Results from the double digging simulation demonstrate that the choice of digging depth does not affect the main conclusions stated in Chapter 3 about the melt rate of LCIS.

4.6 Concluding remarks

The simulations presented in this chapter, which used the Brisbane, Bedmap2 and Mueller geometries, produced very different ocean circulation patterns in

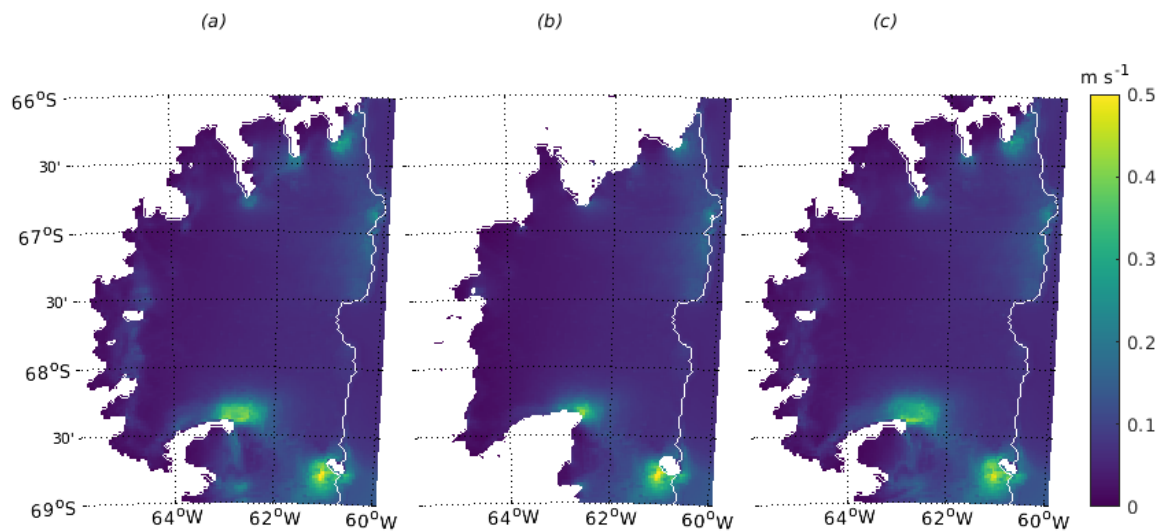


Figure 4.21: Flow speeds directly beneath the ice in the standard (a), no digging (b) and double digging (c) runs.

each case. Differences in bathymetries have had a particularly noticeable effect on the initial path of the meltwater plume upon leaving Mobiloil Inlet. The simpler geometry of the Bedmap2 run, which has a relatively flat seabed compared with the Brisbane bathymetry, leads to a single-component circulation under the ice shelf, steered primarily by ice shelf topography. The thin water column in the north of the Mueller cavity leads to a strong circulation cell here, with separated inflow and outflow circulation components. The dual-component circulation indicated by the barotropic streamfunction in the Brisbane cavity (Figure 4.3) appears to be a middle ground between the simple, single-cell circulation of the flat Bedmap2 seabed geometry and the multifaceted circulation of the northward thinning Mueller bathymetry. The Brisbane bathymetry is in much better agreement with available data and therefore, the circulation and melt/freeze pattern results found in the standard run are assumed to be closer to reality than results found in previous modelling studies. The new bathymetry product that was created for this study and presented in this thesis is an important contribution to our knowledge of LCIS which can be utilised in future modelling studies.

While locations of refreezing in these domains are seen to result from the greatest negative thermal driving, regions of high melt rates coincide with shallow water column thicknesses. Areas with a water column thickness which substantially narrows have been identified as leading to higher speeds under the ice base, resulting in local patches of melting in different places in each of the three cases. This shows the value of using an accurate bathymetry in order to simulate the correct melt pattern. In particular, the shape of the seabed at Bawden Ice Rise

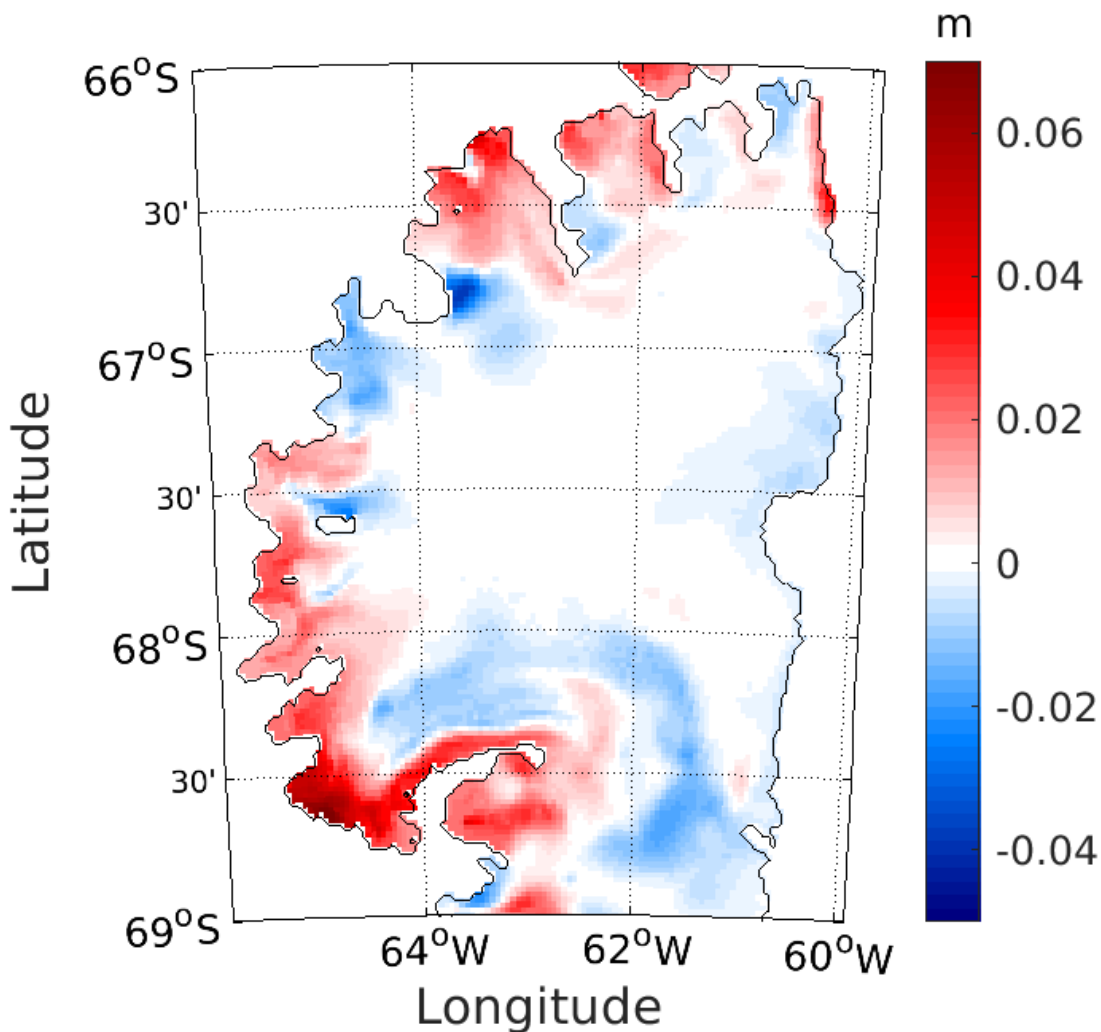


Figure 4.22: Difference between thermal driving in the standard run and double digging simulation. Red shows where the double digging run has greater thermal driving than the standard run; blue shows areas where thermal driving is lower in the double digging run.

has been found to influence the resultant melt rate and extent at this important location for LCIS stability. These simulations have demonstrated for the first time how imperative accurate knowledge of the shape of Bawden Ice Rise is for ocean circulation and melt rate results in models of LCIS, and will consequently inform the priorities of future data gathering field campaigns on the ice shelf.

Results presented here show the cavity shape overall to be vital to simulated conditions under LCIS, as water column thickness is found to drive the majority of the flow and determine positions of localized, enhanced melting. The bathymetry is the least well charted of all datasets relating to the shape of the cavity. Therefore, future work is required to take more direct measurements to better constrain the seabed and water column thickness estimates in models of LCIS.

Chapter 5

Sensitivity of LCIS cavity to changes in ocean temperature forcing

Intrusions of warm water onto the continental shelves surrounding Antarctica leave ice shelves fringing the continent vulnerable to changes in Southern Ocean heat content. There is a need to understand whether the observed changes of LCIS are ocean-driven and if these changes may lead to destabilisation, leaving the ice shelf in danger of collapse. To explore whether changes in the ocean are responsible for the observed lowering and fracture of LCIS, a series of warmer ocean scenarios were simulated to investigate the response of the cavity and impact on sub-ice shelf circulation, melting and refreezing.

Several simulations with the same set up as the standard run but different initial and boundary condition temperatures, ranging from -1.9°C to -1.0°C , were run. This is a wide temperature range for this region of the ocean; such a large range was chosen to illustrate the vulnerability of the ice shelf to both small and large temperature perturbations, with evidence for the upper bound of this range coming from observations. Ocean temperatures found in contact with the ice front by Bathmann et al. (1994) were recorded as approximately -1.4°C , but with temperatures at the sea surface of up to 2°C . Over a decade later, researchers found temperatures just offshore of the continental shelf at a depth of 400 m of up to -0.5°C (Absy et al., 2008). Water at these much higher temperatures has not been found to make its way into the ice shelf cavity (Nicholls et al., 2012), which is why the model range was restricted to a top temperature of -1.0°C .

Although there have been no persistent measurements of ocean warming in this region of the Southern Ocean, the evidence of warm waters on the continental shelf in front of LCIS show it has happened, at least sporadically, in recent

decades. Ocean temperatures in the cavity have likely varied in the past. The standard run temperature of -1.9°C was chosen because Nicholls et al. (2012) found water at this temperature beneath the ice shelf and these are the only direct measurements we have inside the cavity to inform the model initial conditions. Changes in larger ocean circulation in the Weddell Sea could alter the flow of warm waters to upwell onto the continental shelf but there are not enough measurements of this remote area of the Southern Ocean to know if this scenario has happened. Therefore, this set of experiments aimed to identify expected changes in LCIS melt/freeze rates and ocean circulation in the event the cavity did experience a hypothetical ocean warming of these magnitudes, either recently or in the future. The mechanisms of potential warming are not considered in this thesis. The difference in steady state melt rates between the standard run (-1.9°C), which is believed to be a close match to current conditions of the cavity, and warmer runs demonstrates the sensitivity of cavity circulation and melt/freeze rates to spatially uniform changes in ocean forcing.

5.1 Circulation changes in a warmer cavity

With higher ocean temperatures, velocities in the domain increase as expected, owing to the larger density gradients created between warm, salty inflow and greater amounts of cold, fresh meltwater. This is a well-known feature of circulation within Antarctic ice shelf cavities (e.g. Jacobs et al. (2011)) as well as Greenlandic Fjords (Cottier et al., 2010). The higher velocities are shown by the greater concentration of streamfunction contours in the warmer cases (Figure 5.1); the shape of the streamfunction contours shows that the direction of depth-averaged flow under the ice shelf also changes in a warmer ocean.

The largest change in circulation is seen mid-cavity, where the two discrete components of circulation are connected in the standard run. Meltwater drives flow eastward across the shelf towards the calving front in this coldest (-1.9°C) simulation (Figure 5.1, left column), but when the temperature is increased, the flow travels steadily more north rather than east (Figure 5.1, middle and right columns). This results in a simpler, single cell of circulation once temperatures reach the higher end of the range, rather than separate inflow and outflow (i.e. southern and northern circulation) components connected by a flow which crosses the cavity beneath the ice shelf, travelling eastward. This distinction takes place once the temperature rises above -1.6°C .

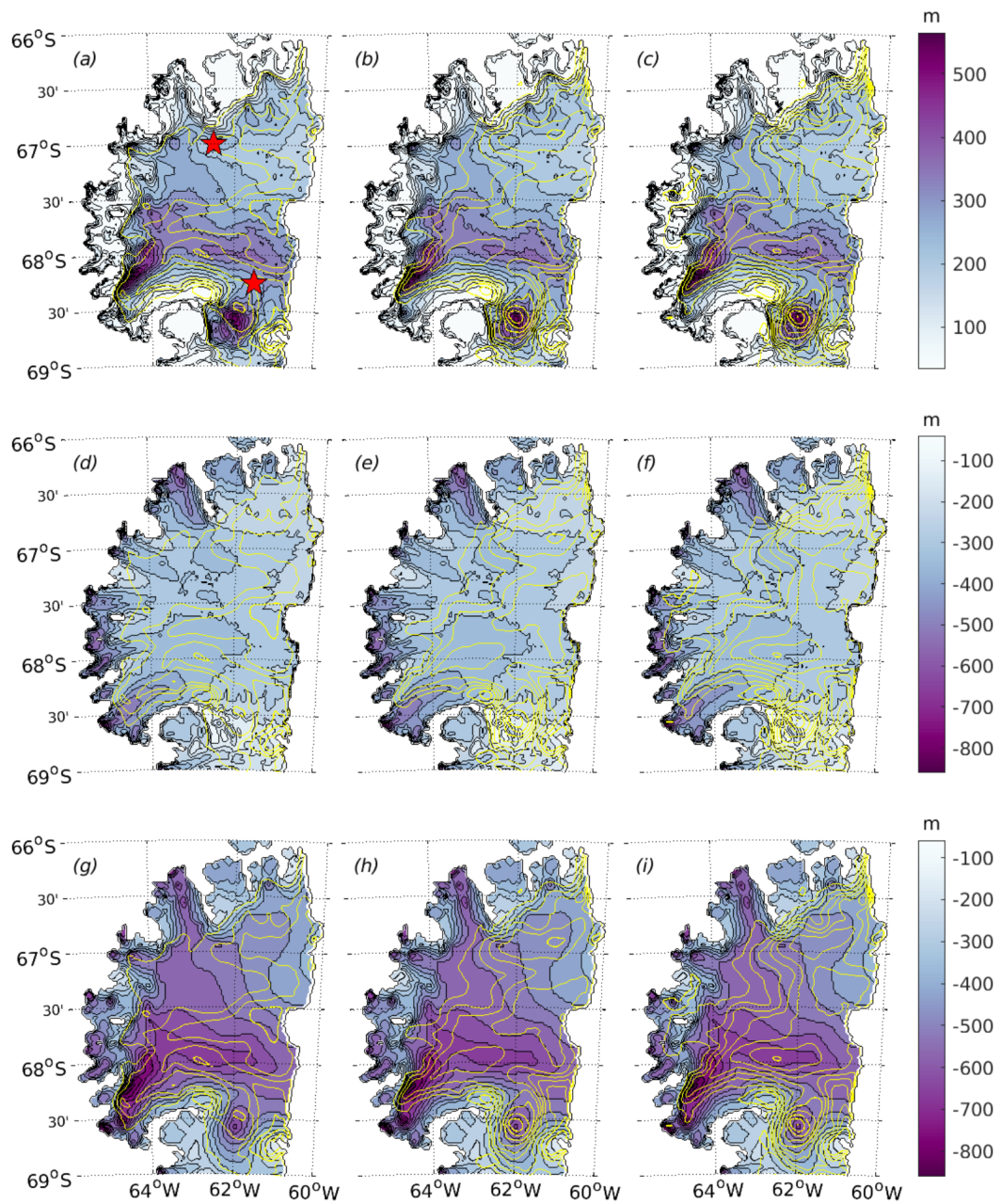


Figure 5.1: Barotropic streamfunction contours, in yellow, overlaid onto filled purple contours of water column thickness (top row, a-c), ice base depth (middle, d-f), and bathymetry (bottom row, g-i) for three temperature cases. Left column shows the standard run (-1.9°C), middle column shows a mid-temperature case (-1.5°C), and right column shows the warmest case modelled here (-1.0°C). Red stars indicate locations of density profiles shown in Figure 5.2 and discussed in the text.

Ocean circulation in the south of the cavity, near the inflow region, is more barotropic in the colder cases than with a warmer ocean forcing. An increase in meltwater across the domain with greater ocean forcing results in greater stratification (Figure 5.2a), leading to stronger baroclinicity and therefore a

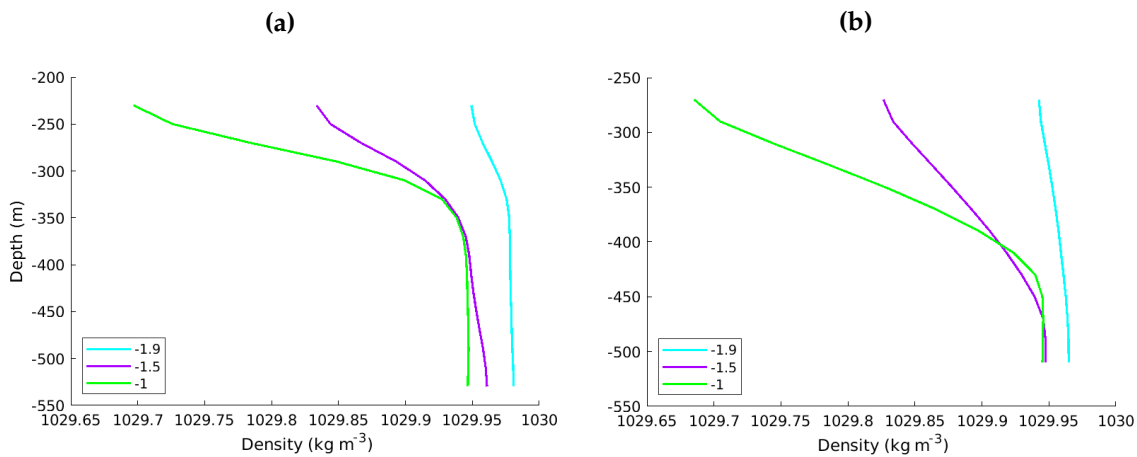


Figure 5.2: Density distribution of the water column is shown for three temperature cases near the inflow region in the south of the cavity (a) and in the path of the meltwater outflow region in the north (b). Locations of these profiles are shown by red stars in Figure 5.1a.

difference in surface and bottom flow (Figures 5.3 & 5.4). With higher ocean temperatures, circulation in the north of the cavity is more greatly influenced by the shape of the ice topography rather than bathymetry, because the plume is stronger as a consequence of larger amounts of meltwater being produced (Figure 5.1d-f). In all three temperature cases, surface currents in the northern half of the cavity follow the path outlined by the barotropic streamfunction contours. Circulation beneath the ice can be seen changing direction between ~ 67 - 67.5°S to form the single circulation cell in the warmer cases, which more closely follows contours of ice shelf thickness.

In the warmer cases, the circulation is similar to that in the Bedmap2 case discussed in Chapter 4, despite the plume in the Bedmap2 run not being as strong as the warm cases here. The Bedmap2 and warm cases exhibit similar features in this region because the ice topography has a greater influence on the direction of flow in both cases. The bathymetry in Bedmap2 is quite flat and hence, does not affect contours of water column thickness as much as the ice shape, while in the warmer simulations, even with the more topographically irregular seabed, the strong plume does not feel the presence of the seabed as keenly as in the standard run, as a result of the greater stratification (Figure 5.2b).

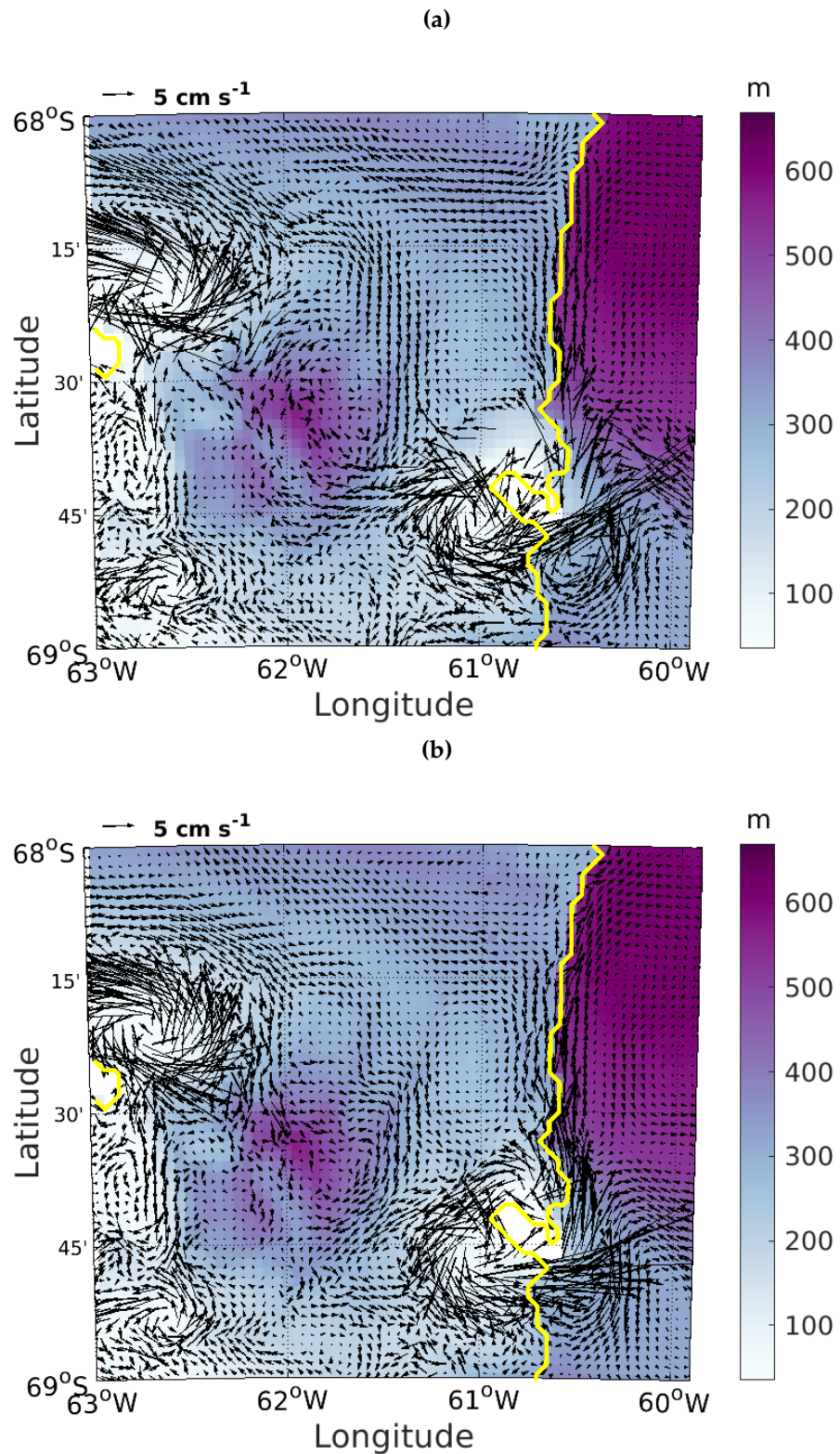


Figure 5.3: A closer view of the inflow region in the standard run. Colours show water column thickness with bottom vectors overlaid (a). Vectors at the sea surface or directly under the ice shelf in the same region (b) show that the flow is barotropic. Yellow contour indicates position of ice front.

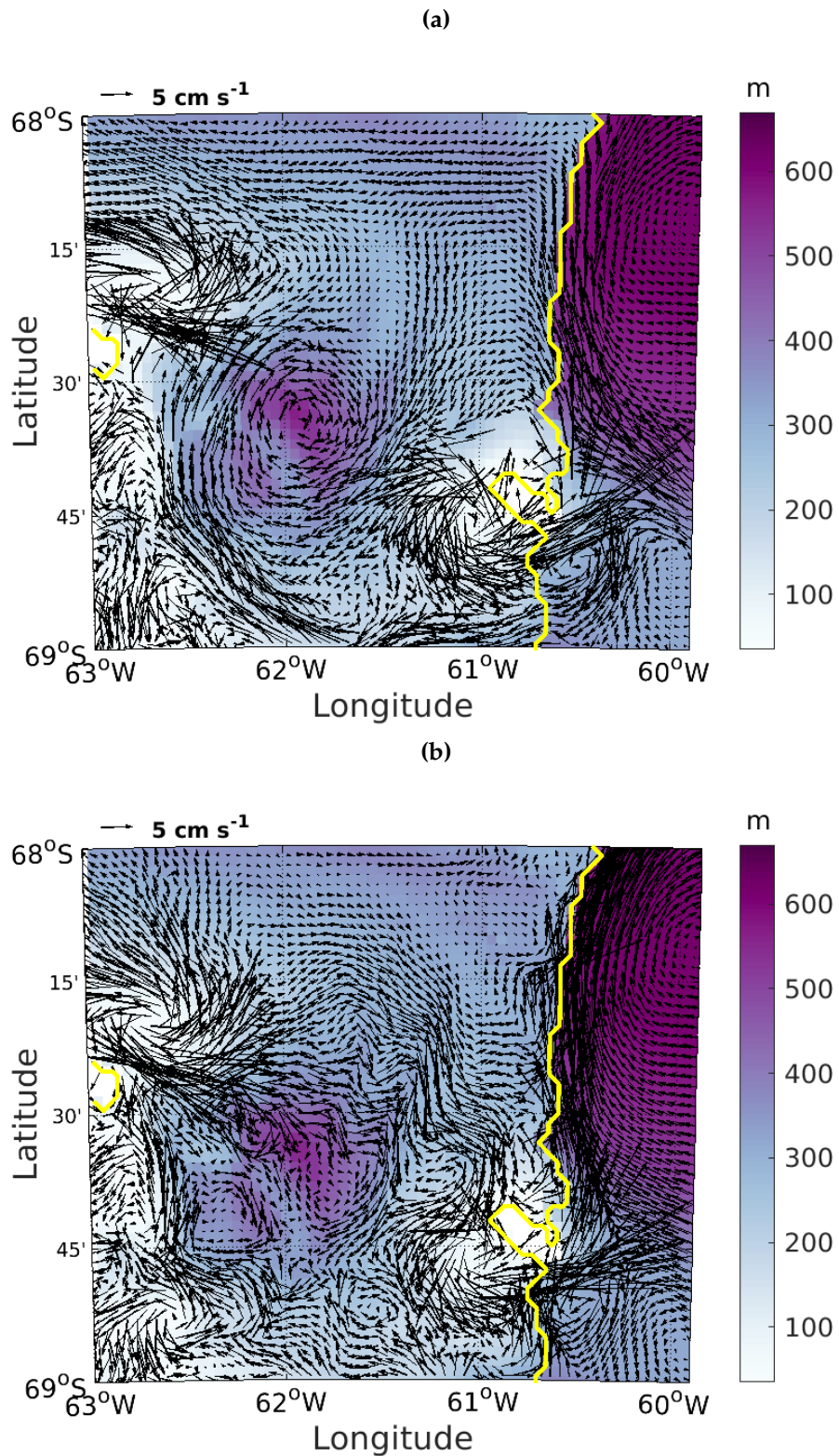


Figure 5.4: Similar to Figure 5.3, (a) shows sea floor velocities and (b) shows surface velocities for the inflow region of the -1.0°C case. The flow is far less barotropic in this warmer case.

5.2 Melt rate increases

The melting patterns for all temperature sensitivity cases are shown in Figure 5.5. The spatial distribution of melt rate is very similar in each case, with an expected increase in melting magnitude and extent at higher ocean temperatures. This result matches other modelling studies of LCIS (Mueller et al., 2012), which found that the spatial distribution of the melting pattern is governed by the water column thickness of the domain, while the magnitude of melting is primarily determined by the ocean temperature forcing. The domain-averaged steady state melt rate almost doubles when the model ocean temperature increases by just 0.1°C from the standard run temperature (-1.9°C) to -1.8°C . Mueller et al. (2012) reported a 200% increase in melt rate with a change in ocean temperature from -1.9°C to -1.7°C , which was replicated here as the melt rate increased from 0.1 m yr^{-1} to 0.3 m yr^{-1} . Similarities between results found here and those of Mueller et al. (2012) show the modelled melt rate is responding sensibly to small increases in ocean temperature forcing. This increases confidence in the modelled response to a much more extensive range of temperatures which this study has tested for the first time. Understanding the cavity's response to a greater range of conceivable ocean temperatures the cavity may experience in the future is a vital contribution to our knowledge of LCIS.

When ocean temperatures were raised by 0.5°C in the study by Holland et al. (2009), the steady state melt rate increased by 1 m yr^{-1} , whereas here, the melt rate only increased by 0.8 m yr^{-1} with the same change in ocean forcing. This difference results from the contrast in ocean forcing of each model. The warm ocean in the plume model of Holland et al. (2009) is forced directly beneath the plume layer, while the three-dimensional model described here forces the domain with warm waters at the lateral boundaries. This water loses some heat as it progresses through the domain to reach the underside of the ice, leading to a lower melt rate. This shows that the ice shelf is somewhat protected from ocean warming through negative feedbacks within the cavity, resulting from mixing caused by bathymetric slopes and tides. Models of LCIS that do not include these features will not capture these feedback mechanisms and will overestimate the affect of ocean warming on basal melt rates.

Holland et al. (2015) estimated that an average increase in basal melting of 0.26 m yr^{-1} was required to explain the mean ice loss along their survey line (red line in Figure 5.6a), noting that they also included ice divergence as a mechanism contributing to ice loss, compared with an estimated steady state melt rate of

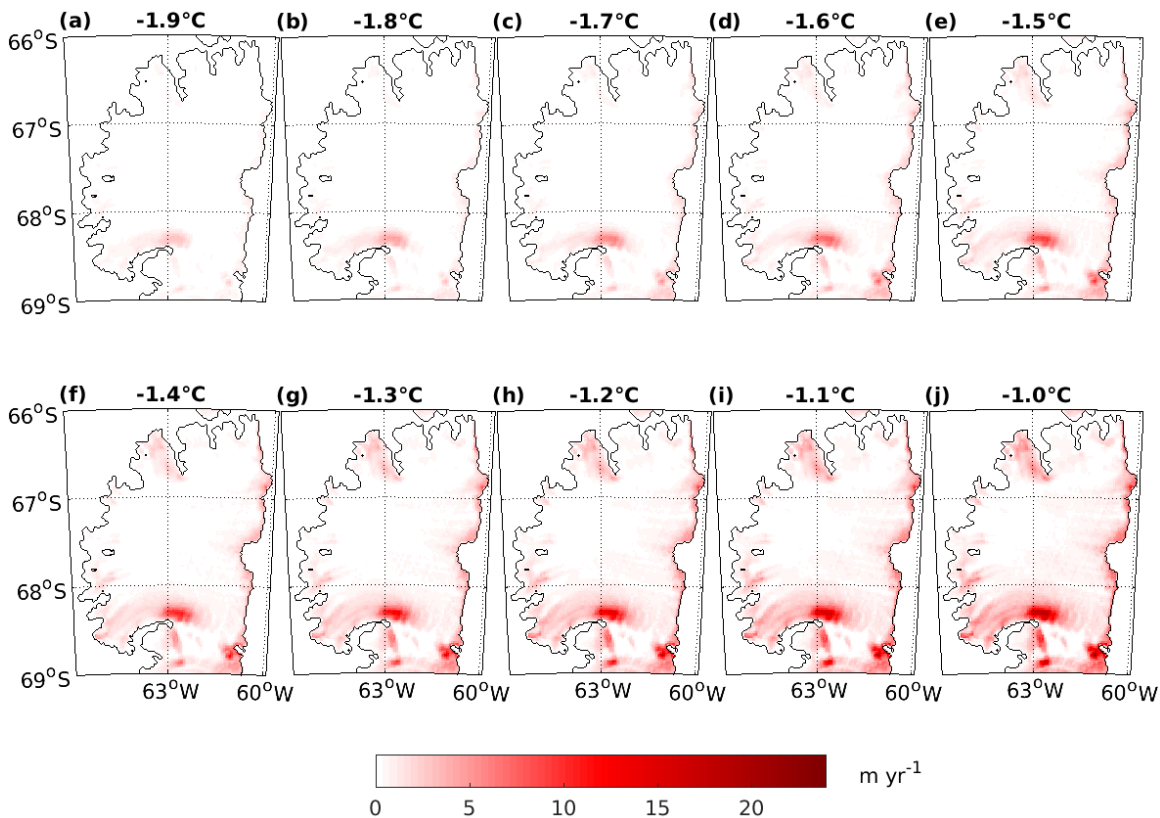


Figure 5.5: Melt rates resulting from ten different temperature sensitivity simulations. Only melting is shown here; freezing rates are shown in Figure 5.8 for more detail.

only 0.06 m yr^{-1} . In simulations performed here, the domain-averaged melt rate increased by 0.2 m yr^{-1} from the standard run (-1.9°C) to the -1.7°C case and by 0.4 m yr^{-1} from the standard run to the -1.6°C case. Therefore, an ocean temperature increase of $0.2\text{-}0.3^\circ\text{C}$ would be consistent with observed rates of ice loss.

5.2.1 Relationship between temperature and melt rate

The change in melt rate of LCIS as the ocean forcing temperature is increased is found to be non-linear (Figure 5.7). The net melt rate change averaged over the ice shelf (black circles) and the purely melting increases (red circles), i.e. neglecting any change in freeze rate, show the same quadratic relationship, which becomes slightly more linear as the ocean transitions to higher temperatures. The difference between the standard run (-1.9°C) and the -1.8°C temperature case leads to a net change sensitivity of $5.1 \text{ Gt yr}^{-1} \text{ }^\circ\text{C}^{-1}$, whereas, the change from -1.1°C and -1.0°C results in a sensitivity of $15.7 \text{ Gt yr}^{-1} \text{ }^\circ\text{C}^{-1}$. This demonstrates that the overall relationship is non-linear because melt rates show a greater sensitivity to ocean temperature increases at higher temperatures.

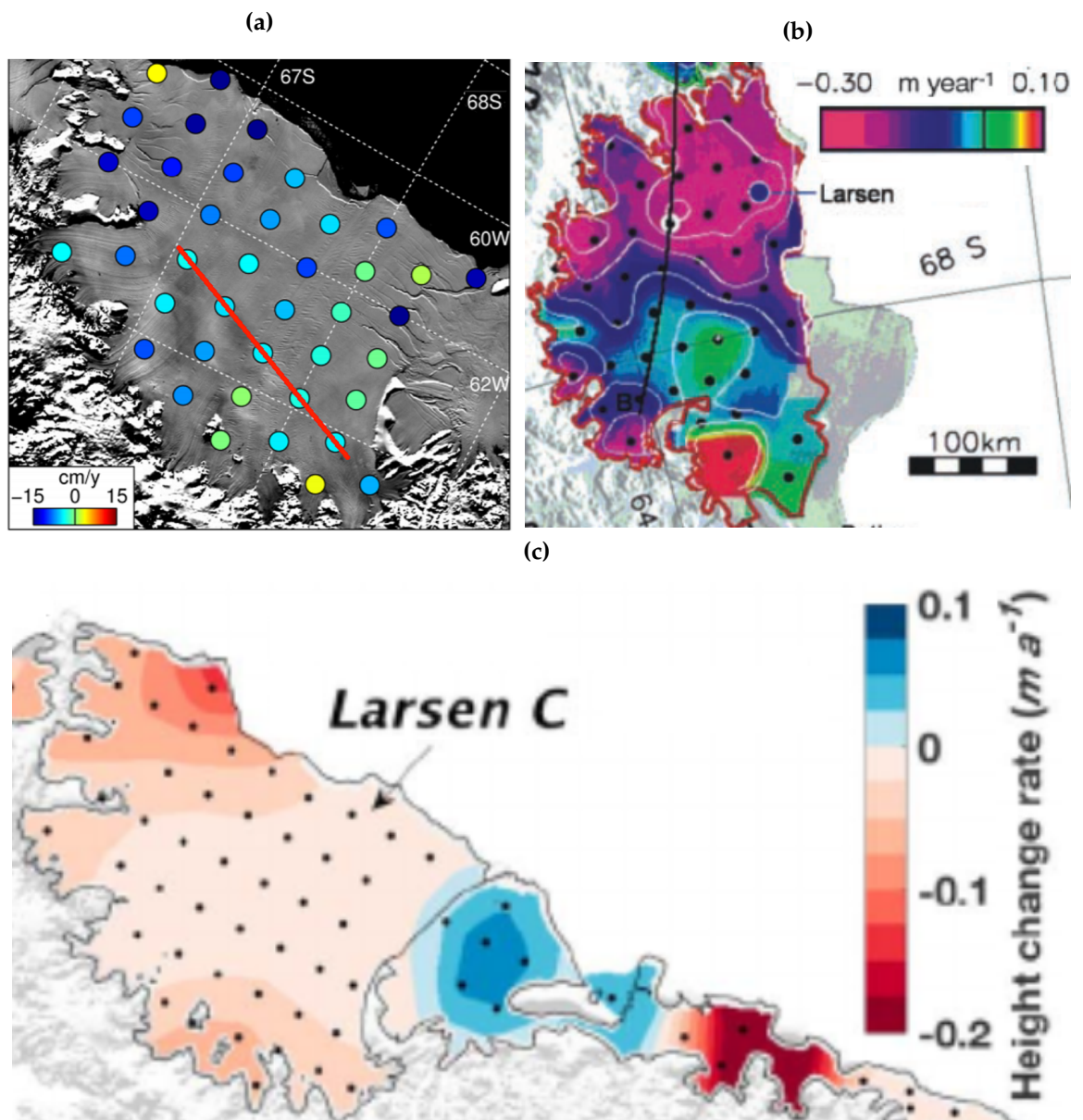


Figure 5.6: Surface lowering recorded from radar altimeters over the period 1994-2011, adapted from Holland et al. (2015) (a). The red line shows the profile of repeated radar surveys discussed in the text. (b) Altimetry-derived lowering between 1992-2001 is shown using both a colour scale and white contours at intervals of 0.1 m yr⁻¹, adapted from Shepherd et al. (2003). The red contour shows the 1990 extent of the ice shelf; black dots show locations of data points used to create the map; the blue dot is the Larsen meteorological station and the black line starting at point 'B' indicates a transect used for analysis in Shepherd et al. (2003) which is not discussed here. (c) Surface lowering seen by radar altimeters between 1994-2016, adapted from Adusumilli et al. (2018). Black dots indicate regions where results have a confidence interval above 67%.

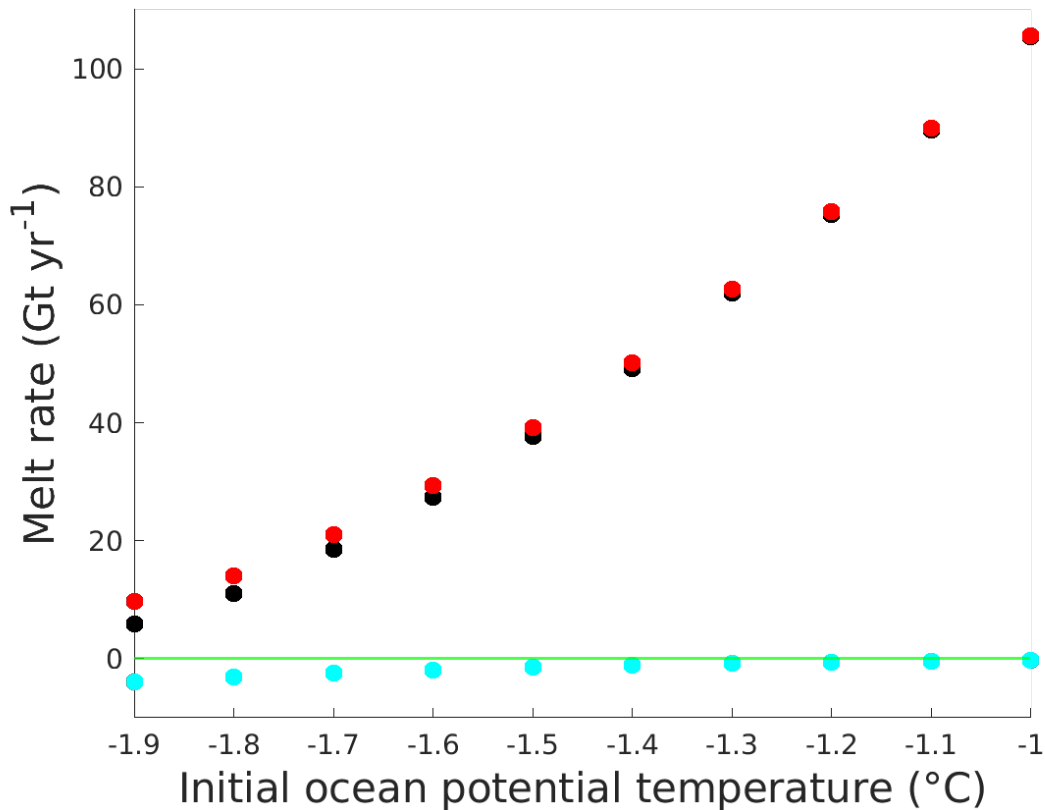


Figure 5.7: Relationship between melt rate and ocean forcing temperature. Black circles show the domain-averaged net melt rate; red circles are melting only, leading to ice loss; cyan circles are freezing only, leading to ice mass gain under LCIS, all shown in units of Gt yr^{-1} . Green line indicates a melt/freeze rate of zero.

The relationship is quadratic because increased meltwater with warmer ocean temperatures accelerates buoyancy-driven circulation, which increases turbulence. As the melt rate is calculated from a product of the ocean temperature and velocity, the increase in both quantities leads to a quadratic response. Holland et al. (2008) similarly found a quadratic relationship between temperature and melt rate using multiple simulations of different idealised ice shelf cavities. Jenkins et al. (2018) discovered a quadratic fit to melt rate data, inferred from observations of the Dotson Ice Shelf in the Amundsen Sea, which varied along with observed changes in ocean temperature over a 16-year period.

5.2.2 Changes to the melt pattern

Temperature changes in simulations presented here were idealised and can therefore only serve as an indication of the magnitude of basal melt rate changes

resulting from alterations in ocean forcing. Greater confidence in changes of the pattern of basal melting across LCIS with rising ocean temperatures results from using the latest, detailed bathymetry. The difference between the standard run melting pattern and that of the warmer cases shows where we would expect to see lowering of the ice shelf if these ocean temperature increases occurred. Values shown in Figure 5.5 are absolute melt rate values for the steady state of each temperature case; figures depicting the differences between the standard run melt pattern and that of the higher temperature runs show the same pattern.

The largest local increases in modelled melt rates occur in the south of LCIS, coinciding with the locations of greatest melting in the standard run: the northern tip of Kenyon Peninsula and surrounding Gipps Ice Rise, as well as along the ice front and the deepest ice at the grounding line. Previous studies which used satellite altimetry data to show surface height changes have reported regions of lowering that do not correspond to many of these locations of increased basal melting. Holland et al. (2015) determined that some of the greatest lowering rates across the ice shelf took place in the north, particularly at Bawden Ice Rise (Figure 5.6a). In their observations of LCIS from satellite data, Shepherd et al. (2003) showed substantial lowering in the north of LCIS and at the southwest grounding line, in Mobiloil Inlet (Figure 5.6b). Adusumilli et al. (2018) reported surface lowering across their observation period of 1994-2016 at the grounding line in the south of LCIS and the ice front in the northeast of LCIS, namely at Bawden Ice Rise (Figure 5.6c). Other studies have also reported that the greatest elevation changes of LCIS have been observed in the north of the ice shelf (Fricker and Padman, 2012; Paolo et al., 2015, 2016), along with concurrent atmospheric warming over the northern Antarctic Peninsula (Vaughan et al., 2003), suggesting that the lowering is more influenced by surface processes than basal processes.

Holland et al. (2015) determined that ice loss, as opposed to surface-forced firn densification, was the dominant contributor to lowering over the southernmost portion of their survey line (Figure 5.6a), implying that changes in basal melting are enhanced in the south compared with the rest of their study area. Combined with model results presented here, it is possible that this signal reflects a local ocean-driven melting increase. The intense basal melting increase at Kenyon Peninsula simulated by the model as ocean temperatures rise is not reflected in any of the lowering patterns shown in Figure 5.6. Further, evidence of basal melt increases close to Bawden Ice Rise in the northeast, where the greatest lowering is measured in these observations, is not seen. Overall, these results indicate that high basal melt rates at the grounding line in Mobiloil Inlet found in the warming

ocean simulations performed here, may have led to the observed lowering in the southwest, but lowering seen elsewhere, particularly in the northeast, likely has an alternative explanation to ocean-driven melting.

Interestingly, despite a far greater modelled absolute increase in the magnitude of basal melting taking place in the southern half of the cavity with warming ocean temperatures, the relative fraction of melt increase across the ice shelf as a whole is greater in the northern half of the cavity. Table 5.1 shows the total ice loss from LCIS, in units of Gt yr^{-1} , and how this mass loss is proportionally split between the northern and southern halves of the ice shelf in each temperature case. The percentage total of ice loss in each half of the model domain shows that in the standard run, the vast majority of ice loss from LCIS is seen in the southern half of the cavity (99%), but this majority decreases substantially to approximately two thirds with ocean temperatures of -1.3°C , with the change in fractional melt distribution slowing considerably with temperatures above -1.6°C . Ice-ocean interactions under LCIS are part of a delicately balanced system and these results indicate that small changes in the north could have a greater effect on the force balance of the ice shelf than in the south.

5.2.3 Bawden Ice Rise

Several previous studies have reported greater elevation changes around Bawden Ice Rise than other regions of the ice shelf (Paolo et al., 2015; Adusumilli et al., 2018). Borstad et al. (2013) reported the ice in contact with Bawden Ice Rise is fractured and noted that weakening of the ice in this region, as a result of fracturing and thinning, could destabilise LCIS. They concluded that Bawden and Gipps ice rises were extremely important pinning points for stability of the ice shelf at the time of their study in 2013. Adusumilli et al. (2018) deduced a highly variable basal melt rate of up to $5 \pm 2 \text{ m yr}^{-1}$ at Bawden Ice Rise. They hypothesized that a decrease in melting in the south of LCIS had slowed the transport of cold meltwater downstream, meaning outflow in the north was less able to prevent warm water flowing in along the northern trough from reaching the ice front.

Modelled melting around Bawden Ice Rise is shown to increase as ocean temperatures rise (Figure 5.5). The increase in melt rate at Bawden Ice Rise is 0.5 m yr^{-1} with just a 0.1°C increase in ocean temperature from the standard run (-1.9°C). This would result in the ice shelf ungrounding from Bawden Ice Rise in ~ 80 years if temperatures were to rise by this amount, assuming all other

Table 5.1: Net ice loss from LCIS resulting from basal melting in each ocean temperature case, including differences between mass changes in the north and south of the model domain.

Temperature (°C)	Domain-averaged (Gt yr ⁻¹)	North (Gt yr ⁻¹)	South (Gt yr ⁻¹)	North (%)	South (%)
-1.9	5.9	0.1	5.8	1	99
-1.8	11.0	1.5	9.5	13	87
-1.7	18.5	3.6	14.9	20	80
-1.6	27.4	7.0	20.4	26	74
-1.5	37.7	10.6	27.1	28	72
-1.4	49.2	14.7	34.5	30	70
-1.3	61.9	18.9	43.0	31	69
-1.2	75.3	23.3	52.0	31	69
-1.1	89.7	28.0	61.7	31	69
-1.0	105.4	33.0	73.4	31	69

processes remain steady. Holland et al. (2015) calculated an ice loss rate across their survey line of 0.3 m yr⁻¹, which they noted would unground Bawden Ice Rise in 130 years. However, their survey line (Figure 5.6a) did not reach Bawden Ice Rise and so this melt rate may not be applicable in the northeast region of LCIS, considering melt rates across the shelf have been shown to be highly spatially variable. Model results are therefore consistent with the measurements of Holland et al. (2015), as they found ice loss dominated the lowering signal in the south of the ice shelf. While results show the increase in basal melting with a warmer ocean is not focused around Bawden Ice Rise, there is nevertheless a melting increase at this location, which is critical in terms of LCIS stability, with a relatively small ocean warming.

It is important to note that the results shown in Figure 5.5 reflect the response to a spatially uniform ocean temperature perturbation. If greater ocean warming had occurred in the northern region of LCIS, the response may be different. If non-uniform warming were to occur, such as greater warming in the northern Weddell Sea, it is difficult to envision how this would affect the spatial distribution of melt rate within the cavity considering the sole inflow region is in the south of LCIS. Even if warmer water in the north of the Weddell Sea were able to travel to the inflow regions, it would still make its way into Mobiloil Inlet first, presumably affecting the melting there, as is the case when the ocean is warmed uniformly. If greater melting in the south of LCIS is a result of heat from warm inflowing water being used up in the south and therefore protecting the north from basal melting, then the same process would happen with non-spatially uniform ocean warming. Future work is needed to run simulations with non-uniform warming

of ocean waters at model boundaries to test this theory. Additionally, including a sea ice component into model simulations would be useful as changes in the salinity field adjacent to the ice shelf are expected to alter the currents entering the cavity, while sea ice simultaneously offers protection from ocean warming by cooling the waters over the continental shelf to the surface freezing point. This would involve modelling a significantly larger domain to capture the relevant sea ice dynamics.

5.3 Freezing changes

Despite large changes in melt rate with increases in ocean temperature forcing, freeze rates across the ice shelf show much smaller changes as temperatures are raised (Figure 5.7). In simulations with an ocean temperature of -1.3°C and above, there is a slight downturn in freezing but even at -1.0°C , the domain-averaged freeze rate is still greater than half the magnitude of freezing in the standard run (-1.9°C).

Figure 5.8 shows that when ocean temperatures are raised, freezing gradually reduces in a spatially uniform manner across the ice shelf, with the notable exception of the freezing patch in Hess Inlet. This inlet has a large area of shallow ice as a result of the shape of the promontories on either side of it (Figure 5.9). Consequently, a large volume of buoyant meltwater can become trapped under the ice and supercool, refreezing to the ice base at this location. The rate of marine ice accretion in Hess Inlet is maintained in warmer cavities as a result of persistent negative thermal driving at the ice base here (Figure 5.10).

When Holland et al. (2009) perturbed ocean conditions in their model to raise temperatures to -1.4°C from -1.9°C , freezing halted everywhere except at Churchill Peninsula. With the same increase in ocean temperature, results from the current study show freezing continues at all peninsulas. Their model contained a relatively sophisticated frazil ice model, but lacked any representation of barotropic flow, which cools the cavity by recirculating meltwater, or tides, which have been found to increase modelled freeze rates (Makinson et al., 2011; Mueller et al., 2018). This is further evidence that the mixing induced by the model bathymetry and tidal forcing is necessary to facilitate internal feedbacks within the model cavity, which provide some protection from ocean warming at the ice base.

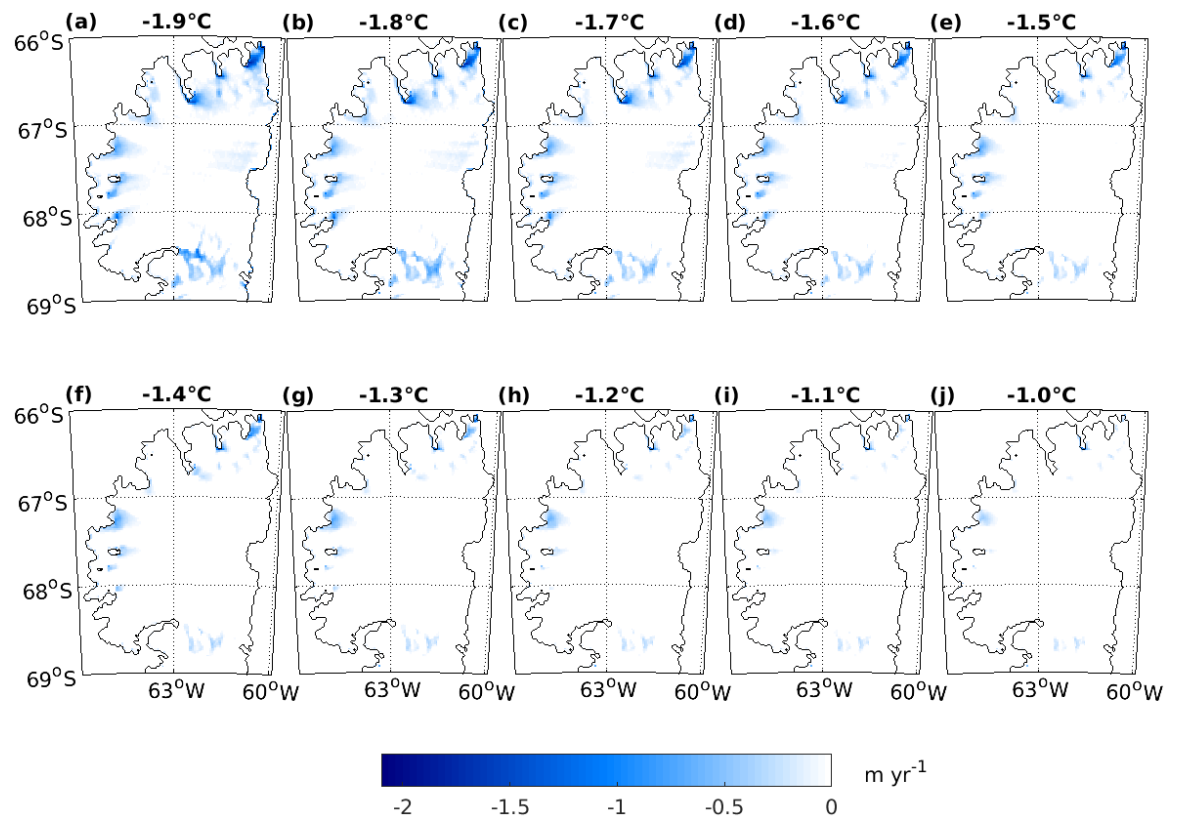


Figure 5.8: Locations and rates of refreezing to the base of LCIS resulting from ten different temperature sensitivity simulations.

5.4 Marine ice changes and implications for the stability of LCIS

Although the pattern of basal melting and freezing remains constant with changing ocean temperatures, the relationship between rising ocean temperatures and the stability of LCIS is not a simple one because of the presence of marine ice at the base of the ice shelf. Brittle, meteoric ice allows rifts to propagate through the shelf as a mechanism to relieve stress, leading to fracture and potential subsequent retreat. Marine ice is thought to impose a stabilising effect on ice shelves because it has a much higher temperature than meteoric ice and is therefore more viscous, meaning it can accommodate strain placed on the ice by deforming in response to such a stress, rather than failing (Holland et al., 2009; Jansen et al., 2015). Jansen et al. (2010) noted that marine ice appears to have stabilised the ice shelf because locations of fracture predicted by their ice model, which did not include a marine ice component, cannot be seen in visible imagery. Therefore, they concluded that marine ice must be present on the ice shelf and has prevented these projected fissures. Further to this, the rift which calved iceberg

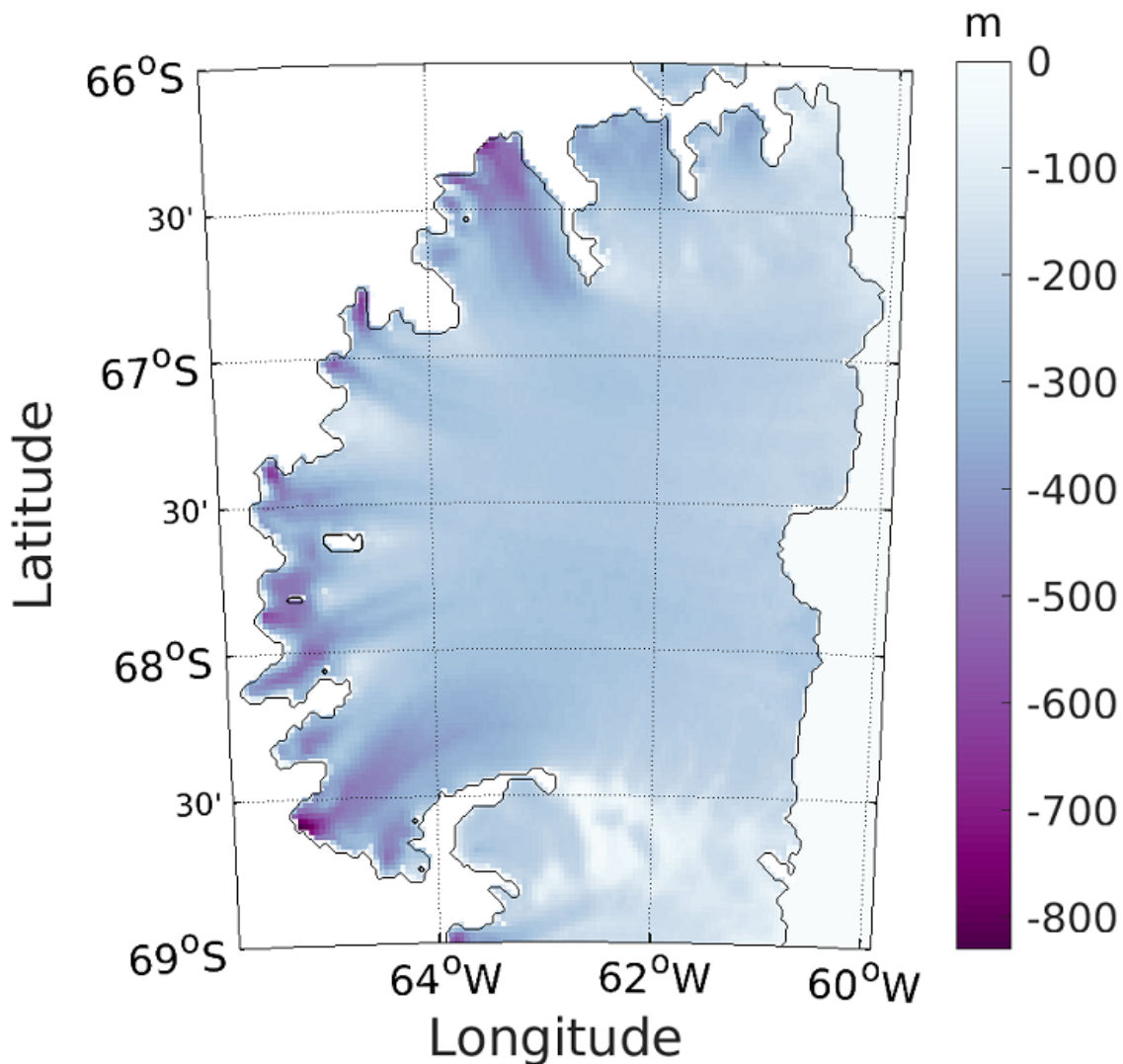


Figure 5.9: Depth of the ice draft below the sea surface, comprised of both meteoric and marine ice.

A68 slowed its propagation whenever its tip reached a band of proposed marine ice (Jansen et al., 2015). Craven et al. (2009) suggested that the porosity of lower layers of marine ice in direct contact with the ocean, compared with meteoric ice, means marine ice may be more sensitive to changes in ocean forcing.

It has been suggested that if LCIS did not have its marine ice, the stress field of the ice shelf would resemble that of Larsen B Ice Shelf just prior to its collapse (Jansen et al., 2010; Kulesa et al., 2014). Therefore, if the marine ice beneath LCIS were to weaken, or erode entirely, the dynamics of the ice shelf would be altered. A reduction in the thickness or extent of bands of marine ice beneath LCIS, possibly resulting from a change in ocean forcing, could have implications for the stability of this ice shelf.

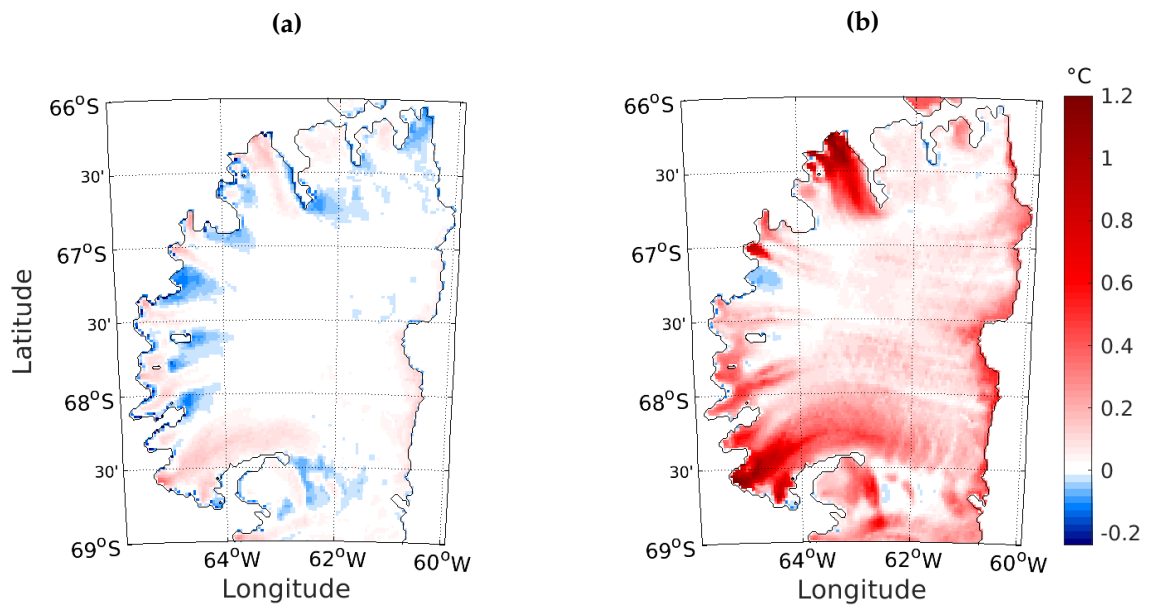


Figure 5.10: Thermal driving, defined as the difference between potential temperature in the ice-ocean boundary layer and that of the potential freezing point at the ice base pressure, in the standard run (-1.9°C) (a) and the warmest run (-1.0°C) (b).

To illustrate the influence of ocean conditions on marine ice, the steady state marine ice thickness produced by the melting and freezing field for each ocean temperature simulation are presented here. Figure 5.11 shows how much marine ice would have accreted and propagated under the ice shelf if these steady state melt and freeze rates were to persist for 500 years.¹ The differences between each temperature case give an indication of changes in thickness and extent which would result from such a change in ocean forcing. Without an ice model, these figures provide only a suggestion of the consequences of the imposed model changes, allowing speculation about the marine ice changes that may occur beneath LCIS and what implications this might have for the future stability of the ice shelf.

5.4.1 Thickness and extent reductions

With higher ocean temperatures, steady state freezing of ocean water onto the base of LCIS reduces near almost all peninsulas and islands at the grounding line. As a consequence, marine ice is progressively thinned and reduced in extent. Increases in melt rate across the domain also reduce the size and scale of marine ice bands that had formed and advected downstream. However, even with a temperature

¹The code to calculate and produce the grids of marine ice thicknesses is not my work. This code was written by Paul Holland.

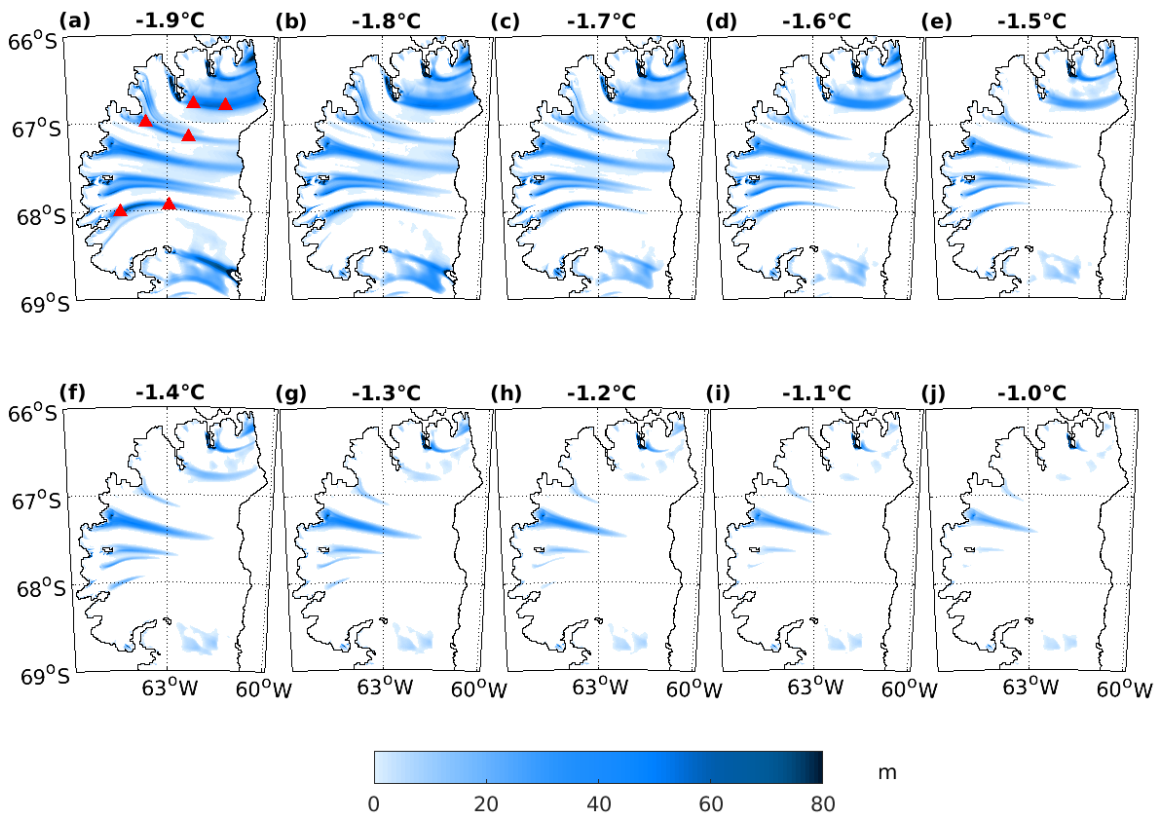


Figure 5.11: Marine ice thickness after 500 years of advecting steady state melt/freeze rates in each temperature case. Red triangles indicate locations of thickness calculations detailed in Table 5.2.

increase of 0.7°C from the standard run conditions (-1.9°C), marine ice still forms in almost all the same places as for the standard run, though with the freezing rate significantly reduced in notable regions such as Joerg and Cole Peninsulas, which generate marine bands that have been identified as particularly important for LCIS in terms of curtailing rift propagation (McGrath et al., 2014).

Table 5.2 shows the reductions in thickness and extent that might be expected with changing ocean conditions. Estimates of the thicknesses of the Joerg, Cole and Churchill marine ice bands have been published and those of Cole and Churchill marine bands agree well with model results from the standard run (-1.9°C), but thickness results of the Joerg marine band are too low (see Section 3.4). McGrath et al. (2014) measured a thickness of greater than 45 m of marine ice in the Churchill Peninsula marine band, where a rift from within Adie Inlet (see Figure 0.1 for location) terminates. The standard run produced marine ice around this location of 45-54 m, showing good agreement with observed values (Table 5.2). With an ocean temperature of -1.3°C , marine ice in this location has almost entirely melted away, which could have severe implications for the stability

of LCIS.

The marine ice band initiated from the tip of Joerg Peninsula appears to have prevented several rifts propagating across the ice shelf from the south of LCIS and Borstad et al. (2017) speculated that the stability of LCIS hinges solely on this marine band. Marine ice stops forming at Joerg Peninsula when ocean temperatures reach -1.1°C , but with a more modest ocean temperature increase to -1.5°C , reduced freezing at Joerg Peninsula and enhanced melting downstream leads to a significant reduction in the extent of its marine ice band, which would still greatly affect ice shelf stability. With marine ice no longer extending beyond the tip of Kenyon Peninsula, rifts further west than the one that broke through and calved A68, seen in the south of LCIS, may be permitted to propagate into the centre of LCIS and trigger significant ice shelf retreat. Therefore, marine ice downstream of the tip of Kenyon Peninsula is critical to maintaining the present stability of LCIS. Higher stresses on rifts closer to Kenyon Peninsula were found by Borstad et al. (2017) than on the rift which broke through the Joerg Peninsula marine ice band in 2013 (Jansen et al., 2015) and eventually calved A68, suggesting that marine ice further downstream has weakened, allowing the crack to get through the ice at this position. However, the model provides no evidence to suggest that ocean-driven melting has increased as the change in melt pattern does not match observations of lowering, indicating that marine ice has not thinned under LCIS.

While the majority of marine ice bands almost entirely cease production at -1.2°C , the marine band emanating from Hess Inlet still produces a significant band which propagates to the middle of the ice shelf even in the warmest case presented here (-1.0°C), as a result of persistent high freezing rates being maintained compared with the rest of the grounding line (Figure 5.8). Despite the sustained accumulation of marine ice close to the grounding line in this region, increased melting further downstream means that this and all other marine ice bands south of 67°S do not reach the present day calving front with an ocean temperature forcing of -1.5°C and above. This could potentially lead to widespread destabilisation because the removal of certain portions of ice at the calving front have been shown to result in unstable geometries, leading to a shelf-wide collapse, as was thought to be the case with the collapse of Larsen B Ice Shelf in 2002 (Doake et al., 1998).

Jansen et al. (2010) hypothesized that ice flow units in the mid-shelf region may accelerate if marine ice at Cole and Joerg peninsulas erodes. Observations of the acceleration of ice flow in the north, where the greatest thinning has

Table 5.2: Thickness of three important marine ice bands close to the region of initial refreezing (GL) and further downstream (MS), calculated from advection of steady state melt/freeze rates from each of the ten temperature simulations. Red triangles in Figure 5.11a show locations of calculated thicknesses. Abbreviations: GL is grounding line; MS is mid-shelf.

Temperature (°C)	Churchill GL (m)	Churchill MS (m)	Cole GL (m)	Cole MS (m)	Joerg GL (m)	Joerg MS (m)
-1.9	45	54	73	27	79	37
-1.8	44	49	54	26	71	32
-1.7	41	43	48	19	62	24
-1.6	32	35	39	10	47	10
-1.5	19	23	30	2	35	0
-1.4	6	10	21	0	23	0
-1.3	0	0	16	0	11	0
-1.2	0	0	11	0	2	0
-1.1	0	0	8	0	0	0
-1.0	0	0	6	0	0	0

been observed, have been attributed to the possible weakening of marine ice (Khazendar et al., 2011). On the other hand, it has been suggested that marine ice in the north may even stabilise LCIS in the event of an ungrounding from Bawden Ice Rise (Borstad et al., 2013). Model results show that marine bands in the very north of the cavity, where the greatest refreezing rates are found in the standard run, persist in warmer temperatures. While basal processes may cause southward-focused marine ice weakening in the event of potential future ocean warming, the north of LCIS may be less vulnerable to fracture as a result of more resilient marine ice.

5.4.2 Current versus historical marine ice weakening

The standard run is close to what is believed to be the current conditions in the LCIS cavity and is forced by the coldest possible waters on the continental shelf. Any warming that has occurred in the LCIS cavity over the observed lowering period would affect marine ice accumulation close to the the grounding line and melting of existing marine ice across the ice shelf. Therefore, any such warming may not affect the ice shelf stability for several centuries as thinner marine ice advects from the grounding line to the crucial mid-shelf region (e.g. seaward of Kenyon Peninsula for the Joerg marine band), if reduced accumulation is the main mechanism for marine ice retreat.

For many decades, the Joerg Peninsula marine ice band restrained the rift that

subsequently calved iceberg A68 (Jansen et al., 2015). The eventual propagation of that rift through the marine ice may be evidence of a gradual weakening of the marine band, or may simply reflect a change in the stresses acting on the rift. Present day failure of marine ice at this location could result from ocean conditions at the grounding line changing/warming approximately 250-300 years ago. This, in turn, implies that the grounding line portion of the ice shelf may be out of steady state with ice closer to the calving front. If the marine ice near the tip of Kenyon Peninsula has weakened, that could either reflect a decrease in upstream freezing that occurred several centuries ago, or a more recent increase in melting that thins the marine ice more rapidly as it traverses the ice shelf.

Figure 5.8 shows that freezing across LCIS is robust to ocean forcing changes as refreezing still takes place downstream of all peninsulas and islands even when temperatures are raised to -1.3°C , although in much smaller magnitudes than in the standard run at -1.9°C . This suggests that thinning marine ice bands would be most affected by the great increase in melt rate across the domain if the ocean warms. Figure 5.11 shows that quite extreme changes in ocean forcing are required to significantly reduce the extent of marine ice bands beneath LCIS, leaving the ice shelf vulnerable to rift propagation and calving, which may result in collapse.

5.5 Is ocean warming responsible for the observed changes?

Historical changes in ocean temperature beneath LCIS are unknown. Warming of $0.013 \pm 0.007^{\circ}\text{C yr}^{-1}$ in the Weddell Sea has been recorded over three decades, up to the end of the 20th century (Robertson et al., 2002), but no measurements closer to the ice shelf have been repeated. The only oceanographic section along the southern ice front shows warm waters of $\sim -1.4^{\circ}\text{C}$ throughout the water column during the austral summer of 1992/3 (Bathmann et al., 1994). These recorded temperatures were from a single point in time, and cruises that have attempted to re-sample these waters have failed to penetrate thick sea ice and reach the area in front of the ice shelf. It is not known if this was a remarkable year in terms of deeper ocean temperatures on the continental shelf.

Similarly warm waters have since been observed at the northern ice front (Nicholls et al., 2004). Despite this, Nicholls et al. (2004) and Nicholls et al. (2012) determined that no waters warmer than -1.9°C entered the cavity during their

sampling periods; they argued that water loses its sensible heat while crossing the continental shelf and was therefore cooled to the freezing temperature before reaching the ice front every winter, as evidenced by sea ice formation. They also noted that water at -1.4°C had access to the ice front but determined from outflow in the north that this warm water was not the source of the melting, indicating it did not enter the cavity.

The water sampled by Nicholls et al. (2004) and Nicholls et al. (2012) in austral summertime may have entered the cavity in winter and taken several months, or even years, to travel to the locations of the observation sites and the outflow region sampled in the north, explaining the low source temperatures. The distance from the ice front where water enters the cavity to the southern observation site is approximately 115 km and Figure 5.3 shows that the average speed of this inflow upon entry is $\sim 1\text{-}2\text{ cm s}^{-1}$. Given these constraints, inflowing parcels of water would take two-four months to travel directly to the southern observation site. In fact, the distance travelled by the water to get the mooring site is even greater as the path is not direct, so these estimates are likely too low.

It is therefore possible that warmer waters are entering the cavity at certain times of the year and interacting with the ice shelf at later periods. This could suggest that water sampled at the southern observation site in summer by Nicholls et al. (2012) had in fact entered the cavity nearer wintertime. It is also possible that the outflow sampled by Nicholls et al. (2004) resulted from a different, colder water source entering the cavity during austral winter and exiting the cavity after years of residence within it. Future work to add dye tracers to the model and calculate the residence time of water in the LCIS cavity would indicate what time of year the water sampled in the north by Nicholls et al. (2004) might have entered the cavity.

Any changes to the ocean forcing of the LCIS cavity would have to have originated from either an increase in modified Warm Deep Water making its way onto the continental shelf, as a result of circulation changes in the Weddell Sea, or a decline in sea ice production over the continental shelf, which would alter the primary water source flushing of the cavity as it crosses the continental shelf (Holland et al., 2009). Nicholls et al. (2012) pointed out that even if the temperature of water entering the cavity is not increasing, as they found evidence to suggest, then flushing of the cavity resulting from a changing salinity field across the continental shelf could be increasing. Extra water flushing the cavity would lead to greater velocities and provide more heat, both of which would increase melt rates. However, a decrease in sea ice production over the continental

shelf might also lead to a greater loss of heat from modified Warm Deep Water crossing the shelf before reaching the cavity, therefore mitigating some of the effects of an increase in flushing. Observations of sea ice in the northern Weddell Sea have shown a slight decline between 1979-2006 (Hellmer et al., 2011; Jullion et al., 2013). Overall, the evidence suggests that a change in ocean temperature forcing large enough to explain the surface lowering over the last few decades has not taken place.

5.6 Concluding remarks

Determining if changing ocean conditions are responsible for the lowering of LCIS or weakening of marine ice underneath the ice shelf is not possible as a result of the lack of historical observations (Borstad et al., 2017). However, results presented here show the sensitivity of LCIS to certain levels of change within the ocean, providing an indication of the great impact ocean temperature increases might lead to in terms of ice mass loss and marine ice decline at the base of LCIS, and any subsequent instability.

These results, combined with reports of atmospheric changes over LCIS (Vaughan et al., 2003) and remote sensing observations of the pattern of lowering (Shepherd et al., 2003; Holland et al., 2015; Adusumilli et al., 2018), point to surface processes being a more plausible explanation for the height changes than oceanic causes. This is a significant step forward in our understanding of the changes seen on LCIS. Speculation about the source of the surface lowering is currently ongoing and this important result strongly indicates that the signal most likely has an atmospheric, as opposed to oceanic, origin. However, it is possible that some local ocean-driven lowering has taken place in the south of LCIS, based on much higher melt rates in the south with warmer ocean temperatures. Ocean warming simulations performed here indicate that a temperature increase of 0.2°C-0.3°C would explain the observed ice loss. However, as melt rates in the standard run were found to be too high at the location of the southern mooring site, it is likely that this estimate is also too high and a more modest ocean temperature increase would result in the overall amount of lowering seen.

Refreezing of meltwater to the underside of LCIS has been shown to be extremely robust to even radical changes in ocean temperature forcing. The average melt rate in the cavity is amplified by a factor of eight with an increase in ocean temperature of 0.9°C (the temperature difference between the coldest and

warmest cases modelled here), yet the average freeze rate in the cavity decreased by less than a factor of two. Proportionally speaking, changes seen in the thickness and extent of modelled marine ice are more likely be a consequence of higher melt rates across the ice shelf in the warmer cases than lower freeze rates. However, as frazil ice is not represented in the model, freeze rates and subsequent estimates of marine ice thickness should be considered with caution.

Results presented here show that the expected overall pattern of ice loss from LCIS in the event of a change in ocean temperature does not match observations of surface lowering on the ice shelf. Therefore, a change in ocean forcing large enough to weaken the marine ice at the base of LCIS does not appear to have taken place. Instead, these results indicate a strong sensitivity of marine ice distribution to any potential future warming LCIS may experience.

Previous studies have noted the non-linear relationship between ocean temperature and the stability of LCIS, as a result of the presence of marine ice, and remarked that the stability imparted on the ice shelf through its marine ice leaves LCIS particularly vulnerable to changes in ocean forcing (Holland et al., 2009; Khazendar et al., 2011; McGrath et al., 2014). Results presented here reinforce this message as changing ocean forcing within the cavity could destabilise LCIS through weakening of crucial marine ice bands. In particular, an ocean temperature increase to -1.5°C has been shown to cause retreat of the important Joerg Peninsula marine ice band beyond the point where the rift that led to the 2017 calving event broke through. It is important to note that without an ice model to confirm these marine ice results or repeated measurements of marine ice beneath LCIS to observe any reduction in thickness or extent of particular marine bands, marine ice results presented here are only an indication of the potential consequences of warmer ocean conditions. However, results discovered through these temperature sensitivity tests, detailing the vulnerability of the Joerg Peninsula marine ice band which has been identified as critical to curtailing rift propagation across the ice shelf, represent a key advancement in our knowledge of the future stability of LCIS.

Chapter 6

Conclusions

Changes seen in recent decades on the Antarctic Peninsula have prompted questions about the ocean conditions within the LCIS cavity and the stability of the ice shelf. This thesis was motivated by a need to understand whether satellite-observed surface lowering of the ice shelf (Shepherd et al., 2003; Fricker and Padman, 2012; Pritchard et al., 2012; Holland et al., 2015; Paolo et al., 2015; Adusumilli et al., 2018) was triggered primarily by an increase in oceanic basal melting, and whether ocean-driven changes may have left LCIS in danger of collapse. Results from a high resolution numerical ocean model of the LCIS cavity, with a new bathymetry constructed entirely from an interpolation of direct seismic measurements taken through the ice shelf (Brisbourne et al., 2020), have been presented here and provide a new assessment of melting and freezing at the ice base, as well as a better understanding of ocean processes beneath the ice.

Evaluation of the model's performance has been carried out in Chapter 3 by comparing output from the standard run, a simulation set up with initial and boundary conditions believed to be close to the conditions currently found around the Antarctic Peninsula using available observations from near to and within the cavity. In particular, observations from instruments moored underneath the ice shelf (Nicholls et al., 2012; Davis and Nicholls, 2019a), while only two points beneath a large ice shelf, provided a novel test of the new model, something previous models of LCIS have not had.

6.1 Importance of bathymetry for circulation and melt rate

In order to effectively answer the driving questions behind this research, some ambitions of this project included determining the circulation in the LCIS cavity and learning what processes control the melt rate of the ice shelf. The new bathymetry has proven to have a great effect on the flow throughout the cavity, with the newly discovered extent and depth of the southern seabed trough playing a large role in guiding both inflow to the grounding line at Mobiloil Inlet and the initial direction of the meltwater plume after leaving Mobiloil Inlet and travelling across the cavity. Two separate components of circulation are seen that each mostly follow contours of water column thickness, which are primarily influenced by bathymetry. Chapter 3 demonstrated that key features of the cavity circulation, namely inflow and outflow, have been captured by the model at the correct locations, as inferred from observations (Nicholls et al., 2004, 2012).

The sole direct observation of melt rate under LCIS, recorded at the southern mooring site, shows a smaller melt rate, in line with slower flow speeds under the ice, than that modelled at this location. This could be a result of inaccurate model bathymetry driving faster flow in this location. Modelled melt rates are calculated using several melting parameters, and there is very limited current knowledge to inform the choices of these parameters. The drag coefficient is the only measured parameter under LCIS and was determined at only one point beneath the ice base. This parameter may vary at different locations under LCIS.

Consequently, there is greater confidence in the melt pattern than the melt rate. Melting across the domain was found to be greater in the south of LCIS, with the highest steady state melt rates in the model domain seen just north of Kenyon Peninsula, where the southern trough directs fast, inflowing water towards the grounding line. This melt pattern contrasts with earlier simulations that used a different bathymetry (Mueller et al., 2012). Chapter 4 showed the effect different model cavity geometries have on both the ocean circulation and subsequent melt/freeze pattern, which demonstrates the importance of using an accurate model bathymetry to simulate these processes correctly. Locations of enhanced melting in the model have been identified as coinciding with regions of strong currents in areas of the cavity where the water column thickness shallows.

The new bathymetry created for this modelling study is a notable contribution to this field of research, informing the heretofore least known aspect of cavity

geometry. In addition to its impact on the results of this study, namely the influence over ocean circulation within the cavity and the melt/freeze pattern of the ice shelf, the bathymetry grid is a product that has been and will be utilised in further studies of LCIS. This bathymetry has aided the planning of observational surveys of the cavity by Autonomous Underwater Vehicles and can be used to improve larger ocean models of Antarctica such as CATS, where bathymetry beneath ice shelves requires improvement to yield more accurate circulation.

6.2 Atmospheric or oceanic drivers of surface lowering

Establishing how much of the remotely-observed surface elevation lowering can be attributed to oceanic basal melting is a key question. As a result of the floating nature of the ice shelf, the observed rate of surface lowering resulting from oceanic melting means an ice mass loss rate ten times larger would have to take place at the base of the ice shelf. Contributions to lowering at the same rate from surface process indicate a much smaller change to the overall thickness of the ice, but such surface processes can lead to greater dangers to ice shelf stability, such as melt ponding (Scambos et al., 2000; Luckman et al., 2014). Identifying the source of the lowering signal therefore aids future projections of the potential timescale for collapse and resultant sea level rise, which are an important contribution to Intergovernmental Panel on Climate Change reports and worldwide flood-risk planning.

As records from this region of the Antarctic are historically rare, the framework of this research was not to force the model with realistic boundary conditions to produce an accurate hindcast in order to answer this question, but to show the vulnerability of LCIS to ocean warming by determining the ice shelf's response to a hypothetical, uniform ocean warming. Modelling LCIS' response to higher temperatures, detailed in Chapter 5, demonstrates the changes we might expect to see should the ice shelf be subjected to such a change in ocean forcing over the continental shelf. While the pattern of basal melting remains steady when initial and boundary condition temperatures are raised, the melt rate increases significantly. Overall, greater increases in basal melting with uniform ocean warming take place in the south of the ice shelf, suggesting periods of lowering in the north, observed by satellites (Shepherd et al., 2003; Fricker and Padman, 2012; Holland et al., 2015; Adusumilli et al., 2018), are not the result of basal melting

increases in response to a change in ocean forcing, but instead result from surface processes. However, the possibility that differences between modelled melting and observed lowering patterns result from spatially non-uniform ocean changes cannot be precluded.

Holland et al. (2015) found ice loss alone, which they defined as resulting from either increased basal melting or ice divergence, accounted for the lowering they observed between 1994-2011 over the parts of their survey nearest the grounding line, whereas in the mid-shelf region, they determined that both air and ice loss are responsible for the surface height changes. Air loss results from surface melting and firn compaction. Despite the differing patterns of satellite-derived lowering and modelled basal melting, it is possible that some of the large modelled melting changes seen in this study, in the south of LCIS, could account for part of the observed lowering, while surface processes are responsible for lowering in other regions across the ice shelf.

Nicholls et al. (2012) concluded that no water at temperatures higher than the surface freezing point was entering the cavity and therefore their measured melt rate is assumed to be the steady state melt rate at the location of the southern drill site. The surface freezing point is the coldest temperature at which water could be entering the cavity to interact with the ice, meaning that the cavity cannot have been in a state of warming at the time of these measurements. Any variability in ocean temperature over time that might have taken place has therefore not been captured by Nicholls et al. (2012). While it is possible that basal melting may simply not have been increasing at the time they took their measurements in December 2011, or during the year-long period of observations reported from the mooring data since (Davis and Nicholls, 2019a), combined with results presented here, these observations suggest that an increase in basal melting is not responsible for the observed lowering of LCIS. Within the context of observations of cold recent conditions in the cavity (Nicholls et al., 2012), and warm historical conditions offshore (Bathmann et al., 1994; Nicholls et al., 2004), it is hard to envision how substantial ocean warming could have occurred in recent decades to explain the recent ice mass loss.

Knowledge gained from this study, in conjunction with previous research, presents strong evidence that changes in ocean forcing are not responsible for the surface lowering. This is a significant contribution to this field of research because LCIS is a remote area which is difficult to access in order to take direct measurements. Tools such as the model developed for this project and described in this thesis are therefore crucial to aiding and developing our current

understanding of the ocean processes beneath LCIS.

6.3 Threat to the stability of LCIS imposed by the retreat of marine ice

An increase in ice discharge from the grounded ice sheet, resulting from ice shelf thinning or collapse, can affect global sea level rise on decadal time scales (Schannwell et al., 2018), as well as affecting the formation of water masses and dynamics of ocean currents around Antarctica (Jullion et al., 2013; Fogwill et al., 2015). Given the rapid deterioration of ice shelves on the northern Antarctic Peninsula over the course of the past few decades (Vaughan and Doake, 1996; Skvarca et al., 1999) and reports of the changing climate in this region (Vaughan et al., 2003; Khazendar et al., 2011; Turner et al., 2016), there is also a need to understand if there is a link between Antarctic Peninsula warming and ice shelf collapse. While this study cannot answer that question directly, it has helped to illuminate how vulnerable LCIS is to collapse as a result of changes in marine ice at the base of the ice shelf.

Given the findings presented here and the lack of observational evidence to suggest that ocean warming and a subsequent increase in melting of ice at the base of LCIS has occurred, save for perhaps some local basal melting in the south of LCIS, the melting of existing marine ice under LCIS is also unlikely to have taken place. However, the changes in marine ice distribution presented here as a result of perturbations in ocean forcing provide an indication of the consequences any potential future ocean warming may have on the stability of LCIS, by indirectly contributing to fracture of the ice shelf.

Refreezing of marine ice onto the base of LCIS has been simulated downflow of promontories, in agreement with observations (Holland et al., 2009). Warming experiments performed here revealed changes in ocean freezing at the base of LCIS, and the resulting changes in marine ice thicknesses were predicted by a steady state advection calculation. Marine ice bands terminate before the ice front in response to ocean warming, suggesting a general retreat of LCIS would occur if pivotal portions of the ice front were removed through calving. Present day marine ice thinning near the ice front could either result from a historical reduction in freezing at the grounding line or a recent increase in melting closer to the calving front, or a combination of both processes. Any reduction in accumulation of marine ice at the grounding line which might weaken the ice shelf

would take several centuries to advect to the more vulnerable ice front region. This demonstrates the uncertainty in the timescales needed for ocean changes to affect LCIS stability. The effect of a change in freezing on marine ice would take centuries to propagate through the ice shelf, while a change in melting could thin existing marine ice bands rapidly. One important implication of these results is the centuries-long record of ocean melt/freeze and ice flow conditions that the marine ice bands possess. The marine ice we observe today is the integrated result of many centuries of such changes.

Results presented here of advected marine ice bands show retreat of the extent of marine ice away from the calving front when ocean temperatures are raised, whereas simulated refreezing close to the grounding line, while decreasing in magnitude, showed greater resilience. Some marine ice accumulation is maintained even with substantial increases in ocean temperature. In the framework of this modelling study, it has been shown that small changes in ocean forcing, most likely just 0.1°C-0.2°C, would have a significant effect on the melting of marine ice in key regions, presumably leading to ice shelf instability if the ocean warming were to occur. In particular, a reduction in the extent of the marine ice band emanating from Joerg Peninsula with small increases in ocean temperature is found. The calving of iceberg A68 indicates a failure of marine ice may have already occurred; the rift that generated this iceberg broke through the Joerg Peninsula marine band relatively close to the ice front (Jansen et al., 2015; Hogg and Gudmundsson, 2017), which does not preclude the possibility that marine ice in this area has weakened, perhaps as a result of changes in ocean forcing that have not been simulated in this thesis.

Our knowledge of the history of LCIS marine ice is extremely limited. Although the current extent of marine ice bands can be inferred from missing radar signal returns (Holland et al., 2009) or surface features seen in visible imagery, such as rift arrest seen downstream of Cole and Joerg peninsulas (Jansen et al., 2010), our knowledge of past or current marine band thicknesses is lacking as a result of the paucity of direct observations (Jansen et al., 2013; McGrath et al., 2014). This means it is impossible to tell whether any ocean forcing changes that may have occurred in the past and/or more recently have affected the marine ice at the base of LCIS. However, one thing that has been learned from these idealised simulations is that substantial retreat of marine ice at critical regions is seen with even small changes in ocean forcing.

If uniform warming of the ocean were to occur, as has been modelled here, changes in the thickness and extent of marine ice beneath LCIS could lead

to fracture and widespread destabilisation. A significant retreat of the Joerg Peninsula marine ice band with an ocean temperature forcing of -1.5°C was found. This important result, combined with previous knowledge that marine ice is understood to curtail rift propagation, implies LCIS would experience significant instability if ocean temperatures were to increase by this amount in the future. This information has a substantial impact on our knowledge of the future stability of LCIS. This result also has implications for other cold-water ice shelves around the continent, which are equally susceptible to destabilisation resulting from a reduction in the thickness or extent of marine ice bands as the ocean warms. Marine ice weakening under the Amery or Filchner-Ronne ice shelves may decouple adjacent ice flow units with different velocities, joining an ice shelf from different inland glaciers (Grosfeld et al., 1998; Oerter et al., 1992; Craven et al., 2009).

6.4 Future work

This idealised modelling study has yielded important results about two dangers to the stability of LCIS. Advances in knowledge, with respect to the surface lowering of LCIS and the extent of marine ice beneath the ice shelf, will be useful for making future predictions about potential collapse, as well as demonstrating areas of research to focus observation and modelling efforts on.

Future work is needed to conduct more seismic measurements to further constrain the interpolation of the seabed beneath the ice shelf, which will ensure ocean circulation is captured in models correctly and will allow a more accurate prediction of patterns of basal melting and freezing. Further to this, additional observations of the ocean beneath the ice base, which are crucial to our understanding of ocean processes in the cavity, are required to more substantially validate ocean models of LCIS. A greater abundance of long-term measurements from moorings beneath the ice shelf would be invaluable to further constrain properties such as ocean velocities and melt rates and provide more rigorous testing of model output in future.

This study has also highlighted a need for sampling of the marine ice in LCIS to determine how dominant the basally-accreted ice examined here is across the ice shelf. Two other mechanisms of marine ice accumulation have been identified (see Section 1.7) that have not been investigated here. Determining the fraction of LCIS' marine ice that is basally-accreted during the refreezing of meltwater to

the base of the ice shelf would indicate how much weight the warnings about marine ice reduction delivered here should be given when considering future ocean warming.

The development of this model will be a useful tool which future studies of LCIS could benefit from. Further simulations forced with non-uniform ocean warming and changes in salinity have been identified as useful next steps to further scrutinise fluctuations to the flushing of the cavity, and the subsequent effects on ocean circulation and the pattern of basal melting found here. As the model is idealised, certain processes which are fundamental to the ocean dynamics in and around the LCIS cavity, such as a seasonal cycle or sea ice, were not necessary to address the aims of this research. These limitations could be managed in future by including such extra components to fully quantify specific processes that may require more realistic forcing. With these additions, simulations might better inform the answers to key questions about the current state and future projections of LCIS. In addition, the model could be coupled to an atmospheric or ice model to produce more robust evaluations of the the surface lowering and marine ice retreat discussed here. Coupling of ocean and ice sheet models (including a marine ice component) would be invaluable to our understanding of changes in melt/freeze patterns and marine ice distribution at the base of the ice shelf, and ultimately, the implications for the stability of LCIS in response to changes in ocean forcing.

6.5 Summary

This research has resulted in two valuable outcomes which contribute to our knowledge of ocean control of the current state and future stability projections of LCIS. Firstly, ocean forcing sensitivity tests, performed with a high resolution model of the ice shelf cavity, indicate that an increase in ocean-driven melting would lead to a pattern of greater melting under the south of the ice shelf rather than the north. As the lowering of LCIS has been measured using altimetry and found to be greater in the north, this suggests that oceanic basal melting has not led to the observed changes and that the lowering results from a predominantly atmospheric-based signal. The second outcome concerns the future stability of LCIS if the ocean were to undergo any warming over the continental shelf surrounding the cavity. Marine ice, thought to be critical to the stability of the ice shelf, is seen to undergo substantial retreat in a warmer modelled ocean. If ocean

melting of established marine ice close to the ice front occurs, this could rapidly have significant implications for the future stability of LCIS.

Appendix A

Model input parameters

Table A.1: Description of model parameters and values used in the ‘standard run’.

Parameter	Value	Units	Description
$T_{initial}$	-1.9	°C	Initial and boundary condition potential temperature
$S_{initial}$	34.5	psu	Initial and boundary condition practical salinity
Δt	60	seconds	Timestep
$viscAh$	50	$\text{m}^2 \text{s}^{-1}$	Horizontal eddy viscosity/friction dissipation coefficient
$viscAr$	1×10^{-3}	$\text{m}^2 \text{s}^{-1}$	Vertical eddy viscosity/friction dissipation coefficient
$diffKhT$	10	$\text{m}^2 \text{s}^{-1}$	Horizontal diffusion of heat
$diffKrT$	1×10^{-4}	$\text{m}^2 \text{s}^{-1}$	Vertical diffusion of heat
$diffKhS$	10	$\text{m}^2 \text{s}^{-1}$	Horizontal diffusion of salt
$diffKrS$	1×10^{-4}	$\text{m}^2 \text{s}^{-1}$	Vertical diffusion of salt

Table A.1 continued from previous page

Parameter	Value	Units	Description
$t\alpha$	3.9×10^{-5}	$^{\circ}\text{C}^{-1}$	Thermal expansion coefficient
$s\beta$	7.41×10^{-4}	psu^{-1}	Haline contraction coefficient
f	-1.4×10^{-4}	s^{-1}	Coriolis parameter
g	9.81	m s^{-2}	Acceleration due to gravity
$\rho_{initial,o}$	1030	kg m^{-3}	Initial ocean density
$C_{p,o}$	3974	$\text{J kg}^{-1} \text{K}^{-1}$	Specific heat capacity of ocean water
$bottomDragQuadratic$	2.5×10^{-3}		Drag coefficient for seabed floor
$hFacMin$	0.3		Minimum fixed partial cell ocean fraction
$hFacInf$	0.05		Minimum partial cell ocean fraction as free surface varies
$hFacSup$	2		Maximum partial cell ocean fraction as free surface varies
Γ_T	1.1×10^{-2}		Turbulent heat transfer coefficient
Γ_S	3.1×10^{-4}		Turbulent salt transfer coefficient
T_i	-20	$^{\circ}\text{C}$	Ice interior temperature
$C_{p,i}$	2×10^3	$\text{J kg}^{-1} \text{K}^{-1}$	Specific heat capacity of ice
L	3.34×10^5	J kg^{-1}	Latent heat of fusion

Table A.1 continued from previous page

Parameter	Value	Units	Description
ρ_i	917	kg m^{-3}	Ice density
<i>quadraticDragCoeff</i>	2.2×10^{-3}		Drag coefficient at ice base
C_d	2.2×10^{-3}		Drag coefficient at ice base used in calculation of melting
<i>spongeThickness</i>	10	cells	Thickness of sponge layer
<i>Urelaxobcsinner</i>	2592000	seconds	Timescale for relaxation of zonal velocities at inner edge of sponge
<i>Urelaxobcsbound</i>	60	seconds	Timescale for relaxation of zonal velocities at domain wall boundary
<i>Vrelaxobcsinner</i>	2592000	seconds	Timescale for relaxation of meridional velocities at inner edge of sponge
<i>Vrelaxobcsbound</i>	60	seconds	Timescale for relaxation of meridional velocities at domain wall boundary

References

- Absy, J. M., Schröder, M., Muench, R., Hellmer, H. (2008) Early summer thermohaline characteristics and mixing in the western Weddell Sea. *Deep Sea Research Part II: Topical Studies in Oceanography*. 55 (8-9), 1117–1131. URL: <https://www.doi.org/10.1016/j.dsr2.2007.12.023>.
- Adcroft, A., Campin, J. M., Doddridge, E., Dutkiewicz, S., Evangelinos, C., Ferreira, D., Follows, M., Forget, G., Fox-Kemper, B., Heimbach, P., Hill, C., Hill, E., Hill, H., Jahn, O., Klymak, J., Losch, M., Marshall, J., Maze, G., Mazloff, M., Menemenlis, D., Molod, A., Scott, J. (1997) *MITgcm's User Manual. Revision e9328369*. URL: <https://mitgcm.readthedocs.io/en/latest>.
- Adusumilli, S., Fricker, H. A., Siegfried, M. R., Padman, L., Paolo, F. S., Ligtenberg, S. R. M. (2018) Variable Basal Melt Rates of Antarctic Peninsula Ice Shelves, 1994–2016. *Geophysical Research Letters*. 45 (9), 4086–4095. URL: <https://www.doi.org/10.1002/2017GL076652>.
- Bathmann, U., Smetacek, V., de Baar, H., Fahrbach, E., Krause, G. (1994) The expeditions ANTARKTIS X/6-8 of the research vessel "POLARSTERN" in 1992/93. Report. Alfred–Wegener Inst., Bremerhaven, Germany. 236 pp.
- Bernales, J., Rogozhina, I., Thomas, M. (2017) Melting and freezing under Antarctic ice shelves from a combination of ice-sheet modelling and observations. *Journal of Glaciology*. 63 (240), 731–744. URL: <https://www.doi.org/10.1017/jog.2017.42>.
- Bevan, S. L., Luckman, A. J., Kuipers Munneke, P., Hubbard, B., Kulesa, B., Ashmore, D. W. (2018) Decline in surface melt duration on Larsen C Ice Shelf revealed by the advanced scatterometer (ASCAT). *Earth and Space Science*. 5 (10), 578–591. URL: <https://www.doi.org/10.1029/2018EA000421>.
- Bombosch, A., Jenkins, A. (1995) Modeling the formation and deposition of frazil ice beneath Filchner-Ronne Ice Shelf. *Journal of Geophysical Research: Oceans*. 100 (C4), 6983–6992. URL: <https://www.doi.org/10.1029/94JC03224>.

- Borstad, C., McGrath, D., Pope, A. (2017) Fracture propagation and stability of ice shelves governed by ice shelf heterogeneity. *Geophysical Research Letters*. 44 (9), 4186–4194. URL: <https://www.doi.org/10.1002/2017GL072648>.
- Borstad, C., Rignot, E., Mouginot, J., Schodlok, M. P. (2013) Creep deformation and buttressing capacity of damaged ice shelves: theory and application to Larsen C ice shelf. *The Cryosphere*. 7 (6), 1931–1947. URL: <https://www.doi.org/10.5194/tc-7-1931-2013>.
- Brisbourne, A., Kulesa, B., Hudson, T., Harrison, L., Holland, P., Luckman, A., Bevan, S., Ashmore, D., Hubbard, B., Pearce, E., White, J., Booth, A., Nichols, K., Smith, A. (2020) An updated seabed bathymetry beneath Larsen C Ice Shelf, Antarctic Peninsula. *Earth System Science Data*. 12 (2), 887–896. URL: <https://doi.org/10.5194/essd-12-887-2020>.
- Brisbourne, A., Smith, A., King, E., Nicholls, K., Holland, P., Makinson, K. (2014) Seabed topography beneath Larsen C Ice Shelf from seismic soundings. *The Cryosphere*. 8 (1), 1–13. URL: <https://www.doi.org/10.5194/tc-8-1-2014>.
- Cochran, J. R., Bell, R. E. (2012) Inversion of IceBridge gravity data for continental shelf bathymetry beneath the Larsen Ice Shelf, Antarctica. *Journal of Glaciology*. 58 (209), 540–552. URL: <https://www.doi.org/10.3189/2012JoG11J033>.
- Codiga, D. L. (2011) Unified Tidal Analysis and Prediction Using the UTide Matlab Functions. Technical Report 2011-01. Graduate School of Oceanography, University of Rhode Island, Narragansett, RI. 59 pp. URL: <https://www.doi.org/10.13140/RG.2.1.3761.2008>.
- Cook, A. J., Vaughan, D. G. (2010) Overview of areal changes of the ice shelves on the Antarctic Peninsula over the past 50 years. *The Cryosphere*. 4 (1), 77–98. URL: <https://www.doi.org/10.5194/tc-4-77-2010>.
- Cottier, F., Nilsen, F., Skogseth, R., Tverberg, V., Skarðhamar, J., Svendsen, H. (2010) Arctic fjords: a review of the oceanographic environment and dominant physical processes. In: Howe, J. A., Austin, W. E. N., Forwick, M. Paetzel, M. (Eds.) *Fjord Systems and Archives*. Geological Society, London, Special Publications, Vol. 344, pp. 35–50. URL: <https://www.doi.org/10.1144/SP344.4>.
- Craven, M., Allison, I., Fricker, H. A., Warner, R. (2009) Properties of a marine ice layer under the Amery Ice Shelf, East Antarctica. *Journal of Glaciology*. 55 (192), 717–728. URL: <https://www.doi.org/10.3189/002214309789470941>.

- Davis, P. E. D., Nicholls, K. W. (2019a) Turbulence Observations Beneath Larsen C Ice Shelf, Antarctica. *Journal of Geophysical Research: Oceans*. 124 (8), 5529–5550. URL: <https://www.doi.org/10.1029/2019jc015164>.
- Davis, P. E. D., Nicholls, K. W. (2019b) URL: <https://doi.org/10.5285/16ee2665-d0d0-41b9-a046-23b0a7369c61>.
- Doake, C., Corr, H., Rott, H., Skvarca, P., Young, N. (1998) Breakup and conditions for stability of the northern Larsen Ice Shelf, Antarctica. *Nature*. 391 (6669), 778–780. URL: <https://www.doi.org/10.1038/35832>.
- Fogwill, C., Phipps, S., Turney, C., Golledge, N. (2015) Sensitivity of the Southern Ocean to enhanced regional Antarctic ice sheet meltwater input. *Earth's Future*. 3 (10), 317–329. URL: <https://www.doi.org/10.1002/2015EF000306>.
- Fretwell, P., Pritchard, H. D., Vaughan, D. G., et al. (2013) Bedmap2: improved ice bed, surface and thickness datasets for Antarctica. *The Cryosphere*. 7 (1), 375–393. URL: <https://www.doi.org/10.5194/tc-7-375-2013>.
- Fricker, H. A., Padman, L. (2012) Thirty years of elevation change on Antarctic Peninsula ice shelves from multimission satellite radar altimetry. *Journal of Geophysical Research: Oceans*. 117 (C2), 1–17. URL: <https://www.doi.org/10.1029/2011JC007126>.
- Fürst, J. J., Durand, G., Gillet-Chaulet, F., Tavard, L., Rankl, M., Braun, M., Gagliardini, O. (2016) The safety band of Antarctic ice shelves. *Nature Climate Change*. 6 (5), 479–482. URL: <https://www.doi.org/10.1038/NCLIMATE2912>.
- Glasser, N. F., Kulesa, B., Luckman, A., Jansen, D., King, E. C., Sammonds, P. R., Scambos, T. A., Jezek, K. C. (2009) Surface structure and stability of the Larsen C ice shelf, Antarctic Peninsula. *Journal of Glaciology*. 55 (191), 400–410. URL: <https://www.doi.org/10.3189/002214309788816597>.
- Gordon, A. L., of Principal Investigators, I. S. W. G., Scientists, C. (1993) Weddell Sea exploration from ice station. *Eos, Transactions American Geophysical Union*. 74 (11), 121–126. URL: <https://www.doi.org/10.1029/93EO00260>.
- Grosfeld, K., Hellmer, H., Jonas, M., Sandhäger, H., Schulte, M., Vaughan, D. G. (1998) Marine ice beneath Filchner Ice Shelf: Evidence from a multi-disciplinary approach. In: Jacobs, S., Weiss, R. (Eds.) *Ocean, Ice and Atmosphere Interactions at the Antarctic Continental Margin*. Antarctic Research Series, Vol. 75. Washington

- DC, American Geophysical Union, pp. 319–339. URL: <https://www.doi.org/10.1029/AR075p0319>.
- Hallberg, R. (2013) Using a resolution function to regulate parameterizations of oceanic mesoscale eddy effects. *Ocean Modelling*. 72, 92–103. URL: <https://www.doi.org/10.1016/j.ocemod.2013.08.007>.
- Hellmer, H., Schröder, M., Haas, C., Dieckmann, G., Spindler, M. (2008) The ispol drift experiment. *Deep Sea Research Part II: Topical Studies in Oceanography*. 55 (8-9), 913–917. URL: <https://www.doi.org/10.1016/j.dsr2.2008.01.001>.
- Hellmer, H. H., Huhn, O., Gomis, D., Timmermann, R. (2011) On the freshening of the northwestern Weddell Sea continental shelf. *Ocean Science*. 7, 305–316. URL: <https://www.doi.org/10.5194/os-7-305-2011>.
- Hogg, A. E., Gudmundsson, G. H. (2017) Impacts of the Larsen–C Ice Shelf calving event. *Nature Climate Change*. 7 (8), 540–542. URL: <https://www.doi.org/10.1038/nclimate3359>.
- Holland, D. M., Jenkins, A. (1999) Modeling thermodynamic ice–ocean interactions at the base of an ice shelf. *Journal of Physical Oceanography*. 29 (8), 1787–1800. URL: [https://www.doi.org/10.1175/1520-0485\(1999\)029<1787:MTIOIA>2.0.CO;2](https://www.doi.org/10.1175/1520-0485(1999)029<1787:MTIOIA>2.0.CO;2).
- Holland, P. R. (2017) The transient response of ice shelf melting to ocean change. *Journal of Physical Oceanography*. 47 (8), 2101–2114. URL: <https://www.doi.org/10.1175/JPO-D-17-0071.1>.
- Holland, P. R., Brisbourne, A., Corr, H. F. J., Mcgrath, D., Purdon, K., Paden, J., Fricker, H. A., Paolo, F. S., Fleming, A. H. (2015) Oceanic and atmospheric forcing of Larsen C Ice–Shelf thinning. *The Cryosphere*. 9 (3), 1005–1024. URL: <https://www.doi.org/10.5194/tc-9-1005-2015>.
- Holland, P. R., Corr, H. F. J., Vaughan, D. G., Jenkins, A., Skvarca, P. (2009) Marine ice in Larsen Ice Shelf. *Geophysical Research Letters*. 36 (11), 1–6. URL: <https://www.doi.org/10.1029/2009GL038162>.
- Holland, P. R., Jenkins, A., Holland, D. M. (2008) The response of ice shelf basal melting to variations in ocean temperature. *Journal of Climate*. 21 (11), 2558–2572. URL: <https://www.doi.org/10.1175/2007JCLI1909.1>.

- Howard, S. L., Padman, L., Erofeeva, S. (2019) "CATS2008: Circum-Antarctic Tidal Simulation version 2008." U.S. Antarctic Program (USAP) Data Center. URL: <https://www.doi.org/10.15784/601235>.
- Huhn, O., Hellmer, H. H., Rhein, M., Rodehacke, C., Roether, W., Schodlok, M. P., Schröder, M. (2008) Evidence of deep- and bottom-water formation in the western Weddell Sea. *Deep Sea Research Part II: Topical Studies in Oceanography*. 55 (8-9), 1098–1116. URL: <https://www.doi.org/10.1016/j.dsr2.2007.12.015>.
- IPCC (2014) *Climate Change 2014: Synthesis Report. Contribution of Working Groups I, II and III to the Fifth Assessment Report of the Intergovernmental Panel on Climate Change* [Core Writing Team, R.K. Pachauri and L.A. Meyer (Eds.)]. IPCC, Geneva, Switzerland, 151 pp.
- IPCC (2018) Summary for Policymakers. In: *Global Warming of 1.5°C. An IPCC Special Report on the impacts of global warming of 1.5°C above pre-industrial levels and related global greenhouse gas emission pathways, in the context of strengthening the global response to the threat of climate change, sustainable development, and efforts to eradicate poverty* [Masson-Delmotte, V. and Zhai, P. and Pörtner, H.-O. and Roberts, D. and Skea, J. and Shukla, P.R. and Pirani, A. and Moufouma-Okia, W. and Péan, C. and Pidcock, R. and Connors, S. and Matthews, J.B.R. and Chen, Y. and Zhou, X. and Gomis, M.I. and Lonnoy, E. and Maycock, T. and Tignor, M. and Waterfield T. (Eds.)]. World Meteorological Organization, Geneva, Switzerland, 32 pp.
- IPCC (2019) Summary for Policymakers. In: *IPCC Special Report on the Ocean and Cryosphere in a Changing Climate* [Pörtner, HO and Roberts, DC and Masson-Delmotte, V and Zhai, P and Tignor, M and Poloczanska, E and Mintenbeck, K and Nicolai, M and Okem, A and Petzold, J. Rama, B. Weyer, N.M. (Eds.)]. In press.
- Jacobs, S. (2006) Observations of change in the Southern Ocean. *Philosophical Transactions of the Royal Society A: Mathematical, Physical and Engineering Sciences*. 364 (1844), 1657–1681. URL: <https://doi.org/10.1098/rsta.2006.1794>.
- Jacobs, S., Helmer, H., Doake, C., Jenkins, A., Frolich, R. (1992) Melting of ice shelves and the mass balance of Antarctica. *Journal of Glaciology*. 38 (130), 375–387. URL: <https://www.doi.org/10.3189/S0022143000002252>.
- Jacobs, S. S. (2004) Bottom water production and its links with the thermohaline

- circulation. *Antarctic Science*. 16 (4), 427. URL: <https://doi.org/10.1017/S095410200400224X>.
- Jacobs, S. S., Jenkins, A., Giulivi, C. F., Dutrieux, P. (2011) Stronger ocean circulation and increased melting under Pine Island Glacier ice shelf. *Nature Geoscience*. 4 (8), 519–523. URL: <https://doi.org/10.1038/ngeo1188>.
- Jansen, D., Kulesa, B., Sammonds, P., Luckman, A., King, E., Glasser, N. F. (2010) Present stability of the Larsen C ice shelf, Antarctic Peninsula. *Journal of Glaciology*. 56 (198), 593–600. URL: <https://www.doi.org/10.3189/002214310793146223>.
- Jansen, D., Luckman, A., Kulesa, B., Holland, P. R., King, E. C. (2013) Marine ice formation in a suture zone on the Larsen C Ice Shelf and its influence on ice shelf dynamics. *Journal of Geophysical Research: Earth Surface*. 118 (3), 1628–1640. URL: <https://www.doi.org/10.1002/jgrf.20120>.
- Jansen, D., Luckman, A. J., Cook, A., Bevan, S., Kulesa, B., Hubbard, B., Holland, P. R. (2015) Brief Communication: Newly developing rift in Larsen C Ice Shelf presents significant risk to stability. *The Cryosphere*. 9 (3), 1223–1227. URL: <https://www.doi.org/10.5194/tc-9-1223-2015>.
- Jenkins, A., Holland, D. (2007) Melting of floating ice and sea level rise. *Geophysical Research Letters*. 34 (16), 1–5. URL: <https://www.doi.org/10.1029/2007GL030784>.
- Jenkins, A., Nicholls, K. W., Corr, H. F. J. (2010) Observation and Parameterization of Ablation at the Base of Ronne Ice Shelf, Antarctica. *Journal of Physical Oceanography*. 40 (10), 2298–2312. URL: <https://www.doi.org/10.1175/2010JPO4317.1>.
- Jenkins, A., Shoosmith, D., Dutrieux, P., Jacobs, S., Kim, T. W., Lee, S. H., Ha, H. K., Stammerjohn, S. (2018) West Antarctic Ice Sheet retreat in the Amundsen Sea driven by decadal oceanic variability. *Nature Geoscience*. 11 (10), 733–738. URL: <https://www.doi.org/10.1038/s41561-018-0207-4>.
- Jullion, L., Naveira Garabato, A. C., Meredith, M. P., Holland, P. R., Courtois, P., King, B. A. (2013) Decadal freshening of the Antarctic Bottom Water exported from the Weddell Sea. *Journal of Climate*. 26 (20), 8111–8125. URL: <https://www.doi.org/10.1175/JCLI-D-12-00765.1>.

- Khazendar, A., Rignot, E., Larour, E. (2011) Acceleration and spatial rheology of Larsen C ice shelf, Antarctic Peninsula. *Geophysical Research Letters*. 38 (9), 1–5. URL: <https://www.doi.org/10.1029/2011GL046775>.
- King, M. A., Makinson, K., Gudmundsson, G. H. (2011a) Nonlinear interaction between ocean tides and the Larsen C Ice Shelf system. *Geophysical Research Letters*. 38 (8), 1–5. URL: <https://www.doi.org/10.1029/2011GL046680>.
- King, M. A., Padman, L., Nicholls, K., Clarke, P. J., Gudmundsson, G. H., Kulesa, B., Shepherd, A. (2011b) Ocean tides in the Weddell Sea: New observations on the Filchner-Ronne and Larsen C ice shelves and model validation. *Journal of Geophysical Research: Oceans*. 116 (C6), 1–18. URL: <http://www.doi.org/10.1029/2011JC006949>.
- Kuipers Munneke, P., McGrath, D., Medley, B., Luckman, A., Bevan, S., Kulesa, B., Jansen, D., Booth, A., Smeets, P., Hubbard, B., et al. (2017) Observationally constrained surface mass balance of Larsen C ice shelf, Antarctica. *The Cryosphere*. 11 (6), 2411–2426. URL: <https://www.doi.org/10.5194/tc-11-2411-2017>.
- Kulesa, B., Booth, A. D., O’Leary, M., McGrath, D., King, E. C., Luckman, A. J., Holland, P. R., Jansen, D., Bevan, S. L., Thompson, S. S., Hubbard, B. (2019) Seawater softening of suture zones inhibits fracture propagation in Antarctic ice shelves. *Nature Communications*. 10 (5491), 1–12. URL: <https://www.doi.org/10.1038/s41467-019-13539-x>.
- Kulesa, B., Jansen, D., Luckman, A. J., King, E. C., Sammonds, P. R. (2014) Marine ice regulates the future stability of a large Antarctic ice shelf. *Nature communications*. 5 (1), 1–7. URL: <https://www.doi.org/10.1038/ncomms4707>.
- Liu, Y., Moore, J. C., Cheng, X., Gladstone, R. M., Bassis, J. N., Liu, H., Wen, J., Hui, F. (2015) Ocean-driven thinning enhances iceberg calving and retreat of Antarctic ice shelves. *Proceedings of the National Academy of Sciences*. 112 (11), 3263–3268. URL: <https://www.doi.org/10.1073/pnas.1415137112>.
- Losch, M. (2008) Modeling ice shelf cavities in a z coordinate ocean general circulation model. *Journal of Geophysical Research: Oceans*. 113 (C8). URL: <https://www.doi.org/10.1029/2007JC004368>.
- Luckman, A., Elvidge, A., Jansen, D., Kulesa, B., Munneke, P. K., King, J., Barrand, N. E. (2014) Surface melt and ponding on Larsen C Ice Shelf and

- the impact of föhn winds. *Antarctic Science*. 26 (6), 625–635. URL: <https://www.doi.org/10.1017/S0954102014000339>.
- Makinson, K., Holland, P. R., Jenkins, A., Nicholls, K. W., Holland, D. M. (2011) Influence of tides on melting and freezing beneath Filchner–Ronne Ice Shelf, Antarctica. *Geophysical Research Letters*. 38 (6), 1–6. URL: <https://www.doi.org/10.1029/2010GL046462>.
- Marshall, J., Adcroft, A., Hill, C., Perelman, L., Heisey, C. (1997a) A finite-volume, incompressible Navier Stokes model for studies of the ocean on parallel computers. *Journal of Geophysical Research: Oceans*. 102 (C3), 5753–5766. URL: <https://www.doi.org/10.1029/96JC02775>.
- Marshall, J., Hill, C., Perelman, L., Adcroft, A. (1997b) Hydrostatic, quasi-hydrostatic, and nonhydrostatic ocean modeling. *Journal of Geophysical Research: Oceans*. 102 (C3), 5733–5752. URL: <https://www.doi.org/10.1029/96JC02776>.
- McDougall, T. J., Jackett, D. R., Wright, D. G., Feistel, R. (2003) Accurate and computationally efficient algorithms for potential temperature and density of seawater. *Journal of Atmospheric and Oceanic Technology*. 20 (5), 730–741. URL: [https://www.doi.org/10.1175/1520-0426\(2003\)20<730:AAAEAF>2.0.CO;2](https://www.doi.org/10.1175/1520-0426(2003)20<730:AAAEAF>2.0.CO;2).
- McGrath, D., Steffen, K., Holland, P. R., Scambos, T., Rajaram, H., Abdalati, W., Rignot, E. (2014) The structure and effect of suture zones in the Larsen C Ice Shelf, Antarctica. *Journal of Geophysical Research: Earth Surface*. 119 (3), 588–602. URL: <https://www.doi.org/10.1002/2013JF002935>.
- McPhee, M. G. (1992) Turbulent heat flux in the upper ocean under sea ice. *Journal of Geophysical Research: Oceans*. 97 (C4), 5365–5379. URL: <https://www.doi.org/10.1029/92JC00239>.
- Mouginot, J., Scheuchl, B., Rignot, E. (2012) Mapping of Ice Motion in Antarctica using Synthetic–Aperture Radar Data. *Remote Sensing*. 4 (9), 2753–2767. URL: <https://www.doi.org/10.3390/rs4092753>.
- Mueller, R. D., Hattermann, T., Howard, S. L., Padman, L. (2018) Tidal influences on a future evolution of the Filchner–Ronne Ice Shelf cavity in the Weddell Sea, Antarctica. *The Cryosphere*. 12 (2), 453–476. URL: <https://www.doi.org/10.5194/tc-12-453-2018>.

- Mueller, R. D., Padman, L., Dinniman, M. S., Erofeeva, S. Y., Fricker, H. A., King, M. A. (2012) Impact of tide–topography interactions on basal melting of Larsen C Ice Shelf, Antarctica. *Journal of Geophysical Research: Oceans*. 117 (C5), 1–20. URL: <https://www.doi.org/10.1029/2011JC007263>.
- Nicholls, K., Østerhus, S., Makinson, K., Gammelsrød, T., Fahrbach, E. (2009) Ice-ocean processes over the continental shelf of the southern Weddell Sea, Antarctica: A review. *Rev. Geophys.* 47 (3), 1–23. URL: <https://www.doi.org/10.1029/2007RG000250>.
- Nicholls, K. W., Makinson, K., Venables, E. J. (2012) Ocean circulation beneath Larsen C Ice Shelf, Antarctica from *in situ* observations. *Geophysical Research Letters*. 39 (19), 1–6. URL: <https://www.doi.org/10.1029/2012GL053187>.
- Nicholls, K. W., Pudsey, C. J., Morris, P. (2004) Summertime water masses off the northern Larsen C Ice Shelf, Antarctica. *Geophysical Research Letters*. 31 (9), 1–4. URL: <https://www.doi.org/10.1029/2004GL019924>.
- Nitsche, F., Porter, D., Williams, G., Cougnon, E., Fraser, A., Correia, R., Guerrero, R. (2017) Bathymetric control of warm ocean water access along the East Antarctic Margin. *Geophysical Research Letters*. 44 (17), 8936–8944. URL: <https://www.doi.org/10.1002/2017GL074433>.
- Oerter, H., Kipfstuhl, J., Determann, J., Miller, H., Wagenbach, D., Minikin, A., Graft, W. (1992) Evidence for basal marine ice in the Filchner–Ronne Ice Shelf. *Nature*. 358 (6385), 399–401. URL: <https://www.doi.org/10.1038/358399a0>.
- O’Leary, M., Luckman, A., Project MIDAS (12 July 2017) Larsen C calved trillion ton iceberg. *Project MIDAS*. URL: <http://www.projectmidas.org/blog/calving/>.
- Padman, L., Fricker, H. A., Coleman, R., Howard, S., Erofeeva, L. (2002) A new tide model for the Antarctic ice shelves and seas. *Annals of Glaciology*. 34, 247–254. URL: <https://www.doi.org/10.3189/172756402781817752>.
- Padman, L., Siegfried, M. R., Fricker, H. A. (2018) Ocean tide influences on the Antarctic and Greenland Ice Sheets. *Reviews of Geophysics*. 56 (1), 142–184. URL: <https://www.doi.org/10.1002/2016RG000546>.
- Paolo, F. S., Fricker, H. A., Padman, L. (2015) Volume loss from Antarctic ice shelves is accelerating. *Science*. 348 (6232), 327–331. URL: <https://www.doi.org/10.1126/science.aaa0940>.

- Paolo, F. S., Fricker, H. A., Padman, L. (2016) Constructing improved decadal records of Antarctic ice shelf height change from multiple satellite radar altimeters. *Remote Sensing of Environment*. 177, 192–205. URL: <https://www.doi.org/10.1016/j.rse.2016.01.026>.
- Petty, A., Feltham, D., Holland, P. (2013) Impact of atmospheric forcing on antarctic continental shelf water masses. *Journal of Physical Oceanography*. 43 (5), 920–940. URL: <https://www.doi.org/10.1175/JPO-D-12-0172.1>.
- Pritchard, H., Ligtenberg, S., Fricker, H., Vaughan, D., van den Broeke, M., Padman, L. (2012) Antarctic ice-sheet loss driven by basal melting of ice shelves. *Nature*. 484 (7395), 502–505. URL: <https://www.doi.org/10.1038/nature10968>.
- Rack, W., Rott, H. (2004) Pattern of retreat and disintegration of the Larsen B ice shelf, Antarctic Peninsula. *Annals of Glaciology*. 39, 505–510. URL: <https://www.doi.org/10.3189/172756404781814005>.
- Reese, R., Gudmundsson, G. H., Levermann, A., Winkelmann, R. (2018) The far reach of ice-shelf thinning in Antarctica. *Nature Climate Change*. 8 (1), 53–57. URL: <https://www.doi.org/10.1038/s41558-017-0020-x>.
- Riedl, C., Rott, H., Rack, W. (2004) Recent variations of Larsen Ice Shelf, Antarctic Peninsula, observed by Envisat. *Proc. of the 2004 Envisat & ERS Symposium, Salzburg, Austria, 6-10 September 2004 (ESA SP-572, April 2005)*. URL: <https://www.doi.org/10013/epic.38206.d001>.
- Rignot, E., Casassa, G., Gogineni, P., Krabill, W., Rivera, A., Thomas, R. (2004) Accelerated ice discharge from the Antarctic Peninsula following the collapse of Larsen B ice shelf. *Geophysical Research Letters*. 31 (18), 1–4. URL: <https://www.doi.org/10.1029/2004GL020697>.
- Rignot, E., Jacobs, S., Mouginot, J., Scheuchl, B. (2013) Ice-shelf melting around Antarctica. *Science*. 341 (6143), 266–270. URL: <https://www.doi.org/10.1126/science.1235798>.
- Rignot, E., Mouginot, J., Scheuchl, B. (2011a) Ice flow of the Antarctic ice sheet. *Science*. 333 (6048), 1427–1430. URL: <https://www.doi.org/10.1126/science.1208336>.
- Rignot, E., Velicogna, I., van den Broeke, M. R., Monaghan, A., Lenaerts, J. (2011b) Acceleration of the contribution of the Greenland and Antarctic ice

- sheets to sea level rise. *Geophysical Research Letters*. 38 (5), L05503. URL: <https://www.doi.org/10.1029/2011GL046583>.
- Rintoul, S. R. (2018) The global influence of localized dynamics in the Southern Ocean. *Nature*. 558 (7709), 209–218. URL: <https://www.doi.org/10.1038/s41586-018-0182-3>.
- Robertson, R., Visbeck, M., Gordon, A. L., Fahrbach, E. (2002) Long-term temperature trends in the deep waters of the Weddell Sea. *Deep Sea Research Part II: Topical Studies in Oceanography*. 49 (21), 4791–4806. URL: [https://www.doi.org/10.1016/S0967-0645\(02\)00159-5](https://www.doi.org/10.1016/S0967-0645(02)00159-5).
- Robin, G. de Q. (1979) Formation, Flow, and Disintegration Of Ice Shelves. *Journal of Glaciology*. 24 (90), 259–271. URL: <https://www.doi.org/10.1017/S0022143000014787>.
- Rott, H., Skvarca, P., Nagler, T. (1996) Rapid collapse of northern Larsen ice shelf, Antarctica. *Science*. 271 (5250), 788–792. URL: <https://www.doi.org/10.1126/science.271.5250.788>.
- Royston, S., Gudmundsson, G. H. (2016) Changes in ice-shelf buttressing following the collapse of Larsen A Ice Shelf, Antarctica, and the resulting impact on tributaries. *Journal of Glaciology*. 62 (235), 905–911. URL: <https://www.doi.org/10.1017/jog.2016.77>.
- Scambos, T. A., Bohlander, J., Shuman, C. A., Skvarca, P. (2004) Glacier acceleration and thinning after ice shelf collapse in the Larsen B embayment, Antarctica. *Geophysical Research Letters*. 31 (18), 1–4. URL: <https://www.doi.org/10.1029/2004GL020670>.
- Scambos, T. A., Hulbe, C., Fahnestock, M., Bohlander, J. (2000) The link between climate warming and break-up of ice shelves in the Antarctic Peninsula. *Journal of Glaciology*. 46 (154), 516–530. URL: <https://www.doi.org/10.3189/172756500781833043>.
- Schannwell, C., Cornford, S., Pollard, D., Barrand, N. E. (2018) Dynamic response of Antarctic Peninsula Ice Sheet to potential collapse of Larsen C and George VI ice shelves. *The Cryosphere*. 12 (7), 2307–2326. URL: <https://www.doi.org/10.5194/tc-12-2307-2018>.
- Seroussi, H., Nakayama, Y., Larour, E., Menemenlis, D., Morlighem, M., Rignot, E., Khazendar, A. (2017) Continued retreat of Thwaites Glacier, West Antarctica,

- controlled by bed topography and ocean circulation. *Geophysical Research Letters*. 44 (12), 6191–6199. URL: <http://www.doi.org/10.1002/2017GL072910>.
- Shchepetkin, A. F., McWilliams, J. C. (2009) Correction and commentary for “Ocean forecasting in terrain-following coordinates: Formulation and skill assessment of the regional ocean modeling system” by Haidvogel et al., *J. Comp. Phys.* 227, pp. 3595–3624. *Journal of Computational Physics*. 228 (24), 8985–9000. URL: <http://www.doi.org/10.1016/j.jcp.2009.09.002>.
- Shepherd, A., Ivins, E., Rignot, E., Smith, B., van den Broeke, M., Velicogna, I., Whitehouse, P., Briggs, K., Joughin, I., Krinner, G., Nowicki, S., Payne, T., Scambos, T., Schlegel, N., et al. (2018) Mass balance of the Antarctic Ice Sheet from 1992 to 2017. *Nature*. 558 (7709), 219–222. URL: <https://doi.org/10.1038/s41586-018-0179-y>.
- Shepherd, A., Wingham, D., Payne, T., Skvarca, P. (2003) Larsen Ice Shelf Has Progressively Thinned. *Science*. 302 (5646), 856–859. URL: <https://www.doi.org/10.1126/science.1089768>.
- Shepherd, A., Wingham, D., Rignot, E. (2004) Warm ocean is eroding West Antarctic Ice Sheet. *Geophysical Research Letters*. 31 (23), 1–4. URL: <https://www.doi.org/10.1029/2004GL021106>.
- Skvarca, P., Rack, W., Rott, H., Donángelo, T. I. (1999) Climatic trend and the retreat and disintegration of ice shelves on the Antarctic Peninsula: an overview. *Polar Research*. 18 (2), 151–157. URL: <https://www.doi.org/10.3402/polar.v18i2.6568>.
- Skvarca, P., Rack, W., Rott, H., Donángelo, T. I. Y. (1998) Evidence of recent climatic warming on the eastern Antarctic Peninsula. *Annals of Glaciology*. 27, 628–632. URL: <https://www.doi.org/10.3189/s0260305500018164>.
- Sutterley, T. C., Markus, T., Neumann, T. A., van den Broeke, M., van Wessem, J. M., Ligtenberg, S. R. M. (2019) Antarctic ice shelf thickness change from multimission lidar mapping. *The Cryosphere*. 13 (7), 1801–1817. URL: <https://www.doi.org/10.5194/tc-13-1801-2019>.
- Thoma, M., Jenkins, A., Holland, D., Jacobs, S. (2008) Modelling circumpolar deep water intrusions on the Amundsen Sea continental shelf, Antarctica. *Geophysical Research Letters*. 35 (18), 1–6. URL: <https://www.doi.org/10.1029/2008GL034939>.

- Timmermann, R., Le Brocq, A., Deen, T., Domack, E., Dutrieux, P., Galton-Fenzi, B., Hellmer, H., Humbert, A., Jansen, D., Jenkins, A., Lambrecht, A., Makinson, K., Niederjasper, F., Nitsche, F., Nøst, O. A., Smedsrud, L. H., Smith, W. H. F. (2010) A consistent data set of Antarctic ice sheet topography, cavity geometry, and global bathymetry. *Earth System Science Data*. 2 (2), 261–273. URL: <https://www.doi.org/10.5194/essd-2-261-2010>.
- Turner, J., Guarino, M. V., Arnatt, J., Jena, B., Marshall, G. J., Phillips, T., Bajish, C., Clem, K., Wang, Z., Andersson, T., Murphy, E., Cavanagh, R. (2020) Recent decrease of summer sea ice in the Weddell Sea, Antarctica. *Geophysical Research Letters*. 47 (11), 1–11. URL: <https://www.doi.org/10.1029/2020GL087127>.
- Turner, J., Lu, H., White, I., King, J. C., Phillips, T., Hosking, J. S., Bracegirdle, T. J., Marshall, G. J., Mulvaney, R., Deb, P. (2016) Absence of 21st century warming on Antarctic Peninsula consistent with natural variability. *Nature*. 535 (7612), 411–415. URL: <https://www.doi.org/10.1038/nature18645>.
- Vaughan, D. G., Doake, C. (1996) Recent atmospheric warming and retreat of ice shelves on the Antarctic Peninsula. *Nature*. 379 (6563), 328–331. URL: <https://www.doi.org/10.1038/379328a0>.
- Vaughan, D. G., Marshall, G. J., Connolley, W. M., Parkinson, C., Mulvaney, R., Hodgson, D. A., King, J. C., Pudsey, C. J., Turner, J. (2003) Recent Rapid Regional Climate Warming on the Antarctic Peninsula. *Climatic change*. 60 (3), 243–274. URL: <https://www.doi.org/10.1023/A:1026021217991>.
- Vieli, A., Payne, A. J., Shepherd, A., Du, Z. (2007) Causes of pre-collapse changes of the Larsen B ice shelf: Numerical modelling and assimilation of satellite observations. *Earth and Planetary Science Letters*. 259 (3-4), 297–306. URL: <https://www.doi.org/10.1016/j.epsl.2007.04.050>.
- Walker, D. P., Brandon, M. A., Jenkins, A., Allen, J. T., Dowdeswell, J. A., Evans, J. (2007) Oceanic heat transport onto the Amundsen Sea shelf through a submarine glacial trough. *Geophysical Research Letters*. 34 (2), 1–4. URL: <https://www.doi.org/10.1029/2006GL028154>.
- Wuite, J., Rott, H., Hetzenecker, M., Floricioiu, D., De Rydt, J., Gudmundsson, H., Nagler, T., Kern, M. (2015) Evolution of surface velocities and ice discharge of Larsen B outlet glaciers from 1995 to 2013. *The Cryosphere*. 9 (3), 957–969. URL: <https://www.doi.org/10.5194/tc-9-957-2015>.